

LEONIE KOCH

FIRST-PRINCIPLES STUDY OF THE DEFECT CHEMISTRY AND CONDUCTIVITY
IN SODIUM BISMUTH TITANATE

Zur Erlangung des akademischen Grades
Doktor der Naturwissenschaften (Dr. rer. nat.)
genehmigte Dissertation vorgelegt von
M. Sc. Leonie Koch
geboren in Wiesbaden

Fachbereich Material- und Geowissenschaften
Fachgebiet Materialmodellierung
Technische Universität Darmstadt

Referent: Prof. Dr. Karsten Albe,
Technische Universität Darmstadt

Korreferent: Prof. Dr. Wolfgang Donner,
Technische Universität Darmstadt

Tag der Einreichung: 30.03.2021
Tag der mündlichen Prüfung: 18.06.2021

Darmstadt, 2021
D17

TUprints Data

This document is provided by tuprints, the E-Publishing-Service of the TU Darmstadt:

<http://tuprints.ulb.tu-darmstadt.de>

tuprints@ulb.tu-darmstadt.de

Koch, Leonie: First-principles study of the defect chemistry and conductivity in sodium bismuth titanate

Darmstadt, Technische Universität Darmstadt, 2021

Tag der mündlichen Prüfung: 18.06.2021

Bibliographical Data

Please cite this document as:

URN: urn:nbn:de:tuda-tuprints-198983

URI: <https://tuprints.ulb.tu-darmstadt.de/id/eprint/19898>

This work is published under the Creative Commons License:



Attribution-NonCommercial-ShareAlike 4.0 International (CC BY-NC-SA 4.0)

URL: <https://creativecommons.org/licenses/by-nc-sa/4.0/>

LEONIE KOCH

FIRST-PRINCIPLES STUDY OF THE DEFECT CHEMISTRY AND
CONDUCTIVITY IN SODIUM BISMUTH TITANATE

Leonie Koch: *First-principles study of the defect chemistry and conductivity in sodium bismuth titanate*

ABSTRACT

The present thesis is an endeavor to understand the defect chemistry and conductivity in polymorphic sodium bismuth titanate (NBT) and NBT-based systems with the ultimate goal to design the next generation of ionic conductors for solid oxide fuel cells. Structural modifications such as non-stoichiometry and doping lead to unexpected high oxygen ionic conductivities in these A-site mixed perovskite structures. Particularly, the non-linear dependency of mobile oxygen vacancies on the defect concentration represents a challenge for scientists worldwide in terms of reliability and controllability [1].

What are the fundamental mechanisms during oxygen vacancy migration and how can we use this knowledge to manipulate electric conductivities in our favor? These two central questions will guide us through the present thesis, where we will explore defect interaction, migration, and charge states in doped and undoped NBT.

We discuss these results in the light of different chemical A-site orders, polar, and tilt distortions [2]. For this purpose, we employ density functional theory calculations and focus our analysis on the following main aspects: Electrostatic, covalent, and elastic interactions between defects as well as their coupling to the host lattice. Such a comprehensive defect chemical understanding will allow deriving material properties of structurally and chemically more complex systems such as solid solutions. Furthermore, this knowledge is necessary to establish NBT in versatile industrial applications, ranging from low-loss piezoelectrics to high ionic conductors.

After a broad overview of the present research and an introduction to the most relevant concepts in the field of ferroelectric perovskite oxides in the Chapters 1, 2, and 3, we introduce a macroscopic defect chemical model in Chapter 4. This approach is an over-simplification of the defect chemical complexity and neglects several degrees of freedom, for instance, displacement or electronic state occupation fluctuations [3]. However, it illustrates how phase symmetries, dopant concentrations, and dopant types influence the conductivity in NBT.

In Chapter 5, we present several novel material properties for the undoped and stoichiometric NBT structure, calculated mainly by density functional perturbation theory. These properties are necessary input parameters for all remaining chapters' calculations and serve as a benchmark of density functional theory approaches for A-site disordered perovskite oxides.

A detailed comparison between a Mg-, Fe-, and Al-doping follows in the Chapters 6, 8, 9, and 10. In the former, we primarily deal with the electrostatic interaction between different defect types and local relaxation patterns. In the latter, we focus on charge transition states, elastic effects, and the covalent binding environments. All chapters show a delicate interplay between the electrostatic and the elastic interaction, leading to a reduction of the effective charge carrier concentration. The elastic contribution is

particularly prevalent for small dopant types. We further identify the importance of polar and tilt distortions on the association energy between an oxygen vacancy and a neighboring B-site acceptor dopant. Especially in Chapter 6, we contrast our results to experimental impedance spectroscopy measurements.

The formation of defect associates between an oxygen vacancy and an aluminium dopant in a $((\text{Na,K})_{0.5}\text{Bi}_{0.5})\text{TiO}_3\text{-BiAlO}_3$ solid solution is addressed by a combination of nuclear magnetic resonance spectroscopy and *ab-initio* calculations. In the framework of “Smarter Crystallography” [4], we show that stable first-order defect associates only exist at small Al-dopant concentrations.

ZUSAMMENFASSUNG

Die vorliegende Dissertation beschäftigt sich mit der Defektchemie und Leitfähigkeit in polymorphem Natrium-Bismut-Titanat (NBT) und NBT-basierten festen Lösungen mit dem übergeordneten Ziel, die nächste Generation von Festkörper-Elektrolyten für Brennstoffzellen zu entwickeln. Strukturelle Modifikationen, wie Abweichungen von der idealen Stöchiometrie und Dotierungen, führen zu unerwartet hohen Sauerstoffionen-Leitfähigkeiten in diesen chemisch ungeordneten Perowskit-Strukturen. Insbesondere die nichtlineare Abhängigkeit der mobilen Sauerstoff-Leerstellen von der Defektkonzentration stellt eine Herausforderung für Wissenschaftler weltweit in Bezug auf die Zuverlässigkeit und Kontrollierbarkeit des Materials in industriellen Anwendungen dar [1].

Was sind die grundlegenden Mechanismen während der Sauerstoff-Leerstellen-Migration und wie können wir dieses Wissen nutzen, um elektrische Leitfähigkeiten zu unseren Gunsten zu manipulieren? Diese beiden zentralen Fragen werden uns durch die vorliegende Arbeit leiten, in der wir Defektwechselwirkung, Migration und Ladungszustände in dotiertem und undotiertem NBT untersuchen. Wir diskutieren diese Ergebnisse im Lichte verschiedener chemischer A-Platz-Ordnungen, polarer Verschiebungen und der Rotation von Koordinationspolyedern [2]. Zu diesem Zweck verwenden wir Dichtefunktionaltheorie-Berechnungen und konzentrieren unsere Analyse auf die folgenden Hauptaspekte: Elektrostatische, kovalente und elastische Wechselwirkungen zwischen Defekten sowie deren Kopplung mit dem Wirtsgitter. Ein solch umfassendes Verständnis der Defektchemie ermöglicht die Ableitung von Materialeigenschaften strukturell und chemisch komplexerer Systeme, wie z.B. Mischkristallen. Darüber hinaus ist dieses Wissen notwendig, um NBT in vielfältigen industriellen Anwendungen, von Piezoelektrika bis zu ionischen Leitern, zu etablieren.

Nach einem breiten Überblick über die gegenwärtige Forschung und einer Einführung in die wichtigsten Konzepte auf dem Gebiet der ferroelektrischen Perowskite in den Kapiteln 1, 2 und 3, stellen wir in Kapitel 4 ein makroskopisches Defektchemiemodell vor. Dieser Ansatz ist eine Vereinfachung der komplexen Defektchemie in NBT und vernachlässigt mehrere Freiheitsgrade, z. B. die Fluktuationen in der topologischen und chemischen Ordnung [3]. Wir können mit diesem einfachen Modell dennoch veranschaulichen, wie Phasensymmetrien als auch die Art und Konzentration des Dotanden die Leitfähigkeit in NBT beeinflussen.

In Kapitel 5 stellen wir mehrere neue Materialeigenschaften für die undotierte und stöchiometrische NBT-Struktur vor, welche hauptsächlich mittels der Dichtefunktional-Störungstheorie berechnet wurden. Diese Eigenschaften sind notwendige Eingangsparameter für die Berechnungen aller übrigen Kapitel und dienen als Benchmark für DFT-Berechnungen in ungeordneten Perowskit-Strukturen.

Ein detaillierter Vergleich zwischen einer Mg-, Fe- und Al-Dotierung folgt in den Kapiteln 6, 8, 9 und 10. Im ersten Kapitel beschäftigen wir uns hauptsächlich mit der elektrostatischen Wechselwirkung zwischen verschiedenen Defekttypen und lokalen Relaxationsmustern. Im zweiten Kapitel konzentrieren wir uns auf Ladungsübergangszustände, elastische Effekte und die kovalenten Bindungsumgebungen. Alle Kapitel zeigen ein komplexes Zusammenspiel zwischen der elektrostatischen und der elastischen Wechselwirkung, die zu einer Verringerung der effektiven Ladungsträgerkonzentration führt. Der elastische Beitrag ist besonders bei kleinen Dotanden vorherrschend. Weiterhin wird die Bedeutung von polaren Verschiebungen der Kationen und Oktaederverkippungen auf die Assoziationsenergie zwischen einer Sauerstoff-Leerstelle und einem benachbarten B-Platz Dotanden aufgezeigt. Insbesondere in Kapitel 6 stellen wir unsere Ergebnisse experimentellen Impedanzspektroskopie-Messungen gegenüber.

Die Bildung von Defektassoziaten zwischen einer Sauerstoff-Leerstelle und einem Aluminium-Dotant in einem $((\text{Na},\text{K})_{0.5}\text{Bi}_{0.5})\text{TiO}_3\text{-BiAlO}_3$ Mischkristall wird mit Hilfe einer Kombination aus Kernspinresonanz-Messungen und *ab-initio*-Rechnungen untersucht. Entsprechend der Philosophie "Smarter Crystallography" [4] zeigen wir, dass stabile Defektassoziationen erster Ordnung nur bei kleinen Al-Dotierkonzentrationen existieren.

Start where you are. Use what you have. Do what you can.

— ARTHUR ASHE

ACKNOWLEDGEMENTS – DANKSAGUNG

Dieses Zitat von Arthur Ashe ist ein scheinbar einfaches und erfolgsversprechendes Rezept. Um eine Herausforderung in der Zukunft zu meistern, solle man nicht nur einfach starten, sondern alle verfügbaren Mittel verwenden und sich der Aufgabe vollends hingeben. Neben der zahlreichen Literatur, den großartigen Errungenschaften von Wissenschaftlern auf der ganzen Welt und durchdachten Code-Strukturen, zähle ich besonders die Menschen, welche mich während meiner Zeit als Doktorandin (und darüber hinaus) begleitet haben als eines der wertvollsten “Hilfsmittel”.

Zuallererst möchte ich Prof. Dr. Karsten Albe, sowohl für die Bereitstellung dieser Arbeit, als auch seine fortwährende Unterstützung bedanken.

Einen großen Dank möchte ich ebenfalls an Prof. Dr. Wolfgang Donner für die Begutachtung dieser Arbeit, als auch Prof. Dr. Vera Krewald und Dr. Till Frömlich für Ihren Einsatz in der Prüfungskommission aussprechen.

In diesem Zusammenhang möchte ich besonders Till Frömlich hervorheben, der in den vergangenen Jahren mit Dr. Sebastian Steiner an meiner Seite stand. Beide waren nicht nur bereit mit Ideen zu jonglieren, sondern diese im Experiment zu verwirklichen. Wichtige Resultate und Erkenntnisse aus diesen Daten sind der Grundstein dieser Thesis. Vielen Dank für eine kollegiale und angenehme Zusammenarbeit!

Einen weiteren großen Beitrag zu dieser Arbeit habe ich Dr. Pedro Groszewicz zu verdanken. Ohne seine Hilfe und sorgsamem NMR-Messungen würden entscheidende Bausteine in der vorliegenden Dissertation fehlen.

Besonders gerne erinnere ich mich an meine Hiwine Sonja Egert. Ich hoffe, ich konnte ihr genauso viel beibringen, wie sie mir.

I am incredibly grateful for my extended stay in the Theoretical Materials Physics Group at the University of Liège. Especially, I want to thank Prof. Philippe Ghosez for the numerous fruitful discussions and “light bulb” moments, new perspectives, and a slight idea on how powerful perovskites really are. Furthermore, I am greatly indebted to Dr. Marcus Schmitt, Dr. Fabio Ricci, Dr. Eric Bousquet, who have been great colleagues and friends. Thank you for being patient with me and answering all my questions.

Besides, I want to thank Prof. Kai Nordlund from the Materials Physics Department of the University of Helsinki for hosting me several times and for all discussions on the mechanical behavior of materials.

Mehrere Jahre darf ich bereits ein Mitglied der Materialmodellierer in Darmstadt sein. Auf diesem Weg bin ich vielen besonderen Menschen begegnet, die mich wissenschaftlich und auch persönlich auf unterschiedliche Weise unterstützt und geprägt haben. Auch wenn mein Dank jedem Einzelnen gilt, möchte ich an dieser Stelle die Gelegenheit nutzen, um ganz besondere Freunde hervorzuheben.

An erster Stelle kann keine andere als Dr. Constanze Kalcher stehen, eine der coolsten Personen, denen ich bisher begegnen durfte, und die mich schon mein ganzes "MM"-Leben begleitet.

A big thank you to Dr. Daniel Barragan-Yani for your patience with me and all the supporting conversations about just everything.

Ich möchte mir die vergangenen Jahre nicht ohne Dr. Kai-Christian Meyer, Dr. Tobias Brink und Dr. Alexander Stukowski vorstellen, von denen ich in jeder Hinsicht unglaublich viel lernen durfte.

Auch wenn Abschiede von lieb gewonnenen Kollegen immer schwierig sind, so gehen mit ihnen auch immer neue Freundschaften einher. Ein großer Dank gilt Marcel Sadowski, der sich alle meine Ideen anhören musste und in meinen verzweifelten Momenten oft einen kühnen Kopf bewahrt hat.

Was wäre eine Tasse Tee ohne ein Gespräch mit Arne Klomp und Daniel Utt? Danke, für Eure Freundschaft, Unterstützung und vor allem, dass Du mich auch im Home-Office nicht vergessen hast, Arne!

Ein großer Dank gilt auch Gabriele Rühl und Renate Hernichel. Danke für euren beherzten Einsatz und eure Energie für uns alle!

Neben den vielen lieben Menschen am Institut, möchte ich mich hiermit auch herzlich bei Karoline Wowra bedanken. Danke für die vielen Crossfit-Workouts, die zahlreichen Gespräche und Deine aufmunternde Art. Ich möchte mich auch ganz besonders bei meinen Freunden in der "Ferne", Mara Ackermann, Dr. Svenja Heise, Jan Preusker, Christine Breinich und Claudia Basic für viele schöne Erinnerungen bedanken.

Keine Worte vermögen meinen Dank für meine Eltern, Annette und Andreas Koch, auszudrücken. Danke für Eure Unterstützung, Eure Liebe, die Gewissheit, dass Ihr stolz auf mich seid und dass ich es auch sein darf. Ich habe unendlich großes Glück Euch, Rebekka Waiblinger und Johanna Koch, als Geschwister und natürlich Euch, Rainer Waiblinger und Marius Schmitt in meiner "erweiterten" Familie zu haben. Ein herzliches Dankeschön möchte ich auch meiner Oma, Irmgard Feige, aussprechen!

Danke Dirk Gründung, dass Du an meiner Seite stehst und in all der Zeit so geduldig mit mir warst. Vor allem danke ich Dir jedoch, dass Du mich nie aufgeben lässt.

I gratefully acknowledge financial support by the Deutsche Forschungsgemeinschaft (DFG) through the project Grant No. AL 578/20-1. Computing time was granted by the John von Neumann Institut for Computing (NIC) and provided on the supercomputer JURECA [5] at the Jülich Supercomputing Centre (JSC). Additional calculations for this research were conducted on the Lichtenberg high performance computer of

the TU Darmstadt.

Mein abschließender Dank gilt der Koch Prepress GmbH, für den Druck dieser Arbeit.

CONTENTS

LIST OF FIGURES	xvii
LIST OF TABLES	xxi
ACRONYMS	xxii
NOMENCLATURE	xxv
I INTRODUCTION	1
1 MOTIVATION	3
2 STATE OF THE ART	5
2.1 Lead-free piezoelectrics – Laboratory vs. market	5
2.1.1 Reasons for a sustainable research and continuous development of lead-free piezoelectrics and why PZT has not been replaced so far	5
2.1.2 Does lead-free mean environmentally friendly? Why did we in- vestigate sodium bismuth titanate?	6
2.1.3 NBT–A friend for all situations?	7
2.2 The perovskite structure – An all-rounder?	7
2.3 Sodium bismuth titanate – A chameleon?	10
2.3.1 Searching for the ground state of NBT	11
2.3.2 The consequence of disorder on the computational complexity .	14
2.4 Structural instabilities–The triumph of broken symmetry	15
2.4.1 Ginzburg-Landau-Devonshire theory–Competition or coopera- tion?	16
2.4.2 Lattice dynamics–The phonon mode picture	18
2.4.3 The theory of ferroelectricity–ferroelectricity as a collective phe- nomenon	20
2.5 Functional properties	22
2.5.1 The concept of Born effective charges	24
2.5.2 Interatomic force constants	25
2.5.3 Covalent bonding in perovskite oxides and the lone pair effect .	25
2.6 Ionic conductivity	27
2.6.1 Conductivity – A description on the macroscopic scale	27
2.6.2 Conductivity – Interactions on the microscopic scale	29
2.6.3 Defect association – A way to manipulate ionic conductivities? .	29
2.6.4 What we can learn from Arrhenius plots	30
2.6.5 Activation and migration barriers – key parameters for a smooth flow?	31
2.6.6 Three conductor types in one material and the power of A-site non-stoichiometry	34
2.6.7 Acceptor doping – NBT’s breakthrough as a solid electrolyte? .	35
2.6.8 NBT-based solid solutions – “Too many cooks spoil the broth” or “the more the better”?	39
2.6.9 Stoichiometric doping – The wolf in sheep’s clothing	40
2.6.10 Aluminium – the individualists among the acceptor dopants? .	41

2.6.11	Things to remember	46
2.7	Open questions and roadmap	47
3	METHODS	49
3.1	General Methods	49
3.2	The Born-Oppenheimer and Hartree-Fock approximation	50
3.3	The density functional theory	52
3.3.1	The Hohenberg-Kohn theorem	52
3.3.2	Kohn-Sham equations	54
3.3.3	The band gap problem	56
3.4	The exchange correlations functional	57
3.4.1	Local density approximation	57
3.4.2	Generalized gradient approximation	57
3.4.3	Hybrid potentials	58
3.4.4	Is the GGA functional sufficient to represent the electronic structure of NBT?	61
3.5	Periodicity in solids	61
3.5.1	Pseudopotential approximation	62
3.6	Density functional perturbation theory	62
3.7	Ionic relaxation and the Hellmann-Feynman theorem	64
3.8	Modern theory of polarization	65
3.9	Charged-defect supercell calculations	67
3.9.1	Formation energies	68
3.9.2	Charge transition levels	70
3.9.3	Electrostatic interaction in charged supercells	71
3.10	Ab-initio meets elasticity theory	74
3.10.1	Relaxation volumes	74
3.10.2	Correction of long-range elastic field effects	77
3.10.3	Elastic dipole tensor	78
3.10.4	Absolute deformation potential	79
3.11	Nudged elastic band method	81
3.12	Nuclear magnetic resonance spectroscopy	82
3.13	Visualization of chemical bonding in solids	84
3.14	Conclusion	86
II	RESULTS	89
4	IONIC CONDUCTIVITY: A MACROSCOPIC MODEL	91
4.1	Computational methods	92
4.2	An analytical model	93
4.2.1	Phase dependency	94
4.3	Things to remember	98
5	PHYSICAL PROPERTIES OF SODIUM BISMUTH TITANATE	99
5.1	Computational methods	99
5.2	Elastic and dielectric tensors	99
5.3	Influence of symmetry on the electronic structure	103
5.3.1	Band structures	103
5.3.2	Density of states and bonding analysis of bulk structures	107
5.4	Phonon dispersion curves	111

5.5	Polarization in $Pmc2_1$	113
5.6	Born effective charges and interatomic force constants	117
5.6.1	Born effective charges in a $P4/mmm$ structure	117
5.6.2	Interatomic force constants	118
5.7	Things to remember	123
6	THE EFFECT OF ACCEPTOR DOPANTS IN NBT	127
6.1	Computational methods	127
6.2	Binding energies in different model scenarios	128
6.2.1	Defect association leads to a local displacement disorder	129
6.2.2	Energy lowering by the formation of defect associates	133
6.3	A-site doping does not lead to the formation of defect associates	137
6.4	Dopant clusters change the defect binding energy	138
6.5	Oxygen vacancy pinning caused by natural Bi non-stoichiometry	140
6.6	The effect of NBT-BT solid solutions on dopant-vacancy associations	141
6.7	Influence of lattice symmetry on the defect thermodynamics	147
6.7.1	Tetragonal structure	147
6.7.2	Cubic structure	149
6.7.3	Orthorhombic structure	150
6.8	Migration barriers in a R_3 host lattice	150
6.9	Ab-initio vs. Model vs. Experiment – Does it match?	153
6.9.1	Comparison with the macroscopic defect model	153
6.9.2	Comparison with the experiments	154
6.10	Things to remember	154
7	THE FATE OF AL IN NBT: SEEING IS BELIEVING	157
7.1	Computational methods	157
7.2	Assignment of chemical shifts to structural motifs by DFT	159
7.3	Predictions about the formation of defect associates	162
7.4	Things to remember	164
8	CHARGE TRANSITION STATES	167
8.1	Computational methods	168
8.2	The isolated oxygen vacancy wants to stay positive	169
8.3	The charge state of a vacancy-dopant associate – The vacancy wins	174
8.4	Things to remember	181
9	LONG-RANGE STRAIN FIELDS – THE ELASTIC EFFECT OF VACANCIES	183
9.1	Computational methods	183
9.2	Elastic dipole tensor and relaxation volumes	184
9.3	Things to remember	190
10	COVALENT BONDING CONTRIBUTION TO THE STABILITY OF DEFECT ASSOCIATES	191
10.1	Fighting against charge loss: Rehybridization of Fe-O quantum states	191
10.2	A solid solution with $BaTiO_3$ stabilizes the Fe-V defect associate	194
10.3	Electronic conductivity due to shallow dopant-oxygen states?	196
10.4	A-site order hardly influences covalent bonding contribution	198
10.5	Things to remember	198
III	CONCLUSIONS	201
11	SUMMARY	203

12	OUTLOOK	209
IV	APPENDIX	211
A	APPENDIX	213
A.1	Crystal field splitting in the R_3 structure	213
A.2	Can we compare the density of states of for several symmetries at the Γ -point?	216
A.3	Linearity of the hybrid potential	217
A.4	Structural parameters	217
	DECLARATION	219
	BIBLIOGRAPHY	221

LIST OF FIGURES

Figure 1	Cubic perovskite oxide structure	8
Figure 2	Structural instabilities depending on Goldschmidt's tolerance factor	9
Figure 3	Visualization of the in- and anti-phase tilt in NBT	10
Figure 4	Visualization of the different structural degrees of freedom in NBT	11
Figure 5	Temperature dependent phase sequence in NBT	11
Figure 6	Illustration of the local and global order in NBT	14
Figure 7	Group-subgroup relations of A-site ordered cubic NBT	15
Figure 8	Examples for a first- and second-order phase transition	17
Figure 9	Illustration of a competitive mode coupling	18
Figure 10	Schematic representation of a lattice mode softening	21
Figure 11	Schematic illustration of the lone-pair effect	27
Figure 12	Oxygen neighbor shells in the R3 structure	30
Figure 13	Scheme of the three stages of the ionic conductivity	31
Figure 14	Illustration of the formation, migration, and association energy	32
Figure 15	Scheme of the saddle point configuration during migration of oxygen	33
Figure 16	Bulk conductivity of NBT at 600 °C for different A-site non-stoichiometries	35
Figure 17	Bulk conductivity of Mg-, Al-, and Fe-doped NBT and NBT-6BT	37
Figure 18	Concentration dependent bulk conductivity at 500 °C for Mg-, Al-, and Fe-doped NBT	39
Figure 19	Coordination polyhedra as a function of the chemical shift	42
Figure 20	Impedance spectra of Al-doped NBT at 500 °C	44
Figure 21	²⁷ Al MAS NMR spectra of Al acceptor doped NBT-xAl and NKBT-xBA solid solutions	45
Figure 22	²⁷ Al 3QMAS NMR spectrum of a NKBT-7BA solid-solution	46
Figure 23	Correspondence between the external potential, the ground state, and the ground state density in DFT approaches	53
Figure 24	Density of states for an R3 unit cell, calculated with GGA, Hybrid and a G ₀ W ₀ approach	60
Figure 25	Definition of spontaneous polarization and the concept of a polarization lattice	66
Figure 26	Relationship between the defect concentration, the formation energy, and the Fermi energy	69
Figure 27	Definition of charge transition levels in defective supercells	70
Figure 28	Schematic energy level diagram of the electronic states needed to calculate the absolute deformation potential	80
Figure 29	Schematic illustration of the kink in the ionic conductivity	92
Figure 30	Conductivity model for 1 % Mg-dopant concentration with phase dependent and phase independent association energies	95

Figure 31	Phase dependent conductivity model for different doping concentrations	97
Figure 32	Binding energies for a defect associate in the presence of two Mg-dopants	98
Figure 33	Temperature and frequency dependent permittivity of NBT . . .	101
Figure 34	Electronic band structure (GGA) of the a) rhombohedral and the b) tetragonal structure with a 111 cation order	104
Figure 35	Projected band structure (GGA) of the R3 NBT unit cell	105
Figure 36	Energy and band gap size for several distortion amplitude in 111-ordered NBT	106
Figure 37	Visualization of the symmetry-adapted distortion modes Γ_5^- and Γ_4^- within the R3 structure	107
Figure 38	Density of states for bulk structures of several symmetries . . .	108
Figure 39	Bond-weighted distribution function for a Mg dopant in a R3 matrix	109
Figure 40	Crystal orbital hamiltonian population for Bi-O, Ti-O, and Bi-Ti interactions	110
Figure 41	Charge density of a Na-deficient NBT structure	111
Figure 42	Phonon dispersion curve and projected phonon density of states for a P4/mmm structure	112
Figure 43	Phonon dispersion curve and projected phonon density of states for a Pmc2 ₁ structure	114
Figure 44	Spontaneous polarization and energy as a function of mode distortion amplitudes	115
Figure 45	Visualization of the symmetry-adapted modes within a Pmc2 ₁ structure	116
Figure 46	Development of symmetry-adapted distortion modes of the Pmc2 ₁ structure	117
Figure 47	Energy-distortion curves for several symmetry-adapted distortion modes in Pmc2 ₁	118
Figure 48	Lattice sites in a P4/mmm, a Pmc2 ₁ and a R3 structure	119
Figure 49	Interatomic force constants for a Ti-Ti interaction as function of distance in a P4/mmm structure	121
Figure 50	Interatomic force constants as a function of distance in a P4/mmm structure	122
Figure 51	Interatomic force constants as a function of distance in a R3 structure	124
Figure 52	Interatomic force constants as a function of distance in a Pmc2 ₁ and R3 structure	125
Figure 53	Oxygen octahedral tilts in a R3 symmetry and oxygen octahedral tilt distribution after the relaxation of a defect associate configuration in R3	129
Figure 54	Relationship between the defect dipole and the spontaneous polarization in a R3 host symmetry	131
Figure 55	Ion displacements upon introducing a Fe-acceptor dopant and oxygen vacancy	132

Figure 56	Binding energy between an oxygen vacancy and an acceptor dopant on the B-site	133
Figure 57	A-site cation displacements caused by acceptor doping or oxygen non-stoichiometry	135
Figure 58	Coulomb energy of the supercell as a function of the distance between an oxygen vacancy and a Mg-dopant	136
Figure 59	Binding energy between an oxygen vacancy and an Al dopant on the A-site	137
Figure 60	Binding energy between an oxygen vacancy and a first neighbor Fe'_{Ti} cluster	138
Figure 61	Different dopant cluster arrangements and the comparison of two different spin arrangements in Fe-doped NBT	140
Figure 62	Binding energy between an oxygen vacancy and a bismuth vacancy	141
Figure 63	Energies for a Fe-oxygen associate in a NBT-3BT solid solution	142
Figure 64	Five different NBT-3BT configurations with a Fe-oxygen associate	143
Figure 65	Five different NBT-3BT configurations containing a Fe dopant and an oxygen vacancy for the calculation of association energies	144
Figure 66	Binding energies between a Fe dopant and an oxygen vacancy in various NBT-3BT model structures	145
Figure 67	Schematic illustration of a percolation path of topological distorted regions	146
Figure 68	Binding energy of a Mg dopant and an oxygen vacancy in a 111-ordered tetragonal structure	147
Figure 69	Energy of an oxygen vacancy in a 111-ordered structure with varying Γ_5^- mode amplitude	148
Figure 70	Binding energy in an initially cubic NBT host structure	149
Figure 71	Energies of different dopant-oxygen associates in a 001-ordered orthorhombic structure	150
Figure 72	Migration energies in acceptor doped NBT with an R_3 host lattice	151
Figure 73	Summary of the different charge compensating oxygen vacancy concentration, and the Coulomb interaction in acceptor doped NBT	155
Figure 74	Determination of a reference curve for theoretical σ_{iso} values	159
Figure 75	Different chemical environments and their theoretical chemical shift	160
Figure 76	Structure model of $\text{Bi}_2\text{Al}_4\text{O}_9$	162
Figure 77	Visualization of the charge correction scheme of Freysoldt and Kumagai	169
Figure 78	Charge transition states for an isolated oxygen vacancy	170
Figure 79	A-site displacements for two different neutral oxygen vacancy positions in undoped NBT	171
Figure 80	Charge density difference between a V_{O} and a $\text{V}_{\text{O}}^{\cdot\cdot}$ defect	171
Figure 81	Density of states for different charged defects of defect complexes	172

Figure 82	Band decomposed charge density for defect states in undoped NBT with different charge states of the supercell	173
Figure 83	Arrhenius plot for NBT under reducing conditions	174
Figure 84	Comparison of the thermodynamic transition states between the single vacancy and a defect associate	175
Figure 85	Comparison between the thermodynamic transition states of a defect associate in a rhombohedral and the tetragonal structure	176
Figure 86	Comparison of thermodynamic transition states in Mg-doped NBT at different strain states	177
Figure 87	Comparison of thermodynamic transition states between Fe-, Al-, Mg-doped NBT	177
Figure 88	Band decomposed charge density for Fe-doped NBT with different charge states of the supercell	178
Figure 89	Band decomposed charge density for defect states in Fe-doped NBT with different charge states of the supercell	180
Figure 90	Main diagonal components of the elastic dipole tensor for Mg-, Al-, and Fe-doped NBT	187
Figure 91	Comparison between the relaxation volume of a defect dipole and the ionic radii of the dopant in Mg-, Al-, and Fe-doped NBT	188
Figure 92	Summary of the different charge compensating oxygen vacancy concentration, the Coulomb, and the elastic interaction in acceptor doped NBT	190
Figure 93	Density of states for different Fe-doped structures	192
Figure 94	Crystal Orbital Hamiltonian Population for acceptor doped NBT	194
Figure 95	Crystal Orbital Hamiltonian Population for Fe-doped NBT in several configurations	195
Figure 96	Comparison of the charge density between a Fe-doped NBT and a Fe-doped NBT-BT structure	196
Figure 97	Summary of the different charge compensating oxygen vacancy concentration, the Coulomb, the elastic, and the covalent interaction in acceptor doped NBT	199
Figure 98	Schematic energy-level diagram for an octahedral environment .	214
Figure 99	Schematic energy-level diagram for a C_3 point symmetry . .	214
Figure 100	Density of states for the d-orbitals in Fe-doped NBT	215
Figure 101	Band unfolding of a Γ_5^- distorted supercell	216
Figure 102	Linearity of the hybrid potential	217

LIST OF TABLES

Table 1	Physical quantities (frozen-ion) related to first and second-order derivatives of the total energy	63
Table 2	Elastic constants in different symmetries of NBT	100
Table 3	Additional pseudocubic components of the elastic constant tensor in R_3	102
Table 4	Dielectric tensor for NBT with R_3 and $Pmc2_1$ symmetry	103
Table 5	Average I_pCOHP per bond in the 111-ordered tetragonal, cubic, and rhombohedral, as well as 001-ordered orthorhombic bulk structures	111
Table 6	Born effective charges of different atom types in a $P4/mmm$ structure	118
Table 7	Total self-force constants for $P4/mmm$, $Pmc2_1$, and R_3	120
Table 8	Migration barriers for different acceptor dopants in a R_3 host lattice	152
Table 9	Relaxation volumes and elastic dipole tensor components for doped an undoped NBT	185
Table 10	Relaxation volumes and elastic dipole tensor components for doped an undoped NBT	186
Table 11	Difference of relaxation volumes of vacancy-dopant associates on various neighbor sites	189
Table 12	Structural parameters for various NBT structures	218

ACRONYMS

AFD	Antiferrodistortive
AE	All-electron
BA	Bismuth aluminate
BSE	Backscattered electron diffraction
BT	Barium titanate
BWDF	Band-weighted distribution function
CB	Conduction band
CBM	Conduction band minimum
COHP	Crystal orbital Hamiltonian population
COOP	Crystal orbital overlap population
DFT	Density functional theory
DLS	Defect localized state
DOS	Density of states
EA	Electron affinity
EPR	Paramagnetic resonance
FNV	Freysoldt, Neugebauer, van der Walle
FWHM	Full width half maximum
GGA	Generalized gradient approximation
GIPAW	Gauge-including projector augmented wave
HSE	Heyd-Scuseria-Ernzerhof screened-exchange hybrid functional
IP	Ionization potential
IpCOHP	Integrated projected crystal orbital Hamiltonian population
iso	Isotropic
KBT	Potassium bismuth titanate
KNN	Potassium sodium niobate
KS	Kohn-Sham
LDA	Local density approximation

LOBSTER Local orbital basis suite towards electronic-structure-reconstructions

lr Long range

MAS Magnetic angle spinning

MEMS Micro-electro-mechanical systems

MQ Multiple-quantum

NBT Sodium bismuth titanate

NMR Nuclear Resonance Spectroscopy

NN Next neighbor shell

PA Potential alignment

PAW Projector augmented wave

PBE Perdew-Burke-Ernzerhof

pc Pseudo cubic

pCOHP Projected crystal orbital hamiltonian population

pDOS Projected density of states

PS Pseudised

PZT Lead zirconate titanate

REACH Registration, Evaluation, Authorization, and Restriction of Chemicals

RoHS Restriction of Hazardous Substances

SOFC Solid oxide fuel cell

sr Short range

STO Strontium titanate

sX Screened exchange

U Orbital-dependent on-site repulsion interaction

VASP Vienna *ab-initio* simulation package

VB Valence band

VBM Valence band maximum

WEEE Waste Electrical and Electronic Equipment

XAFS X-ray absorption fine structure

XRD X-ray diffraction

YAG Yttrium aluminium garnet

YSZ Yttrium-stabilized zirconia

NOMENCLATURE

NOTATION FOR DEFECTS

D_i^q	Dopant of type D on lattice site i with charge q
e'	Electron
h'	Hole
V_i^q	Vacancy of species i with charge q

PHYSICAL CONSTANTS

k_B	Boltzmann constant
F	Faraday constant
R	Ideal gas constant
\hbar	Reduced planck constant
m	Electron rest mass

MATHEMATICAL SYMBOLS

∇	Nabla operator
Γ_i	Irreducible representation (irrep)
γ	Homomorphism
Tr	Trace of tensor
\Im	Imaginary part
\Re	Real part
\mathcal{V}	Vector space
\mathcal{G}/\mathcal{H}	Space groups
$g \in \mathcal{G}$	Symmetry operation of space group \mathcal{G}
\mathbf{t}_i	Tangent
H	Hamilton operator
T_n/T_e	Kinetic energy operator for cores and electrons, respectively
V_{nn}/V_{ee}	Potential energy operator for cores and electrons, respectively

OTHER SYMBOLS (GREEK)

α	Madelung constant
Γ	Jump frequency
γ_{nj}	Internal strain tensor
Δ_q	Energy alignment constant
δ	δ -function
δ_{qis}	Quadrupolar induced shift
δ_{iso}	Isotropic chemical shift tensor
$\tan \delta$	Dielectric loss
ϵ_i	Eigenvalue
$\epsilon_{\alpha\beta}$	Dielectric tensor
η	Order parameter
η_{ij}	Strain
Θ_α	Occupation of state α
κ_i	Atom i in the unit cell
μ_i	Chemical potential
σ	Conductivity
σ_{ij}	Stress
σ_{iso}	Isotropic magnetic shielding tensor
ϕ^\pm	Tilt mode
ϕ_i	Solution of single-particle Schrödinger equation (eigenstate)
$\chi_{\alpha\beta}$	Susceptibility tensor
Ψ	Many-body wave function
Ψ_0	Ground state
$\psi_{n,k}$	Bloch function
$\Delta\Omega_f$	Formation volume
$\Delta\Omega_r$	Relaxation volume
Ω_H	Volume of host cell
Ω	Supercell volume
Ω_0	Unit cell volume
ω_{scr}	Screening factor in hybrid functionals
ω	Frequency of phonon mode

OTHER SYMBOLS (LATIN)

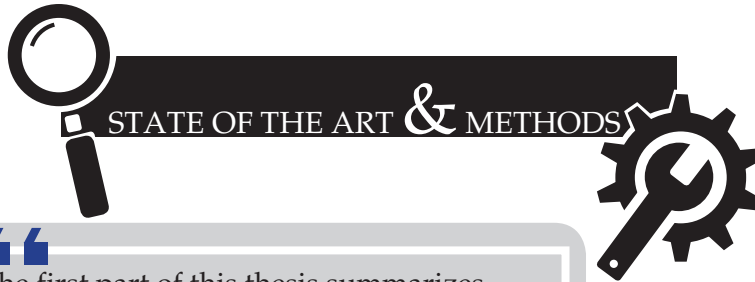
\mathcal{A}	Bijjective map
$\mathcal{A}_{\tau,m}$	Amplitude of displacement
a	Jump distance
a	Lattice constant
α_i	Deformation potential

B	Magnetic field
B	Bulk modulus
B_{AB}	Bond population
C_{jk}	Elastic constant tensor
C_q	Coupling constant
c_k	Concentration of species k
$c_{n,k}$	Expansion coefficient of Bloch function
D	Diffusion constant
$d_{\alpha j}$	Piezoelectric tensor
$\mathcal{D}_{\text{mac},\alpha}$	Macroscopic displacement field
E_a	Activation energy
E_F	Fermi energy
E_g	Band gap
E_H	Hartree energy
$E_i[X^q]$	Energy (of type i) of supercell with defect type X of charge q
E_{int}	Interaction energy
E^{lat}	Screened lattice energy of model charge
$\mathcal{E}_{\text{mac},\beta}$	Macroscopic electric field in direction β
E_{xc}	Exchange correlation energy
F	Free energy
$F_{i\alpha}^a$	Interatomic force constant
$f_{\kappa,\alpha}$	Force in direction α at atom κ
\mathcal{G}	Set of ground states
G	Gibbs free energy
G	Reciprocal lattice vector
$G_{ik,jl}$	Second derivative of anisotropic Green's function
ΔH_a	Activation enthalpy
ΔH_{asso}	Association enthalpy
ΔH_b	Energy barrier
ΔH_f	Formation enthalpy
ΔH_m	Migration enthalpy
ΔH_r	Relaxation energy
j	Flux
K_{nm}	Interatomic force constant tensor
k,q	Wave vectors
L	Linear dimension of supercell
M_α	Mass of nucleus α
\mathcal{N}	Set of ground state densities
n_0	Ground state density
n_b	Background charge

P	Pressure
\mathbf{P}	Polarization
P_{ij}	Elastic dipole tensor
$P_{\mu\nu j}^{\text{proj}}$	Projected density matrix
$p_{m,\alpha}$	Mode polarity
Q	Second radial moment
q	Charge
\mathbf{R}	Real lattice vector
R_{WS}	Wigner Seitz radius
r_c	Critical radius
r_X	Radius of species X
r_{X-Y}	Distance between species X and Y
\mathbf{r}	Position of atom in supercell
ΔS_{asso}	Association entropy
S_{ijkl}	Elastic compliance tensor
ΔS_{mig}	Migration entropy
T	Temperature
T_c	Curie temperature
T_d	Depolarization temperature
$T_{j\mu}$	Transfer matrix (overlap matrix)
t	Tolerance factor
t_{ion}	Ionic transport number
\mathbf{u}	Displacement
$\bar{\mathbf{u}}$	Polarization vector
u_k	Mobility of species k
$u_{n,k}$	Periodic function
$\tilde{V}_{q/0}$	Periodic defect potential
V_X	Polyhedral volume of species X
v_{ext}	External potential
v_H	Hartree potential
v_{xc}	Exchange correlation potential
Z	Number of neighbor sites
Z_α	Charge of nucleus α
$Z_{\kappa,\alpha\beta}^*$	Born effective charge tensor

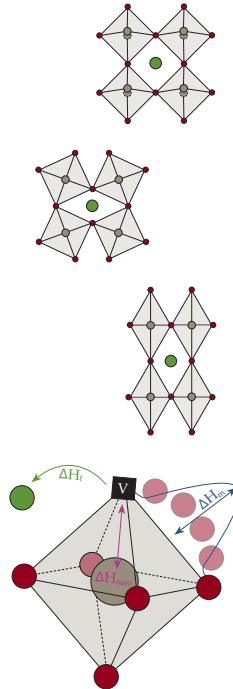
Part I

INTRODUCTION



The first part of this thesis summarizes the theoretical foundations of ferroelectric perovskites and their properties. In particular, we will address the defect chemistry in sodium bismuth titanate, a promising candidate to replace lead-based piezoelectrics. At the end of this part, we will explain the most important technical advances and challenges to study material properties by first-principles methods.

Open questions in the following section serve as a short roadmap through this study and illustrate the importance of a continuous and intense search for environmentally friendly and yet performant materials.



MOTIVATION

A particular important class of piezoelectric materials are perovskite oxides. Although they have a rather simple chemical formula, ABO_3 , a series of different phenomena have been observed in this material class, which arise from various interaction types (e.g. spin, charge, lattice, orbital) and might be simultaneously present [6, 7].

Decisive advantages of the perovskite family are a high degree of chemical flexibility, a huge structural diversity, and the ease to undergo structural phase transitions [8]. This includes the possibility to manipulate perovskites by pressure, temperature, doping, magnetic and electric fields as well as to fabricate thin films or even to generate superlattices [6]. Especially, the creation of multifunctional materials by the formation of solid solutions or heterointerfaces between different representatives of the perovskite class, becomes increasingly important [9–11].

Recently, Uchino [9] paraphrased this variety of complex phenomena as the “glory of piezoelectric perovskites” and summarized the current trends in the research of piezoelectric materials: „Performance to reliability, hard to soft, macro to nano, homo to hetero, and single to multi-functional “.

Lead zirconate titanate contributes to a large extend to the billion dollar market size of piezoelectric devices [12]. However, legislative exemptions, for instance the “Restriction of Hazardous Substances” (RoHS)[13] or the “Waste Electrical and Electronic Equipment” Directive [14], try to gradually remove toxic lead from the market such that lead-free alternatives are desperately needed.

More than 60 years of research and optimization of lead-containing piezoelectrics have contributed to today’s multifaceted production technologies and product supply chains [15]. Thus, a promising lead-free candidate material not only has to pass environmental and legal standards or provide microstructural control and excellent physical responses, but also has to guarantee reasonable costs for the modification of production processes, scalability as well as reliability [12, 15].

Although NBT is a lead-free alternative and great progress has been made in recent years to understand and tune its behavior [16], it is still no “drop-in” solution for the substitution of lead zirconate titanate. This is primarily due to the fact that the defect chemistry of NBT deviates from other members of the perovskite family (e.g. $BaTiO_3$ or $SrTiO_3$) such that the attained knowledge is hardly transferable [17].

Particularly noticeable is the sensitive dependency of the dielectric loss on the A-site stoichiometry as wells as the amount of dopants, leading to bulk conductivities of approximately 0.01 S cm^{-1} . Such high conductivities would be detrimental for multi-layer ceramic capacitors or other dielectric based applications [1].

It turned out that the ionic conductivity is based on the migration of oxygen vacancies, which are introduced as intrinsic “killer defects” [18] to compensate the charge of extrinsic dopants or process-related Bi-vacancies [1]. Only recently, this ionic conductivity has been proven useful for intermediate temperature solid electrolytes, in-

tegrated in solid oxide fuel cells [1, 19].

Until now, it is still unclear, if the high ionic conductivity is caused by the amount of mobile charge carriers, their enhanced mobility, or even by both. Furthermore, there is hardly any knowledge about the influence of local structure patterns, defined by topological order/disorder and various temperature dependent crystal symmetries, on the migration barriers.

Chemical trends in acceptor doped NBT have been obtained empirically and for most dopants the presence of thermodynamic stable defect associates with oxygen vacancies is assumed [20]. The formation of such defect associates might not only change the effective charge carrier concentration, but also affects the ferroelectric hardening of NBT and NBT-based solid solutions [21, 22]. Nevertheless, although the control of composition and impurity levels are of major importance to achieve a high degree of chemical, structural, and functional flexibility, oxygen ion conduction in NBT is still a relatively uncharted territory .

As already realized by Thomas in 1989 [23], the understanding of the defect chemistry might be a “lengthy process of trial and error”. However, computer simulations substantially contribute to the decoding of structure-property relationships and are even considered as revolutionary for the discovery and understanding of defect properties [24]. Especially, density functional theory (DFT) calculations have become a valuable tool to determine ground structures, electronic properties, and the thermodynamics of lattice defects in condensed matter [25].

In the present thesis, we intensively studied the defect chemistry and the conductivity in acceptor doped NBT by first-principles calculations. Many of the results reported have been achieved in close collaboration with Dr. Sebastian Steiner, who carefully performed impedance measurements, and Dr. Pedro Groszewicz, who carried out nuclear resonance spectroscopy experiments. Although we will concentrate on the theoretical investigation of NBT, we will partially summarize the experimental results for comparison.

2.1 LEAD-FREE PIEZOELECTRICS – LABORATORY VS. MARKET

A total market size of USD 28.9 billion and an annual growth rate of 3.7% in 2020 – These numbers leave no doubt that the piezoelectric material and device market is a highly important economic sector and an integral part of the automotive, chemical, consumer electronics, and medical industry [26].

Did you know that the worldwide production of lead zirconate titanate (PZT) ranges between 1250 and 4000 tons annually and therefore substantially contributes to this market success [12]? Did you further know that lead is a toxicant, which accumulates in the brain, liver, kidney, and bones, irreversibly reducing the intelligent quotient, causing anemia, hypertension, or renal impairment [12]? How does this fit together? Which risks are associated with the life cycle of PZT? Which opportunities does the future hold for the development of lead-free alternatives? And are they really more environmentally friendly?

In the following, we want to shed light on health, environmental, and regulatory issues of piezoelectrics while emphasizing the benefits, necessities, and challenges of future developments “in a world interconnected by networked product supply chains, multifaceted production technologies, and consumption patterns that are nonlinear” [15]. For this purpose, we will solely refer to the References [12, 15, 27, 28] and the references therein.

2.1.1 *Reasons for a sustainable research and continuous development of lead-free piezoelectrics and why PZT has not been replaced so far*

Although the toxic heavy metal lead has been greatly reduced in electronics over the past years, PZT, which is used in typical piezoelectric applications and contains more than 60 wt% PbO, is currently exempt from environmental legislations. These are, for instance, the EU’s Restriction of Hazardous Substances (RoHS) [13], the Waste Electrical and Electronic Equipment Directive (WEEE) [14], trying to prevent environmental damage ¹ by lead from electronic waste, or the Registration, Evaluation, Authorization, and Restriction of Chemicals (REACH), which already classifies PZT as a substance of very high concern.

Especially mining, manufacturing (e.g., volatilization of PbO at high temperatures during calcination and sintering), and disposal of lead-based products constitute a significant risk for health and the environment, although the actual risk factor for poisoning strongly depends on whether industrialized (low risk, processes are well regulated and monitored) or developing nations (high risk) are considered. This raises

¹ For example energy consumption during fabrication, marine aquatic ecotoxicity, freshwater sediment ecotoxicity, freshwater aquatic ecotoxicity, and terrestrial ecotoxicity

the question of why PZT is not withdrawn from the market if it is harmful to nature as well as human life and possible lead-free candidates seemingly exist?

Commercial availability of lead-free materials (no established supply chain), intellectual property (protection of lead-free discoveries), costs, and complete exclusion of PZT from the market, if there will be a few successful integrations of lead-free materials in modern technology are only a few reasons why lead-free alternatives still serve as “a testing bed for different condensed matter theories” [3]. Apart from these facts, Bell *et al.* [12] correctly point out that although there is a massive increase in publications about PZT substituents, only a few of them deal with the “full electromechanical property matrix, the aging characteristics, electrode compatibility, machinability, and process cost”, necessary to reasonably plan manufacturing processes without socioeconomic highly important PZT-based products.

More than 60 years of research on PZT-based technologies led to sophisticated solutions and a whole “world-catalog” [12] of lead-containing devices. This makes it difficult to find a single suitable material with the same elastic, dielectric, conductive, and other physical properties or to redesign all construction units to suit to a new material.

Let us summarize the main requirements a lead-free alternative has to fulfill: First, the benefit of lead-free materials must exceed the risk of removing PZT from the market. That means that similar electromechanical responses, managing of volatility (stoichiometry), and microstructural control have to be guaranteed and understood. Secondly, the benefits must exceed or at least cover all related costs, including modifying of production equipment and processes, mass production yield, reliability, and scalability. Finally, social, environmental, legal, and institutional impacts must be clarified. In the following thesis, we primarily want to concentrate on the first point by completing the sodium bismuth titanate property matrix (NBT). However, we understand that a successful integration or even exchange of new materials requires much more than an exact match of properties.

2.1.2 *Does lead-free mean environmentally friendly? Why did we investigate sodium bismuth titanate?*

The awareness that lead-free not necessarily implies environmentally friendly has arisen only recently when life cycle assessments (raw material extraction, processing, application, disposal) and environmental profiles of PZT and the most prominent lead-free piezoelectrics, sodium bismuth titanate and potassium sodium niobate (KNN), have been compared. This study revealed that either toxic precursors or, in the case of KNN, the processing of niobium ores are environmentally harmful, making KNN not any “greener” than PZT. The availability of niobium ores is further limited by the EU Conflict Minerals Regulation, which observes the import of minerals from crisis regions.

The comparison between PZT, KNN, and NBT further showed that NBT is generally superior to PZT or KNN and that the poor absorption of bismuth compounds leads

to lower human toxicity than PbO. The reason for the former is a lower thermal and electrical energy consumption during fabrication. Besides these environmental and health factors, which already justifies our decision for NBT, we are faced with a lot of interesting and unexplored properties, which are tunable by chemical modifications or external fields [2]. However, Ibn-Mohammed *et al.* [15] also pointed out that Bi₂O₃ is even more harmful than PbO across multiple environmental indicators, caused by multiple processing, purification, and refining steps during bismuth production. Especially, high refining and recycling costs of bismuth (one-shot application) as well as the fact that bismuth is mainly obtained as a by-product of lead smelting are detrimental in terms of economy of scale. Likewise, the evaporation of bismuth at high temperatures increases energy consumption during processing and might lead to limited reliability of the end product. We should not forget these opposing sides, even if NBT is our material of choice.

2.1.3 NBT—A friend for all situations?

All in all, until today, there is no single, lead-free “drop-in” solution to substitute PZT. Thus, a goal should be to find an application-specific solution rather than an all-round substitute. This allows us to maintain high-performance standards and discover new technologies, which facilitate our lives. These could be bio-micro-electro-mechanical systems (bio-MEMS) or in vivo piezoelectric sensors, for which toxic PZT is unsuitable. *A general understanding of structure-property relationships is therefore inevitable and serves as a primary motivation for the present thesis, which has been designed to reveal fundamental structure-property relationships of NBT.* However, we should keep in mind that functional properties and economic factors (“ease of processing”) are crucial constraints for a successful implementation in electric devices. Only a comprehensive analysis paves the way for a smooth transition of lead-free materials from the laboratory to industrial markets.

2.2 THE PEROVSKITE STRUCTURE – AN ALL-ROUNDER?

“Is there anything perovskites can not do?” [29], *“The power of perovskites”* [30], or the *“glory of piezoelectric perovskites”* [9] are a few examples of recent publications, trying to summarize the multifunctionality of these mixed oxides. In the last century, both, the discovery and exploitation of perovskites, as well as their diverse functional properties have advanced at an amazing pace [9, 31]. Since the beginning of the 1990s they further became a paradigm for *ab-initio* simulations, studying structural instabilities, spontaneous polarization, lattice-dynamical phenomena, dielectric and piezoelectric properties, and even structural phase transitions at finite temperature [31]. What are perovskites? What makes them so unique? And what are advanced research trends? In the following, we want to address these questions and build a solid foundation for the topics we will discuss in the present thesis.

Perovskites are mixed or complex oxides, where different cations of various oxidation states, ionic radii, and coordination numbers occupy the A- and B-sublattice of an ABX₃ compound. Typically, the A-site is 12-fold coordinated, while the B-site is

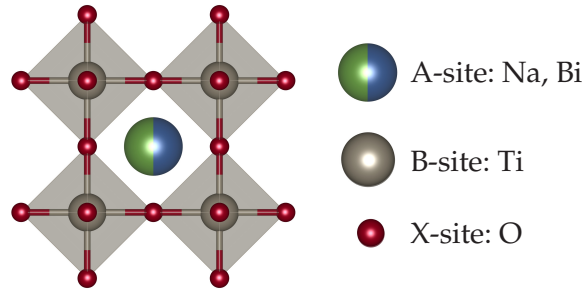


Figure 1: Cubic perovskite oxide structure of A-site mixed sodium bismuth titanate as a representative example.

surrounded by regular corner-linked anion octahedra of atom type X. In total, this leads to four A-site and two B-site neighbors in the direct vicinity of X [23, 32–34]. Interestingly, almost all elements are suitable candidates (except for the noble gases) for regular A- and B-site cations, leading to the widely used term “perovskite family” [35–38] or inorganic chameleon [39]. This compositional flexibility implies a variety of different behaviors, for instance, insulating, semi-conducting, and metallic properties [3].

Perovskite oxides are a famous subgroup of this perovskite family, where the X site is occupied by oxygen, transition metals fill the B-sublattice, and the A-site ions are identified with alkali, alkaline earth, or rare earth metals (see Figure 1). An even higher degree of freedom is obtained by $AA'BB'X_6$ compositions, where two different cation species occupy either the A-site, the B-site, or both sublattices. The arrangement of the atoms can be ordered or random, leading to different symmetries and unit cell sizes (maintaining translational symmetry). The consequences of A-site ordering in NBT will be discussed in detail below.

Depending on the temperature, pressure, or composition, different phases might be stable (hettotypes [33]) such that perovskites generally crystallize in polymorphous structures. Although they often hardly vary from the cubic aristotype, only a few compositions adapt to the ideal, centrosymmetric $Pm\bar{3}m$ symmetry at room temperature, where the only variable parameter is the lattice constant [40]. Deviations from this structure are described by static, symmetry-breaking structural distortions, superposing the parent structure. These distortions can be categorized into two groups if magnetism is neglected [41]. They either result from a displacive or an order-disorder phase transition [42], where a variation of site occupancies effectively reduces the symmetry. Consequently, different orderings appear in perovskite oxides, including polar, spin, orbital, and charge arrangements, which significantly influence the physical properties.

The stability of the cubic parent structure strongly depends on the chemical nature of the ions and the ratio of their radii. The Goldschmidt tolerance factor [43], t , allows for a surprisingly accurate prediction about the preference for ideal cubic arrangements and is given by [35, 43],

$$t = \frac{r_A + r_O}{\sqrt{2}(r_B + r_O)} = \frac{r_{A-O}}{\sqrt{2}r_{B-O}}, \quad (1)$$

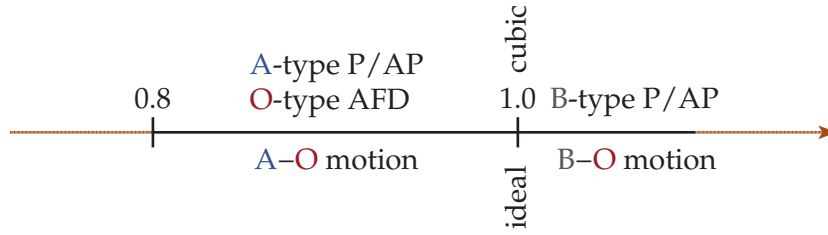


Figure 2: Structural instabilities depending on Goldschmidt’s tolerance factor. P and AP represents polar and anti-polar instabilities, respectively. In turn, AFD describes an antiferrodistortive instability. Adapted from Reference [49].

where r_X is the radius of species X and r_{X-Y} is the distance between species X and Y, respectively. If the tolerance factor is approximately one, the ideal perovskite structure is often favored. This is reached for large A-site cations and B–O π bonding, stabilizing the cubic symmetry [36]. In turn, if t is not equal one, either the B ($t > 1$) or the A ($t < 1$) cation is too small [44]. As a result, these cations will displace from their regular position to optimize their local bonding environment (increased bonding to the surrounding oxygen 2p orbitals). Another way to improve chemical bondings and to release elastic stresses are cooperative rotations of the BO_6 unit about a cubic axis [37]. If we assume a mean value $\bar{r}_{\text{Bi/Na-O}}$, the tolerance factor in NBT amounts to 0.958 [45], suggesting that the A-site instability (polar/antipolar) and O-type antiferro-distortive rotations must not be neglected. Naturally, this value will depend on the exact cation order and fluctuate between the two limiting cases 0.937 (solely Bi on the A-site) and 0.979 (exclusively Na occupies the A-site). Although this tolerance factor is close to one, the ground state of NBT is not cubic at low temperatures. This deviation has been attributed to the Bi lone pair [46].

A thorough qualitative analysis of BX_6 octahedral tilt patterns has been established by Glazer [47, 48]. Basically, the tilts are described in the reference framework of the cubic aristotype. This means that the $[100]$, $[010]$, and the $[001]$ “pseudo-cubic” axes are used to define the tilt in the x , y , and z direction. Glazer’s classification is based on the assumption that the corner connectivity is strictly preserved, and the regularity of the octahedra is approximately maintained [40]. Hence, the octahedral tilt in the plane perpendicular to the rotation axis is constrained, while octahedra parallel to this direction are allowed to tilt either in-phase (+) or out-of-phase (-) with respect to the neighboring BX_6 unit. In turn, the magnitude of the tilt in different directions is arbitrary. All this information is condensed into a three-letter symbol $a^\#b^\#c^\#$, where the literals describe the tilt around the x , y , and z axis of the $\text{Pm}\bar{3}\text{m}$ space group and the # symbol has to be replaced by the corresponding plus or minus sign. Note that the tilt operations are not abelian such that the total tilt depends on the specific sequence of these operations. Especially $a^-b^+a^-$ and $a^-a^-a^-$ patterns occur rather frequently within the perovskite family. A $a^+b^-b^-$ configuration is favored, if the tilt angles become large [36].

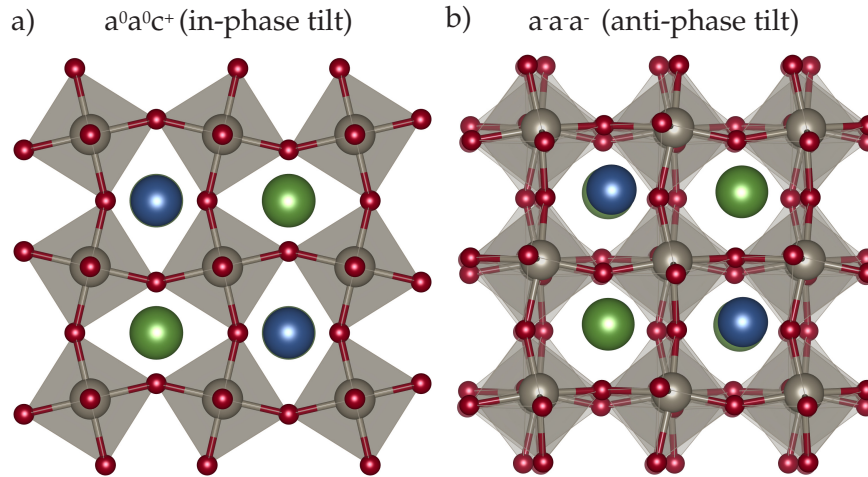


Figure 3: Visualization of the a) in- and b) anti-phase tilt in NBT.

Generally, three types of distortions can be distinguished [32, 48]:

- i) The tilting of the octahedra,
- ii) parallel or antiparallel displacements of the cations,
- iii) and the distortion of the octahedra itself (e.g., bond-angle variance or quadratic elongation, which should be second order in the tilt angle [23, 33]).

The latter two are correlated, and (ii) is often caused by the electronic instability of the B-site cation. We provide a short summary of these structural instabilities dependent on the Goldschmidt tolerance factor in Figure 2 and visualize an in- and anti-phase tilt distortion in Figure 3.

The ferroelectric Ti displacement in BaTiO₃ is a well-known and extensively studied example for this type of instability [50]. Instead, octahedral tilting is mainly driven by optimizing of the A–O bonding distance if the A-site cation is too small. During this process, the chemical bonding properties around the B-site cation are hardly changed [36]. Especially in the context of soft-phonon modes near the phase transition, octahedral tilts play an essential role. Whereas octahedral tilting takes place on short timescales and quickly adjusts to chemical or structural modifications, cation rearrangements are usually slow, diffusion-controlled processes [40].

2.3 SODIUM BISMUTH TITANATE – A CHAMELEON?

The knowledge of the temperature-dependent structure is a prerequisite to calculate functional properties of NBT [51]. Thus, in the following part, we will present experimental and theoretical achievements in the field of structural resolution.

NBT is a mixed relaxor-ferroelectric,² with a globally random distribution of Na⁺ and Bi³⁺ cations on the A-site. Although pure NBT was first reported in 1961 by

² Relaxors have a frequency-dependent relative permittivity with a broad maximum. Generally, their behavior is attributed to polar nano-regions [52–54].

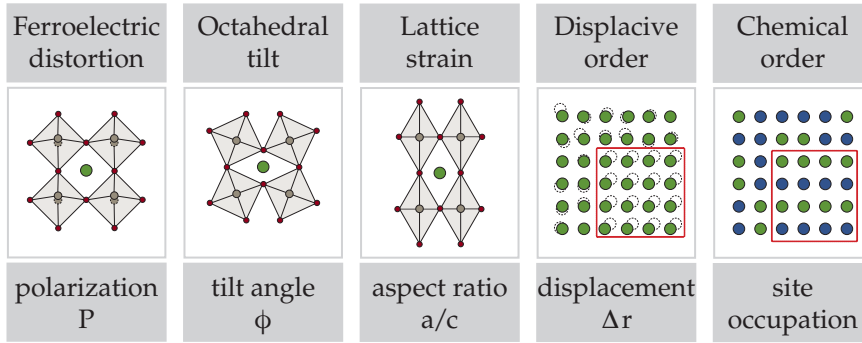


Figure 4: Visualization of the different structural degrees of freedom in NBT, which might be simultaneously present. Adapted from Reference [2].

Smolenskii [55], the defect chemistry, the sequence of structural phase transitions, and the average phase symmetry are still under debate. This disagreement is caused by a complex structure with cation displacements, octahedral tilts, potential A-site ordering, and local deviations from a higher-level average structure (see Figure 4). The latter are further susceptible to external stimuli as electric fields, thermal treatments, or mechanical stresses, making it even more challenging to establish structure-property relationships.

2.3.1 Searching for the ground state of NBT

An enormous amount of experimental techniques combined with the strength of first-principles calculations have been employed to decode the temperature-dependent structure of NBT and to investigate the coupling or competition between the several degrees of freedom mentioned above [56]. Without being exhaustive, we will review the most important findings of recent publications. The experienced reader, however, is advised to review Figure 5, and to skip to the next subsection. Figure 5 provides a summary on the temperature-dependent phase sequence in NBT as well as the methods from which this information has been obtained [56].

In 2002 Jones *et al.* [57] performed a comprehensive neutron powder analysis of NBT in the temperature range between 5 K and 873 K. Their analysis demonstrated that a pure rhombohedral structure is stable from 5 K to 528 K, while the amount of tetrag-

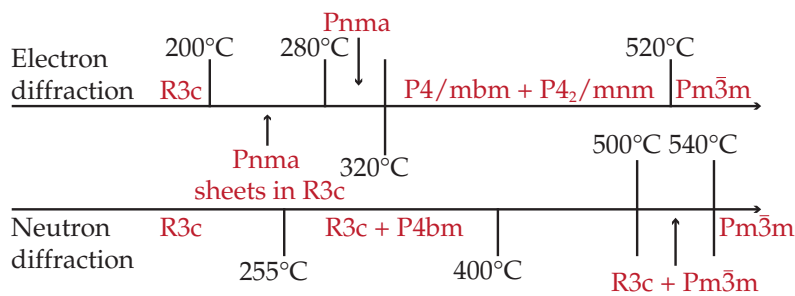


Figure 5: Temperature dependent phase sequence in NBT. Adapted from Reference [56].

onal phase continuously increases with increasing temperature until the transformation is completed at 673 K.

The rhombohedral phase is characterized by an $a^-a^-a^-$ anti-phase oxygen octahedral tilt pattern around the threefold pseudocubic (pc) axes, which leads to a cell-doubling along all three dimensions. In addition, Na/Bi and Ti cations are displaced in parallel along the $[111]_{pc^-}$ axis. At low temperatures, the Na/Bi displacement is approximately twice as large as the one of Ti but becomes comparable when temperatures approach the stability region of the tetragonal phase. These displacements are necessary to accommodate the stereo active Bi^{3+} lone-pair and minimize the electrostatic energy resulting from the TiO_6 -tilt, leading to a coupling between those two degrees of freedom. However, despite this large off-centering, Bi remains under-coordinated with a non-ideal valency. In total, these deviations from the ideal cubic structure yield a $R3c$ space group symmetry.

In contrast, a weakly polar anti-parallel cation displacement of the A- and B-site cations along the c-axis has been observed in the tetragonal phase. The octahedral unit is tilted in an $a^0a^0c^+$ in-phase fashion, and a $P4bm$ symmetry determines the atomic positions. However, in this state, the distortion from the cubic symmetry is as low as 0.14 %. The continuous, temperature-dependent phase transformation naturally results in a broad region, where rhombohedral and tetragonal phase fractions coexist. At approximately 813 K, NBT transforms to a high-temperature average cubic structure, following a tetragonal-cubic phase coexistence region first appearing at 773 K. We use the word “average” intentionally to hint at the persisting doubt of local cubic symmetries at high temperatures.

According to Troliard *et al.* [58] the tetragonal phase is still present as “relics” in the cubic phase, while others consider the measured phase symmetry as an average of local minima attainable on the energy landscape at a given temperature (order-disorder instead of displacive phase transition) [39, 59].

Furthermore, Jones *et al.* [57] could not verify any long-range A-site cation order by X-ray or neutron measurements and Levin *et al.* [60] revealed this coexisting global chemical and displacive disorder by high-angle angular dark field imaging in scanning transmission electron microscopy and electron diffraction. Only weak diffuse scattering suggests a preference for short-range ordering (nanometre-scale), which was also indicated by Raman spectroscopy [61, 62], and further diffraction studies on the tetragonal phase [58]. This was in accordance with their expectations since the size mismatch between Na^+ and Bi^{3+} is negligibly small, and the charge difference is not large enough to justify significant ordering tendencies. *Ab-initio* calculations support this hypothesis by showing a flat energy landscape for differently A-site ordered supercell structures, and tilt displacements [63, 64], such that the energetic gain for A-site ordering should be comparable to thermal energies [56]. However, it was also pointed out by the same authors that A-site layers of large Bi-content are specially stabilized by the hybridization of Bi 6sp and O 2p orbitals, leading to an energetic advantage over random A-site distributions.

In 2008 Dorcet and Troliard [58, 65, 66] investigated NBT with electron diffraction techniques and demonstrated that an intermediate modulated phase occurs already

at 200 °C, which consists of the R3c host interspersed by orthorhombic Pnma sheets grown by a micro twinning process. At approximately 320 °C this orthorhombic phase transforms into a tetragonal P4/mbm polymorph by a second-order phase transition. For temperatures above 400 °C these nanodomains are assumed to be of non-polar P4₂/mnm symmetry. The former two characteristic temperatures are related to the depolarization temperature, and the maximum of the relative permittivity [56]. In this sense, the depolarization can be better understood by a decreasing long-range ferroelectric order rather than a structural phase transition [67].

Levin *et al.* [60] showed that the orthorhombic nanoscale domains possess an $a^-a^-c^+$ oxygen octahedral tilt with a coherence length of a few unit cells, which is at least one order of magnitude smaller than the anti-phase tilt of the surrounding rhombohedral matrix. These alternating $a^-a^-c^+/a^-a^-a^-$ motifs occur along the pseudocubic {100} twin domain boundaries, and their appearance resulted in the “continuous tilt model”. NMR measurements [68] as well as *ab-initio* molecular dynamics [64] support these results.

However, as a consequence of the nanoscale platelets, the average low temperature structure is better fitted using a monoclinic structure model of space group Cc with an overall tilt pattern of $a^-a^-c^-$ rather than the average R3c symmetry [60, 69–72]. Also, the local Bi-environment with Bi-O bond lengths of 2.22 Å as obtained from X-ray absorption fine structure (XAFS), which are shorter than those expected from X-ray diffraction for an R3c environment, indicate large distortions compared to the average structure (Bi-O bond lengths greater than 2.53 Å) [59]. Gorfman *et al.* [70] concluded from their observations that the symmetry must be lower and proposed the subgroup Cc as a more probable alternative. Nevertheless, even in this symmetry, such short Bi-O bond lengths do not occur. By means of temperature-dependent Bi-O pair distribution functions, Keeble *et al.* [73] showed that a bifurcated polarization causes this inconsistency.

Another low temperature structural model was proposed by Rao *et al.* [74–76] and later supported by Beanland *et al.* [77]. Their model is based on an ensemble of experimental and theoretical techniques, involving X-ray, neutron and electron diffraction, Raman spectroscopy, and first-principles calculations. Essentially, they assume a co-existence of R3c and Cc symmetries. However, the equilibrium ratio of both phases is susceptible to external stimuli as thermal and mechanical treatments or electric fields. Indeed, strong electric fields irreversibly transform the mixed R3c and Cc composition into a purely R3c phase and convert the relaxor to a standard ferroelectric. Only annealing above 300 °C and subsequent cooling restore the sensitive equilibrium. Thus, a global monoclinic structure results from nano-sized structural heterogeneities and elastic strain in the average lattice. Since the R3c structure is more favorable (lower total energy compared to Cc), the monoclinic bulk distortion is a fingerprint of the strain, which is generated by the local in-phase tilts present in the R3c matrix. If an external electric field is applied, the coherent length of this tilt pattern is reduced, and the rhombohedral phase occurs on the global length scale. Beanland *et al.* [77] go a step further by supposing a R3c average structure even in unpoled NBT structures. The presence of Cc symmetry is thus degraded to a phenomenon that purely results from a structural average.

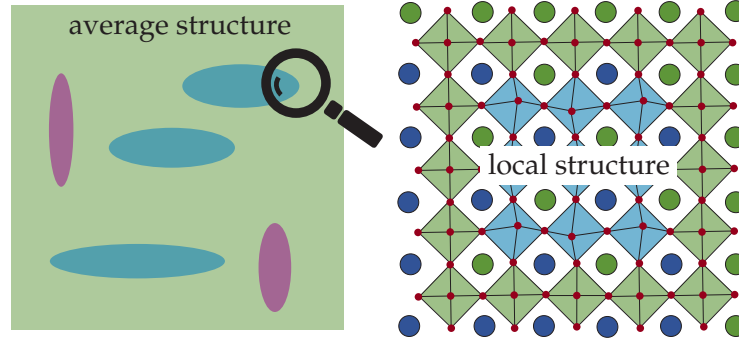


Figure 6: Illustration of the local and global chemical as well as topological order in NBT. Small nanodomains can deviate from the overall structure by the A-site order or off-site displacements.

Figure 6 exemplary illustrates the local and global chemical as well as topological order in NBT. Note that nanodomains might deviate from the average structure by a different A-site order, off-site displacements of the cations, or octahedral tilt distortions.

2.3.2 The consequence of disorder on the computational complexity

As evident from the above descriptions, polymorphism and incomplete ordering in NBT are signs of a flat energy surface, leading to a complex structure [39]. This structure is mainly characterized by a global and a local contribution, which can deviate from each other. Besides this inherent complexity, chemical substitution (doping or formation of solid solutions) or non-stoichiometry further allows for varying electric and elastic fields and significantly impacts physical properties [73].

Indeed, only 1% non-stoichiometry in PbTiO_3 is enough to produce a change in the diffraction pattern [78].

Due to size restrictions in *ab-initio* calculations, as further explained in Chapter 3, we are unable to simulate a phase coexistence, high dopant concentrations, or truly random A-site distributions. Thus, we will concentrate on two important A-site orderings in their theoretical ground state configuration, namely the 111-ordered and the 001-ordered structure [2].

Figure 7 shows an example of the group-subgroup relations for cubic NBT, where the low symmetry structures (subgroups of the parent space group) are derived from the cubic aristotype [2, 79]. Due to A-site ordering, the cation sites are no longer equivalent, and the symmetry is lowered [32]. In the 111-ordered structure, Na^+ and Bi^{3+} are arranged in a rock-salt fashion, while in the 001-ordered structure Bi^{3+} and Na^+ layers alternate along the pseudocubic c-axis. Figure 7 shows both A-site cubic sublattices, where the TiO_6 unit was omitted for clarity reasons. We adopted this notation from the excellent study of Gröting [2] about the relaxor ferroelectric NBT and its solid solutions.

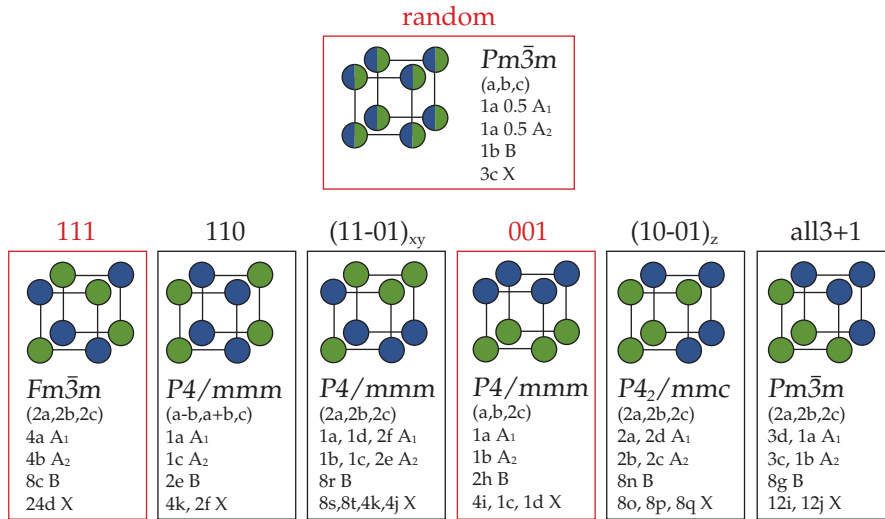


Figure 7: Group-subgroup relations of A-site ordered cubic NBT including the splitting of the Wyckoff positions [2].

We understand these A-site ordered structures as representative models for studying the main structure-property relationships of local minima in NBT, which will contribute to the average of the macroscopic sample [39]. Moreover, it has been shown that the rhombohedral model structure with a “simple” 111-ordering could produce reasonable lattice parameters and frequencies of transverse and longitudinal optical modes [76, 80]. However, we will repeatedly return to the *limitations of DFT in the context of the defect chemistry in NBT and NBT-based systems and discuss how restrictions affect our defect analysis*. We conclude this section by listing some of the important experimentally derived properties of disordered NBT. NBT has a relatively high Curie temperature of approximately 325 °C, a remnant polarization of 38 $\mu\text{C cm}^{-2}$, a coercive field of 7.3 kV mm^{-1} , and a piezoelectric constant of 73 pC N^{-1} [19, 20, 81].

2.4 STRUCTURAL INSTABILITIES—THE TRIUMPH OF BROKEN SYMMETRY

The following section recovers the origin of ferroelectric instabilities in terms of lattice modes. Particularly, this knowledge is a prerequisite for understanding chapter 5. If the reader is familiar with the nomenclature, this section may be skipped. However, we recommend focussing on sections about the Born effective charge tensor (2.5.1), the interatomic force constants (2.5.2), and the lone pair effect (2.5.3), respectively. These concepts are rarely used, but the basis of our discussion below.

Phase transitions between two crystal structures, related by a group-subgroup relation, can be described by a symmetry breaking condensation of a set of collective degrees of freedom. The physical property, whose amplitude spontaneously changes from zero in the high-symmetry phase to a finite value in the low-symmetry distorted structure, is called the order parameter. Generally, a single active n-dimensional irreducible representation of the high-symmetry phase space group sufficiently describes the phase transition and the transformation of the order parameter accordingly [82]. For instance, on a microscopic level, the set of atomic distortions, or equivalently the

macroscopic polarization, constitute an appropriate order parameter to describe a ferroelectric phase transition (spatially uniform polarization). As we will see below, both quantities are coupled by the Born effective charges. Even non-polar oxygen octahedral rotations or spontaneous strain during a ferroelastic phase transition might serve as suitable order parameters. This shows that the choice of the order parameter is generally arbitrary. In the following, we will briefly summarize the most important theories to describe a phase transition on both a macroscopic as well as a microscopic level.

2.4.1 Ginzburg-Landau-Devonshire theory—Competition or cooperation?

The Ginzburg-Landau-Devonshire theory [42, 83–88] is a mean-field theory, which phenomenologically describes the temperature dependent behavior of crystalline solids in the vicinity of a second order phase transition. Although this theory might be applicable to discontinuous phase transitions, its validity is not ensured. Essentially, the Ginzburg-Landau-Devonshire theory is based on a Taylor expansion of the free energy F around the high-symmetry non-polar phase. However, it is assumed that the expansion remains valid at temperatures other than the transition temperature, which implies that small distortions are sufficient to obtain the non-centrosymmetric distorted structure and that the expression is invariant for both the high and the low-temperature phase. The Landau expansion (in the following, we will refer to the Ginzburg-Landau-Devonshire theory loosely as Landau theory) is given by,

$$F(\eta) = F_0 + \frac{1}{2}\alpha\eta^2 + \frac{1}{4}\beta\eta^4 + \frac{1}{6}\gamma\eta^6 \dots, \quad (2)$$

where η is the order parameter, and $\alpha = \alpha_0(T - T_0)$ is assumed to be the only temperature-dependent coefficient, where α_0 is a positive constant and T_0 denotes the temperature where α changes sign. Here, the strain (secondary order parameter), which is caused by small relaxations induced by the appearance of polarization, is neglected. An example for a first- and second-order phase transition is given in Figure 8. Although the phonon-strain couplings are fundamental to describe phase transitions in perovskites accurately, we will ignore these terms for reasons of simplicity [8]. Note that the conditions $\partial F/\partial\eta = 0$ and $\partial^2 F/\partial\eta^2 > 0$ eliminate the linear term, and if $F(\eta)$ does not depend on the sign of the order parameter, odd powers can be neglected in the Taylor series.

The sign of the fourth-order term depends on whether the phase transition is of first- (discontinuous change in structure and entropy with $\beta < 0$) or second-order (continuous change with $\beta > 0$). During a second-order phase transition, the order parameter evolves continuously as a function of temperature such that at the phase transition temperature T_0 the single-well transforms into a double-well profile with two stable spontaneous polarizations at $\pm P_0$ (if the primary order parameter is the polarization as it is the case in proper ferroelectrics).

Instead, two non-vanishing polarization states become local energetic minima in a first-order transition, even at temperatures above T_0 . Only at the Curie temperature T_C , the polar and non-polar minima are degenerate, and a full double well is first

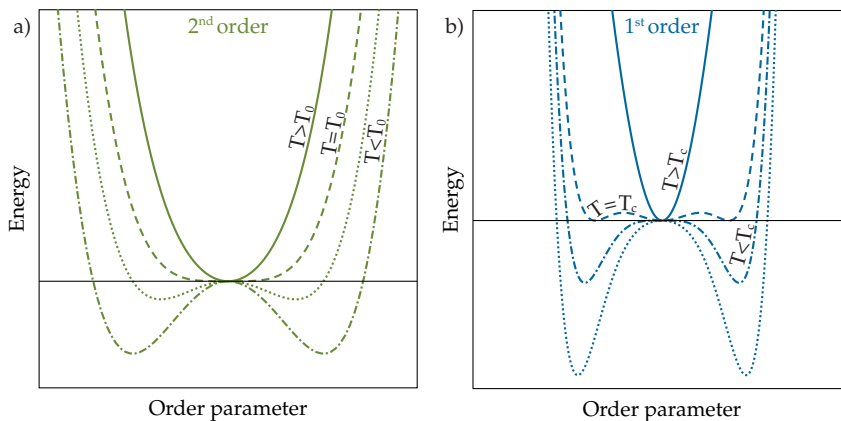


Figure 8: Examples for a first- and second-order phase transition. An explanation of T_0 and T_c is provided in the main text.

obtained below this characteristic temperature. The spontaneous polarization at T is determined by minimizing F with respect to P .

Besides the polar zone-center distortions, antiferrodistortive oxygen octahedral rotations, Jahn-Teller distortions, or breathing modes have been observed in perovskite structures [89, 90]. The two latter, however, strongly distort the oxygen octahedra around the B-site cation, such that they are generally high in energy (typically hard modes) and responsible for a charge or orbital ordering [91]. In turn, the rotation (ϕ^\pm) of the oxygen cage as a primary order parameter has been observed often [92, 93] and is especially well known for the incipient ferroelectric SrTiO₃ [94], where the Γ -point phonon mode has not been observed in experiments. In these cases, the Landau expansion is not only a sum of the single $F(P)$ and $F(\phi^\pm)$ terms but further include coupling terms of higher-order, e.g. bi-quadratic $b_{220}\phi^2P^2$ (the notation for constants like b_{220} have been introduced by Gröting [2]). If, for instance, the coupling coefficient b_{220} is negative, both modes cooperate and form multiple energy minima on a complex energy landscape (simultaneous presence of a rotational and a polar distortion decrease the energy even further). On the other hand, if the coupling term increases the free energy, both modes compete against each other. Generally, both scenarios result in a renormalization of the curvature, which is caused by the first mode, if a second one appears (see Figure 9).

For instance, if the condensation of one non-polar mode solely drives the polarization in a crystal (e.g., $b_{130}\phi^3P$), implying that the polar mode is not intrinsically unstable, we call it an improper ferroelectric [95, 96]. Systems, which are termed hybrid improper ferroelectric, develop two rotational modes (in-phase ϕ^+ and out-of-phase ϕ^-) and a polar displacement (P) with decreasing temperature. In this case, the polarization is often linearly coupled with the two independent rotational modes (trilinear coupling) [10, 97]. Finally, the already mentioned cooperative bi-quadratic coupling describes a triggered phase transition [98].

As mentioned at the beginning of this section, Landau-type theories are mean-field approaches, suited to reproduce the temperature-dependent behavior of perovskite

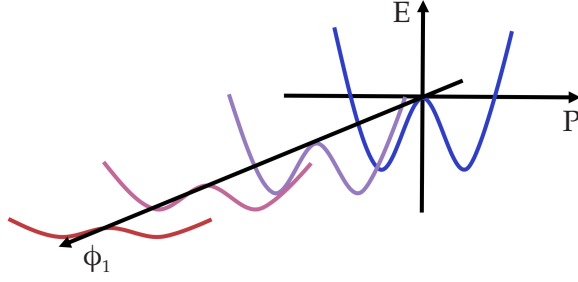


Figure 9: Illustration of a competitive mode coupling. Adapted from Reference [49].

oxides on a macroscopic scale. However, they provide relatively little knowledge of the underlying physics of the phase transition. Thus, we will take a closer look at lattice dynamical theories, based on the ideas of Cochran [99, 100], and the origin of the ferroelectric instability.

2.4.2 Lattice dynamics—The phonon mode picture

Although many material properties can be described satisfactorily by static models, almost as many depend on the crystal lattice dynamics. These include, amongst others, thermal properties, phase transitions, and electrical properties [101]. In the following, we will pay special attention to phase transitions in the context of mode crystallography, which allows us to describe distorted structures by symmetry-adapted collective atomic displacements [102]. In this context, a distortion is assumed to be any global change to the crystal lattice, which breaks its symmetry [41]. Below, we will easily see that phonons form a complete basis to characterize the asymmetric unit of a distorted structure. For this purpose let us define the atomic positions in the low symmetry structure by [102],

$$\mathbf{r}(\mu, i) = \mathbf{r}_0(\mu, i) + \mathbf{u}(\mu, i), \quad (3)$$

where $\mathbf{r}_0(\mu, i)$ denotes the position of the atoms $\mu = 1, \dots, s$ of the high symmetry structure with space group \mathcal{G} in the setting of the distorted structure of space group \mathcal{H} (reference cell). Generally, the structure of space group \mathcal{H} will have a larger unit cell than its supergroup of space group \mathcal{G} such that the displacive phase transition will cause a splitting of the Wyckoff orbits (symmetry-equivalent site) [102, 103]. Thus, the parameter $i = 1, \dots, n_\mu$ enumerates the orbits derived from a single Wyckoff position in \mathcal{G} . The atomic displacements $\mathbf{u}(\mu, i)$ relate the parent structure in the reference configuration and the low symmetry structure, and are given by a linear combination of independent, local symmetry-adapted modes [41, 102]:

$$\mathbf{u}(\mu, i) = \sum_{\tau, m} A_{\tau, m} \bar{\mathbf{u}}(\tau, m | \mu, i). \quad (4)$$

Here, τ describes the symmetry of the mode and $m = 1, \dots, n_\tau$ represents the index of an independent mode of symmetry τ . $A_{\tau, m}$ and $\bar{\mathbf{u}}(\tau, m | \mu, i)$ are both real quantities and describe the amplitude and a set of normalized atomic displacements (polarization vector), respectively. The relative weights of the polarization vector components define the space group of the distorted structure [41].

Effectively, Equation 4 is nothing else than a change of basis in the vector space of structural parameters. It is a unitary transformation between the parameters $\{\mathbf{u}(\mu, i)\}$ in the low symmetry structure and the amplitudes $\{A_{\tau, m}\}$ of a given basis of symmetry-adapted modes.

Why is this transformation beneficial? It allows us to decompose displacive distortions into specific basis modes and to compare various collective displacements solely by the set of amplitudes $\{A_{\tau, m}\}$ [102].

Each mode can be associated with an irreducible representation of the parent space group ($Pm\bar{3}m$ in the case of perovskite oxides). Mathematically, a representation of a group \mathcal{G} can be understood as a homomorphism from \mathcal{G} into the group of automorphisms of a vector space.

DEFINITION A representation of a group \mathcal{G} is a homomorphism γ of \mathcal{G} onto a group \mathbf{T} of non-singular, linear operators acting on a finite-dimensional vector space \mathcal{V} . We write $\gamma g = \mathbf{T}_g$ for all $g \in \mathcal{G}$ [104].

The matrix, which represents g with respect to the basis $\langle \mathbf{x} |$ of the vector space \mathcal{V} in the representation γ , is given by $\Gamma_{\mathbf{x}}$ such that [41, 104],

$$\mathbf{T}_g \mathbf{x}_i = \sum_{j=1}^d \mathbf{x}_j \Gamma_{\mathbf{x}}(g)_{ji}, \quad (5)$$

where d is the dimension of \mathcal{V} . A representation is called irreducible, if and only if for every $g \in \mathcal{G}$ the vector space \mathcal{V} is mapped onto itself or $\{0\}$ and if \mathcal{V} is not the zero vector space [104].

In short, a representation of \mathcal{G} is a map of group elements $g \in \mathcal{G}$ onto a set of $n \times n$ matrices. The basis functions of these irreducible representations transform like the vector components of the atomic displacements [41]. All operations $g \in \mathcal{G}$, which leave the symmetry of the distorted structure invariant, form an isotropy subgroup of \mathcal{G} , which can be of space group \mathcal{H} (primary distortion mode) or be a supergroup of \mathcal{H} (secondary distortion mode). While primary distortions (soft modes) are sufficient to break the parent symmetry, usually of higher weights and generally intrinsically unstable, secondary (induced hard) modes contribute only slightly to the actual distortion and transform as the identity irreducible representation [40, 102].

Suppose the distorted and the parent structure are pseudosymmetric, which means that they lie close together on the potential energy surface. In that case, the low symmetry structure can be described by a truncated Taylor expansion around the saddle point configuration of the high symmetry structure. This Landau-type harmonic approximation can be expressed as [102]

$$E = E_0 + \sum_{\kappa_i \alpha a} F_{\kappa_i \alpha}^a u_{\kappa_i \alpha}^a + \frac{1}{2} \sum_{\kappa_i \alpha a} \sum_{\kappa_j \beta b} \underbrace{C_{\kappa_i \alpha, \kappa_j \beta}^{ab}}_{\frac{\partial^2 E}{\partial r_{\kappa_i \alpha}^a \partial r_{\kappa_j \beta}^b}} u_{\kappa_i \alpha}^a u_{\kappa_j \beta}^b \quad (6)$$

$$= E_0 + \sum \lambda_m \rho_{\Gamma_1 m} + \frac{1}{2} \sum k_{\tau n} \left(\sum_j \rho_{\tau n j}^2 \right) + \dots, \quad (7)$$

where $u_{\kappa_i \alpha}^a$ is the displacement of atom κ_i in the unit cell a along the direction α , and $\rho_{\tau n j}^2$ are the normal dispersive mode amplitudes with a symmetry characterized by the irreducible representation τ . The index m and j denote the multiplicity and the formal number of the degenerate mode, respectively. Note, that only modes which transform as the identity irreducible representation Γ_1 contribute to the linear term in Equation 7 such that the energy is extremal with respect to all symmetry-breaking displacements (see also Figure 10, where instable modes are characterized by imaginary frequencies). The parameter $k_{\tau n}$ represents the stiffness coefficient, which is positive for hard and negative for soft modes. If we compare Equation 6 and Equation 7, we see that the symmetry-adapted modes are also the eigenmodes of the matrix of second derivatives of the energy with respect to atomic displacements [102]. From this, as well as the equivalence between the linear temperature dependence of the soft mode and the α parameter of the Landau-type theories [105], we see that both approaches are strictly coupled.

2.4.3 *The theory of ferroelectricity–ferroelectricity as a collective phenomenon*

In the last sections we discussed that phase transitions are inseparably associated with symmetry-breaking lattice distortions [99, 100]. If we assume that there is a multistable equilibrium state between symmetry equivalent distortions and that they can be easily switched into one another, we already understand the concept of ferroelectricity. In the case of ferroelectric materials, a macroscopic nonzero polarization (spontaneous polarization), \mathbf{P} , can be reversed by a large enough electric field into its negative counterpart $-\mathbf{P}$. At high temperatures, a transition into an average prototype paraelectric structure (dynamic disorder [106]) with zero polarization takes place. The B-site cation often undergoes a polar or antipolar off-center distortion against the oxygen octahedral cage (denoted as Γ_4^- mode) and becomes multistable. This off-centering is generally accompanied by macroscopic strain (see piezoelectric coupling below). Indeed, only due to large strains, the tetragonal phase is stabilized in PbTiO_3 [107].

The instability of the paraelectric (cubic) phase is expressed by a double-well profile with energy minima at non-vanishing polarizations if the energy is plotted as a function of the size, the shape, and the internal coordinates at different amplitudes of the distortion mode [31, 108]. Since we know that structural distortions can be described based on lattice modes, this implies that there must be at least one phonon with an imaginary frequency and a negative curvature at the origin of the double-well below the phase transition temperature [109].

Imaginary frequencies are characteristic of a lattice instability, while real frequencies generally indicate structural stability with respect to a particular deformation mode. The correlation between mode frequencies and crystal instabilities was first introduced by Cochran [99, 100], who essentially states that the restoring forces against a deformation become weak (softening) during a phase transition. Specifically, he refers to the paraelectric to ferroelectric phase transition as a condensation (freezing) of a certain zone-center transverse optic phonon below the phase transition temperature, leading to a dipole moment in the unit cell. He further suggests that the soft mode is temperature-dependent and that the frequency can be described by a harmonic part

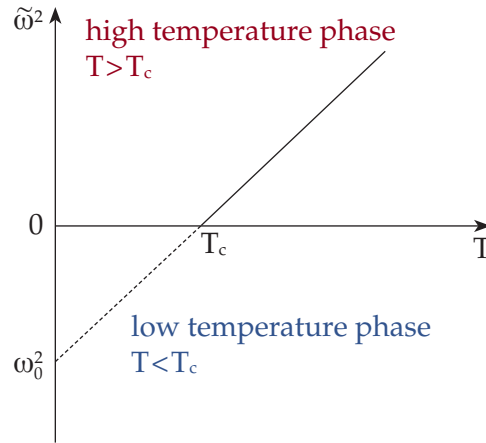


Figure 10: Schematic representation of a lattice mode softening. While at higher temperatures the anharmonic coupling term leads to real frequencies $\tilde{\omega}$, the soft mode becomes unstable below T_c . Adapted from Reference [105].

ω_0 (solution of Equation 86 of Section 3.7) and an anharmonic contribution, giving rise to the following form of $\tilde{\omega}^2$ [105],

$$\tilde{\omega}^2 = -\frac{\omega_0^2}{T_c}(T - T_c) = \omega_0^2 - \frac{\omega_0^2}{T_c}T, \quad (8)$$

where T_c is the phase transition temperature.

Figure 10 illustrates the behavior of a soft mode schematically, where at a higher temperature, the anharmonic coupling term becomes increasingly important and $\tilde{\omega}$ becomes real.

Ferroelectricity plays a significant role in perovskite oxides, where it was discovered in the 1940s [8, 31]. Although we can describe ferroelectricity phenomenologically by the Landau theory or microscopically using lattice dynamics, we still do not know the origin of the ferroelectric instability and why perovskite oxides meet the requirements to become ferroelectric. Let us first take a look at the features of ABO_3 compounds. An intrinsic property of this material family is the mixed ionic-covalent bonding character between oxygen and the A- as well as B-site cations. In particular, the hybridization between the O 2p and the B-site transition metal 3d orbitals contribute to the covalent interaction. Instead, the A-site cation, except Pb in $PbTiO_3$, exhibits a higher ionic nature [8, 107, 109]. This mixed bonding character is assumed to be responsible for anomalously large Born effective charges (see Section 2.5.1).

Indeed, *ab-initio* calculations showed that Born-effective charges might be twice as large as the nominal ionic charges. Harrison [110] proposed that a dynamical charge transfer causes the strong dependency of the hybridization on the bond length during the displacement of a cation sublattice. This charge transfer leads to large dipolar forces, which, in case stabilizing short-range interactions (which favor the cubic phase) are compensated or even exceeded, produce a ferroelectric instability. This delicate interplay between short- and long-range forces can be easily altered by structural or chemical modifications as, for instance, stress or strain effects, the screening of long-range fields by charge carriers, and the manipulation of short-range interac-

tions by dopants [8, 107, 109, 111, 112].

As additionally indicated by the definition of Born effective charges in Section 2.5.1 and apparent from the self-force constants (see Section 2.5.2), ferroelectricity is a collective phenomenon. An isolated off-center displacement is insufficient to produce lattice instability. The restoring forces will always be large enough that the atom will return to its initial position. However, correlation of antipolar Ti/O displacements along Ti–O chains over 4-5 unit cells (chain-like instability in real space) is sufficient to generate ferroelectric instability in BaTiO₃ [109]. Finally, the A-site cation might considerably impact the ground state of the perovskite oxide by firstly hybridizing with the valence states, which additionally modifies the B–O interactions, and secondly by changing the ferroelastic strain, which is coupled to the ferroelectric soft mode.

2.5 FUNCTIONAL PROPERTIES

Many physical properties are obtained from n th order derivatives of the Born-Oppenheimer energy surface and are used to quantitatively compare different materials or the effect of even small chemical as well as structural modifications. In the following, we will deal with a few of them, which are especially important in the context of perovskite oxides. Amongst others, these are the dielectric and the piezoelectric tensor or Born effective charges and interatomic force constants. A complete overview is provided by Table 1 in Section 3.6.

2.5.0.1 Dielectric permittivity

For insulators, the coefficient of proportionality in the linear regime between the macroscopic electric field ($\mathcal{E}_{\text{mac},\beta}$) and the macroscopic displacement field ($\mathcal{D}_{\text{mac},\alpha}$) is given by the piezoelectric permittivity tensor $\epsilon_{\alpha\beta}$ [113]:

$$\mathcal{D}_{\text{mac},\alpha} = \sum_{\beta} \epsilon_{\alpha\beta} \mathcal{E}_{\text{mac},\beta}. \quad (9)$$

The dielectric tensor $\epsilon_{\alpha\beta}$ depends on the susceptibility tensor $\chi_{\alpha\beta}$, the second derivative of the energy with respect to the electric field, and can be defined either at fixed (vanishing) strain ($\epsilon_{\alpha\beta}^{(\eta)}$) or at zero stress ($\epsilon_{\alpha\beta}^{(\sigma)}$) [114],

$$\epsilon_{\alpha\beta}^{(\eta)} = \epsilon_0 (\delta_{\alpha\beta} + \chi_{\alpha\beta}) \quad (10)$$

$$\epsilon_{\alpha\beta}^{(\sigma)} = \epsilon_0 (\delta_{\alpha\beta} + \chi_{\alpha\beta}^{(\sigma)}), \quad (11)$$

where ϵ_0 is the vacuum permittivity and $\delta_{\alpha\beta}$ is the delta function. It is possible to separate the static dielectric constant into an ionic and an electronic ($\epsilon_{\alpha\beta}^{\infty}$, optical dielectric constant) contribution [109],

$$\epsilon_{\alpha\beta} = \epsilon_{\alpha\beta}^{\infty} + \frac{4\pi}{\Omega_0} \sum_{\text{m}} \frac{p_{\text{m}\alpha} p_{\text{m}\beta}}{\omega_{\text{m}}^2}, \quad (12)$$

where Ω_0 is the unit cell volume, and m is a transversal optical mode of frequency ω_m and mode polarity $p_{m\alpha}$. The latter is defined by the Born-effective charge tensor $Z_{\kappa,\alpha\beta}^*$ and the phonon eigendisplacement $U_{\kappa\beta}^m$ [109] as

$$p_{m\alpha} = \sum_{\kappa\beta} Z_{\kappa,\alpha\beta}^* U_{\kappa\beta}^m. \quad (13)$$

We deduce from Equation 12 that perovskites with a highly polar soft mode at a low frequency, which additionally strongly couple to an electric field, exhibit huge dielectric coefficients. The phenomenon of dielectric relaxation is strongly dependent on the electric conductivity, the temperature, as well as the composition and quantifies the time and frequency dependence at alternating applied fields [115].

2.5.0.2 Piezoelectricity

The direct piezoelectric effect describes the electric polarization ($P_{\text{ind},i}$) induced by the application of mechanical stress (σ_j) to the crystal [116, 117]. Usually, the third-rank piezoelectric tensor, $\{d_{\alpha j}\}$, at well defined \mathcal{E} and σ is compared in literature [114, 116, 118],

$$d_{\alpha j} = \left. \frac{\partial \eta_j}{\partial \mathcal{E}_\alpha} \right|_\sigma = \left. \frac{\partial P_\alpha}{\partial \sigma_j} \right|_\mathcal{E}. \quad (14)$$

However, two other definitions are thermodynamically equally valid, describing either the polarization linearly induced by the macroscopic strain (second term of Equation 16) or, alternatively, the measured stress linearly induced by a macroscopic electric field at vanishing strain (third term of Equation 16) [31, 42, 114],

$$\tilde{e}_{\alpha j} = - \left. \frac{\partial^2 E}{\partial \mathcal{E}_\alpha \partial \eta_j} \right|_u \quad (15)$$

$$e_{\alpha j} = - \frac{\partial^2 \bar{E}}{\partial \mathcal{E}_\alpha \partial \eta_j} = \left. \frac{\partial P_\alpha}{\partial \eta_j} \right|_\mathcal{E} = - \left. \frac{\partial \sigma_j}{\partial \mathcal{E}_\alpha} \right|_\eta. \quad (16)$$

Here, E is the energy, \mathcal{E} denotes the electric field, η represents the strain, and the displacement is given by u . Note that $e_{\alpha j}$ (C m^{-2}) and $d_{\alpha j}$ (pC N^{-1}) have different units and are related by the elastic stiffnesses (or equivalently elastic compliances) [116]. The exact quantity depends on whether we calculate the clamped-ion piezoelectric tensor with zero internal strain boundary conditions ($\tilde{e}_{\alpha j}$) or if we are interested in the relaxed-ion response tensor ($e_{\alpha j}$), where $\bar{E}(\eta, \mathcal{E})$ is defined as [114]

$$\bar{E}(\eta, \mathcal{E}) = \min_u E(u, \eta, \mathcal{E}). \quad (17)$$

If we express the relaxed-ion piezoelectric tensor in terms of the clamped-ion counterpart (response to macroscopic strain only), we get [114]

$$e_{\alpha j} = \tilde{e}_{j\alpha} + \Omega_0^{-1} Z_{m\alpha}^* (C^{-1})_{mn} \gamma_{nj}, \quad (18)$$

where the second term defines the effect of microscopic strain on the polarization, which is comparable to a linear alternation of the polarization caused by a phonon at the Γ -point. Precisely, Ω_0 represents the unit cell volume, $Z_{m\alpha}^*$ and $(C^{-1})_{mn}$ are the Born effective charge tensor (see definition below) and the inverse (“pseudoinverse”) force constant matrix, respectively, and γ_{nj} is the internal-strain tensor. Piezoelectricity is a well-defined bulk property and thus independent from the surface termination. Proof thereof was given by R. M. Martin in 1972 [117, 119].

2.5.1 *The concept of Born effective charges*

In the last sections we have seen that a mixed ionic-covalent bonding character in perovskites is essential to observe ferroelectricity [31, 107, 120]. Closely associated with ferroelectric instability is the concept of Born-effective charges, which connects electronic and structural properties [121]. In the following, we will summarize the main ideas behind this property and highlight the benefits over the more familiar static charges.

In the framework of static charges, the ground-state electronic density is allocated to the different atoms of the perovskite structure. Although the concept seems intuitive, static charges are ill-defined quantities due to the arbitrariness of assigning electrons to specific atom types. This is particularly severe if no boundary can be drawn between the atoms where the electron density is sufficiently small [122, 123]. Thus, the most commonly used techniques are based on the electronic density and include the Mulliken population analysis (strongly dependent on the choice of basis functions) [124] and the Bader charge (splitting of the electronic charge density between non-overlapping regions) [125]. Consequently, despite all these charges describing the same physical phenomenon, the quantitative results will be different and are no observables in the strict sense [126].

In order to obtain meaningful ionic charges outside the framework of a specific model, Born and Göppert-Mayer [127] first associated effective charges with an experimentally measurable change of polarization in 1933. Although they are generally known as Born effective charges, transverse charges or dynamic effective charges are equally valid descriptions and are used interchangeably in the present thesis. As we will see in later definitions, Born effective charges are fundamental properties of lattice dynamics and define the long-range dipole interactions, which are responsible for the splitting of the longitudinal and transverse optic phonon mode. They further explain the polarization as an electronic current (localized and delocalized contribution), which is caused by a dynamical variation of the interatomic orbital hybridization mainly between the transition metal d-orbitals and the oxygen 2p-orbitals (for a more detailed explanation see Reference [121]).

The Born effective charge tensor, $Z_{\kappa,\beta\alpha}^*$, relates the screened macroscopic electric field in direction β , $\mathcal{E}_{\text{mac},\beta}$, to the internal (microscopic) strain [31],

$$f_{\kappa,\alpha} = \sum_{\beta} Z_{\kappa,\beta\alpha}^* \mathcal{E}_{\text{mac},\beta}, \quad (19)$$

where $f_{\kappa,\alpha}$ denotes the force in direction α at atom κ . Equivalently, the Born effective charge tensor of atom κ relates the macroscopic polarization along direction α linearly to the collective displacement of the κ -type sublattice, $u_{\kappa,\beta}$, at zero electric field and is given by [31],

$$Z_{\kappa,\beta\alpha}^* = \Omega_0 \left. \frac{\partial P_{\alpha}}{\partial u_{\kappa,\beta}} \right|_{\mathbf{q}=0, \mathcal{E}=0}, \quad (20)$$

where Ω_0 is the unit cell volume. In order to avoid a macroscopic polarization induced by rigid translations, the acoustic sum rule must be fulfilled by the Born effective charge tensors [31, 112].

$$\sum_{\kappa} Z_{\kappa, \beta \alpha}^* = 0. \quad (21)$$

While the amplitude of static charges is generally reduced by covalent bonding, the dynamical equivalent is increased by larger hybridizations of the anion and cation orbitals. *Ab-initio* calculations of Born effective charges demonstrated that they are even anomalously large compared to the static or nominal values. For instance, $Z_{\text{Ti}, \beta \alpha}^*$ in SrTiO_3 , BaTiO_3 , and PbTiO_3 are in the range of 7.0 to 7.56. This is almost twice as large as +4, which is the ionic charge if we entirely neglect covalent bonding contributions. Interestingly, the dynamic charge amplitude changes quasilinearly with the nominal charge of the B-site in ABO_3 compounds and is sensitive to the anisotropic atomic environment along the B–O chain. Instead, except for PbTiO_3 , $Z_{\text{A}, \beta \alpha}^*$ of the A-site cation sublattice hardly shows anomalies. In the case of PbTiO_3 , large Born effective charges for the A-site cation are attributed to an increased hybridization between Pb and oxygen [31, 121, 128].

2.5.2 Interatomic force constants

Isolated displacements do not induce ferroelectric instability. Only the collective displacement of an ionic sublattice might compensate for short-range restoring forces and lowers the total energy in favor of a low symmetry ferroelectric phase. At linear order, the interatomic force constants (IFCs) couple the force $F_{i\alpha}^a$ on atom i along the direction α in the unit cell a with the displacement $u_{j\beta}^b$ of atom j in the unit cell b in the direction of β from its equilibrium position [129–131],

$$F_{i\alpha}^a = -K_{i\alpha, j\beta}(a, b)u_{j\beta}^b. \quad (22)$$

Here, $K_{i\alpha, j\beta}$ is the real-space interatomic force constant matrix (see Equation 85), which is the second derivative of the ground-state energy concerning nuclear displacements \mathbf{u}_i and \mathbf{u}_j . Note that the self-force constant or “on-site” force constant is generally positive, implying a stable off-center displacement of an isolated atom. In contrast, negative values display unstable interactions.

The IFCs can be divided into a short-range (SR) and a long-range dipole-dipole (DD) contribution. They are further decomposed into a longitudinal (\parallel) and a transverse (\perp) part with respect to the bonding direction [131]. In insulators, long-range dipole-dipole interactions between the ions lead to long-ranged interatomic force constants, decaying as $1/d^3$ if d describes the distance between the nuclei [129, 132]. The determination of the IFCs not only reveals the origin of unstable phonon branches but also beneficial couplings of atomic displacements on a more local scale [131].

2.5.3 Covalent bonding in perovskite oxides and the lone pair effect

Perovskite oxides are characterized by a mix of ionic and covalent bondings. Since the charge transfer between oxygen and the B-site cation is incomplete, the electrons

remain partly delocalized on the B-site while effectively reducing the static charge and simultaneously increasing the valence band maximum. In Section 2.4.3 we saw that this covalent bonding contribution and primarily a change in covalency during a collective displacement might be an indicator for ferroelectric instability. In turn, in the case of magnetic cations, covalent interactions might vary the indirect magnetic-exchange interactions, which is important for studying magnetically ordered ferroelectrics or even multiferroics [133, 134].

Actually, the covalent interaction of the A-site cation with oxygen is almost negligible, except if the A-site cation carries an electron lone pair. This lone pair crucially contributes to the ground state's symmetry and is primarily known in the context of PbTiO_3 . Long time it has been assumed that a chemically inert but sterically active Pb(II) lone pair is, at least partly, responsible for the distortion observed in the ground state structures. Two comprehensive studies, conducted by Walsh *et al.* [135, 136], are especially noteworthy, which on the one hand, unveil the mysteries behind the lone pair by comparing PbO with PbS and, on the other hand, constitute a revision of the classical lone pair model with regard to post transition metals. In the following, if not stated otherwise, we will solely refer to References [135, 136].

Originally, structural distortion and electronic asymmetry caused by the lone pair was purely explained by minimization of electrostatic repulsion between the valence bonds and the so-called inert s^2 electron pair. However, already Orgel [137] pointed out that the on-site mixing of cation s and p orbitals are crucial for the formation of a stereochemically active lone pair. The structural distortion was a natural consequence of non-centrosymmetric cation sites, necessary to achieve the same symmetry for s and p orbitals and thus to allow for orbital mixing (pseudo-Jahn-Teller effect [138]). This second-order stabilization has to compensate for a reduced coordination number, making the active lone pair chemically dependent.

Although the classical model was a significant contribution to the understanding of the lone pair effect, the nature of the lone pair and the exact reasons for its stereochemical activity was unclear until electron densities and crystal orbital overlap populations became feasible. The study of Walsh [135, 136] showed that the s^2 electron pair is not chemically inert but forms bonding and anti-bonding states at the bottom and the top of the upper valence band, as schematically illustrated in Figure 11. If the interaction of the unoccupied cation p orbitals with the anti-bonding states becomes symmetry allowed by a lattice distortion, the amount of high energy states at the Fermi level is reduced. The stabilization of the occupied states by the on-site hybridization results in the familiar asymmetric electron density of the lone pair cations away from the anions.

A critical prerequisite for an intra-atomic orbital overlap is a considerable degree of cation s character of the anti-bonding states close to the valence band maximum. Thus, a strong interaction between cation s and anion p orbitals and the relative energy between both states are decisive. We now easily understand that the latter constraint leads to a strong dependency of the stereochemical activity on the chemical nature of the anion and the cation.

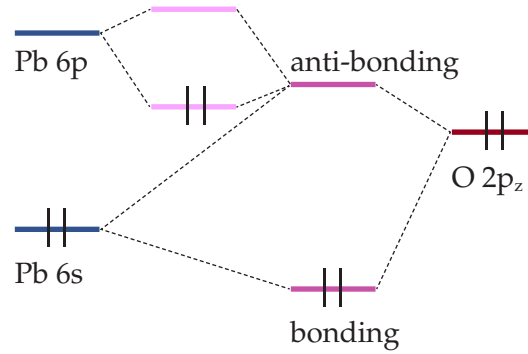


Figure 11: Schematic illustration of the lone-pair effect in PbTiO₃. Adapted from Ref. [136].

Schütz *et al.* [46] showed that structural instabilities at the depolarization temperature are inevitably linked with the loss of hybridization between bismuth and oxygen. This demonstrates the importance of the lone pair induced covalence in NBT and perovskite oxides in general.

2.6 IONIC CONDUCTIVITY

High ionic conductivities at intermediate temperatures are a primary objective in the field of solid oxide fuel cells to avoid impractical thin films, or high operating temperatures [139]. In this regard, the distribution of charge carriers and their diffusion kinetics are central properties, determining the performance and reliability of a device [140]. On the other hand, negligible conductivities are required for high temperature-stable capacitor applications. Similarly, low oxygen vacancy concentrations are preferred, if domain wall pinning must be avoided in piezoelectric ceramics [141]. A detailed understanding of the migration process is inevitable in all mentioned cases to promote or prevent high conductivities. However, before summarizing the most recent developments in the field of lead-free solid electrolytes and high-temperature dielectric materials, we will build a solid foundation of the conduction mechanism in ionic conductors. Moreover, we will introduce all relevant notations, which are used consistently throughout the present thesis.

2.6.1 Conductivity – A description on the macroscopic scale

The flux of a species k , \mathbf{j}_k , is defined by Ficks first law [142, 143] as

$$\mathbf{j}_k = -\mathbf{D}_k \nabla c_k, \quad (23)$$

where \mathbf{D}_k is a second rank tensor, which reduces to a scalar diffusion coefficient for cubic symmetries, and ∇ is the Nabla operator, acting on the scalar concentration field c_k . Note that, despite Equation 23, the real driving force for diffusion is the

gradient in the chemical potential rather than a gradient in the concentration [143]. The diffusion coefficient is given by the Nernst-Einstein relation [142],

$$D_k = \frac{\sigma_k RT}{z^2 F^2 c_k}, \quad (24)$$

where σ is the conductivity, F the Faraday constant, T the temperature, and R the ideal gas constant. In the case of vacancies, the diffusion coefficient can also be expressed as [144]

$$D_k \approx \frac{1}{2} a^2 Z \Gamma_k \exp\left(-\frac{\Delta H_{\text{mig}}}{k_B T}\right). \quad (25)$$

Here, a is the jump distance, Z the number of neighbor sites, ΔH_{mig} the migration enthalpy, and Γ_k the jump frequency. The jump frequency is often assumed to be equal to the Debye-frequency, which is on the order 10^{13} Hz [143, 145].

The total conductivity is the sum of individual contributions, resulting from various charge carriers $\{k\}$, which might be ions, electrons, holes, or polarons [142]:

$$\sigma(P, T) = \sigma_{\text{ion}} + \sigma_{\text{el}} = \sum_k \sigma_k(P, T). \quad (26)$$

The dependency of σ on the partial pressure is indicated by P and T again denotes the temperature. For every single species the following equation applies [142],

$$\sigma_k(P, T) = |q_k| F u_k(T) c_k(P, T), \quad (27)$$

where F is the Faraday constant and $u_k(T)$ is the mobility of species k . Another way to express conductivities is [139],

$$\sigma T = \sigma_0 \exp(-E_a/k_B T), \quad (28)$$

where σ_0 is a pre-exponential constant, primarily dependent on the migration enthalpy, the attempt frequency, the charge carrier concentration as well as the charge itself, and the jump distance. This factor will be analyzed in Chapter 4 in closer detail. We will use T consistently to define the temperature, and k_B to declare the Boltzmann factor. E_a denotes the process enthalpy and is commonly known as activation enthalpy, which strongly depends on the effective charge of the migrating species. Due to the temperature dependency of the mobility we get [142]

$$E_a^k = -R \frac{\partial \ln \sigma_k}{\partial 1/T}, \quad (29)$$

with the ideal gas constant R . We will use this relation later to determine the activation barrier from the slope of experimentally determined Arrhenius plots. From the previous relationships, we easily recognize the following proportionality [142]:

$$u_k T \sim D_k \sim \Gamma_k. \quad (30)$$

2.6.2 Conductivity – Interactions on the microscopic scale

Throughout the present thesis, we will assume a vacancy mediated ionic conductivity, which is based on a thermally activated hopping mechanism. This mechanism is characterized by a jump of a regular species K onto a vacant lattice site, which has an effective charge q . This process can be understood as if the regular species and the vacancy swapped sites [142]:



Here x and x' describe two different positional vectors. Without an external field, the process in Equation 31 is stochastic. However, if a field is applied, a mass transport takes place and the diffusion is superimposed by a drift in the direction of the applied field [143, 146]. This process can be described either by the migration of vacancies or of regular particles. For reasons of simplicity, we prefer to discuss the migration of oxygen vacancies instead of the movement of O^{2-} ions.

Dopants, intentionally introduced aliovalent impurities, are an effective tool to tune material properties. In this study, we assume the dopant concentration to be an *ex-situ* parameter, which has been introduced irreversibly and which is kinetically frozen inside the structure. Thus, the concentration of oppositely charged defects has to increase accordingly until the system is globally charge neutral [139, 142]. If these two oppositely charged species interact, a deviation from a random defect distribution arises. This interaction might be of Coulombic, covalent, or elastic origin and leads to an exothermic formation of defect associates while simultaneously reducing the number of mobile charge carriers.

2.6.3 Defect association – A way to manipulate ionic conductivities?

Generally, ionic association describes the phenomenon that the charge compensating defect passes through an energetic minimum with increasing distance to the dopant. The formation of an ionic defect associate between an (acceptor) dopant and an oxygen vacancy is of paramount importance for this study and can be written conceptionally as



where D denotes the dopant, occupying a regular site of atom type X with an effective charge of q . The defect equilibrium in equation 32 requires that the oxidation number of the dopant does not change during the reaction. The associate, $(D_X^q - V_{\ddot{O}})^{2+q}$, can be understood as a defect dipole with a certain orientation. Depending on q , the resulting defect associate is either charged or neutral. The formation of defect associates has been observed frequently in literature, especially in NBT related systems as strontium titanate [140] and lead titanate [147, 148]. In the present thesis, we will use the term *nearest neighbor associate* if the oxygen vacancy resides on the first neighbor shell. In turn, we will use the expression *higher-order associate* if the vacancy sits on higher neighbor shells. Figure 12 depicts the neighbor shells in a small schematically

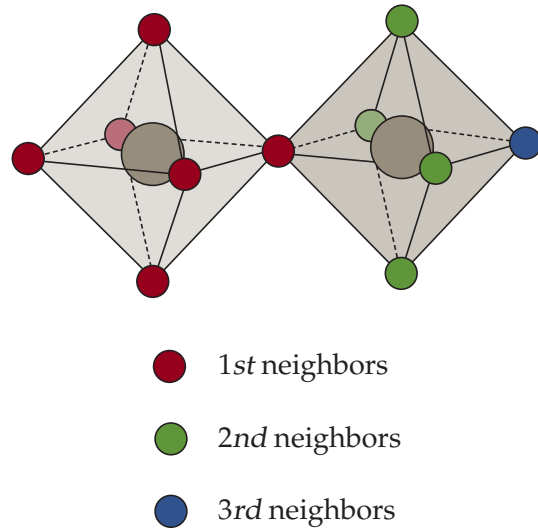


Figure 12: Oxygen neighbor shells in the R3 structure. The first octahedron is considered as the center.

drawn section of the R3 structure if the first octahedron is considered as the center.

Another typical example of a defect associate is the change of the dopant's redox state (at least if the dopant is a transition metal), which essentially describes the interaction between an electron and an ion. However, the electron might also be trapped in a polaronic state at the dopant or localized directly at the vacant site [149]. A suitable scenario is the localization of electrons at the oxygen vacancy, forming a single positively charged or an effectively neutral defect [142] and where V_{O}^{\cdot} and V_{O}^{\times} represent two different donor states:



The formation of associates, ionic or electronic, is one of the main reasons for the non-ideality in mass-action-laws. Non-vanishing source terms are created if the diffusing defect takes part in internal defect chemical reactions. However, it could be shown that if a local equilibrium can be established, chemical diffusion theory can still be applied to the conservative ensemble (total non-stoichiometry, which has no source term) [150, 151]. *If defect associates are such a powerful tool, this leaves us with the question of whether they exist, if they are thermodynamically stable, if the stability depends on the local symmetry, and how they affect the local structure in return?*

2.6.4 What we can learn from Arrhenius plots

The Arrhenius plot in Figure 13 schematically illustrates three distinct stages for ionic conductors, depending on the inverse temperature. At low temperatures, the charge carrier concentration is determined by the thermodynamic equilibrium between the

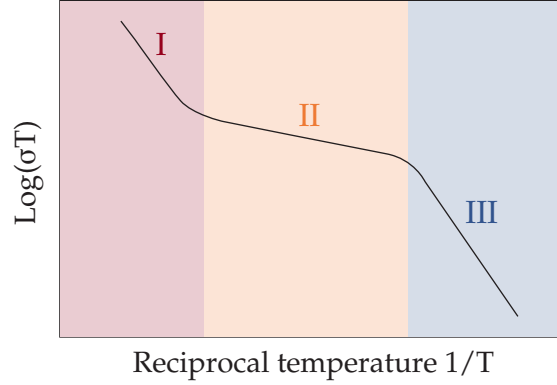


Figure 13: Scheme of the three stages of the temperature dependent ionic conductivity. A pronounced kink at the transition between stage III and II has been discovered in NBT [1]. We will discuss the origin of this kink in Chapter 4. For more details see main text. Adapted from Reference [152].

free and the associated defect species. In this part, the concentration of mobile defects increases continuously until most defect pairs are dissociated. In the second range, the conductivity depends solely on the total concentration of the dopant, while at high temperatures additional intrinsic defects contribute to the overall current [152]. These intrinsic defects might be additionally created oxygen vacancies (Equation 35) or electrons, which fulfill the intrinsic defect equilibrium with an activation enthalpy depending on the band gap (equation 36) [143],



We will discuss equation 36 in greater detail below, when we will *examine the preferred charge states of the defect associate. We will further investigate if there are any dopant and vacancy related states in the band gap, if they are electrically active, and if electron trapping at the vacant site can be expected.* Since we did not observe severe formation of intrinsic oxygen vacancies, we will neglect them and solely consider vacancies originating from a processing related Bi-loss or aliovalent doping.

2.6.5 Activation and migration barriers – key parameters for a smooth flow?

As already mentioned before, we can extract the activation enthalpy from the slope of the conductivity, plotted against the inverse of the temperature. This activation enthalpy can be decomposed into several components [35, 152],

$$\Delta H_\text{a} = \Delta H_\text{m} + \Delta H_\text{f} + b\Delta H_\text{asso}, \quad (37)$$

where ΔH_a is the activation enthalpy, ΔH_m and ΔH_f describe the migration enthalpy and the formation enthalpy, respectively, and ΔH_asso denotes the association enthalpy of the defect associate, which dictates the effective oxygen vacancy concentration. Figure 14 schematically illustrates the three different energy contributions in NBT. The

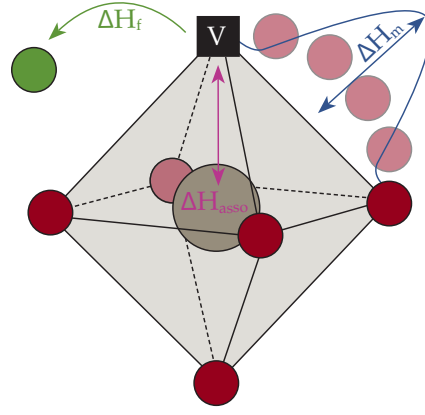


Figure 14: Illustration of the formation, migration, and association energy in NBT. The A-site sublattice has been omitted for clarity. Note that the formation energy is defined with respect to a given reservoir.

A-site sublattice has been omitted for clarity. The factor b depends on the effective defect charge of the dopant. For instance, in the case of Mg_{Ti}'' , b would be 0.5. Instead, for a Fe'_{Ti} dopant, b would amount to 1. This defect associate might persist to high temperatures [152], which has been verified from the experiments performed by our collaborators (see Chapter 4). Both ΔH_m and ΔH_{asso} strongly depend on the dopant size and the dopant/host cation ratio. A comparable radius between the host and the dopant proved to be particularly beneficial for optimizing ionic conductivities, emphasizing the importance of the elastic strain energy for defect interactions [139]. In our case, only the first and the last term of the right-hand side are important since the concentration of the aliovalent dopant determines the vacancy concentration, and we do not assume any additional thermal generation of oxygen vacancies.

The migration energy is composed of two further terms [145],

$$\Delta H_m = \Delta H_b + \Delta H_r, \quad (38)$$

where ΔH_b represents the energy barrier between the saddle point, and the potential minimum and ΔH_r is the relaxation energy, resulting from the equilibration of the metal-oxygen bonds during the transition. Therefore, highly polarizable ions with an electron lone pair on the A-site (e.g., Pb^{2+} or Bi^{3+}) are beneficial for decreasing ΔH_m . In pure NBT, the oxygen vacancy concentration is relatively low. Nevertheless, the measured bulk conductivities indicate high ionic mobilities. It has been assumed that highly polarizable and off-centered Bi ions with a reduced effective coordination number facilitate local lattice relaxations, leading to various Bi-O bond lengths, weak Bi-O bonds, and thus promote a fast migration through the sample. Isovalent doping experiments seem to confirm this trend, showing that a weak bonding strength is an indicator, though not the only one, for fast oxide-ion migration [19, 153].

Especially in perovskite oxides, several studies coupled the migration barrier with the amount of free space at the saddle point configuration. Figure 15 depicts the atomic arrangement at the saddle point, which is characterized by a triangle formed out of two A-site (Bi/Na) and one B-site (Ti) cation (see Figure 15). Essentially, the

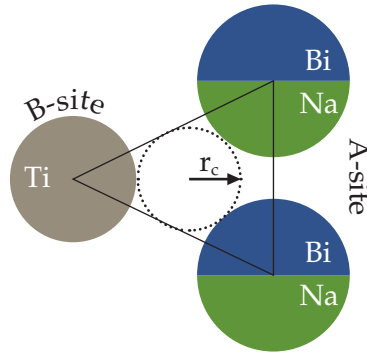


Figure 15: Scheme of the saddle point configuration during migration of oxygen. Adapted from Reference [139].

size of the triangle determines the critical radius of a sphere, which can pass through the saddle point without disturbing the lattice. Thus, the larger the critical radius r_c , the lower the migration barrier. A strategy to increase r_c is the variation of the cation sizes, implying either smaller A-site or larger B-site species. The theory of the critical radius further explains why conductivities might differ in various polymorphs of the same compound [139, 145]. Hayashi *et al.* [154] established a rule of thumb connecting the ionic conductivity with structural parameters. From this study they suggest that a tolerance factor of 0.96, a dopant to host ion radii ratio of 1.05, an increased free volume, as well as a large critical radius at the saddle point position positively impacts the activation energy of the oxygen vacancy [155].

Indeed, these criteria apply to A-site Sr^{2+} -doped NBT, which shows higher conductivities than the isovalent alternatives Ba^{2+} or Ca^{2+} and where $r(\text{Sr}^{2+})/r(\text{Bi}^{3+})$ amounts to a value of roughly 1.05.

In NBT, three different saddle point configurations are conceivable. The cation triangle is either formed by two Bi, two Na, or one Na and one Bi with Ti as the third vertex, respectively. Calculations revealed that the activation energy for a jump through a triangle with two Bi is the lowest and increases if Bi is replaced by Na [156]. However, since no long-range ordering could be confirmed experimentally, the rate-determining migration barrier belongs to the mixed A-site configuration and should be in the range between 0.6 eV to 0.85 eV [19, 156]. Interestingly, estimates from oxygen tracer diffusion experiments showed that vacancy diffusion coefficients are surprisingly similar among the members of the perovskite family [35], irrespective of the atom type occupying the A- and B-site. Thus, it may be concluded that the activation energy depends mainly on the ability to form defect associates, the amount of the mobile vacancy concentration, and the lattice symmetry [35].

If we take a closer look at the formation of a defect associate, we see that the trapping depends, comparable to ΔH_m , on two energy terms. Just as in Equation 38, ΔH_b corresponds to an energy barrier caused by the interaction between the ions, and ΔH_r again describes the structural relaxation. However, in this case the relaxation energy results from an adaption of the local vicinity to the misfit volume of the dopant [145]. Therefore oxygen vacancies will experience a variety of different activation enthalpies depending on the lattice site. Since trapping effectively reduces the amount

of mobile charge carriers, the mechanical impact of the dopant should be reduced to a minimum, if a high conductivity is needed [146].

All in all, ionic conductivities increase with a higher concentration of charge carriers, the number of crystallographic sites, which are involved during the diffusion, the size of the bottleneck at the saddle point configuration, the Goldschmidt tolerance factor, the lattice free volume [39], and the occupancy ratio on different or the same sublattice [35]. From Equations 37 and 28 we further see that the migration, the association, and the formation enthalpy of defects should be small to provide high levels of ionic conductivity. *Thus, we have to determine migration barriers and the exact dependency of the conductivity on the dopant concentration in NBT. In the latter case, we have to distinguish carefully between long- and short-range as well as between electrostatic and purely elastic interactions.* In short, we have to decode the “multidimensional nature of the oxygen vacancy migration” [35].

2.6.6 Three conductor types in one material and the power of A-site non-stoichiometry

NBT and NBT-based solid solutions show high leakage currents, which additionally depend sensitively on the nominal starting composition. Electromotive force measurements and ^{18}O tracer diffusion experiments verified that this leakage current stems from the oxygen ionic conduction, with ionic transport numbers exceeding values of 0.9 in a temperature range from 600 °C to 800 °C [1, 19]. These measurements, as well as pressure-dependent low-frequency impedance data, further suggest negligible Na^+ contribution to the conductivity, rendering oxygen vacancies as the dominant charge carrier in NBT [1, 19]. The rather high conductivity of nominally stoichiometric NBT has been related to the Na and Bi non-stoichiometry, mostly induced by low levels of Bi_2O_3 loss during processing [19]:



In contrast, the Na_2O loss during sintering is much lower than the one of Bi_2O_3 , which is related to the high volatilization temperature of Na_2O (>1132 °C) compared to Bi_2O_3 (>825 °C) [157].

We can draw two conclusions from reaction 39. First, an intentional Bi-deficiency ($\text{Na}_{0.5}\text{Bi}_{0.5+x}\text{TiO}_{3+1.5x}$ with $x \leq 0$) will enhance the oxygen vacancy concentration and therefore increase the conductivity. Second, Bi-excess ($\text{Na}_{0.5}\text{Bi}_{0.5+x}\text{TiO}_{3+1.5x}$ with $0 < x \leq 0.01$) will decrease the ionic conductivity, leading to ionic transport numbers less than 0.1 at 600 °C to 800 °C. In the latter case the excess Bi_2O_3 will compensate for the processing related loss. Indeed, Bi-excess samples are n-type electronic conductors with activation energies of approximately half of the band gap (1.6 eV). Interestingly, the oxide-ion conductivity can be recovered by further increasing the amount of starting Bi-excess ($\text{Na}_{0.5}\text{Bi}_{0.5+x}\text{TiO}_{3+1.5x}$ with $x \geq 0.02$), leading to transport numbers of 0.5. It is suggested that this change is based on the formation of a Bi-rich secondary phase, which depletes the main bulk phase and probably leads to space charge effects [1, 19, 141]. Generally, the amount of Bi non-stoichiometry should be restricted to $x \approx 0.005$ to prevent the formation of secondary phases. A comprehensive list of secondary phases, detected by X-ray diffraction, secondary electron, and

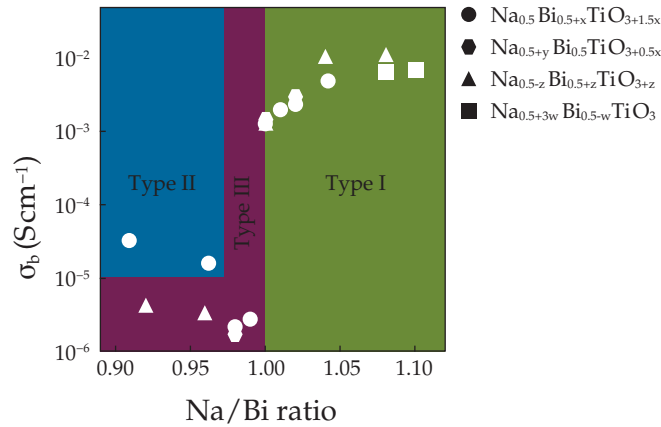


Figure 16: Bulk conductivity of NBT at 600 °C for different A-site non-stoichiometries. Type I specifies predominantly ionic conductors. Type II is characterized by a mixed ionic-electronic conductivity, while in type III electrons are the prevailing charge carriers. Adapted from Reference [19].

transmission electron microscopy, is given by Yang *et al.* [19]. However, these results depend on sintering temperature, sintering time, and other processing conditions.

Even though the allowed level of non-stoichiometry is low, bulk conductivities might change by three orders of magnitude, which is both a curse and a blessing. This delicate interplay between the A-site non-stoichiometry and the conductivity allows categorizing NBT into three types with different conductivities and therefore three different ionic transport numbers, t_{ion} . *Type I is characterized by high ionic bulk conductivities with a t_{ion} of about 0.9. Instead, type II is a mixed ionic-electronic conductor showing an intermediate t_{ion} of around 0.5, while in type III electrons are the dominant charge carriers and t_{ion} remains below 0.1.* An equally adequate criterion to classify type I to type III conductors is the dielectric loss $\tan \delta$, where the temperature-dependent steep rise is shifted to higher temperatures with increasing type specification (I to III) [19].

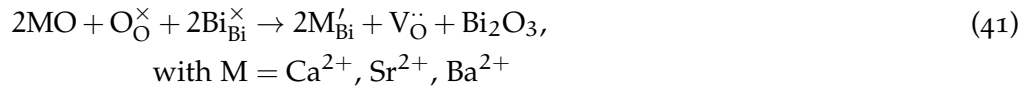
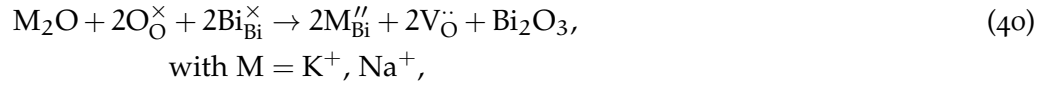
Naturally, Na non-stoichiometry ($\text{Na}_{0.5+y}\text{Bi}_{0.5}\text{TiO}_{3+0.5y}$) is another option to induce insulating or conductive behavior. However, recent studies by Yang *et al.* [19] demonstrated that Na-deficiency ($y < 0$) leads to a bulk composition that is essentially Bi-rich and that the formation of Na-rich secondary phases in samples with $y > 0$ renders NBT effectively Bi-deficient. The effect of Na or Bi non-stoichiometry is, therefore, exactly opposite to each other. Hence, partial elimination of the oxygen vacancies by the introduction of Na_2O is not possible. Figure 16 gives a visual overview of the three different conductor types and how these different electric properties can be accomplished in pure NBT via Bi- or Na-deficiency or excess.

2.6.7 Acceptor doping – NBT’s breakthrough as a solid electrolyte?

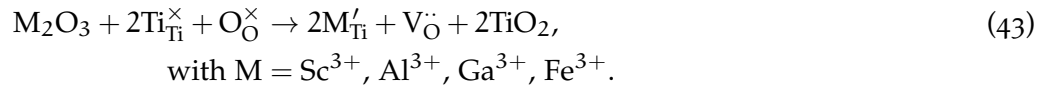
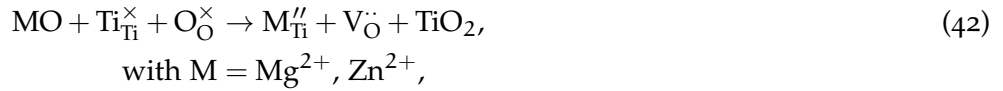
Although non-stoichiometry is a powerful tool to change conductive behavior thoroughly, we will discuss other possibilities to either design promising electrolytes or

obtain candidates for high-temperature dielectric/piezoelectric devices. These possibilities are acceptor, donor, or isovalent doping (“stoichiometric doping”). Let us first discuss acceptor doping since all dopants investigated in the present thesis are acceptors either on the A-site or the B-site. *The preferred lattice site for dopants, especially Al-dopants, and the influence of other components within a NBT-based solid solution will be analyzed in the results section and requires the following defect chemical knowledge.*

If we introduce a dopant with a different charge on a regular lattice site, the charge neutrality of the system must be restored by a compensating electronic or ionic defect. Contrary to SrTiO₃ or BaTiO₃, where electrons, holes, or oxide ions are predominant (depending on the oxygen partial pressure, the annealing temperature, or the cooling rate), in NBT mainly oxygen vacancies are induced by the following reactions on the A-site [19, 158],



or on the B-site



Although the generation of oxygen vacancies by acceptor dopants is beneficial and a powerful tool to increase the conductivity for solid electrolyte applications, the extent of additionally generated charge carriers is restricted by three factors. First, the solubility limits of acceptor dopants in NBT are typically reached at about 2 mol%. At higher dopant concentrations, the formation of secondary phases can not be prevented [159]. Secondly, a fundamental (maximal) diffusivity level in cubic perovskites has been proposed by De Souza [19, 143], which corresponds to an oxygen deficiency of 0.025. Even higher amounts of oxygen vacancies should not lead to significantly larger diffusivities. Finally, the third reason for a saturating effect in acceptor doped NBT is the trapping of oxygen vacancies at the dopant, which, interestingly, depends on whether the oxygen vacancy binds to a dopant located at the B- or A-site [19]. Since trapping seems to be preferable on the B- rather than the A-site, A-site doping has been assumed to be superior to B-site acceptor doping (if a high ionic conductivity is desired). However, conductivity measurements on A-site Sr-doped NBT have shown that low association energies alone are no guarantee for high conductivities and that the bond strength and polarizability of the A-site dopant are equally important [153].

From all possible B-site acceptor dopants, Mg is relatively well known [1, 158, 160]. Mg doping increases the diffusion coefficient up to $1.17 \times 10^{-8} \text{ cm}^2 \text{ s}^{-1}$ at 632 °C and is known for its good phase stability, low grain boundary resistivity, a high sinterability,

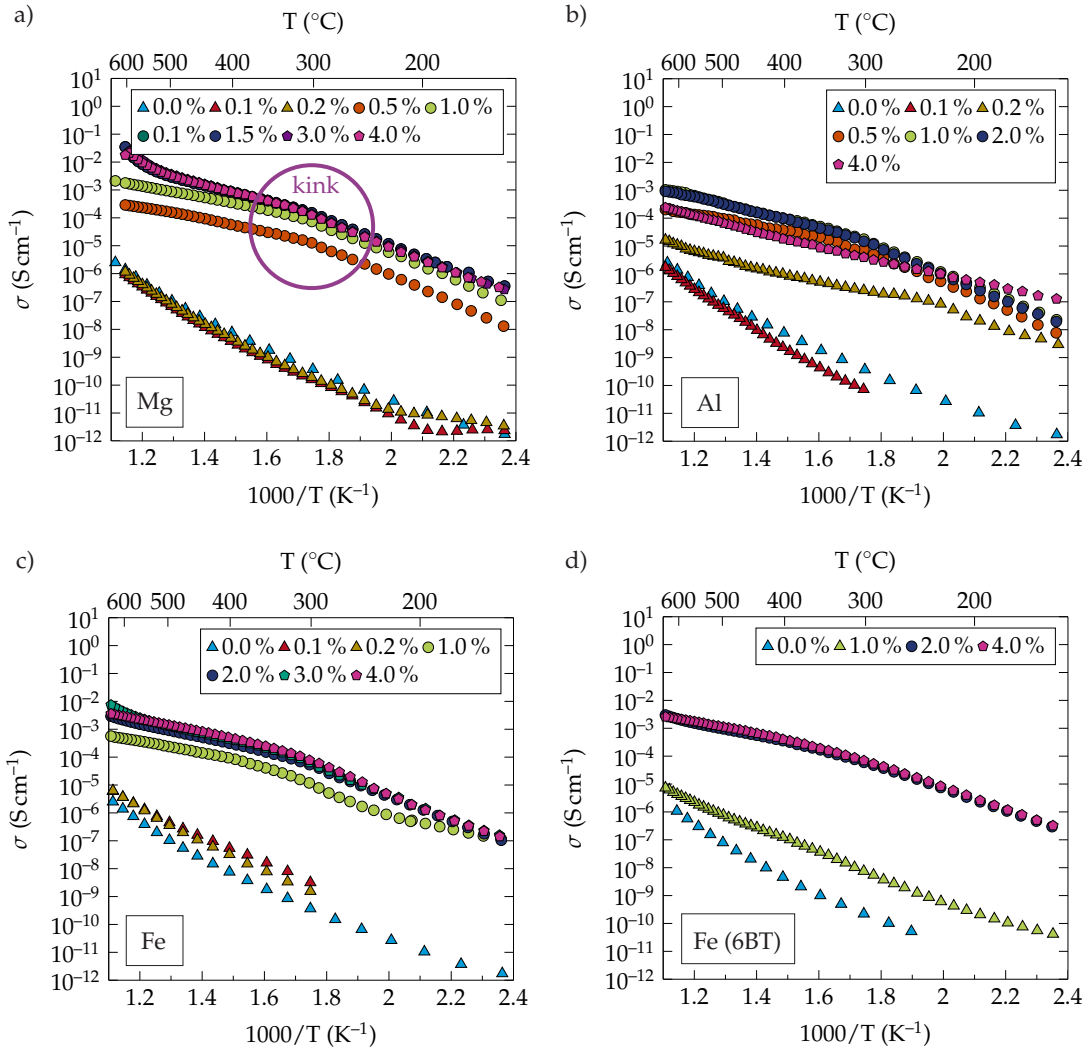


Figure 17: Arrhenius plots for the bulk conductivity of a) Mg-, b) Al-, and c) Fe-doped NBT as well as d) Fe-doped NBT-6BT for several doping concentrations in the range between 0.1 mol% and 4.0 mol%.

and a resistance to reduction at low oxygen partial pressures [1, 161]. However, recent literature equally predicts a comparably high association energy to oxygen vacancies [156], which restricts the mobility of oxygen vacancies and limits ionic conductivities. Comparable to Mg-doped NBT, defect associates between Fe and an oxygen vacancy have been identified in Fe-doped NBT by means of electron paramagnetic resonance (EPR) [21, 22]. Although the formation of defect associates with Fe was assumed to primarily induce ferroelectric hardening by a time-dependent clamping of domain wall motion, the ionic conductivity is strongly affected by the presence of Fe as well [21, 22, 162, 163]. In turn, nuclear magnetic resonance (NMR) measurements have been performed on Al-doped NBT and showed that defect associates are existent but solely at low dopant concentrations. *If you are interested in why the behavior of Al-doped NBT differs from Mg- and Fe-doped NBT, stay tuned and follow our progress!* We will extensively compare the acceptor dopants mentioned above from a theoretical point of view in the results section, where we provide detailed information on the interplay

between elastic and Coulomb interactions.

However, let us first discuss experimentally derived Arrhenius plots (impedance measurements) of Mg-, Fe-, and Al-doped NBT, obtained by Dr. Sebastian Steiner of the nonmetallic-inorganic materials division at Technical University Darmstadt and used with his permission [159]. Particularly, we will focus on the striking dependency of the conductivity on the dopant concentration.

Figure 17 shows the Arrhenius plots for the bulk conductivity in doped NBT and NBT-6BT. For all dopants, we observe a dopant concentration-dependent change in the conduction mechanism. The lower doped samples (0.1 mol% to 0.2 mol% in Mg-doped, 0.1 mol% in Al-doped, and 0.1 mol% to 0.3 mol% in Fe-doped samples) show a semiconducting behavior with an activation energy close to half of the band gap ($E_a \approx 1.44$ eV) above 320 °C. If we increase the doping concentration, the conductivity rises abruptly by at least three orders of magnitude, while the activation energy decreases simultaneously.

Especially at higher defect concentrations, where oxygen vacancies become the main charge carrier, an almost piecewise linear dependency on the inverse temperature can be observed. This indicates that the conductivity is temperature-dependent and can be divided into two regions with different activation barriers. Typically, the activation energy is higher at lower temperatures and decreases after a critical temperature T^* has been reached. In STO, this kink has been attributed solely to the dissociation of the dopant-vacancy associate [140]. In NBT, however, we observe this characteristic kink between 280 °C and 320 °C, independent of the dopant type. In the same temperature region, a phase transition from a rhombohedral to a tetragonal symmetry and the maximum permittivity has been observed [153, 160]. Even more suspicious, no kink is present in KBT, which has an untilted structure with a $P4mm$ symmetry [164, 165]. Thus, although the reason for this noticeable change is still unclear and is one of the major questions we deal with in Chapter 4, these observations already suggest that there must be a correlation between the electric properties and the unique structure of NBT. In short, in NBT, three different scenarios for the kink are conceivable,

- i) The dissociation of the defect associate as in the case of STO,
- ii) the phase transition from a rhombohedral to a tetragonal symmetry with an accompanying phase coexistence,
- iii) and the possibility of other defect chemical reactions, for instance, the trapping of electrons at the oxygen vacancy. We addressed this briefly in Equation 33 above.

At high concentrations (above 2 mol%), we observe a saturation of the ionic conductivity for Mg- and Fe-doped NBT and a slight decrease in the case of Al.

Figure 18 provides a better comparison between the concentration-dependent conductivity in differently doped NBT. Here, we present the conductivity as a function of the dopant concentration at 500 °C.

We classified the data according to their conductivity type. Remember that type I specifies an ionic, type II a mixed ionic-electronic, and type III a predominantly electronic conductor, as explained in detail in Chapter 2.

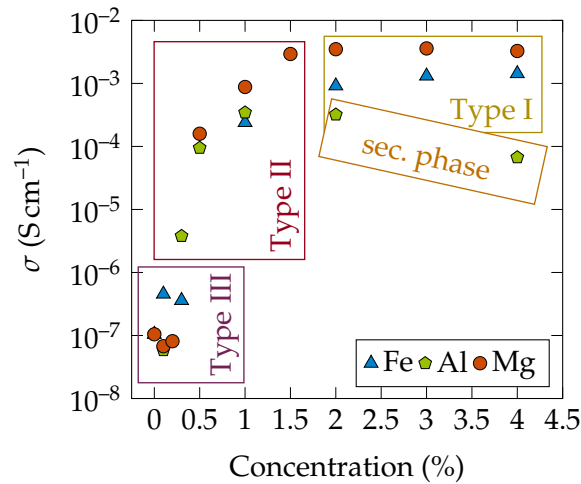


Figure 18: Concentration dependent bulk conductivity at 500 °C for Mg-, Al-, and Fe-doped NBT. We included a gross classification of the conductivities into the three conductor types introduced in Chapter 2 (type I are ionic, type II mixed ionic-electronic, and type III predominantly electronic conductors).

From Figure 18, we clearly see the difference between the different dopant types. For instance, Fe shows an increase of the bulk conductivity, while for Al- and Mg-doped samples, an initial decrease is observable at low concentrations. Above 0.5 mol% dopant concentration, the conductivity increases non-linearly with the number of dopants in all three systems, until a decrease for Al-doped NBT or a plateau for Mg- and Fe-doped samples can be recorded. According to the ideal formal charge states of the ions, the concentration of oxygen vacancies should be highest in Mg-doped NBT (if we assume that Mg is incorporated entirely into the bulk structure) and equal in Al- and Fe-doped NBT. The same remains valid for the strength of the Coulomb interaction. Only with respect to the ionic size, we obtain the following order: $\text{Al} < \text{Fe} < \text{Mg}$. The former explains the similarity between Fe and Al, while the latter seems to be responsible for the formation of secondary phases in Al-doped NBT (as revealed by BSE and EDX [159]) or for the preferential formation of higher-order associates [166] (see Chapter 7). Note that although secondary phases are present at grain boundaries for doping concentrations of about 1 mol% irrespective of the dopant type, Al-doped NBT shows the largest amount thereof.

Unfortunately, we do not have any statistics to quantify errors in Figure 18, which would be particularly interesting at a dopant concentration of 1.0 mol%. The similarity of Fe- and Mg-doped NBT and the initial increase in Fe-doped samples demonstrate, however, that Coulomb interaction and oxygen vacancy concentration might not be the only determining factors.

2.6.8 NBT-based solid solutions – “Too many cooks spoil the broth” or “the more the better”?

The formation of solid solutions ideally combines all useful properties of its end members, which offers higher levels of multifunctionality and frequently occurs in

the design of materials for industrial applications [20, 157]. Thus in the following, we will briefly touch on the most recently investigated binary NBT-bases solid solutions. For most ferroelectric or piezoelectric applications, solid solutions of NBT and related perovskite structures with a morphotropic phase boundary are preferred.

Especially prominent is the composition $0.94(\text{Na}_y\text{Bi}_x)\text{TiO}_3-0.06\text{BaTiO}_3$, where x and y either amount to the nominal stoichiometric value 0.5 or are modified by a defined A-site non-stoichiometry [157].

Regardless of the A-site non-stoichiometry, the NBT- x BT samples behave rather similarly. At high temperatures, the activation energy, which is about half of the band gap, indicates an intrinsic semiconductive behavior. Instead, at lower temperatures, the activation is reduced by approximately 0.5 eV, suggesting a change of conduction mechanism from electronic to ionic [157]. However, no evidence for oxide ion conduction could be found from the electrode polarization response, which is typically a clear sign of an ionic contribution. On this basis, an enhanced conductivity for Bi-deficient compositions has not been conclusively clarified. Nevertheless, it is assumed that defect states within the band gap contribute to a reduction of the activation energy, and a mixed electronic/ionic conduction has not been completely excluded yet.

Generally, an intentional or accidental A-site non-stoichiometry does not drastically impact the conductivity in NBT-BT solid solutions, which predominantly shows electronic leakage currents. Since the ferroelectric properties are more sensitive to modifications on the A-site, non-stoichiometry appears as a more promising tool to tailor the piezo- and ferroelectric behavior.

In contrast, the conductivity in acceptor doped NBT-BT originates from the migration of oxygen vacancies. To shed some light on the recent advancements in the field of doped NBT-based solid solutions, we will briefly summarize the results from Steiner *et al.* [21]. Although EPR measurements verify the presence of $(\text{Fe}_{\text{Ti}}'-\text{V}_{\text{O}}\ddot{\text{O}})'$ defect associates and therefore reveal the importance of oxygen vacancies in the defect chemistry of doped NBT and NBT-based solid solutions, the effective ionic conductivity at the same total defect concentrations differ. While 1 mol% Fe-doped NBT already provides ionic conductivities comparable to Mg-doped equivalents, 1 mol% Fe-doped NBT-6BT shows conductivities that are only slightly higher than undoped, stoichiometric NBT-6BT but still remains semi-conducting. Only at 2 mol% the conductivity increases by several orders of magnitude to almost reach the saturation level (see Figure 17d). The authors attribute this difference to the locally modified A-site bonding environment around Ba-substituted lattice sites. The conductivity hardly changes for concentrations equal or higher than 2.0 mol%, showing that the physical response of $0.94(\text{Na}_y\text{Bi}_x)\text{TiO}_3-0.06\text{BaTiO}_3$ (NBT-6BT) is uniform and stable over certain concentration ranges. This makes doped NBT-6BT particularly interesting for practical applications.

2.6.9 Stoichiometric doping – *The wolf in sheep's clothing*

Another way of doping is the “stoichiometric” doping. Stoichiometric doping does not introduce additional oxygen vacancies such that the conductivity is solely deter-

mined by the processing-related Bi-loss and the formation of defect associates. Thus, this kind of doping provides the opportunity to isolate the effect of trapping from the generation of additional charge compensating oxygen vacancies as expected in the case of aliovalent doping with different atom types.

Very recently Yang *et al.* [20] presented a study about the electric conductivity in $(\text{Na}_{0.5}\text{Bi}_{0.5}\text{TiO}_3)_{1-x}(\text{BiAlO}_3)_x$ with $(0 \leq x \leq 0.08)$, where $x = 0.08$ represents the solid solution limit (small Al-rich secondary phases already occur at $x=0.07$). From Raman spectroscopy measurements, the authors suggest that the Al^{3+} occupies the B-site. Interestingly, in the series from $x=0$ to $x=0.08$ the electric conductivity can be tuned from ionic (type I) at low BiAlO_3 concentrations, to predominantly mixed ionic-electronic at concentrations between 2 mol% to 6 mol%, and finally to a n-type semi-conductor at a BiAlO_3 content larger than 7 mol%. The authors assume that a strong association between Al_{Ti}' and $\text{V}_{\text{O}}^{\bullet}$ primarily causes the decrease in conductivity, which surpasses the binding energy between other dopants as Mg. They further emphasize that a higher amount of Bi^{3+} on the A-site is not beneficial if high oxide ion conductivities are desired. These observations are somewhat counterintuitive since weak Bi-O bonds, and Bi's high polarizability seem to promote high oxygen ion mobilities. Therefore, we conclude that the nature of the chemical bonds is also only one part of the puzzle, and the question remains: *How do substituents on the A-site change the bonding energy of the associate?*

2.6.10 Aluminium – the individualists among the acceptor dopants?

The results of the following chapter were obtained in close collaboration with Dr. Pedro Groszewicz from the Institute of Physical Chemistry (NMR spectroscopy) and Dr. Sebastian Steiner (impedance spectroscopy) of the nonmetallic-inorganic materials division of the Technical University in Darmstadt and are used with their permission. They have been first published in Reference [166].

Similar to aliovalent doping, the formation of solid-solutions with BiMeO_3 end-members (Me is a trivalent cation) is a promising alternative for optimizing material properties [167]. Especially noteworthy is the introduction of Al^{3+} into NBT by the formation of a solid solution with BiAlO_3 ($\text{Na}_{0.5}\text{Bi}_{0.5}\text{TiO}_3$ - BiAlO_3 , NBT-BA), leading to an improvement of the dielectric loss (i.e. increase in resistivity) [168] and a significant increase in the piezoelectric coefficient (d_{33}) [169]. Impedance spectroscopy measurements on NBT- x BA solid solutions ($x \leq 8\%$) demonstrated that NBT-BA could be classified as a Type I conductor at small x , as a Type II conductor at intermediate x , and behaves as a Type III conductor at the highest BA-concentrations. In particular, these end members are applicable as high-temperature dielectrics. Yang *et al.* [20] attributed this variability in the electric properties to a reduction of the effective oxygen vacancy concentration by association as already mentioned above (see also Equation 32). In contrast to pure NBT, Al^{3+} does not induce additional oxygen vacancies in a solid solution with BA, but solely acts as a trap for naturally occurring vacancies. This leads to a decrease rather than an increase of the ionic conductivity at a higher total Al^{3+} concentration. However, this conclusion is based on the hypothesis that no difference exists between the defect chemistry in Mg, Fe, or other acceptor doped NBT structures. However, no Al-dopant associate with oxygen vacancies has

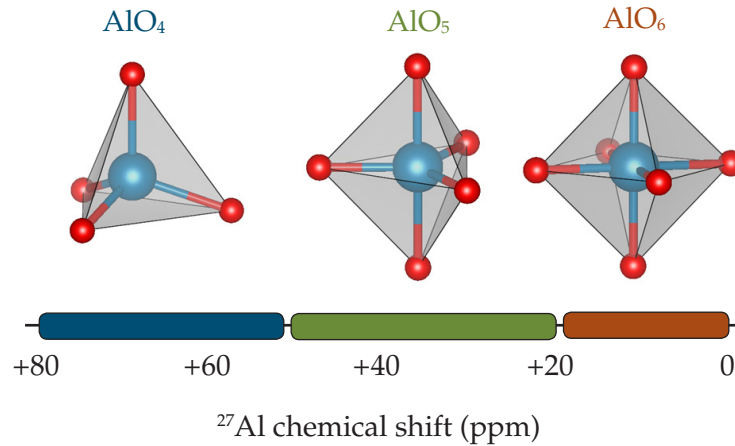


Figure 19: Empirical relation between the ^{27}Al chemical shift and the coordination number of Al^{3+} oxides.

been directly observed, mainly due to the inherent difficulty of local structure characterizations at low defect concentrations.

In the case of Fe^{3+} -doping, electron paramagnetic resonance spectroscopy (EPR) has been proven useful to characterize the local environment of the dopant atoms [170, 171] and to describe the defect structure in pure perovskites such as SrTiO_3 [172], BaTiO_3 [173], PbTiO_3 [174–176], as well as in related solid solutions, such as the economically important PZT [177]. Even in NBT and NBT-6BT the existence of $(\text{Fe}'_{\text{Ti}}-\text{V}_{\text{O}})'$ associates (Fe^{3+} occupies the B-site) as well as the formation of secondary impurity phases at concentrations exceeding 2% have been clearly demonstrated with this technique [21]. However, in the case of diamagnetic cations, for instance Al^{3+} , nuclear magnetic resonance spectroscopy is a valuable method to detect local structural variations even at low concentrations [178–181].

A suitable descriptor for the number, the nature, and the distance of the species surrounding the Al^{3+} cation is the isotropic chemical shift (δ_{iso}) [182]. ^{27}Al NMR has been applied repeatedly in recent literature [183–187] and various polymorphs of Al_2O_3 have been well described using this method [188–191]. Likewise, a few reports about aluminum in perovskites are available, where aluminum represents either the main component (LaAlO_3 [192], YAlO_3 [193]) or an end member in the case of solid solutions (e.g. MgSiO_3 modified with Al^{3+} [194–196] and LaAlO_3 in solid-solutions with alkaline earth metals) [197].

In total, three ranges of chemical shift have been established empirically for aluminum in oxides. Generally, δ_{iso} tends to increase, if the number of nearest neighbor O^{2-} decreases. A rough classification of the most common oxygen polyhedra in Al^{3+} oxides as a function of the chemical shift is depicted in Figure 19. A signal between 0 ppm and 20 ppm refers to an AlO_6 coordination shell, chemical shifts in the range of 20 ppm and 40 ppm suggest an AlO_5 environment, and δ_{iso} values lying between 50 ppm and 80 ppm have been assigned to an AlO_4 arrangement [182, 198, 199].

Although NMR spectroscopy has been proven to be a powerful tool for probing local structural motifs in perovskites [200–202], a distinct mapping of spectral features onto structural characteristics appears to be anything but straightforward. At this point, *ab initio* calculations might contribute the missing piece of information and become exceptionally important for the analysis of complex and new compounds with increasing topological or chemical disorder [203]. Particularly useful in this context is the possibility to explore different, well-defined atomic environments, which is not possible in experiments.

Thus, we aim to elucidate differences in the macroscopic functional properties based on an in-depth investigation of the local chemical environment in two model systems, namely Al acceptor doped NBT and NKBT- x BA (with $0.25\% \leq x \leq 7\%$) solid solutions. However, we will first provide the experimental findings while analyzing the results in greater depth in Chapter 7. For a more detailed description of the experimental methods, the reader is referred to the original publication in Ref. [166].

2.6.10.1 Resistance and the determination of structural motives

Figure 20 depicts the Nyquist plot for 0.1 %, 0.5 %, 1.0 % Al-doped NBT samples as well as pure NBT at 500 °C, where the imaginary part of the impedance (Z'') is plotted against the real part (Z'), and where every semicircle represents a separate electrical process. Similar to Mg- and Fe-doped samples with the same doping concentration [1, 21, 158], Al-doped NBT shows only one semi-circle in pure NBT as well as for a 0.1 % doping concentration (see Figure 20a). This suggests that only one electrical process determines the bulk resistivity in these samples, which has been attributed to the intrinsic electronic contribution.

The results for 0.5 % and 1.0 % doping concentration is illustrated in Figure 20b). We emphasize the significant reduction of resistivity. The appearance of a second semicircle indicates the presence of oxygen vacancies and thus the onset of a predominant ionic conductivity. If we compare the 0.1 % and the 1.0 % Al-doped NBT sample at 500 °C, we realize that the bulk resistance changes by four orders of magnitude. Again, this is an enormous but distinct feature of NBT and NBT-based solid solutions, which has already been observed for other dopant types [1, 19, 21, 158]. Based on these results, it seems reasonable to suppose similar internal defect equilibria in Al acceptor doped NBT and Fe- or Mg-doped samples. This includes the temperature and concentration dependent association and dissociation of Al^{3+} ions with oxygen vacancies for concentrations equal or larger than 0.5 %. Thus, in the following we will investigate the local structure around the Al-dopant by NMR spectroscopy.

The ^{27}Al MAS NMR spectra of acceptor-doped NBT- x Al ($x=0.1\%$, 0.5% , 4.0%) and NKBT- x BA ($x=0.25\%$, 6.0% , 7%) perovskite solid-solutions is shown in Figure 21. Especially noticeable is the broad asymmetric signal centered around 8 ppm, which occurs for all measured Al concentrations. According to Figure 19, this peak can be interpreted as an AlO_6 coordination environment, confirming that Al^{3+} preferably occupies the B-site. Since the ^{27}Al NMR signal of Al_2O_3 appears at 16 ppm [188], unreacted aluminum oxide as the origin of this broad peak can be discarded.

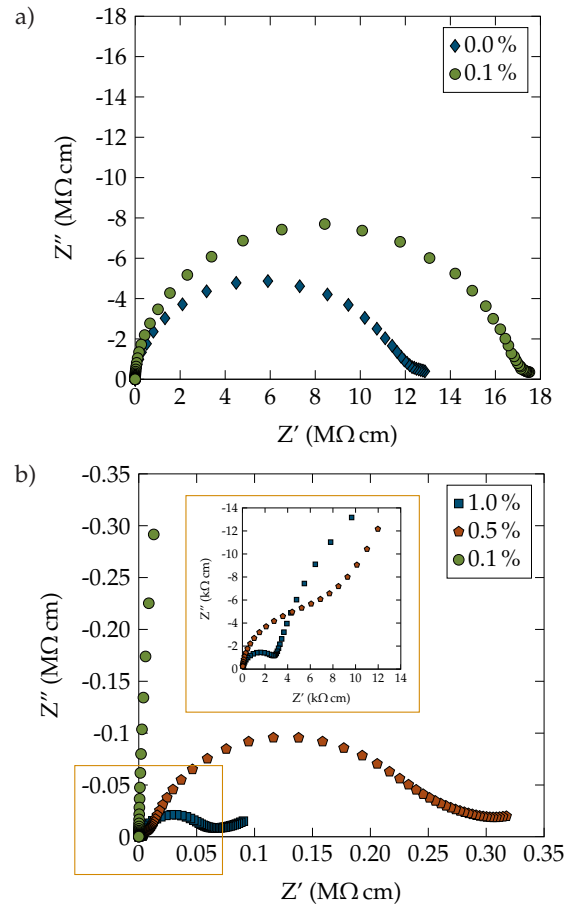


Figure 20: Concentration dependent impedance spectra of Al-doped NBT, recorded at a temperature of 500 °C.

Likewise, a resonance between 60 ppm and 70 ppm appears in all investigated spectra. However, in this case, we observe a strong dependence of the peak intensity on the Al-content in the samples. This peak could represent an AO_4 structural unit if we again compare the observed peak position with Figure 19. Such a coordination deviates significantly from the cation environments commonly found in the perovskite structure. Hence, the resonance at around 70 ppm may be assigned to a secondary phase formed during the solid-state reaction between the precursor oxides or the desired defect associate.

A third resonance has been recorded in NBT-0.1Al and NKBT-0.25BA at chemical shifts of around 30 ppm and 40 ppm. Although this peak is very pronounced in these samples, the relative intensity significantly decreases with increasing Al concentration (e.g., NKBT-6BA or NKBT-7BA). Interestingly, we observe a transition from electronic to ionic conductivity in Al-doped samples at doping concentrations between 0.2 mol% and 0.5 mol% in Figure 17. This corresponds to the threshold of 0.5 mol%, where the NMR peak at 40 ppm in Figure 21 disappeared.

A fourth and last distinct resonance is present at -10 ppm, however, solely in the spectrum of NKBT-7BA. Negative chemical shift values are seldomly observed in ^{27}Al NMR spectra of oxides and correspond to a stronger shielding of the ^{27}Al nuclei, i.e. to longer $\langle\text{Al-O}\rangle$ average distances [204, 205]. In fact, a single report of such a signal has been given by Stebbins *et al.* [196] in a study of Al-substitution in MgSiO_3 . They

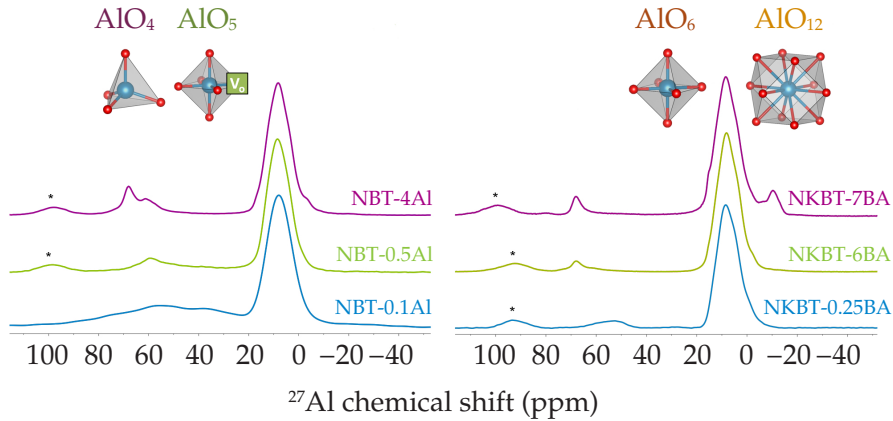


Figure 21: ^{27}Al MAS NMR spectra of Al acceptor doped NBT- $x\text{Al}$ and NKBT- $x\text{BA}$ solid solutions. A spinning frequency of 14 kHz and 13 kHz has been used.

assigned this signal to an AlO_{12} oxygen polygon of a common perovskite structure. This suggests that with increasing Al concentration, the A-site becomes successively occupied.

The two-dimensional 3QMAS NMR spectrum of NKBT-7BA in Figure 22 allows to resolve overlapping signals by differences in the quadrupolar coupling constant (C_Q) [199] and is useful to decompose the asymmetric peak at 8 ppm into individual contributions. In total five different resonances can be observed in Figure 22, out of which three signals are distributed along the isotropic line with δ_{iso} values of 10 ppm, -5 ppm, and -9 ppm. We assign the resonance at $\delta_{\text{iso}}=10$ ppm to the B-site centered oxygen octahedra due to its high intensity and broad shape along the isotropic line (FWHM of 10 ppm). The latter indicates a wide distribution of chemical shift values, reflecting structural disorder, which is probably caused by the large variety of local A-site cation arrangements. Thus NMR also provides indirect proof of local topological disorder. Generally, a small deviation from the isotropic line and a quadrupolar induced shift (δ_{qis}) of approximately 1 ppm is characteristic for small quadrupolar coupling constants (C_Q) in the range of 2 MHz, indicating only marginal distortions from an ideal oxygen octahedron [206]. Interestingly, the AlO_6 resonance is quite similar to the signals found in the 3QMAS of NKBT-6BA and NBT-4Al (not shown here), demonstrating the chemical equivalence of differently B-site substituted NBT samples.

The remaining two signals (δ_{iso} equals to -5 ppm and -9 ppm) are solely present in NKBT-7BA and signalize the occupation of the A-site by Al^{3+} ions. These values suggest a more shielded local environment for aluminum, which translates into a lower mean Al-O bond order [204]. The FWHM amounts to 5 ppm only, showing that the A-site disorder has less influence on the direct vicinity of Al^{3+} on the A-site.

The most striking feature in Figure 22 is the presence of a second signal in the AlO_6 region at a chemical shift of δ_{iso} 19 ppm, overlapping with the signal at $\delta_{\text{iso}}=10$ ppm). However, a greater distance to the isotropic line implies a larger C_Q for this additional octahedral environment. A value of 4.6 MHz has been estimated, which deviates sig-

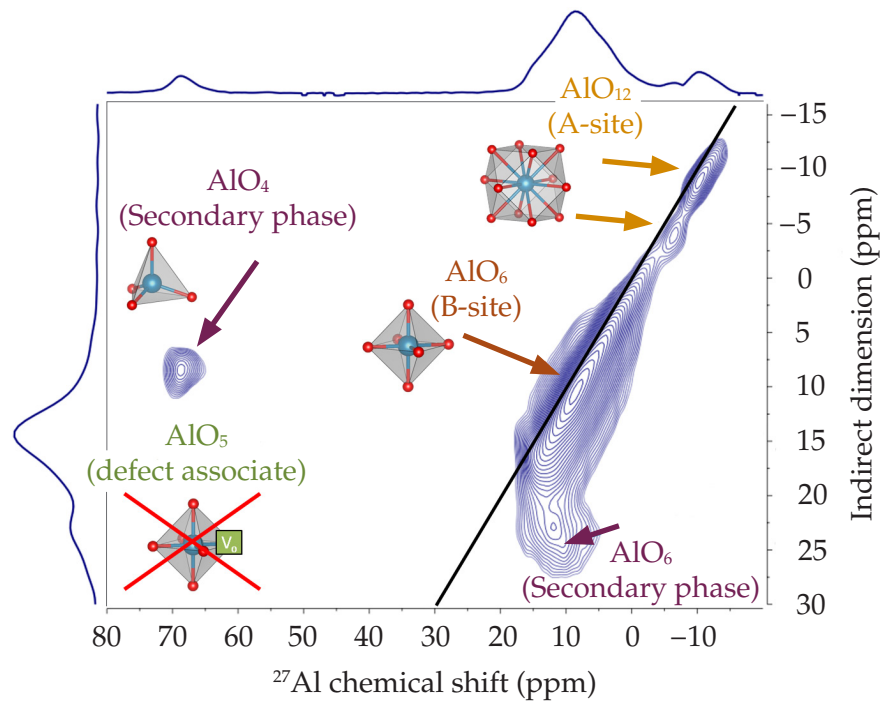


Figure 22: ^{27}Al 3QMAS NMR spectrum of a NKBT-7BA solid-solution at a spinning frequency of 14 kHz. The signals have been assigned according to the chemical shift values, which have been obtained by DFT calculations.

nificantly from the ones observed for Al_2O_3 [188] or for aluminum on the regular B-site and further indicates huge distortions of the local structure. Thus, the 3QMAS NMR spectrum of NKBR-7BA provides further evidence that no or only a negligible amount of unreacted Al_2O_3 is maintained within the samples.

In principle, this resonance could also be related to a defect associate located on the B-site. Without a doubt, the defect associate will distort the local structure, leading to higher C_Q values. However, we emphasize the unexpected slight tilt derivation upon acceptor doping, which we will discuss in more detail in Chapter 6.

2.6.11 Things to remember

Although stoichiometric NBT shows only a low electric conductivity, non-stoichiometry and extrinsic defects, such as A- and B-site acceptor dopants massively improve the ionic conductivity. Li *et al.* [1] reported that the electrical current in NBT is primarily carried by oxygen vacancies and showed that NBT reaches levels of the highest oxide ion conductors such as yttria-stabilized zirconia. Processing related bismuth loss as well as doping profoundly contribute to the total oxygen vacancy concentration such that even small amounts of defects are sufficient to severely affect the ionic conductivity in this compound [56].

Besides the possibility to tune electric responses with A-site non-stoichiometry or doping, low levels of degradation and a satisfactory stability in reducing atmospheres renders NBT a promising candidate for intermediate temperature SOFCs and makes

it superior to $\delta\text{Bi}_2\text{O}_3$. While in $\delta\text{Bi}_2\text{O}_3$ the high oxygen vacancy concentration ($\approx 25\%$) leads to ordering effects on the oxygen sublattice, Bi-deficient and doped NBT possess rather low vacancy levels (≈ 0.5 percent in $\text{NB}_{0.49}\text{T}$), significantly improving the stability of the bulk conductivity at temperatures between $400\text{ }^\circ\text{C}$ and $600\text{ }^\circ\text{C}$ [153]. However, the conductivity depends non-linearly on the dopant concentration, an effect that has not been understood so far and which will be extensively discussed in the present thesis.

2.7 OPEN QUESTIONS AND ROADMAP

In the following, we will recapitulate the questions raised in this chapter, which will serve as a roadmap for the present study and summarize our research aims and motivation:

- Do acceptor dopants and oxygen vacancies form thermodynamically stable defect associates, how large is the association enthalpy, and what characterizes a defect associate? (Chapters 4, 7, 6, and 8)
- What influence does the lattice symmetry (including A-site order) have on the electric properties and the formation of defect associates? (Chapters 6 and 8)
- Which lattice sites will be occupied by the acceptor dopant? (Chapters 7 and 6)
- How do substituents on the A-site change the bonding energy of the associate? (Chapters 6, 10, and 8)
- What effects do different acceptor dopants have on the local structure? (Chapters 6, 9, 10, and 8)
- How large are the barriers for the migration of oxygen vacancies? (Chapter 6)
- Does any phase coexistence significantly alter the conductivity in NBT? (Chapter 4)
- Which role does the dopant concentration play? (Chapters 4, 7, 10, and 6,)
- Are there any electronic defect states in the band gap? (Chapter 8)
- If we do have defect levels inside the band gap, are they electrically active? (Chapter 8)
- What is the preferred charge state of the dopant? (Chapter 8)
- What influence do cation vacancies have on the chemical environment of oxygen vacancies? (Chapter 6)
- What impact does the delicate balance of short- and long-range interaction have on the defect chemistry? (Chapters 6, 10, and 8)
- Can we quantify the mechanical interaction between defects? If so, are they superior to electrostatic interactions? (Chapter 9)

- What are the limitations for a DFT-based defect analysis in NBT? (Chapters 7, 6, 9, and 8)

This list shows that there are still a lot of open question in the field of perovskite solid ion conductors, especially concerning the “multidimensional nature” [35] of the oxygen vacancy migration. However, we are convinced that we shed some light into the “gray” of NBT’s conduction mechanisms, that we are one step closer toward a less harmful but yet high-performant alternative or extension to PZT, and that we are right by talking about the “glory of perovskites” [9], even if we do not yet completely understand their behavior or their structure. For this purpose, we will use electron structure calculations, which consider local relaxation and charge transfer processes. A detailed explanation of the applied methods can be found in the following chapter.

Materials modeling is fundamentally about understanding the structure and dynamics of many-body systems [207]. Recent technological advancements, including increasing computing capacities, not only facilitate the investigation of simple structures but rather complex, poly-atomic systems using first-principles calculations. The system's quantum mechanical ground state can be approximated by density functional theory (DFT), where the electronic energy is a functional of the electronic density for a specific set of nuclear positions [207]. We owe this elegant, parameter-free (first-principles) reformulation of the Schrödinger equation, which, in turn, constitutes a complex many-body problem, the Hohenberg and Kohn theorem [208].

DFT is not limited to the determination of the ground state. Continuous development of available first-principles codes allows for the calculation of several material properties with high accuracy, reliability, and efficient algorithms. The determination of phonon spectra, elastic constants, or even the polarization of the system are just a few examples, which helped these computational methods to achieve worldwide success.

This chapter, we will summarize the main achievements of this theory, forming the basis for the present thesis. Particularly, we are interested in the point defect thermodynamics of NBT, which includes the determination of electron structures for differently doped supercells, the investigation of local relaxation processes, the study of charge transition states of defect associates as well as their impact on the mobility of oxygen vacancies, and most importantly the calculation of the association energy between point defects. These calculations are based on the density functional theory approach's well-known concepts and can be skipped if the reader is familiar with this technique. Furthermore, we will shortly describe the methods used to analyze chemical bonding environments, relaxation volumes, and other functional properties from plane wave based density functional theory. To provide as complete a picture as possible, we will present a comprehensive overview of the current technical developments and their computational challenges. Especially Sections 3.10, 3.10.4, 3.13, and 3.12, which describe pressure corrections in charged supercells, absolute deformation potential calculations, the determination of the crystal orbital hamiltonian population, and the identification of chemical shift values, respectively, are non-standard concepts and should be thoroughly studied. We summarize the used simulation packages and essential parameters directly at the beginning of this chapter for a brief overview.

3.1 GENERAL METHODS

For all total energy calculations, if not otherwise stated, we use the Vienna Ab initio Simulation Package (VASP) [209, 210]. We applied the projector augmented waves method, using the generalized-gradient approximation (GGA) in the Perdew-Burke-Ernzerhof parameterization [211]. For the valence electron configuration we chose O: $2s^2 2p^4$, Na: $2p^6 3s^1$, Ti: $3s^2 3p^6 4s^2 3d^2$, Bi: $5d^{10} 6s^2 6p^3$, and Al: $3s^2 3p^1$, Fe: $3p^6 4s^2$

$3d^6$, Mg: $2p^6 3s^2$, and Ba: $5s^2 5p^6 6s^2$. In the case of iron, the only stable solution carries a spin along the z -direction with a local magnetic moment of approximately $4.2\mu_B$, which is close to the ideal ionic high spin representation ($5\mu_B$) [212]. That is, if we assume for simplicity a cubic O_h crystal field splitting, all t_{2g} and e_g orbitals are equally occupied by one electron of the majority spin channel. An alternative spin configuration would result in $1\mu_B$ (open shell configuration for t_{2g} orbitals), which was only stable for some dopant-vacancy arrangements and consistently higher in energy. We additionally applied an U-correction of 4 eV [213–215] (Dudarev approach [216]) on the d -orbitals of the iron dopant. In case we used a hybrid exchange-correlation potential, we applied an exact exchange fraction of 0.08 and a screening parameter of 0.2 instead of the standard HSE06 setting. The k -point mesh and the cut-off energy depend on the calculation and are given separately for every chapter.

Instead, most results in Chapter 5 have been obtained with the open source code ABINIT [217–220]. In this case, we used norm-conserving PBEsol pseudopotentials from the website PseudoDojo [221]. Except for Na, where we additionally integrate the $2p$ states, we use the same valence electron configuration as given above. For the determination of symmetry-adapted modes and the crystal symmetry in general, we used the Bilbao Crystallographic Server [222–224] (especially the tool AMPLIMODES [225, 226]) and ISODISTORT [227, 228] as well as FINDSYM [229, 230] from the ISOTROPY software suit [231]. Details on the relaxed bulk structures used in this thesis can be found in the Appendix. All structures have been visualized with the open source software VESTA [232, 233], while the determination of octahedral tilt deformations has been performed with the help of OVITO [234]. Finally, pymatgen [235] and abipy [236] have been extensively used to post-process our data.

3.2 THE BORN-OPPENHEIMER AND HARTREE-FOCK APPROXIMATION

The following sections describe the fundamentals of density functional theory in general and are intended for readers who are unfamiliar with the mathematical formulation. If not stated otherwise, we will mainly refer to References [126, 207]. The experienced reader might skip to the Section 3.4.4, where we evaluate three different exchange-correlation functionals for undoped and stoichiometric NBT.

The ground-state energy of a coupled electron-nucleus system is defined by the time independent Schrödinger equation of the following form,

$$H(\mathbf{R}, \mathbf{r})\Psi(\mathbf{R}, \mathbf{r}) = E\Psi(\mathbf{R}, \mathbf{r}), \quad (44)$$

where E is the total energy, \mathbf{R} as well as \mathbf{r} are the set of nuclear and electronic coordinates respectively, and Ψ is the many-body wave function of the system. In this case, the Hamilton operator $H(\mathbf{R}, \mathbf{r})$ consists of an electronic and a nucleus part, which themselves are a sum of the kinetic energy operator ($T_n(\mathbf{R})$ and $T_e(\mathbf{r})$) for the nuclei

and the electron respectively) and the potential energy operator ($V_{\text{nn}}(\mathbf{R})$ and $V_{\text{ee}}(\mathbf{r})$). Explicitly, the individual components of the Hamiltonian can be formulated as

$$T_{\text{n}} = \sum_{\alpha=1}^K \frac{(-i\hbar\nabla_{\mathbf{R}_{\alpha}})^2}{2M_{\alpha}}, \quad (45)$$

$$V_{\text{nn}} = \sum_{\alpha,\beta=1;\alpha<\beta}^K \frac{Z_{\alpha}Z_{\beta}e^2}{|\mathbf{R}_{\alpha} - \mathbf{R}_{\beta}|}, \quad (46)$$

$$T_{\text{e}} = \sum_{i=1}^N \frac{(-i\hbar\nabla_{\mathbf{r}_i})^2}{2m}, \quad (47)$$

$$V_{\text{ee}} = \sum_{i,j=1;i<j}^N \frac{e^2}{|\mathbf{r}_i - \mathbf{r}_j|}, \quad (48)$$

$$V_{\text{ne}} = \sum_{\alpha=1}^K \sum_{i=1}^N \frac{Z_{\alpha}e^2}{|\mathbf{R}_{\alpha} - \mathbf{r}_i|}, \quad (49)$$

where $\nabla_{\mathbf{R}_{\alpha}}$ is the Nabla operator, \mathbf{R}_{α} , M_{α} and Z_{α} represent the position, the mass, and the charge of the nucleus α . Equivalently, \mathbf{r}_i denotes the coordinate vector and m the mass of the i th electron. The last terms take into account the interaction between nuclei and electrons.

The amount of random variables already indicates the complexity of the problem. Especially with increasing system sizes, Equation 44 becomes practically unsolvable. A factorization of the total wave function into an electronic and a nuclei term leads to a considerable simplification, such that the equations can be solved for a fixed set of nuclear positions. If we further assume that the electronic system adiabatically adapts to the current ionic configuration, we have all the necessary ingredients for the so-called Born-Oppenheimer approximation. The Hamiltonian can be reduced to

$$H(\mathbf{R}, \mathbf{r}) = T_{\text{e}}(\mathbf{r}) + V_{\text{ee}}(\mathbf{r}) + V_{\text{ne}}(\mathbf{r}, \mathbf{R}) + V_{\text{nn}}(\mathbf{R}), \quad (50)$$

such that the expectation value of $H(\mathbf{R}, \mathbf{r})$, which is a functional of the many-body wavefunction, can be described as

$$E(\mathbf{R}) = E_{\text{el}}(\mathbf{R}) + E_{\text{nn}}(\mathbf{R}), \quad (51)$$

where $E_{\text{nn}}(\mathbf{R})$ is the potential energy of the nuclei, which is fully determined for a given set of coordinates $\{\mathbf{R}\}$, and $E_{\text{el}}(\mathbf{R})$ is the energy of the electrons in the potential of the ions. $E(\mathbf{R})$, the solution of the stationary eigenvalue problem, is then often called the Born-Oppenheimer energy. Hence, the electronic energy remains the crucial and unknown parameter in Equation 51. If we take a closer look, the mathematical problem at hand is equivalent to minimizing electronic energies by means of the variational principle, under the constraint that the resulting solution belongs to a subset of antisymmetric (Pauli-correlation) and normalizable wavefunctions. The minimal eigenvalue is called the ground-state electronic energy.

Although the problem seems to be mathematically well described, the determination of the ground state energy constitutes a computationally complex task. Especially if we consider, for instance, polymorphous systems or compounds with a high

amount of meta-stable configurations. These materials include not only an increasing number of electrons but also various configurations forming the potential energy surface. Since speed and affordability are necessary for applying computer-aided explorations of material properties, further simplifications significantly contributed to approximate solutions while simultaneously maintaining high accuracy.

A first outstanding example is the Hartree-Fock (Self-Consistent-Field) approximation, where the fictitious electrons are assumed to be independent of each other (meaning that they do not interact). Consequently, the many-body-wave function, which takes the form of Slater determinants, can be constructed from orthogonal single-particle states. Hence, the independence of the electrons leads to a set of coupled ordinary single-particle Schrödinger equations, which can be, as already stated, solved variationally. It should be noted that E_{ee} , the energy contribution resulting from the interaction between the electrons, consists of two components: the Hartree energy (direct Coulomb), which describes the interaction of electrons without taking into account that the probability of finding an electron at position \mathbf{r}_1 depends on the presence of an electron at \mathbf{r}_2 . These conditional probabilities are included in the second negative energy term, which will be further denoted as exchange-correlation energy. Although the exchange part in the Hartree-Fock approximation occurs naturally by the determinantal structure of the single-particle states, the correlation between electrons is not included in this more simplistic picture. The introduction of correlation effects requires the definition of correlated wave functions, which assumes not only N occupied single-particle states of the N particle system but also the introduction of unoccupied states to form a complete basis of the single-particle Hilbert space. The neglect of correlation effects might be detrimental for certain materials, such that density functional theory (DFT) appeared as a natural consequence of the deficiencies within the Hartree-Fock approximation. However, the reduction of the many-body to a non-interacting single-particle problem (the true benefit) is a common property of both theories.

3.3 THE DENSITY FUNCTIONAL THEORY

The basic idea of density functional theory is to reduce spacial variables by mapping the interacting N -particle system effectively onto a problem of non-interacting electrons, with the electron density being the crucial parameter. We start by introducing the Hohenberg-Kohn theorem, a fundamental existence theorem for the application of DFT.

3.3.1 *The Hohenberg-Kohn theorem*

Assume a Hamiltonian consisting of the kinetic energy operator T_e , the electron-electron interaction V_{ee} , and a time independent, external potential $v_{\text{ext}}(\mathbf{r})$ operator,

$$H_{el,v}(\mathbf{r}) = T_e(\mathbf{r}) + V_{ee}(\mathbf{r}) + v_{\text{ext}}(\mathbf{r}), \quad (52)$$

where $v_{\text{ext}}(\mathbf{r})$ is a local function of arbitrary form and the nuclei degrees of freedom are neglected in this context. Essentially, the Hohenberg-Kohn theorem states that

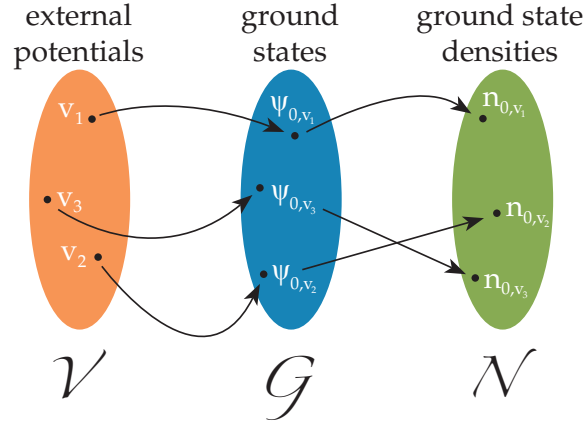


Figure 23: Correspondence between the external potential, the ground state, and the ground state density in DFT approaches. \mathcal{V} , \mathcal{G} , and \mathcal{N} are sets of external potentials, ground states, and ground state densities, respectively. Note that the mapping is bijective. Adapted from Reference [207].

there exists a bijective map \mathcal{A} between the set of external potentials \mathcal{V} and the set of ground states \mathcal{G} (see Figure 23),

$$\mathcal{A} : \mathcal{V} \longrightarrow \mathcal{G}. \quad (53)$$

If we further define the associated ground state density, n_0 , as

$$n_0 = \langle \Psi_0 | \hat{n}_0(\mathbf{r}) | \Psi_0 \rangle, \quad (54)$$

where $\hat{n}_0(\mathbf{r})$ is the density operator and $|\Psi\rangle_0$ is the ground state, we obtain a second bijective map between the set of ground state wavefunctions and the set of ground state densities, \mathcal{N} :

$$\mathcal{B} : \mathcal{G} \longrightarrow \mathcal{N}. \quad (55)$$

Note that the ground states differ by more than a simple phase factor, and the external potentials vary by more than a constant. Said differently, the electronic ground state density is a unique functional of the external potential and the other way around. The same remains true for the ground state density and the corresponding ground state, $|\Psi_0[n_0]\rangle$. Although $|\Psi_0[n_0]\rangle$ has a universal functional form, the exact atomic configuration depends on the structure of the density.

A consequence of the functional dependency of the ground state on the electron density is that all related properties, and most importantly the ground state energy, $E_0 = \min_{n \in \mathcal{N}} E[n]$ with $E[n_0] < E[n'_0]$ (minimum principle), are also a functional of the density. Therefore, the total energy, which has to be minimized, can be formulated as follows:

$$E_{\text{el},v} = \langle \Psi[\mathbf{n}] | H | \Psi[\mathbf{n}] \rangle \quad (56)$$

$$= \langle \Psi[\mathbf{n}] | T_e + V_{\text{ee}} | \Psi[\mathbf{n}] \rangle + \int d^3r v_{\text{ext}}(\mathbf{r}) n(\mathbf{r}) \quad (57)$$

$$= F[n] + \int d^3r v_{\text{ext}}(\mathbf{r}) n(\mathbf{r}). \quad (58)$$

All in all, this means that every change in the external potential is followed by the adjustment of the electronic system, and thus the electron density. The above considerations assume a non-degenerate ground state. Nevertheless, it has been shown that, despite small variations in the mathematical formulation, even in the degenerate case, the ground state energy is uniquely defined by the electron density. This is at the heart of the Hohenberg-Kohn theorem.

3.3.2 Kohn-Sham equations

Until now, we learned from the Hartree-Fock approach that an interacting, N-particle problem can be solved in the framework of non-interacting, fictitious single particles, moving in an external, effective potential. We further understand that the ground state energy can be uniquely determined from the electron density. A combination of these significant discoveries is the foundation of the Kohn-Sham scheme. Precisely, the introduction of a non-interacting, auxiliary particle system leads to a Hamiltonian, where only T_e and $v_s(\mathbf{r})$ survive. The non-degenerate ground state is constructed from a Slater determinant (Equation 60),

$$\begin{aligned} (\mathbf{r}_1, \dots, \mathbf{r}_N) |\Psi_0\rangle &= |\Psi_0\rangle(\mathbf{r}_1, \dots, \mathbf{r}_N) \\ &= \frac{1}{\sqrt{N!}} \det \begin{bmatrix} \phi_1(\mathbf{r}_1) & \dots & \phi_N(\mathbf{r}_1) \\ \vdots & & \vdots \\ \phi_1(\mathbf{r}_N) & \dots & \phi_N(\mathbf{r}_N) \end{bmatrix}. \end{aligned} \quad (59)$$

$$(60)$$

Here, the entries, ϕ_i , are solutions of the single-particle Schrödinger equation (Equation 61 is a non-spinpolarized example),

$$\left[-\frac{\hbar^2 \nabla^2}{2m} + v_s(\mathbf{r})\right] \phi_i(\mathbf{r}) = \epsilon_i \phi_i(\mathbf{r}), \quad (61)$$

where the eigenvalues are $\epsilon_1 \leq \epsilon_2 \leq \dots \leq \epsilon_N = \epsilon_F \leq \epsilon_{N+1} \leq \dots$ and the electron density can be written as

$$n(\mathbf{r}) = \sum_i \Theta_i |\phi_i(\mathbf{r})|^2, \quad (62)$$

with Θ_i being defined as $\Theta(\epsilon_F - \epsilon_i)$. This occupation function, which equals to zero if $\epsilon_i > \epsilon_F$ and to unity otherwise, ensures that only the energetically lowest, occupied single-particle states are included. In particular, this electron density has to be normalized to the total number of electrons in the system (N). From the Hohenberg-Kohn theorem, we can deduce that there will be an appropriate electron density for every external potential, and thus $|\Psi[n]\rangle$, solving the equations above. Furthermore all other quantities, especially $T[n]$ (Kohn-Sham kinetic energy) and $E_{el,v}[n]$, can be obtained. Note that the single-particle states are also functionals of the electron density, $\phi_i[n](\mathbf{r})$. The brilliant core idea of the Kohn-Sham scheme is to represent the interacting many-body, with the auxiliary Kohn-Sham system, assuming that both systems possess the same ground state density n_0 . As a result, v_{ext} of the interacting system must differ from v_s of the fictitious single-particle system, since this term contains/carries the information of the many-body particle interaction. To understand the mapping between both systems (interacting and single-particle system), and thus

the structure of v_s , a comparison between the many-body equations and the Kohn-Sham approach seems to be worthwhile. However, we will skip the mathematical derivation, as the exact formulation exceeds the scope of this chapter, and directly present the results. The total energy can be described as follows,

$$E[n] = T_s[n] + \frac{1}{2} \int d^3r \int d^3r' n(\mathbf{r}) w(\mathbf{r}, \mathbf{r}') n(\mathbf{r}') \quad (63)$$

$$+ \int d^3r v_{\text{ext}}(\mathbf{r}) n(\mathbf{r}) + E_{\text{xc}}[n], \quad (64)$$

where T_s is still the kinetic energy of the Kohn-Sham system (obtained from the single-particle states), the second term represents the Hartree energy with the particle-particle interaction w , the third energy term considers the interaction with an external potential, and the last contribution stems from the exchange-correlation functional of unknown form. Generally, all terms in equation 64 are universal, such that any approximation of this functional is applicable for every system with prevailing Coulomb interaction. Likewise, this equation shows that the Hartree and the external energy contribution can be exactly determined from the electronic density. Note that the E_{xc} derived in the framework of DFT varies from the quantum chemical expression, the difference being that equation 64 contains the non-interacting kinetic energy which is not equal to the interacting counterpart. The latter can only be the infimum of the former. This difference results from the fact that the ground state of the interacting many-body and the independent Kohn-Sham system, leading to the same ground state density, can not be equal. We further understand that v_s can be expressed as

$$v_s(\mathbf{r}) = v_{\text{ext}}(\mathbf{r}) + v_{\text{H}}[n_0](\mathbf{r}) + \frac{\delta E_{\text{xc}}[n]}{\delta n(\mathbf{r})}, \quad (65)$$

where the functional derivative of the exchange-correlation energy describes the exchange-correlation potential. If we further insert the expression for v_s into the single-particle equations, we obtain the set of coupled, non-linear, but local (unlike to the Hartree-Fock approach) Kohn-Sham equations:

$$\left(-\frac{\hbar^2 \nabla^2}{2m} + v_{\text{ext}}(\mathbf{r}) + v_{\text{H}}[n](\mathbf{r}) + v_{\text{xc}}[n](\mathbf{r}) \right) \phi_i(\mathbf{r}) = \epsilon_i \phi_i(\mathbf{r}). \quad (66)$$

Due to their non-linearity, these equations have to be solved self-consistently. The main idea is to insert a trial potential v_s^t into equation 66 to receive appropriate, orthonormal eigenstates ϕ_i^t . Starting with an approximation of the electron density is equally possible since both quantities are related through the Hohenberg-Kohn theorem. Often the superposition of atomic charge densities is a valuable first estimate in solids and the preferred option in most electronic structure codes. The resulting ϕ_i orbitals can then be used to calculate a new density, serving as an improved input for the Kohn-Sham equations and the iterative cycle. The electronic ground state has been reached if the difference between two successive densities is sufficiently small.

At this point, we should emphasize again that the reader should not confuse the ground state of the interacting with the ground state of the effective system, which is constructed from the solutions of the Kohn-Sham single-particle equations. We have to realize that the true value of DFT is solely reflected in the reproducibility of

the electron density and the ground state energy. Particularly, except for the eigenvalue of the Kohn-Sham state at the valence band maximum (ionization potential), the solutions ϕ_i of the Kohn-Sham single-particle equations themselves do not have any physical meaning and should be better understood as a mathematical construct. Consequently, only observables that directly depend on the electron density can be determined in this framework.

Now the question naturally arises, if this unphysical nature has severe implications on the validity of our DFT results and even more important, if so, where is it noticeable?

3.3.3 The band gap problem

The most popular example for the failure of DFT calculations may be the proper prediction of the band gap [237–239]. We will understand the importance of this inaccuracy when dealing with electronic transition states of intrinsic and extrinsic point defects. For this purpose, let us first define the fundamental band gap of semiconductors and insulators, E_g , and compare this exact term with the approximated DFT expression,

$$E_g = [E_{N+1} - E_N] - [E_N - E_{N-1}] \quad (67)$$

$$= \epsilon_{N+1}(N + \delta) - \epsilon_N(N - \delta) \quad (68)$$

$$= \text{IP} - \text{EA}, \quad (69)$$

where E_i is the total energy of an i th particle system, and $\epsilon_i(M)$ is the i th eigenvalue of a M -particle system. This equation corresponds to the difference between the ionization potential (IP) and the electron affinity (EA). If we remember that the ionization potential (the highest occupied state) is correctly reproduced from the orbital energies, ϵ_i , by the Kohn-Sham formalism, we can deduce a band gap in the Kohn-Sham framework according to

$$\Delta_s = \epsilon_{N+1}^{\text{KS}}(N + 1) - \epsilon_N^{\text{KS}}(N). \quad (70)$$

However, if we consider the limit $\delta \rightarrow 0^+$ in equation 68, we obtain:

$$E_g = \epsilon_{N+1}(N) - \epsilon_N(N) \quad (71)$$

$$= \epsilon_{N+1}^{\text{KS}}(N) - \epsilon_N^{\text{KS}}(N) + \Delta_{\text{xc}} \quad (72)$$

$$= \Delta_s + \Delta_{\text{xc}}. \quad (73)$$

Mathematically, Δ_s results from a discontinuous derivative of the kinetic energy functional $T_s[n]$ [238]. In turn, Δ_{xc} considers the discontinuity of the exchange-correlation potential with a varying number of electrons ($\delta E_{\text{xc}}[n]/\delta n(\mathbf{r})$). The second contribution is normally neglected in standard DFT calculations, such that the band gap is often underestimated. This is particularly severe, if a semiconductor becomes a metal as a consequence of this systematic error.

As already mentioned in the introductory part of this chapter, reliability, and accuracy are crucial factors, greatly influencing the quality of a simulation. One possibility to improve the description of material properties is to develop appropriate approximations to the exchange-correlation functional of various complexity. In the next

section, we will introduce the most common approaches in practical applications, which additionally have been used for the simulations of the present work.

3.4 THE EXCHANGE CORRELATIONS FUNCTIONAL

Since the exact mathematical form of the exchange-correlation functional E_{xc} is unknown, several ideas have been developed so far to improve the prediction of physical properties. Due to their varying complexity, the practicability of these approximations have to be carefully considered for all individual quasi-particle systems under consideration. In the present work, we primarily used the Generalized Gradient Approximation (GGA). Since this approach builds on the Local Density Approximation (LDA), it is reasonable to first introduce the concept of this ansatz.

3.4.1 Local density approximation

In the local density approximation, it is assumed that the exchange-correlation energy per particle, $\epsilon_{xc}(\mathbf{r})$, can be sufficiently approximated by the equivalent of the homogeneous electron gas $\epsilon_{xc}^{\text{hom}}(\mathbf{r})$. The homogeneous electron gas describes a system of interacting electrons, moving in a spatially constant external potential, where the charge of the electrons is compensated by a neutralizing background. A valuable, but massive, simplification is that the term $\epsilon_{xc}(\mathbf{r})$, although applied to arbitrarily inhomogeneous systems, only depends on the local electron density, $n(\mathbf{r})$,

$$E_{xc}^{\text{LDA}}[n] = \int n(\mathbf{r})\epsilon_{xc}^{\text{hom}}(\mathbf{r})d\mathbf{r}. \quad (74)$$

As we suppose the system to be locally comparable to a homogeneous electron gas, LDA works particularly well for compounds showing a slowly varying spatial density $n(\mathbf{r})$. However, due to its simplicity, a vast amount of literature can be found using this approximate exchange-correlation functional, where structural and dynamic properties could be reproduced with relatively high accuracy.

Although the exchange part of $\epsilon_{xc}^{\text{hom}}(\mathbf{r})$ can be calculated from the following fixed expression,

$$\epsilon_{xc}^{\text{hom}}[n] = -\frac{3}{4\pi}(3\pi^2)^{1/3}n^{1/3}, \quad (75)$$

the correlation part can be either obtained from exact Monte-Carlo simulations (Ceperley-Alder approximation [240]) or by a polynomial parameterizations (e.g. Teter [241]) of the former.

3.4.2 Generalized gradient approximation

LDA is known for not only underestimating the band gap up to 50% [242] (or equivalently overestimation of static screening [94]) but also to over-predict cohesive energies and bond strengths [243]. This is particularly crucial in the case of ABO_3 perovskite crystals, where ferroelectric (antiferroelectric) instabilities or soft tilting modes sensitively depend on the volume [6, 94, 244]. In order to correct for these

inaccuracies, non-local corrections have been developed, which depend on both the density at position \mathbf{r} and on its gradient [126, 245]

$$E_{xc}^{GGA}[n] = \int n(\mathbf{r}) \epsilon_{xc}^{GGA}[n(\mathbf{r}), |\nabla n(\mathbf{r})|, \nabla^2 n(\mathbf{r})] d\mathbf{r}. \quad (76)$$

Note that this approximation still does not include any long-range effects in the density. That is why GGA potentials are often referred to as semi-local or quasi-local approaches. It might even happen that GGA functionals overcorrect LDA results, similarly implying a systematic bias on structural relaxation processes and thus on lattice constants and bond lengths. This overcorrection results from a decrease of the binding energy between the atoms caused by the introduction of a gradient correction term.

There are numerous advancements to the standard GGA formulation, however, without going into further detail, we will mention one at this point. The DFT + U method has been proposed by Anisimov *et al.* [246] and aims to combine the description of itinerant band states (s- and p-states) and localized states (d- and f-states) with a single exchange-correlation approximation, by applying a repulsive potential U on the localized states. Using the standard form of these potentials, localization of d- and f-electrons within atomic subspaces (n_l) is often prevented by the self-interaction error [247, 248] and a varying occupancy of originally degenerated orbitals (orbital polarization) is often difficult to achieve in defective systems [249]. However, within the DFT + U framework, the d- and f-orbitals are confined within atomic spheres at certain sites i . Practically, the intra-shell Hartree and exchange energy can be reached by the projection of the Kohn-Sham state, $\phi_{nk\sigma}$ (n is the band index, k the reciprocal space vector, and σ the spin), onto a set of atomic orbitals Φ_{inlm} (l and m are the angular and the magnetic quantum number, respectively) such that $\phi_{nk\sigma}(\mathbf{r})$ can be represented as a superposition of the localized, atomic-like states $\Phi_{inlm}(\mathbf{r})$. After applying some further mathematical transformations and additionally considering a double-counting correction, we end up with the orbital energies ϵ_α [216],

$$\epsilon_\alpha = \frac{\partial E^{\text{DFT}+U}}{\partial \Theta_\alpha} \sim \epsilon_\alpha^{\text{DFT}} + U \left(\frac{1}{2} - \Theta_\alpha \right), \quad (77)$$

where Θ_α is the occupation of state $\alpha = nk\sigma$, which equals one or zero. From equation 77 we deduce that occupied states are lowered, and empty states are increased in energy. The U parameter can be determined either by constrained LDA and linear response calculations [250–252] or by a fitting procedure. In the latter, the Hubbard U is modified until experimental band gaps or lattice constants are sufficiently accurately reproduced, energy differences between various magnetic orders are comparable to more complex approaches [253], or by using the energetic variation between supercells with an additional and reduced number of d-shell electrons [252]. As stated by Aryasetiawan *et al.* [251], the latter approach limits the quantitative predictability of the calculated properties and might result in an inaccurate description of the material.

3.4.3 Hybrid potentials

Although DFT+U can predict the Mott-Hubbard character in transition metal oxides [89], accurate predictions of the band gap demand for even more sophisticated

solutions. It is worth mentioning that by using the DFT+U method, decisive improvements are mainly obtained in open-shell systems [25] and that the band gap width is often related to the p-d splitting, still leading to incorrect predictions of band gaps [249]. These shortcomings lead us to different (global, screened, and local) variants of the so-called Hybrid functionals, which have recently been used for the description of diverse material classes, reaching from semiconductors and transition-metal oxides to ferroelectrics and surfaces [6]. Essentially, within the concept of hybrid functionals, it is suggested that a certain percentage of exact exchange to the standard GGA expression significantly improves the predictability of band gaps, structural relaxation, and the localization of d- and f-states [254].

A particular common variant is the screened hybrid functional, where the Coulomb interaction (Coulomb kernel [255]) is separated into a long-range (lr) and a short-range (sr) part,

$$\frac{1}{|\mathbf{r}|} = \underbrace{\frac{\text{erfc}(\omega_{\text{scr}}|\mathbf{r}|)}{|\mathbf{r}|}}_{\text{short-range}} + \underbrace{\frac{\text{erf}(\omega_{\text{scr}}|\mathbf{r}|)}{|\mathbf{r}|}}_{\text{long-range}}, \quad (78)$$

where $\text{erf}(x)$ is the error function, $\text{erfc}(x) = 1 - \text{erf}(x)$, and ω_{scr} is an adjustable parameter, determining the distance at which the non-local exact exchange is screened but compensated by the PBE long-range [256]. The advantage of this approach is an accelerated spacial decay of the Hartree-Fock exchange, such that a downsampling of the reciprocal space representation (usage of a subset $\{\mathbf{q}\}_{\mathbf{k}}$ of the full k-point set $\{\mathbf{k}\}$ for the evaluation of the short-range Hartree-Fock potential) is possible and computational costs can be saved compared to completely unscreened functionals [255, 257]. A famous representative of such a screened functional is given by the short-range exact (Hartree Fock) exchange functional of Heyd, Scuseria, and Ernzerhof (HSE) [256, 258–260]:

$$E_{\text{xc}}^{\text{HSE}} = \alpha E_{\text{x}}^{\text{exact,sr}}(\omega) + (1 - \alpha) E_{\text{x}}^{\text{PBE,sr}}(\omega) + E_{\text{x}}^{\text{PBE,lr}}(\omega) + E_{\text{c}}^{\text{PBE}}. \quad (79)$$

In turn, the correlation functional remains unaffected by this advanced formalism such that $E_{\text{c}}^{\text{HSE}} = E_{\text{c}}^{\text{PBE}}$. This simplification is justified by the limited impact of the self-interaction cancellation on the correlation energy in contrast to the exchange counterpart (a complete cancellation of the self-interaction in the Hartree energy term can be reached when considering the entire exact exchange). Since both parameters are not known *a priori*, α is often set to 0.25, while ω amounts to 0.207 \AA^{-1} (HSE06) [257, 259, 261]. We can easily see that for $\omega \rightarrow \infty$ we reach the limit of a standard PBE calculation. Further famous implementations of the hybrid functional are known as B3LYP [262, 263] and PBE0 ($\omega=0$) [255, 264]. However, suitable values for these semi-empirical parameters might differ amongst various physical systems (or they are even property dependent), such that a sampling of the parameter space ($0 \leq \omega \leq \infty$, and $0 \leq \alpha \leq 1$) prior to a final calculation is often inevitable [6, 265–267]. For instance, He *et al.* [6] demonstrated that mixing parameters in the LaMO₃ series inversely depends on the occupancy of the d-orbitals and that the optimum values are often significantly smaller than the standard mixing parameter of 0.25. It has further been proposed that the optimum mixing factor is solely related to the dielectric constant by $\alpha \approx 1/\epsilon_{\infty}$ in the context of PBE0 functionals but loses its justification

within the framework of screened hybrid potentials [6]. Nevertheless, the lack of a double-counting term and inclusion of all states, delocalized and localized, into the treatment of exchange effects, is a crucial advantage over the DFT+U functional [6].

Amongst the presented functionals, the hybrid formulation is computationally most expensive. Therefore, it should be carefully considered, if an increasing precision outweighs these costs. In 2011 a relatively comprehensive study on the properties of STO has been conducted by El-Mellouhi *et al.* [268]. They investigated the effect of several exchange-correlation functionals on the antiferrodistortive (D_{4h}) and the cubic phase (O_h). Particularly the properties in the antiferrodistortive phase proved to be sensitive to the choice of the exchange-correlation potential. This sensitivity is especially noticeable from the overestimation of the octahedral tilt in the tetragonal STO structure. They further pointed out that a precise description can be obtained for metal oxides, if screened hybrid functionals, complete localized basis sets, and large supercells are used to simulate the structure.

In contrast, recent studies have shown that exchange-correlation functionals beyond the standard approximation are often not necessary to observe displacement and occupation fluctuations, allowing for structural and electronic varying local environments. Interestingly, Varignon *et al.* [89] reported that structural symmetry breaking (polymorphous description of the material) and gapping trends in ABO_3 compounds can be sufficiently reproduced by meta-GGA functionals with improved treatment of the self-interaction error (“SCAN” functional), even though this description is based on “a mean-field, single-determinant, Bloch periodic band structure approach, with an electron-gas-based description of the exchange and correlation.” More precisely, they did not use an on-site potential U or hybrid functionals to capture the physics of this exceptionally diverse material class. Let us evaluate if a standard GGA potential is sufficient to describe NBT.

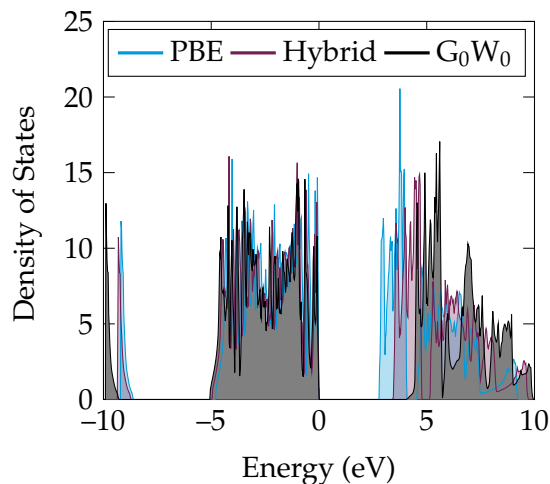


Figure 24: Density of states of a rhombohedral, 111-ordered NBT unit cell calculated with PBE (GGA), Hybrid (see text for parameters), and the G_0W_0 approach.

3.4.4 Is the GGA functional sufficient to represent the electronic structure of NBT?

Although we assume that the GGA functional is sufficient to represent and investigate the electronic properties of NBT (rhombohedral ground state structure and the theoretical band gap is a good approximation to experimental measurements, see Chapter 8), we will shortly compare our results with more advanced techniques. Figure 24 shows the density of states of a rhombohedral, 111-ordered unit cell for three different approximations (GGA, Hybrid, and G_0W_0).

In general, we see that the density of states are rather similar, except for the deep states at approximately -10 eV and a shift of the conduction band minimum to higher energies. The band gap grows successively with the increasing complexity of the calculation and is even overestimated in the G_0W_0 approach, the non-self-consistent perturbative version of the GW-approximation, which reduces the self-interaction error [25, 244, 269–271]. Therefore, and for reasons which become apparent in Chapter 8, the GGA functional appears to be sufficient for the analysis of charge transition states and the electronic structure in general.

3.5 PERIODICITY IN SOLIDS

If we study material properties, we are generally interested in the macroscopic behavior obtained in the limit of ever-increasing system sizes. Despite the approximations made in the framework of density functional theory, a considerable amount of non-interacting electrons present in supercell calculations results in great computational effort. On the one hand, every electron has to be described by a separate wave function. On the other hand, since those wave functions expand over the entire solid, the basis set to represent the wave function would have an infinite cardinality [272]. One possibility to reduce simulation cell sizes while simultaneously determining bulk properties (elimination of surface contributions) with high computational efficiency is to impose Born-von-Kármán periodic boundary conditions [273–276]. In the periodic density functional theory atomic positions are then described by a lattice vector \mathbf{R}_α , added to the coordinates of atom κ within the reference unit cell $\boldsymbol{\tau}_\kappa$ [126],

$$\mathbf{R}_{\alpha,\kappa} = \mathbf{R}_\alpha + \boldsymbol{\tau}_\kappa. \quad (80)$$

A significant consequence of infinite periodic systems is the description of electronic wave functions, $\psi_{n,\mathbf{k}}$, in Bloch form, with a band index n and dependent on the wave vector \mathbf{k} [272]:

$$\begin{aligned} \psi_{n,\mathbf{k}} &= \frac{1}{\sqrt{N\omega_0}} \exp(i\mathbf{k}\mathbf{r}) u_{n,\mathbf{k}}(\mathbf{r}) \\ &= \frac{1}{\sqrt{N\omega_0}} \sum_{\mathbf{G}} c_{n,\mathbf{k}}(\mathbf{G}) \exp(i(\mathbf{k} + \mathbf{G})\mathbf{r}). \end{aligned} \quad (81)$$

Here, ω_0 is the volume of the unit cell, N is the number of unit cells repeated in the Born-von-Kármán periodic box, $\exp(i\mathbf{k}\mathbf{r})$ is a plane wave, and $u_{n,\mathbf{k}}(\mathbf{r})$ is a function with the same periodicity as the crystal lattice. The latter condition allows expanding $u_{n,\mathbf{k}}(\mathbf{r})$ in terms of a discrete set of plane waves, where \mathbf{G} is a reciprocal lattice vector. Although, in principle, an infinite basis set would be needed to represent the wave

function in Equation 81, in practice, only plane waves with kinetic energies smaller than a specific cutoff ($(\hbar^2/2m) |\mathbf{k} + \mathbf{G}|^2$) are used in the expansion. A finite energy cutoff will introduce an error in the total energy, which, however, can be reduced by successively increasing the truncation threshold.

Most quantities (e.g., electronic densities) are extracted from integrals over the Brillouin zone, implying that electronic wave functions have to be sampled on an infinite number of \mathbf{k} -points in reciprocal space. Fortunately, wave functions defined at \mathbf{k} -points lying close together are almost identical such that regions in \mathbf{k} -space can be sufficiently described by one representative \mathbf{k} -point [272]. These representatives form a finite set of special \mathbf{k} -points [277–280], such that the integral over the Brillouin zone can be replaced by a sum. Equivalent to the energy cutoff, the sampling on a finite \mathbf{k} -point set involves a careful convergence study for the grid density in order to prevent numerical inaccuracies [272].

3.5.1 Pseudopotential approximation

In the last section, we learned that using Bloch functions significantly reduces the computational expense to determine total energies. However, two difficulties remain with this approach, which unnecessarily increases the number of plane waves needed to expand electronic wave functions appropriately. Firstly, plane waves are not suitable to accurately describe tightly bound core states, and secondly, valence electron wave functions oscillate rapidly in the core region to remain orthogonal to the core electrons as required by the exclusion principle. One solution to this problem is the pseudopotential approximation combined with a frozen-core [132, 272, 281–283], where the core electrons and the strong ionic potential are replaced by a pseudopotential, acting on smooth pseudo wave functions without nodes inside the core region. Ideally, scattering properties and phase shifts are preserved outside the core region such that pseudoelectron and all-electron approaches correspond to each other. This simplification is reasonable, considering the strong dependency of material properties on the valence electrons instead of core electrons, which are hardly affected by different chemical environments and bond modifications. Another pleasant side effect of the pseudopotential approach is an overall smaller amount of electrons, which has to be treated self-consistently.

3.6 DENSITY FUNCTIONAL PERTURBATION THEORY

As discussed in the previous sections, DFT proves particularly helpful in accessing the total energy corresponding to a set of fixed nuclear positions. In the following, we will learn which important functional properties of NBT can be obtained from the derivatives of the Born-Oppenheimer energy surface and how this is accomplished in practice. These quantities are beneficial to correct for artificial interactions in charged simulation cells or to evaluate elastic properties, which become important in the Chapters 8 and 9. Let us first take a look at the different material properties and their relation to the three perturbations atomic displacement ($\partial\mathbf{R}$), strain ($\partial\eta$), and electric field ($\partial\mathcal{E}$), as shown in Table 1.

The first order derivatives of the total energy lead to the force F_n , the stress σ_k , and the polarization P_β . In turn, the second order derivatives describe the linear re-

	E	$\partial E/\partial R_m$	$\partial E/\partial \eta_j$	$\partial E/\partial \mathcal{E}_\alpha$
$\partial/\partial R_n$	F_n	K_{mn}	γ_{jn}	$Z_{\alpha n}^*$
$\partial/\partial \eta_k$	σ_k	γ_{mk}	C_{jk}	$e_{\alpha k}$
$\partial/\partial \mathcal{E}_\beta$	P_β	$Z_{m\beta}^*$	$e_{j\beta}$	$\chi_{\alpha\beta}$

Table 1: Physical quantities related to first and second-order derivatives of the total energy. Here, m and n are composite indices, describing the atom and the direction of the displacement, j and k are indices for a strain components in Voigt notation, and α and β are cartesian directions. For a description of the parameters, see text. Adapted from Reference [109].

sponse of the material. These include the interatomic force constant K_{mn} , the dielectric susceptibility $\chi_{\alpha\beta}$, the clamped-ion elastic constants C_{jk} , the Born effective charges $Z_{m\alpha}^*$, the clamped-ion piezoelectric tensor $e_{\alpha j}$, and the internal strain coupling parameter (force-response internal-strain tensor) γ_{mj} [109, 114]. At fixed strain and electric fields, relaxed-ion macroscopic dielectric, piezoelectric and elastic tensors (“relaxed-ion” or “dressed” response tensors) are provided. In turn, elastic compliance tensors, stress-free dielectric tensors, fixed-electric-displacement elastic tensors, alternative piezoelectric tensors, and electromechanical coupling constants are obtained from a subsequent post-processing step [114].

The finite-difference or “direct” [284] technique is a common approach to evaluate the first- and second-order derivatives since it can be realized without any additional computational cost (except of the implementation of the Berry-phase formulation) and can be easily integrated into current software. The principal idea is a comparison between a perturbed system and the perfect crystal at equilibrium, for instance, in frozen phonon calculations, where atoms are collectively displaced by a finite and periodic amplitude.

We will use the example of a frozen phonon calculation to reveal the main difficulties connected to the finite-difference approach. To investigate a phonon mode of wave vector \mathbf{q} , this vector has to be a reciprocal lattice vector of the supercell with lattice dimensions of at least $2\pi/|\mathbf{q}|$ (homogeneous electric fields or linear potentials are, for instance, not possible) [284, 285]. Indeed, too small simulation cells can provide information on a few discretely distributed wavelengths only [286]. In these cases, the computation of phonon modes is often restricted to the zone center.

Density functional perturbation theory, can elegantly avoid these limitations. A milestone paper on the linear response of solids was published in 1987 by Baroni, Gianozzi, and Testa [284, 287]. Extensions to perturbations other than atomic displacements very rapidly followed, and a generalization to arbitrary order of perturbation was proposed by Gonze *et al.* [288] in 1995. In this context, and for the determination of nonlinear responses, the $2n + 1$ theorem proved to be especially useful, which ensures that the derivatives of the energy up to order $2n + 1$ can be calculated if the n th derivative of the wave functions is known.

For a detailed discussion including information on the practical implementation into current density functional theory codes, the reader is referred to References [113, 114, 118, 129, 284–291].

A particular advantage of DFPT is that both perturbations commensurate and incommensurate to the crystal lattice can be investigated such that macroscopic electric fields can be applied without the need for large supercells. Additionally, it is not necessary to perform several ground state calculations and response tensors can be determined in a more automated, systematic, and reliable fashion [113, 114, 289]. For a more detailed introduction, including a formulation of the mathematical ansatz, we recommend reviewing this chapter’s references.

3.7 IONIC RELAXATION AND THE HELLMANN-FEYNMAN THEOREM

Thus far, we exclusively dealt with the electronic relaxation at fixed ionic configurations. However, finding a an energetic global minimum (ground state) in the $3 \times N_{\text{atoms}}$ parameter space, crucially depends on the optimization of ionic positions, the shape, and the unit cell volume.

An equilibrium atomic arrangement is characterized by vanishing forces on individual nuclei. The force on ion I can be determined from the negative first derivative of the total energy with respect to the nuclear position, which can be expressed as [272]

$$\mathbf{F}_I = -\frac{\partial E(\mathbf{R})}{\partial \mathbf{R}_I} = 0, \quad (82)$$

where $E(\mathbf{R})$ is the Born-Oppenheimer energy surface. Owing to the Hellmann-Feynman theorem (the $2n + 1$ theorem for $n = 0$) [292, 293], the first derivative of the Kohn-Sham energy with respect to a parameter λ is defined as the expectation value associated to the derivative of the Hamiltonian H_λ [132],

$$\frac{\partial E_\lambda}{\partial \lambda} = \langle \Psi_\lambda | \frac{\partial H_\lambda}{\partial \lambda} | \Psi_\lambda \rangle, \quad (83)$$

where Ψ_λ is the eigenfunction corresponding to the eigenvalue E_λ . If we compare Equation 82 with Equation 83, we easily recognize that in this specific case λ is given by the nuclear coordinates \mathbf{R} . Thus, the forces are given by [132]

$$\mathbf{F}_I = -\int d\mathbf{r} n_{\mathbf{R}}(\mathbf{r}) \frac{\partial V_{\mathbf{R}}(\mathbf{r})}{\partial \mathbf{R}_I} - \frac{\partial E_{\mathbf{N}}(\mathbf{R})}{\partial \mathbf{R}_I}, \quad (84)$$

where $V_{\mathbf{R}}(\mathbf{r})$ denotes the electron-nucleus interaction, $n_{\mathbf{R}}(\mathbf{r})$ describes the optimized electronic charge density for a specific set of nuclear positions, and $E_{\mathbf{N}}(\mathbf{R})$ denotes the electrostatic interaction between different nuclei. Note that forces calculated by Equation 83 are susceptible to errors such that they need to be evaluated after approaching the electronic ground state configuration. Finally, the equilibrium state is found iteratively by varying \mathbf{R} and subsequently optimizing all electronic degrees of

freedom until a user-defined criterion (force, energy) is met.

The Hessian of the Born-Oppenheimer energy surface is formulated as [132]

$$\begin{aligned} \frac{\partial^2 E(\mathbf{R})}{\partial \mathbf{R}_I \partial \mathbf{R}_J} &= -\frac{\partial \mathbf{F}_I}{\partial \mathbf{R}_J} \\ &= \int \frac{\partial n_{\mathbf{R}}(\mathbf{r})}{\partial \mathbf{R}_J} \frac{\partial V_{\mathbf{R}}(\mathbf{r})}{\partial \mathbf{R}_I} d\mathbf{r} \\ &\quad + \int n_{\mathbf{R}}(\mathbf{r}) \frac{\partial^2 V_{\mathbf{R}}(\mathbf{r})}{\partial \mathbf{R}_I \partial \mathbf{R}_J} d\mathbf{r} + \frac{\partial^2 E_N(\mathbf{R})}{\partial \mathbf{R}_I \partial \mathbf{R}_J}. \end{aligned} \quad (85)$$

Equation 85 is usually referred to as matrix of the interatomic force constants and involves the calculation of the optimized electron charge density $n_{\mathbf{R}}(\mathbf{r})$ and its linear response, $\partial n_{\mathbf{R}}(\mathbf{r})/\partial \mathbf{R}_I$, with respect to a displacement \mathbf{R}_I . The eigenvalues of the interatomic force matrix are the vibrational frequencies, which can be extracted from the solutions of the secular equation [112, 132] and provide access to phonon dispersion curves,

$$\det \left| \frac{1}{\sqrt{M_I M_J}} \tilde{K}_{I\alpha, J\beta}(\mathbf{q}) - \omega^2(\mathbf{q}) \right| = 0. \quad (86)$$

Precisely, $\tilde{K}_{I\alpha, J\beta}(\mathbf{q})$ is the Fourier transform of the interatomic force matrix, which can be separated into an electronic part and a contribution from the electrostatic interaction energy between the ions [113]. The term [113],

$$\tilde{D}_{I\alpha, J\beta}(\mathbf{q}) = \frac{\tilde{K}_{I\alpha, J\beta}(\mathbf{q})}{\sqrt{M_I M_J}}, \quad (87)$$

is known as the dynamical matrix $\tilde{D}_{I\alpha, J\beta}(\mathbf{q})$. The homogeneous translation of the crystal at the Γ -point is an eigenvector of the dynamical matrix with vanishing eigenfrequency. The acoustic-sum rule assures that the energy of a rigid translation is invariant [113],

$$\sum_J \tilde{K}_{I\alpha, J\beta}(\mathbf{q} = \mathbf{0}) = 0. \quad (88)$$

3.8 MODERN THEORY OF POLARIZATION

Electric polarization is an essential property related to several other phenomena as ferroelectricity, Born effective charges, piezoelectricity, dielectric susceptibility, and pyroelectricity [294]. In Chapter 5, we will calculate this fundamental quantity in pure NBT and study the dependency of the polarization on other distortion modes. This will give us insight into the complex coupling of distortion modes and serve as a benchmark of the GGA exchange potential for characterizing NBT and of DFT/DFPT in general.

The easiest and most obvious way to define macroscopic polarization seems to be the dipole moment in a unit cell of volume Ω_0 . Figure 25, however, illustrates the difficulties arising with the specification of a unit cell in infinite crystals (thermodynamic limit).

Both variants are appropriate choices for the unit cell origin and are equally suitable to describe the underlying lattice. This arbitrariness results from the absence of any

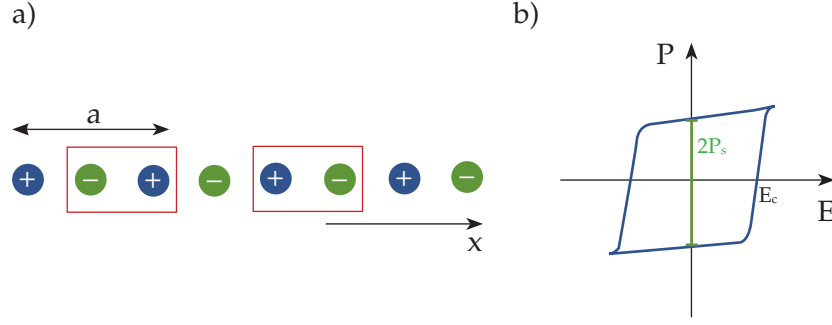


Figure 25: One dimensional atom chain with a lattice constant of a and two different unit cell definitions (a). Definition of the spontaneous polarization as $\Delta\mathbf{P}$, measured during a reversal of the polarization direction (b). Figure a) has been adapted from Reference [295].

surfaces and leads to ill-defined (dependent on shape and truncation) polarization quantities, especially in covalent crystals with delocalized electric charges [294, 296]. Whether the polarization is a bulk property remained unclear until the modern theory of polarization was established in the early 1990s. Pioneers of this theory, and in this context especially noteworthy, are Resta [294, 297], King-Smith, and Vanderbilt [298]. The realization that changes between differently polarized states can properly define polarizations is at the heart of this modern theory and is inherently coupled to a polarization current flowing through the bulk during a reversal of the polarization direction. Indeed, only finite differences, $\Delta\mathbf{P}$, between different states of the same material are measured experimentally, since surface charges or other charged defects compensate electric dipoles at equilibrium [294]. One example is the measurement of the spontaneous polarization in ferroelectrics, which corresponds to half of the difference of $\Delta\mathbf{P}$ between two ferroelectric enantiomorphous states at zero electric field, determined from a \mathbf{P} - \mathcal{E} -hysteresis loop [295, 297]. If we assume a continuous adiabatic transformation of the Kohn-Sham Hamiltonian between two states of the same solid at zero electric field and further claim that the system remains insulating, we define $\Delta\mathbf{P}$ as the flow of polarization current in the solid [298],

$$\Delta\mathbf{P} = \int_0^1 d\lambda \frac{\partial \mathbf{P}(\lambda)}{\partial \lambda}, \quad (89)$$

where λ is a parameter, which describes the transformation and takes values in a range from 0 to 1. Strictly, $\Delta\mathbf{P}$ additionally has to be smaller than the polarization quantum (see below) to be independent of the path chosen in parameter space. Generally, λ might represent time such that $\Delta\mathbf{P}$ represents an integrated current. In ferroelectrics λ can be identified with a relative displacement of sublattices, as in the case of polar zone-center transverse-optic phonons [297].

The total polarization consists of an ionic and an electronic contribution [109],

$$\mathbf{P}(\lambda) = \mathbf{P}_{\text{ion}}(\lambda) + \mathbf{P}_{\text{el}}(\lambda), \quad (90)$$

where the ionic term is given by

$$\mathbf{P}_{\text{ion}}(\lambda) = \frac{e}{\Omega_0} \sum_{\kappa}^{\text{cell}} Z_{\kappa} \mathbf{R}_{\kappa}. \quad (91)$$

Here, e is the absolute electronic charge, \mathbf{R}_κ is the position, and Z_κ is the atomic number of atom κ . Instead, the electronic part is defined as the Berry phase (Brillouin zone integral over the Berry connection $i \langle u_{n\mathbf{k}}^\lambda(\mathbf{r}) | \nabla_{\mathbf{k}} | u_{n\mathbf{k}}^\lambda(\mathbf{r}) \rangle$) of the occupied band n and independent from the path chosen in parameter space [109, 298, 299],

$$\mathbf{P}_{\text{el}}(\lambda) = \frac{e}{8\pi^3} \mathcal{J} \sum_{n=1}^N \int_{\text{BZ}} d\mathbf{k} \langle u_{n\mathbf{k}}^\lambda(\mathbf{r}) | \nabla_{\mathbf{k}} | u_{n\mathbf{k}}^\lambda(\mathbf{r}) \rangle, \quad (92)$$

where $u_{n\mathbf{k}}^\lambda$ is an implicit function of λ and satisfies the periodic gauge condition

$$u_{n\mathbf{k}}^\lambda(\mathbf{r}) = \exp(i\mathbf{G}\mathbf{R}) u_{n(\mathbf{k}+\mathbf{G})}^\lambda(\mathbf{r}). \quad (93)$$

In short, variations in the polarization are caused by changes in the Kohn-Sham Hamiltonian and can be determined through the initial and final valence band wave functions [298]. Thus $\Delta\mathbf{P}$ is related to the current (gauge-invariant phase information of occupied Kohn-Sham orbitals) and not the charge. King-Smith and Vanderbilt [298] interpreted the Berry phase in terms of displacements, resulting from the center of charge of the Wannier functions, which are induced by the adiabatic change of the Hamiltonian [109]. Although $\Delta\mathbf{P}$ is a gauge-invariant macroscopic observable, it can only be defined modulo the polarization quantum $(2e/\Omega)\mathbf{R}$. The variable \mathbf{R} might be any lattice vector, and the set of polarization values is often referred to as polarization lattice. The understanding of polarization as a multivalued vector quantity is a central outcome of the modern theory of polarization. To avoid misunderstandings, we should mention that experimentally measured polarization values are naturally single-valued [295].

Born effective charges (Z_{ij}^*) provide another way to quantify polarizations, which is particularly helpful for calculating spontaneous polarizations in ferroelectrics. Remember that Z_{ij}^* is defined as the change in polarization in direction i , caused by the displacement u of atom j (using periodic boundaries, this is equivalent to a displacement of a periodic sublattice) [295]:

$$\partial P_i = \frac{e}{\Omega} Z_{ij}^* \partial u_j. \quad (94)$$

3.9 CHARGED-DEFECT SUPERCELL CALCULATIONS

Defects can be beneficial [300]! Although defects are a discontinuity of the crystal lattice, the targeted use of doping may open up the possibility for improved solutions in modern technology [6]. To achieve this high degree of chemical, structural, and functional flexibility, a deep understanding of defect structures (electric and geometrical) is inevitable.

Computer simulations might substantially contribute to the decoding of structure-property relationships such that with increasing theoretical advancement even more complex configurations, as defect clusters, become manageable. Freysoldt *et al.* [24] even talk about a revolutionary character of DFT concerning the discovery and understanding of defect properties. However, these techniques are still under development, especially if charged simulation cells are involved (no universal method, which is equally suited to handle charged defects in all material classes). Finite-size effects,

inevitable due to the rapidly increasing computational effort for large system sizes, often result in artificial long-range Coulomb interaction between charged point defects. However, even neutral defects might cause deviations from the “true” defect properties, caused by elastic or charge multipole (dipolar and quadrupolar) interactions between local aperiodicities [301]. In the following section, we will review the current state of the art to characterize defects in the framework of periodic boundary *ab-initio* calculations. We will particularly focus on the correct handling of the long-range electric and elastic interaction between periodic images while calculating binding energies, migration energies, charge transition states, the elastic dipole tensor, and the relaxation volume. A careful treatment of charged-defect simulation cells will be of paramount importance and is inevitable since most of the studied defects and defect complexes favor a non-vanishing charge state (e.g., oxygen vacancies $V_{\text{O}}^{\cdot\cdot}$). They are urgently needed in Chapter 8.

For a more detailed discussion of the topic and a rigorous derivation of formulas, the reader is referred to the references given in this chapter. We will end this introductory part by quoting Bruneval *et al.* [302] again: “The combined use of charged simulation cells and periodic boundary conditions leads to intricacies that require a lot of care”.

3.9.1 Formation energies

The thermodynamics of a system heavily depends on the formation energies of defects, their migration energies, as well as their chemical reactions [303]. In recent years, DFT emerges as a valuable tool for investigating atomistic details of point defects. Besides the calculation of the above mentioned thermodynamic properties, *ab-initio* methods are equally useful to extract defect geometries and wavefunction characters almost without any prior assumptions [304]. Thus, the predictive power of first-principles calculations regarding to point defects is of central importance.

According to the approach of Zhang and Northrup [305], the formation energy is determined from the difference between the Gibbs free energies of a defective and a bulk supercell, considering the chemical potential (at standard conditions), μ_s , of the defect specific reservoirs, and the Fermi energy E_F (relative to the valence band maximum ϵ_{vbm}) [304, 306],

$$G_f[X^q](P, T, \{\mu_s\}, E_F) = F[X^q](\Omega', T) - F[\text{bulk}](\Omega, T) + PV^f - \sum_s n_s \mu_s + q(E_F + \epsilon_{\text{vbm}}) + \underbrace{q\Delta_q - E^{\text{lat}}[q_{\text{model}}]}_{\text{finite-size correction}}, \quad (95)$$

where $F[X^q]$ is the free energy of a supercell with a defect type X of charge q , $F[\text{bulk}]$ is the reference energy of the bulk with an equal amount of atoms, and n_s is the integer number of the chemical species s , which has been removed ($n_s < 0$) or added ($n_s > 0$) to the supercell. Furthermore, Ω' and Ω are the volumes of the defective and the bulk cell, while V^f denotes the defect formation volume (see Section 3.10). The free energy of both supercells includes the contributions of vibrational, electronic, and magnetic entropy. However, these contributions are small compared to the configurational entropy and the computational cost to determine them is high. Thus, they are typically neglected and the free energies in Equation 95 is replaced by the

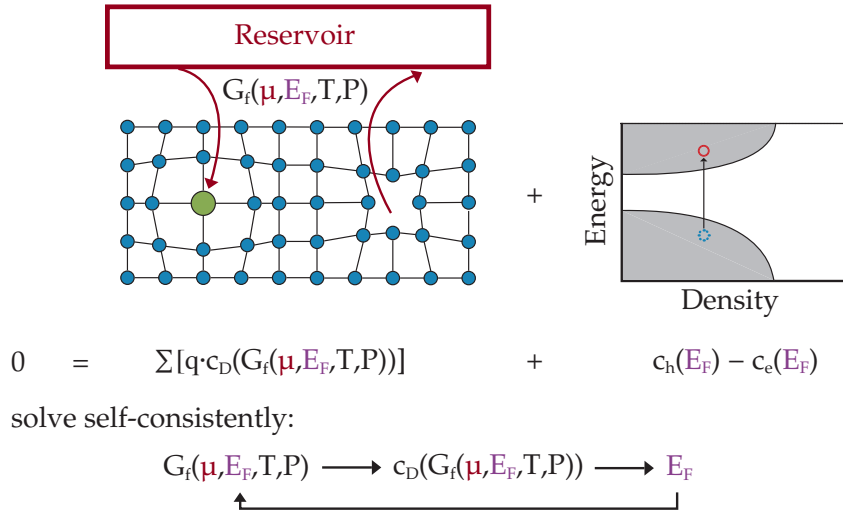


Figure 26: Relationship between the defect concentration, the formation energy, and the Fermi energy under the constraint of a charge-neutral cell.

total energy $E_f[X^q]^{\text{DFT}}$ from regular DFT calculations. The finite-size correction term will be described in the next section and currently has been added for completeness only. Note that in Equation 95 thermal entropy contributions for the bulk and the defective system are assumed to be identical such that they completely cancel out, and that the pV term is neglected for solids [303].

In the following study, we will exclusively concentrate on the zero temperature formation energy, where quasi-harmonic and anharmonic excitations are neglected. An accurate determination of these quantities not only requires expensive calculations, but it is also assumed that they are significantly smaller than the deviations introduced by the band gap problem in semiconductors. Furthermore, in these materials, the defect concentration is primarily influenced by the configurational entropy [307]. Equation 95 allows to calculate the most valuable input variable for the determination of the equilibrium concentrations in the dilute defect limit, which is formulated as follows [306]:

$$c_{\text{eq}}(T) = N \exp(-G_f[X^q]/k_B T). \quad (96)$$

Here, k_B is the Boltzmann constant, T is the temperature, and N is the number of symmetry equivalent lattice sites.

Figure 26 summarizes the relationship between the defect concentration, the formation energy, and the Fermi energy under the constraint of a charge-neutral cell. The concentration c_D denotes all possible defects, except electrons and holes, which are present in the lattice and contribute to the charge neutrality. In the case of NBT, this includes the number of oxygen vacancies as well as acceptor dopants. It is necessary that the Fermi energy decisively determines the formation energy, which, in turn, is crucial to extract equilibrium defect concentrations and conductivities.

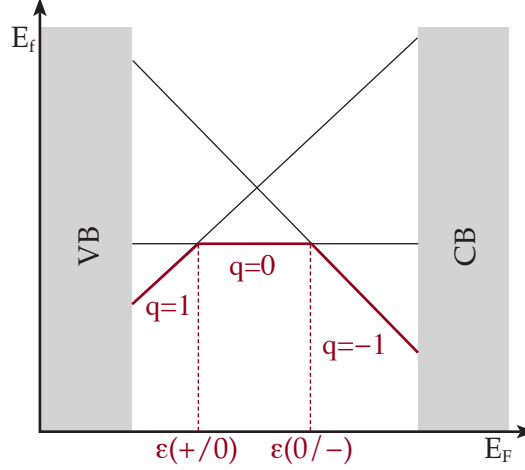


Figure 27: Definition charge transition levels in defective supercells. The intersects represent the Fermi level at which the defect changes its charge state. Adapted from Reference [306].

3.9.2 Charge transition levels

While formation energies are the essential quantity for the determination of equilibrium defect concentrations, charge-transition levels (alternatively ionization levels or thermodynamic transition levels) provide information about the charge state of the defect level, depending on the Fermi energy and the defect symmetry. These quantities are useful to explain a temperature dependent conductive behavior, including a change of the defect mobility with various charge states [308] or the formation of defect associates, where binding energies sensitively depend on the electrostatic interaction of the individual point defects.

Indeed, Janotti *et al.* [149] showed that even the formation of polarons is influenced by the exact charge state of oxygen vacancies in SrTiO₃. The charge transition level is given by [242, 309, 310]

$$\epsilon(q_1/q_2) = \frac{E_f[X^{q_1}] - E_f[X^{q_2}]}{q_2 - q_1} - \epsilon_{vbm}, \quad (97)$$

where $E_f[X^{q_i}]$ denotes the formation energy of the defect in the charge state q_i , and ϵ_{vbm} is the valence band maximum calculated in the pristine host.

The determination of charge transition levels relies on the accurate calculation of defect formation energies for different charge states and corresponds to the Fermi level position at which the defect with charge q_2 becomes thermodynamically more stable than the defect in the charge state q_1 . Visually, these transition states correspond to the intercept between the two curves $E_f[X^{q_1}]$ and $E_f[X^{q_2}]$, as illustrated in Figure 27. If the charge transition level is located close to the conduction or valence band edge, it is denoted as shallow. In turn, if $\epsilon(q_1/q_2)$ occurs at Fermi energies around the middle of the band gap, it is said to be a deep charge transition level.

The necessity of a careful evaluation of $E_f[X^{q_i}]$ has already been addressed in the previous section, and all challenges related to this quantity persist. In the case of charge transition levels, artificial charged-defect interactions tend to systematically decrease the spacing between these levels [309], which might lead to misinterpretations of experimental data. Note that charge transition states do not depend on the chemi-

cal potentials of the constituents. We will take advantage of this fact in the present thesis, since the calculation of all relevant boundary phases for the four component perovskite NBT exceeds the scope of this study.

As already indicated in Equation 95, the calculation of defect properties suffers from two main approximations inherent to regular DFT calculations. This includes, first, the use of local or semi-local exchange-correlation functionals, and secondly, finite-size supercells and periodic boundary conditions. The former has already been discussed above and is crucial for the dispersion, the occupancy, and the position of the defect state compared to the valence and conduction band edge. In turn, the latter results in electrostatic correction and potential alignment terms, which sensitively affect atomic relaxation patterns for small supercells [303]. In the following section, we will review the most common approaches to determine electrostatic corrections with a preference on the method of Freysoldt *et al.* [24], which has been used in the present thesis.

3.9.3 Electrostatic interaction in charged supercells

Common density functional theory codes apply periodic boundary conditions (“supercell approach”), which is equivalent to an infinite repetition of a finite-size supercell along all cartesian coordinates. This approach offers enormous practical advantages (in combination with a plane-wave expansion), especially for the computation of bulk properties [24]. However, in the case of defects, this repetition results in an artificial sublattice of defects with a lattice constant equal to the supercell’s length. The introduction of such a periodic array has several consequences: First, the point charge lattice leads to spurious long-range Coulomb interactions between the images, imitating an exceedingly high defect concentration [304, 310]. Secondly, a relatively dense defect grid leads to elastic interactions and might allow for an artificial overlap (hybridization) between the wavefunctions of the periodic defect images. Finally, a compensating background charge density or “jellium”, has to be included such that a divergency of the energy is avoided. Nonetheless, the electrostatic potential is a conditionally convergent series and the Madelung constant depends on the truncation of this series [302, 311]. As a result, the energy of the charged system might converge particularly slow (or even diverge) to the dilute limit ($L \rightarrow \infty$) with an increasing linear dimension L of the supercell, which is crucial for the calculation of formation energies or the elastic dipole tensor [24, 312].

Does this mean that the supercell method is impractical for charged cell calculations, where no periodic unit cell exists? No, this approach is legitimate, if appropriate corrections are considered to predict the properties of the aperiodic system and unambiguously explain experimental measurements. Several theoretical approaches exist so far [242, 310, 313–316]. Especially noteworthy are the correction proposed by Leslie and Gillan [312] and developed by Makov and Payne [315] and abstracted by Castleton *et al.* [301, 313]. More specifically, they proposed a correction for electrostatic charge multipole interactions which depend on the supercell size. In turn, Lany and Zunger [242] additionally introduced a potential alignment term for supercells with charged defects. In case the reader is unfamiliar with these concepts, we refer to the

References [242, 301, 312, 313, 315, 317, 318].

Freysoldt, Neugebauer, and Van de Walle [24] (FNV) demonstrate that corrections of the Makov and Payne type do not reliably improve the convergency of the energy and criticize the lack of physical significance for higher-order terms in the context of scaling laws. Especially higher order terms include several different contributions, which can hardly be distinguished from wavefunction overlaps or differences in simulation cell shapes encountered in scaling approaches. These include higher-order moments of the charge distribution, non-linear effects, and microscopic screening caused by local field effects (oscillating behavior on the length scale of a few bonds) [304]. Thus Freysoldt *et al.* [24] proposed an *ab-initio* finite-size correction method with the particular advantage that only single supercell calculations are necessary and no non-interpretable fitting constants are involved. In the following, we will shortly summarize the key equations of this approach.

The correction term is composed of two parts, E_{inter} and E_{intra} , which describe the interaction energies caused by the application of periodic boundary conditions and by the artificial interaction between the background, n_b , and the defect charge, q , in the reference supercell, respectively,

$$E_{\text{inter}} = \int_{\Omega} d^3\mathbf{r} [q_d(\mathbf{r}) + n_b] [\tilde{V}_{q/0}(\mathbf{r}) - V_{q/0}(\mathbf{r})], \quad (98)$$

$$E_{\text{intra}} = \int_{\Omega} d^3\mathbf{r} n_b V_{q/0}(\mathbf{r}) = -q \left(\frac{1}{\Omega} \int_{\Omega} d^3\mathbf{r} V_{q/0}(\mathbf{r}) \right). \quad (99)$$

Here, q_d is the unscreened defect charge, Ω is the supercell volume and $V_{q/0}$ is the difference between the electrostatic potential of the supercell, containing a charged and a neutral defect. Instead, $\tilde{V}_{q/0}$ describes the periodic defect potential, formulated as a Fourier series. If $V_{q/0}$ is divided into a long-range and a short-range contribution and we assume that $V_{q/0}$ approaches the macroscopically screened Coulomb potential in the limit of large $|\mathbf{r}|$, we receive the following form for the correction term,

$$\begin{aligned} E_{\text{inter}} + E_{\text{intra}} &= E_q^{\text{lat}} - q\Delta_{q/0} \\ &= \int_{\Omega} d^3\mathbf{r} \left[\frac{1}{2} [q_d(\mathbf{r}) + n_b] [\tilde{V}_q^{\text{lr}}(\mathbf{r}) - V_q^{\text{lr}}(\mathbf{r})] + n_b V_q^{\text{lr}}(\mathbf{r}) \right] \\ &\quad - q \left(\frac{1}{\Omega} \int_{\Omega} d^3\mathbf{r} V_{q/0}^{\text{sr}}(\mathbf{r}) \right), \end{aligned} \quad (100)$$

where $V_{q/0}^{\text{sr}}(\mathbf{r}) = \tilde{V}_{q/0}(\mathbf{r}) - \tilde{V}_q^{\text{lr}}(\mathbf{r}) - C$ for $\mathbf{r} \in \Omega$ and C is an alignment constant. Practically, the alignment term is obtained from the difference between the potential of a model charge and the potential of the charged-defect DFT calculation with respect to the bulk potential. Since E_q^{lat} and $\Delta_{q/0}$ hardly depend on defect charge distribution, a combination of a Gaussian and an exponentially decaying part is appropriate in most practical applications. However, a more general defect model was introduced in 2011 [304],

$$q(r) = qxN_{\gamma} \exp(-r/\gamma) + q(1-x)N_{\beta} \exp(-x^2/\beta^2), \quad (101)$$

where r denotes the radius, N_{β} and N_{γ} are normalization constants, γ reflects a decay constant, x describes a tail weight, and β is a constant, whose value is only

essential for delocalized defect charge densities.

Rather than referencing to the supercell containing a neutral defect, it is equally valid to use the perfect bulk system such that $\tilde{V}_{q/0}$ becomes $\tilde{V}_{q/b}$. The periodic defect potential itself can be directly obtained from standard DFT calculations. Suppose the short-range potential approaches zero at the simulation cell boundaries, which means that the short-range interaction of the defect located in a periodic array of image defects is equal to the short-range interaction of the isolated case. In that case, we can extract the alignment constant from the plateau of the plane averaged $\tilde{V}_{q/b} - \tilde{V}_q^{\text{lr}}$ curve. Note that in the limit of a point charge model, the E_q^{lat} term inversely depends on the linear cell dimension, L , and the expression for the alignment correction scales with L^{-3} . This means that the Freysoldt correction approaches the solution of Makov and Payne [315] as well as the scaling law of Castleton *et al.* [301], however, with an explicit description of the cubic term. A potential shift is reasonable to align the reference energies for the electrons in the charged and bulk supercell [314]. Nevertheless, it is different from the term in the Lany and Zunger approach [242].

A particular advantage of this correction scheme is the transferability to more complex problems as, for instance, interfaces or dislocations. In contrast, difficulties occur if the atoms are allowed to relax, leading to several off-site displacements. In such cases, the defect-induced potential becomes wavy, and the description by the standard defect model becomes poor and size-dependent. As a consequence, no plateau can be reached between the defects of the periodic array. Ionic hosts, which might screen the long-range interaction by their inherent dipole character, also constitute rather complex cases, if the defect geometry changes during the simulation [316]. In these cases, Kumagai *et al.* [316] suggest to average the FNV alignment term in a sampling region outside the Wigner-Seitz cell of radius, R_{WS} , instead of using planar averages as originally proposed in the original FNV scheme. Essentially, they rewrote the energy correction of the FNV scheme as

$$E_{\text{FNV}} = E_{\text{PC}} - q\Delta V_{\text{PC},q/b} |_{\text{far}}, \quad (102)$$

where $\Delta V_{\text{PC},q/b} |_{\text{far}}$ is the difference between the potential $V_{q/b} = V_{\text{defect},q} - V_{\text{bulk}}$, which is caused by the defect, and the point-charge potential at positions far from the defect site. Instead of a Gaussian model, they apply a point charge model and calculate the screened potential in an anisotropic dielectric medium. From the above, the method of Kumagai *et al.* [316] can be referred to as extended FNV scheme. Although the sampling region is independent of the supercell size in this scheme, only an insufficient amount of reference points are available for small simulation cells. However, these possible inaccuracies drastically reduce for larger cell sizes.

Since it turned out that the relaxation of the defect structure is indispensable and crucially reduces the energy of the system, we will use the extended FNV scheme in the following thesis.

Generally, a point defect induces a defect-localized state (DLS), a deep state in the middle of the band gap, or a shallow state, which resonates with the host bands. In the latter case, the corresponding charge carrier occupies a delocalized, perturbed host state [242]. Several studies showed that the success of the correction method often depends on the exact position of the defect state relative to the band edges

and is drastically influenced by the delocalization (hybridization of the defect with band edge states) of the defect charge density. In these cases, a point charge or Gaussian model is not applicable to separate the long-range from the short-range part efficiently and to determine the alignment constant.

Currently, the screening, quantum-mechanical effects (wavefunction overlap), and hybridization are still nontrivial behaviors [317], such that a general prerequisite for all electrostatics-based finite-size corrections can be formulated: To reliably correct formation energies, the defect charge should be entirely enclosed by the supercell, and the distribution should not be size-dependent [316]. In case this condition is fulfilled, the extended FNV scheme seems to be superior over the Lany and Zunger [242] or the Markov and Payne approach. This is especially true for relaxed defect geometries [317].

We will conclude this part by shortly listing additional sources for inconsistent formation energies. These errors might be introduced by the \mathbf{k} -point integration, the size of the basis set, the lack of thermal effects, the pseudopotential, elastic errors, and the choice of the exchange-correlation functional [301, 318]. Naturally, a convolution of different effects is possible, leading to deviations of the standard scaling behavior [242]. However, although extensive research has been carried out on this topic, there is still no common procedure how to access the correction terms discussed above. There is confusion on whether to explicitly include a potential alignment and the sign convention used in different approaches. Indeed, Komsa *et al.* [317] showed that the L^{-3} term in the Makov and Payne correction already includes a potential alignment effect (see also Ref. [316]). Castleton *et al.* [313] captured the ongoing discussion about the validity of correction terms in a nutshell: “There seems to be no *a priori* method for determining whether the corrections will make things better or worse in a specific case”, as no general ansatz takes into account the subtleties of several defect types in various material classes. Nieminen [303] comes to a similar conclusion and stresses that “the devil is unfortunately often in the detail”.

3.10 AB-INITIO MEETS ELASTICITY THEORY

In the last section, we comprehensively discussed the consequences of charged defects on defect formation energies. We concentrate on the elastic interaction of defects, their relaxation volume, and the elastic dipole tensor in the following part. The elastic interaction is caused by the long-range perturbation of the bulk lattice, originating from the induced point defect, and is the main emphasis of Chapter 9. Huge progress in understanding the above quantities has been made only recently, which is, to a large extent, based on the work of Bruneval, Clouet, and Varvenne [311, 319–322]. Unfortunately, this topic is still largely unnoticed, such that we will take this opportunity to present some of the most important concepts.

3.10.1 Relaxation volumes

Besides the formation energy, the formation volume is another important characteristic, influencing the concentration, the diffusion, the segregation of a defect, or, more generally, the evolution of the microstructure [322, 323]. It is closely related to the

relaxation volume Ω_r and describes a finite, macroscopic volume change after introducing a defect X^q of charge state q into the system [323]. Precisely, it is defined as [322]

$$\begin{aligned}\Delta\Omega_f &= \Omega(X^q) - \frac{N_{\text{defective}}}{N_{\text{perfect}}}\Omega_H \\ &= \Delta\Omega_r \pm \Omega_0,\end{aligned}\tag{103}$$

where Ω_H is the volume of the host, $\Omega(X^q)$ is the equilibrium volume of the defective cell, and Ω_0 is the volume of a single atom in the pristine supercell. The plus sign applies in the case of a vacancy, while the negative sign represents the adequate formula for self-interstitial atoms. It is worthwhile mentioning that Equation 103 is only entirely valid for elemental solids. More generally, the formation volume is the derivative of the Gibbs free energy with respect to the pressure:

$$\Delta\Omega_f = \left. \frac{\partial\Delta G_f(P, T)}{\partial P} \right|_{T, n_i}.\tag{104}$$

In practice, the formation volume is obtained by minimizing the energy of the defective supercell while applying zero-pressure boundary conditions. In turn, the relaxation volume quantifies the change of the lattice parameters caused by the point defect and thus gives an estimate on the elastic interaction with other defects or external strain [323]. It is given by [321, 322]

$$\Delta\Omega_r = \Omega(X^q) - \Omega_H = \oint_S \mathbf{u}_i(\mathbf{r}) \, dS_i,\tag{105}$$

where S is an external surface surrounding a point defect and $\mathbf{u}(\mathbf{r})$ describes the superposition of the displacement generated by the point-defect. In contrast to the formation volume, the relaxation volume does not depend on a reference volume associated with a reservoir [323]. Although these volumes typically depend on the type and the point group of the defect, it should be almost independent of the defect charge state if significant and charge-dependent relaxations can be excluded. However, a linear relationship between the charge and the formation volume has been observed practically, even for finite-size converged values [322]. Bruneval *et al.* [322] verified that this observation is caused by the non-vanishing derivative of the potential alignment and the electrostatic correction with respect to the volume. Particularly the potential alignment correction significantly improves the pressure description, leading to almost constant defect volumes. The remaining deviations or discontinuities might be related to structural distortions in certain charge states. For instance, in the case of a silicon vacancy, where the stability of Jahn-Teller modes depends on q . Thus, a properly defined pressure is a decisive factor for calculating the defect volumes through *ab-initio* calculations using periodic boundary conditions.

However, even converged pressure values, extracted from different plane-wave codes with the same pseudopotentials and the same convergence parameters, show another dependency on the charge state [311]. As pointed out by Bruneval *et al.* [311], this behavior is caused by different conventions used to calculate the average electrostatic potential. It does not represent the physical property of the defect. Precisely, the pressure and the stress tensor are mathematically ill-defined quantities in charged supercells. Hence, the relaxation volume is equally dependent on the calculation method

(convention of code, pseudopotentials, projector-augmented atomic data) if q is non-zero [324].

To circumvent this ambiguity, they elaborate appropriate absolute expressions for the *a posteriori* evaluation of the pressure. Combining the general description of the pressure in a charged system,

$$P(q) = -\frac{\partial E(X^q)}{\partial \Omega}, \quad (106)$$

where $E(X^q)$ is the energy of a charged system and Ω is again the cell volume, with Janak's theorem [325], the following properly defined, absolute pressures can be calculated as

$$\bar{P}(q) = P(0) + \frac{q}{\Omega} \bar{a}_v \quad \text{when } q > 0 \quad (107)$$

$$\bar{P}(q) = P(0) + \frac{q}{\Omega} \bar{a}_c \quad \text{when } q < 0. \quad (108)$$

$$(109)$$

Here, \bar{a}_v and \bar{a}_c are the absolute deformation potentials for the valence band maximum and the conduction band minimum, respectively. Instead, the pressure in a neutral simulation cell is well defined and independent of the convention. If the uncorrected pressure of a charged simulation is used as a reference, Equation 107 can be rewritten in the following form,

$$\bar{P}(q) = P(q) + \frac{q}{\Omega} (\bar{a}_i - a_i), \quad (110)$$

where a_i is the deformation potential of state i ,

$$a_i = \frac{\partial \epsilon_i}{\partial \ln \Omega}, \quad (111)$$

$\partial \ln \Omega = d\Omega/\Omega$, and ϵ_i is the Kohn-Sham orbital energy respectively. Using the corrected pressures calculated at the equilibrium volume of the host and assuming that the bulk modulus, B , is hardly affected by the defect, the relaxation volume can be calculated as follows [311, 324],

$$\Delta \Omega \approx \frac{P(q)\Omega}{B}. \quad (112)$$

The absolute deformation potential calculation usually requires much effort if strained lattice calculations are used instead of the model solid theory [326]. However, the latter method is assumed to be less accurate [311], such that additional calculations seem inevitable.

Only recently, Bruneval *et al.* [324], proposed an alternative procedure to calculate defect relaxation volumes without prior knowledge of the absolute deformation potential. Their approach relies on the formation of a charge-neutral group by including charge compensating defects, for instance, free holes or electrons, self-trapped holes, and charged vacancies.

3.10.2 Correction of long-range elastic field effects

Absolute pressures prove to be particularly important for the determination and correction of long-range elastic field effects evoked by periodic boundary conditions in the context of supercell techniques. Precisely, the magnitude of elastic displacements scale with the inverse squared distance from the defect site [320], which can be particularly severe in the case of finite-size systems. Thus, long-range interactions might crucially affect the formation energies of point defects such that they largely deviate from the dilute limit. In contrast to electrostatic correction methods, even neutral defect properties are adversely affected by spurious interaction terms, especially if large distortions result from the defect's incorporation. Such large atomic rearrangements are conceivable for defect clusters, elements with many electrons, or interstitials, where increasing supercells might not cure for strong elastic fields [311]. In the following, we will summarize the modeling approach to calculate the elastic interaction energy between periodic images in common *ab-initio* approaches. As in the electrostatic correction, elastic interactions are evaluated *a posteriori*. This post-process mainly restricts deviations from the dilute limit to small supercells, which has been attributed to the increasing modification of atomic forces by the periodic images during geometrical optimization procedures. If not stated otherwise, we will exclusively refer to References [319–321, 327].

Assume we want to calculate the energy of a supercell, $E[X^q]$, containing a defect X with a charge state q . We further apply zero-strain boundary conditions, meaning that although atomic positions are allowed to relax, the shape and the volume of the simulation cell remain fixed. Equally, zero-stress boundary conditions may be used, leading to the same quantitative result but usually constitute a badly preconditioned problem. For this reason, we will solely employ $\epsilon = 0$ conditions in our calculations. If we, for simplicity, investigate a charge-neutral defect, our calculated *ab-initio* energy consists of two terms, the energy of the isolated point defect, $E_\infty[X^0]$, and half of the interaction energy between the neighbors of the periodic defect array, E_{int} (the other half is attributed to the periodic image),

$$E[X^0, \epsilon = 0] = E_\infty[X^0] + \frac{1}{2}E_{\text{int}}. \quad (113)$$

Equation 113 is equally valid for charged defects with just one limitation: Before calculating E_{int} , the residual stress tensor of the defective cell has to be corrected from any electrostatic contribution. To define E_{int} a continuous linear elasticity theory ansatz has been chosen, where a point defect is represented by an equilibrated, finite distribution of point forces, $\{\mathbf{F}^q\}$ [328]. This implies that both the net force and the torque amounts to zero,

$$\sum_q \mathbf{F}^q = \mathbf{o}, \quad \sum_q \mathbf{F}^q \times \mathbf{a} = \mathbf{o}, \quad (114)$$

where $\{\mathbf{a}^q\}$ is the set of positions on which the forces act. If we concentrate solely on the first moment of the force distribution, which can be identified as the second-rank elastic dipole tensor, the interaction term due to periodic boundaries can be described as follows,

$$E_{\text{int}} = -P_{ij}\eta_{ij}, \quad (115)$$

where η_{ij} is the strain introduced by the periodic images of the defect and is defined as

$$\eta_{ij} = - \sum_{n,m,p} G_{ik,jl}(\mathbf{R}_{nmp}) P_{kl}. \quad (116)$$

The vector $\mathbf{R}_{nmp} = n\mathbf{a}_1 + m\mathbf{a}_2 + p\mathbf{a}_3$ points to the position of the periodic image, where \mathbf{a}_i are the lattice vectors and $n, m, \text{ and } p \in \{x \mid x \in \mathbb{Z}, x \neq 0\}$ (no self-interaction is included). $G_{ik,jl}$ specifies the second derivative of the anisotropic Green's function with respect to the Cartesian coordinates x_j and x_l . The latter can be obtained using a numerical scheme developed by Barnett [329]. The resulting conditionally convergent sum is then regularized by a method first proposed by Cai *et al.* [330]. The whole procedure has been implemented into the open-source tool ANETO [320], which has been used in this study and presents a quick and convenient post-processing step.

3.10.3 Elastic dipole tensor

Let us summarize the input data needed to treat elastic interactions: First, the elastic constants have to be determined for the host lattice. Once they are extracted from an *ab-initio* calculation, the residual stress tensor is the only additional quantity needed to apply Equation 115. In turn, the residual stress tensor is a natural by-product of a standard DFT calculation, making this procedure quite effortless. However, to ensure that the point defect solely causes residual stress after atomic relaxation and largely exclude numerical errors (incompleteness of wave-function-basis, finite convergence criterion), the residual stress of the bulk cell should be subtracted from the tensor of the defective cell. This quantity is further used to determine the elastic dipole tensor,

$$P_{ij} = -\Omega \langle \sigma_{ij} \rangle, \quad (117)$$

where $\langle \sigma_{ij} \rangle$ is the residual stress tensor, and Ω is, according to the conventional notation, the supercell volume. Since the torque is zero, the elastic dipole tensor has to be symmetric. Remember that Equation 117 is only valid for zero-strain calculations. Although there exist different methods to obtain P_{ij} (Kanzaki force or displacement field method), the residual stress approach appears to be the most accurate in the framework of *ab-initio* calculations. The elastic dipole tensor provides information on the long-range part of the strain introduced by the defect. It can itself be modified by the strain field introduced by periodic images. Since this strain decays like $1/r^3$ (r is the distance to the defect), the elastic dipole tensor converges with the inverse volume of the supercell. Even the interaction with external strain fields can be determined from this tensor such that elasticity theory can fully describe point defect interactions. This is particularly useful for time-dependent, mesoscale material simulations. In order to close the circle, we will emphasize the direct relationship between the elastic dipole tensor and the relaxation volume, $\Delta\Omega_r$,

$$\Delta\Omega_r = S_{ijkl} P_{kl}, \quad (118)$$

where S_{ijkl} denotes the elastic compliances. While the trace of P_{ij} characterizes the size interaction, the deviatoric part as well as differences in the main diagonal are representative for the shape interaction.

3.10.4 Absolute deformation potential

We already introduced absolute deformation potentials in the context of absolute pressures without explicitly discussing this property. In this section, we will concentrate on recent advances on how to calculate absolute deformation potentials using the supercell approach. Deformation potentials were first introduced by Bardeen and Shockley [331] in the context of electron-phonon interactions in non-polar crystals. In this study, the strain-induced shifts of valence and conduction bands act as a scattering source, limiting the mobility of charge carriers. They called these effective potentials, which can be generated by acoustic waves, deformation potentials. Essentially, they describe the variation of electron energies under varying strain conditions (volume deformation) [311, 332].

Although Equation 111 seems to be straightforward, problems occur if not relative energies, but absolute values, referenced to a “vacuum zero”, are needed. For an infinite solid, as mimicked by periodic boundary conditions, an absolute energy reference does not exist [333]. This problem is still the one we faced above and stems from the long-range nature of Coulomb interactions as well as the ambiguous choice of the zero electrostatic potential, such that the absolute deformation potentials differ by an arbitrary constant (the derivative of the reference energy with respect to strain) [332, 334–336]. The consequence of a missing reference is that the energy of a state i can not be compared for two separate calculations in two different strain states. Only if the electrostatic potential in differently strained regions can be related, a comparison becomes reasonable. Consequently, this problem is equivalent to the calculation of band offsets at semiconductor interfaces [333, 337]. However, in this specific case, a homojunction between fractions of the same material in different strain states has to be created. Usually, one side is uniaxially compressed, while the other side is uniaxially expanded by 1%. This setup leads to a pseudomorphic, ideal interface (in-plane lattice parameter remain unchanged) [326].

Even in the homojunction approach, a strain-independent reference level seems to be necessary. Impurity-level transition [338] or core level energies [336] appear promising. However, the latter emerged as a wrong choice since the strain dependence of core level deformation potentials is not negligible [336]. To circumvent this difficulty, the band offset of the core levels, $\Delta E_c^{(+/-)}$, in the superlattice is taken into account. For the sake of clarity, let us rewrite Equation 111 as [336]

$$a_{n,k}^{\alpha,\beta} = \frac{\partial E_{n,k}}{\partial \epsilon_{\alpha,\beta}} \approx \frac{\Delta E_{n,k}^{(+/-)}}{\Delta \epsilon}, \quad (119)$$

where $E_{n,k}$ describes the single-particle energy of the state (n, \mathbf{k}) , $\epsilon_{\alpha,\beta}$ denotes a component of the strain tensor, and $\Delta E_{n,k}^{(+/-)}$ is defined as

$$\Delta E_{n,k}^{(+/-)} = (E_{n,k}^+ - E_c^+) - (E_{n,k}^- - E_c^-) + \Delta E_c^{(+/-)}. \quad (120)$$

Note that $E_{n,k}^i - E_c^i$ is calculated in the 1% expanded and compressed structure without homojunction, since the valence band maximum and conduction band minimum states are not localized in finite-size superlattices [332, 339]. Furthermore, during the structural optimization of the superlattice, the atoms at the interface are fixed while

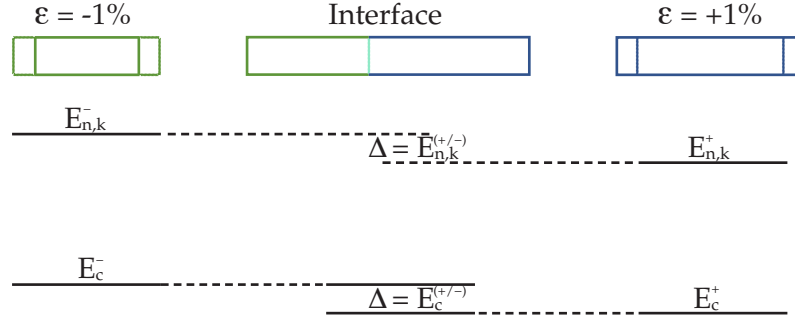


Figure 28: Schematic energy level diagram of the electronic states needed to calculate the absolute deformation potential. For a description of the symbols, the reader is referred to the main text. Adapted from Reference [336].

all other internal parameters are allowed to relax [339]. A schematic energy level diagram of the electronic states needed to calculate the absolute deformation potential is presented in Figure 28.

Since this method describes the absolute deformation potential for one direction (direction of the interface normal) only, several separate calculations have to be conducted. If a proper average over these directions is carried out, the resulting hydrostatic absolute deformation potential is a well-defined bulk property [339]. In this thesis, as proposed by Li *et al.* [339, 340], we calculate the absolute deformation potential for three different directions, namely [100], [110], and [111]. In order to obtain an angular averaged absolute deformation potential from these values, the results of the uniaxial calculations are first expanded in terms of lattice harmonics, K_ν . These lattice harmonics, in turn, are symmetry-adapted linear combinations of spherical harmonics,

$$\alpha_i^{\text{uniaxial}}(\mathbf{r}) = a + \sum_{\nu} c_{\nu} K_{\nu}(\mathbf{r}), \quad (121)$$

where the a and c_{ν} on the right hand side of Equation 121 are expansion coefficients, which can be obtained by a least square fitting procedure. For cubic symmetry and considering orthonormal relations of the lattice harmonics, we obtain a hydrostatic absolute deformation potential of

$$\bar{\alpha}_i = a = \frac{4\alpha_i^{110} + \alpha_i^{100}}{5} \pm \frac{|4\alpha_i^{110} - \alpha_i^{100} - 3\alpha_i^{111}|}{5}, \quad (122)$$

for $l_{\text{max}}=4$ and for $l_{\text{max}}=6$ Equation 121 leads to

$$\bar{\alpha}_i = a = \frac{10\alpha_i^{100} + 16\alpha_i^{110} + 9\alpha_i^{111}}{35}. \quad (123)$$

Absolute deformation potentials can also be obtained from the model solid theory as proposed by Van de Walle [326], which is, however, less accurate than the strained lattice approach, and the signs are often misleading [339].

3.11 NUGGED ELASTIC BAND METHOD

In the context of defects, we are often interested in the kinetic evolution of microstructures over time in the presence of temperature or other externally applied fields. The most effortless conceivable way to investigate local atomic-scale processes seems track particle trajectories using classical mechanics. However, often transitions of technical interest occur on time scales much larger than atomic vibrations such that even long term observations are not sufficient to describe the kinetics of so-called “rare events” [341]. A solution for this problem of direct dynamical simulations, at least with current computational technologies, is the harmonic approximation to transition state theory. This approach turned out to be particularly useful for describing diffusion processes and surface reactions [341].

Indeed, within the transition state theory, transition rates can be estimated by finding the energetically lowest saddle point located between an initial and a final configuration on a potential energy landscape. The path connecting those three crucial points, where the force is acting solely in the direction of the path, is called minimum energy path (MEP). The MEP can be understood as a submanifold on the potential energy surface, where the initial and the final structure represent the boundaries and the maximum describes the saddle point. Generally, more than one local extremum can be found, which indicates meta stable intermediate configurations along the path. However, only the energetically highest transition barrier determines the overall reaction rate [341]. In the following, I will shortly describe how the MEP can be found using nudged elastic band (NEB) calculations. We use this concept in Chapter 6, where we investigate migration barriers of an oxygen vacancy in the presence of different dopant types. For a more detailed discussion, the reader is referred to References [341–343]. If not stated otherwise, we will use the latter references in our description below.

To explain the NEB method, we have to disassemble the name “nudged elastic band”, starting from the end. At the start of a calculation, an “elastic band” is formed by generating a set of images between the initial and final configuration which are connected by a spring with a spring constant k . The set of images can be understood as intermediate structures, describing the diffusion process or another chemical reaction. A subsequent minimization of atomic forces to a prescribed accuracy threshold optimally leads to the MEP of interest.

The “nudging” is the core of the NEB technique and refers to the projection of the force vector onto a component tangential and a component perpendicular to the path. Although the total force is the sum of the spring force, \mathbf{F}_i^s and the “true” force, $\nabla E(\mathbf{R}_i)$, only the parallel component of the spring force, $\mathbf{F}_i^s \parallel$, and the perpendicular component of the “true” force, $\nabla E(\mathbf{R}_i) \perp$, is actually used in the optimization process. Thus, the total force is defined as

$$\mathbf{F}_i = \mathbf{F}_i^s \parallel - \nabla E(\mathbf{R}_i) \perp, \quad (124)$$

$$\nabla E(\mathbf{R}_i) \perp = \nabla E(\mathbf{R}_i) - \nabla E(\mathbf{R}_i) \mathbf{t}_i, \quad (125)$$

$$\mathbf{F}_i^s \parallel = k(|\mathbf{R}_{i+1} - \mathbf{R}_i| - |\mathbf{R}_i - \mathbf{R}_{i-1}|) \mathbf{t}_i, \quad (126)$$

where E denotes the energy and the parameter i identifies the image. For the determination of the tangent \mathbf{t}_i , only the neighboring image ($i + 1$ or $i - 1$) with higher energy than the one of replica i is used to prevent the formation of fluctuating kinks and slow convergence.

The separation of the force components are necessary for two reasons: First, the inclusion of $\nabla E(\mathbf{R}_i) \parallel$ would lead to a depletion of images near the saddle point configuration, where a good representation of the MEP is mandatory for an accurate estimate of the barrier height between two different configurations (“sliding-down” problem). Secondly, perpendicular spring forces would not allow for curved MEP (“corner-cutting” problem), while parallel spring forces are necessary to control the distance between the images (equidistant for uniform spring constants).

In the regular NEB method, typically no image is located at the maximum energy or in the immediate vicinity after relaxation such that the desired value needs to be extracted by an interpolation scheme. The solution to this problem is called climbing image NEB (CI-NEB), in which the force of the energetically highest image is modified to

$$F_{i,\max} = -\nabla E(\mathbf{R}_{i,\max}) + 2\nabla E(\mathbf{R}_{i,\max}) \parallel \quad (127)$$

$$= -\nabla E(\mathbf{R}_{i,\max}) + 2\langle \nabla E(\mathbf{R}_{i,\max}), \mathbf{t}_i \rangle \mathbf{t}_i. \quad (128)$$

This modification facilitates the “climbing” of one image to the saddle point of the potential energy surface, while simultaneously optimizing the energy perpendicular to the elastic band tangent.

3.12 NUCLEAR MAGNETIC RESONANCE SPECTROSCOPY

“Smarter Crystallography” is the name of a relatively new approach, which aims to combine several structural resolution techniques, for instance, X-ray diffraction and nuclear magnetic resonance spectroscopy (NMR) [4], to obtain a comprehensive structural model. Theoretical calculations, particularly in the context of *ab-initio* approaches, are just another piece of the puzzle to create powerful tools for structural analysis. In this thesis, particularly in Chapter 7, we will profit from these tools when we assign experimentally measured chemical shift data to distinct structural models and exclude (Al-V_O)[•] defect associated at high Al-doping concentrations. Naturally, the question arises whether there is an additional benefit of determining NMR parameters as chemical shifts, electric field gradients, dipolar coupling, or indirect J coupling constants by *ab-initio* calculations if the experimental data is already available. The answer is definitely yes, which becomes apparent if we look at the limitations and deficits of standard NMR experiments.

Although NMR is perfectly suited for the investigation of local atomic-scale structures (element- and site-specific), including chemical bonding analysis, the anisotropic nature of nuclear spin interactions complicates the extraction of structural information and decreases the resolution of the spectra by line broadening. This is especially severe if less common species with low sensitivity are studied. Continuous advancements have led to several techniques to circumvent these difficulties, including magnetic angle spinning (MAS), pulse sequence design, or multiple-quantum

(MQ) MAS measurements to remove second-order quadrupolar broadenings [344]. Defined structural models can be used to theoretically calculate these tensor properties, their orientation, and their anisotropic character.

Experimentally, precise control over the local chemical environment is not possible such that the interpretation of NMR data remains a challenging task. Theoretically, however, the effect of atomic substitutions, vacancies, changes in chemical bond length and angles, as well as chemical and structural disorders can be studied by separate models, and cause-effect-relations might be established.

First theoretical calculations in this field suffered from surface effects and non zero electric fields in discrete cluster approaches, limiting the significance of these values [344, 345]. A significant milestone was the pioneering paper by Pickard and Mauri [346] in 2001, in which they developed the gauge-including projector augmented wave (GIPAW method). In 2007 Yates, Pickard, and Mauri [347] extended this theory to non-norm-conserving pseudo-orbitals. The GIPAW approach allows to calculate magnetic shieldings in periodic systems and can be implemented in the wide range of plane wave codes available these days [348–351]. It is based on a reconstruction scheme first proposed by van de Walle and Blöchl [352], which allows regaining all relevant all-electron (AE) from pseudised (PS) wavefunctions by a transformation operator, T , close to the nucleus:

$$\psi_{\text{AE}}(\mathbf{r}) = T\psi_{\text{PS}}(\mathbf{r}). \quad (129)$$

However, within the GIPAW formalism, a field-dependent operator, T_B is used to avoid the gauge-origin problem. The most relevant quantity in this study is the chemical shift tensor, δ , relative to a reference material. Its interaction with a magnetic field determine the peak position in a NMR spectra. In theory, only the absolute magnetic shielding tensor, σ is obtained, which is related to the chemical shift tensor by [344, 348, 353]

$$\delta = \frac{\sigma_{\text{ref}} - \sigma}{1 - \sigma_{\text{ref}}}. \quad (130)$$

The shielding tensor connects an external magnetic field, B_{ext} , with the induced magnetic field, B_{ind} , which results from an orbital current as a response to B_{ext} :

$$\mathbf{B}_{\text{ind}}^{(1)} = -\sigma(\mathbf{r})\mathbf{B}_{\text{ext}}. \quad (131)$$

The current, in turn, is computed by employing perturbation theory (electronic changes are small), which is already indicated by the (1) at B_{ind} . The magnetic shielding is a fingerprint of different chemical environments, which resonate at frequencies different than the Larmor frequency of the bar nucleus [348]. A detailed discussion of the underlying method and equations exceeds the scope of this thesis such that we will concentrate on a few notation conventions. A precise mathematical deviation of the GIPAW approach and the practical implementation can be found in References [345, 346, 348, 351]. After diagonalisation of σ , the isotropic magnetic shielding tensor can be calculated, which is given by [344]

$$\sigma_{\text{iso}} = \frac{1}{3}\text{Tr}[\sigma(\mathbf{r})]. \quad (132)$$

Equation 132 is equally valid for the chemical shift tensor. In analogy to the experimental procedure, where the measured chemical shift is referenced with respect to a well-known system, a similar practice has become established in the literature for computed values [344]. Generally, we compare experimental results of chemical shift values (δ_{iso}) with the calculated isotropic chemical shielding (σ_{iso}). Such a procedure might compensate for errors during the calculation, which include physical (exchange-correlation functional, frozen core approximation, thermal motion) and computational (finite basis set, \mathbf{k} -point density) approximations [348]. In order to reduce inaccuracies, several compounds have to be analyzed such that the calculated chemical shift can be expressed as [344, 351]

$$\delta_{\text{iso}}^{\text{calc}} = \frac{c - \sigma_{\text{iso}}^{\text{calc}}}{m}, \quad (133)$$

where m is the slope and c is the intercept of the linear regression curve.

The most important input for calculating NMR parameters is a valid structural model. This is reasonable since NMR measurements are highly sensitive to the local environment, including already small geometrical changes. Already temperature effects inevitably lead to small deviations between NMR chemical shift measurements at room temperature and calculations, usually performed at zero Kelvin. These deviations include the magnitude of the shift and the shielding anisotropies [348]. Particularly affected are motions at short timescales, for instance, vibrations and conformational changes. An averaging of NMR parameters over several molecular dynamics snapshot would be an appropriate solution to this problem of fast dynamics [344]. A similar approach may also prove helpful for the case of topological and chemical disorders in NBT. In both cases, a subset of structural candidates can be investigated and subsequently weighted by their abundance.

The importance of NMR studies can be shown by a recent study on NBT-xBT relaxor ferroelectrics using ^{23}Na NMR [200]. This study strongly suggests that the behavior of relaxors relies on the coexistence of a cubic non-polar matrix phase as well as of polar nano regions, and therefore excludes the single-phase random field model. We will conclude this part with the words of Bonhomme *et al.* [348]: First principles calculations “serve as a bridge” and “unlock the potential of NMR spectroscopy for understanding solid-state structure”.

3.13 VISUALIZATION OF CHEMICAL BONDING IN SOLIDS

Why are some configurations more stable than others? Are there energetically favored structural motifs in amorphous structures? How do defects manipulate chemical bonds? What are appropriate descriptors to characterize different bonding environments? Most importantly, how can we extract local bonding information from plane wave *ab-initio* calculations? The following section will equip us with all necessary concepts to understand covalent bonding analyses, which have been extensively used in Chapter 10. We will focus mainly on the concept of crystal orbital hamiltonian populations (COHPs) [354, 355], which classify chemical bonds in three categories, namely bonding, antibonding, and non-bonding. In this framework, the band structure energy is partitioned into a sum of orbital pair contributions [354]. Instead,

the crystal orbital overlap population (COOP), a related concept, is based on the distribution of electrons by a Mulliken population [356] analysis. However, the latter approach shows crucial dependencies on the local basis set and equally complicates the comparison between bonding interactions of differently extended orbitals (e.g., d and p orbitals), such that an energy-resolved description is assumed to be of superior significance [354].

The open-source computer program LOBSTER (Local Orbital Basis Suite Towards Electronic-Structure Reconstructions) [357, 358] is an excellent tool to analyze the effect of extrinsic and intrinsic defects in NBT and NBT-based solid solutions. This post-processing code allows us to evaluate all mentioned characteristic descriptors and exploit periodic plane-wave density functional datasets [359]. It thus unites the advantages of the supercell approach with a highly informative local analysis of bonding characters. An essential condition to make periodic DFT information accessible for bonding analysis is a proper scheme to project PAW functions onto a local basis set (tight-binding approach [355]). These “auxiliary” minimal basis sets are generally arbitrary [355] but have to reflect the nodal behavior in the core region accurately.

An important criterion to evaluate the projection’s quality is the absolute charge spilling, which describes the amount of lost electron density during projection. If the charge spilling exceeds 1 %, the basis is incomplete (there must be at least as many bands as basis functions), or the type of basis functions is not appropriate. The validity of the result should be questioned in these cases. In the following, we will shortly describe the theory behind the COHP method. For this purpose I will exclusively refer to References [355, 360]. The result of a self-consistent electronic structure calculation are band functions ψ_j , expanded in plane waves,

$$\psi_j(\mathbf{k}, \mathbf{r}) = \sum_{\mathbf{G}} C_{j\mathbf{k}}(\mathbf{G}) \exp\{i(\mathbf{k} + \mathbf{G})\mathbf{r}\}. \quad (134)$$

An equally valid description of the electronic structure is given by the linear combination of atomic orbitals, $\phi_{\mu}(\mathbf{r})$, which are orthonormal, atom-centered one-electron functions,

$$\Phi_j(\mathbf{k}, \mathbf{r}) = \sum_{\mu} c_{j\mu}(\mathbf{k}) \phi_{\mu}(\mathbf{r}). \quad (135)$$

Within the latter formalism a density matrix $P_{\mu\nu}$ can be directly calculated from the expansion coefficients, $c_{j\mu}(\mathbf{k})$. Since only data from a pseudopotential ansatz is available, we first have to calculate the transfer matrix (overlap matrix) between the plane-wave functions and the local orbitals,

$$T_{j\mu}(\mathbf{k}) = \langle \psi_j(\mathbf{k}) | \phi_{\mu} \rangle, \quad (136)$$

which can be further used to construct a projected density matrix,

$$P_{\mu\nu}^{\text{proj}}(\mathbf{k}) = T_{j\mu}^*(\mathbf{k}) T_{j\nu}(\mathbf{k}). \quad (137)$$

The COHP is the product of the Hamiltonian matrix element in the basis of the local orbitals ($H_{\mu\nu}^{\text{proj}}(\mathbf{k})$), corresponding to the interaction of the μ th and ν th orbital, and the density matrix. If $H_{\mu\nu}^{\text{proj}}(\mathbf{k})$ can be written as

$$H_{\mu\nu}^{\text{proj}}(\mathbf{k}) = \sum_j \epsilon_j(\mathbf{k}) T_{j\mu}^*(\mathbf{k}) T_{j\nu}(\mathbf{k}), \quad (138)$$

such that the final expression of the projected COHP (pCOHP) can be formulated in the following form:

$$\text{pCOHP}_{\mu\nu}(E, \mathbf{k}) = \sum_j \Re[\rho_{\mu\nu j}^{\text{proj}}(\mathbf{k}) H_{\mu\nu}^{\text{proj}}(\mathbf{k})] \times \delta(\epsilon_j(\mathbf{k}) - E). \quad (139)$$

Note that the δ -function rewrites the density matrix into a density of states matrix. To obtain the pCOHP in real space, a \mathbf{k} -space integration over all orbitals μ and ν , centered on the two bonding atoms, is performed by using the tetrahedron [361] method.

Practically, we plot the negative pCOHP with respect to the energy such that bonding contributions (negative COHPs) appear on the right hand side of the energy axis, and a direct comparison to COOP values is feasible. Besides the standard pCOHP analysis, integration of the spectrum up to the Fermi energy provides a suitable measure for bonding strengths,

$$I_{\text{pCOHP}}(\epsilon_F) = \int^{\epsilon_F} \text{pCOHP}(E) dE. \quad (140)$$

The bond-weighted distribution function (BWDF) is another helpful parameter, which can be used to define a bond-length cutoff. Below the cutoff the BWDF is positive, symbolizing attractive interaction, while repulsive interactions are characterized by negative BWDF values. At large distances this functions approaches zero, indicating the short range interaction based on orbital overlaps. The BWDF is expressed as follows [362],

$$\text{BWDF} = \sum_{B>A} [\delta(r - |\mathbf{r}_{AB}|) \times B_{AB}], \quad (141)$$

where B_{AB} is the bond population of atom A and B, which is defined as the integrated, projected COOP (pCOOP),

$$B_{AB} = \int_{-\infty}^{\epsilon_F} \text{pCOOP}_{AB}(E) dE. \quad (142)$$

3.14 CONCLUSION

In conclusion, all presented tools allow evaluating material properties inaccessible to experiments and conducting virtual experiments with precise control of environmental or structural parameters. We learned that there are four significant approximations to calculate quantum-mechanical total energies. These are the density functional theory, the pseudopotential theory, the supercell approximation for aperiodic configurations, and iterative diagonalisation approaches, which facilitate the minimization of the total-energy functional [272]. Furthermore, we do not necessarily have to solve the

many-body Schrödinger equation to obtain the ground state energy and the ground state density of the physical system. By virtue of the adiabatic approximation and the Kohn-Sham formalism, we demonstrated that a mapping between the interacting and the auxiliary, one-body Kohn-Sham system is sufficient to determine these observables. However, the major disadvantage is the lack of transferability between the Kohn-Sham orbitals and the particle states of the interacting system. We emphasize that the computed eigenvectors do not have a physical meaning in general but systematically reduce the computational effort and expense. We further explained that Hubbard U corrections and Hybrid potentials excel over standard LDA or GGA calculations in many cases. These calculations can reach a localization of d-electrons, and band gaps can adjust to their experimental limit. However, these methods are parameterized, and approximations about the mixing as well as screening parameter or the U-corrections are used. The reliability and reproducibility of these advanced approaches have to be precisely compared to experimental results as well. The development of DFPT allows access to several functional properties, which can be obtained from first- and second-order derivatives of the total energy. And last but not least, several electrostatic and elastic corrections have to be applied to the total energy to reduce artificial periodic image interaction in defective and (possibly) charged supercells.

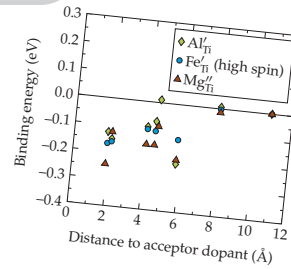
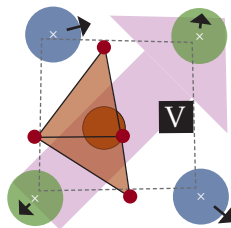
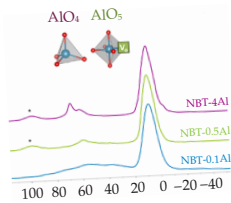
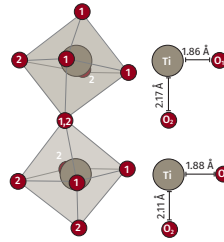
Part II

RESULTS



CONDUCTIVITY & THE EFFECT OF ACCEPTOR DOPANTS

“ The second part of this thesis deals with the ionic conductivity of sodium bismuth titanate. After evaluating some essential functional properties of undoped sodium bismuth titanate, we will particularly focus onto the formation of defect associates, the effect of A-site ordering, and the delicate balance between covalent and Coulomb interactions. ”



The results of the following chapter were first reported in Reference [363], which was written in close collaboration with the nonmetallic-inorganic materials division of the Technical University in Darmstadt. The experimental results were obtained by Dr. Sebastian Steiner and are used with his permission.

After reviewing recent experimental findings, identifying the critical research questions, and describing material modeling techniques in the field of lead-free ionic conductors, it is time to answer these questions in a “top-to-bottom” approach. We will start by developing a macroscopic, analytical model, which neglects locally varying chemical environments. Let us recapitulate the most important facts to get started as quickly and efficiently as possible.

Figure 29 has already been presented in the introductory chapter and shows the ionic conductivity schematically. However, in this chapter, we will neglect any formation of intrinsic defects at high temperatures. The transition between the low and the medium- to high-temperature segment is located at approximately 300 °C and is visible as a kink in the Arrhenius plot. In SrTiO₃, similar observations have been attributed to a temperature and concentration dependent activation energy for a vacancy-mediated migration process. In principle, it is assumed that the effective concentration of oxygen vacancies is reduced by a temporary formation of defect associates (trapping at the defect site) at low temperatures. In contrast, at high temperatures, these vacancies become mobile and contribute to the current with a reduced activation barrier. A close structural relationship within the perovskite family suggests that a similar phenomenon is responsible for the kink in pure and acceptor doped NBT samples. *If this is true, are there other “NBT-specific” possibilities, which might explain the distinct kink in the Arrhenius plots?*

Yang *et al.* [153] were able to reproduce measured conductivities of A-site strontium-doped non-stoichiometric NBT by extrapolating high and low-temperature conductivities to the temperature regime of coexisting rhombohedral and tetragonal phase and inserted these values into a Maxwell model to calculate an effective conductivity of this “composite material”. Due to the excellent agreement of the theoretical and experimental data, they concluded that a phase coexistence might also be a plausible explanation for a change in the curvature. However, they could not explain the very pronounced concentration dependency of the ionic conductivity at doping concentrations between 0% and 2% and could not completely exclude a simple association-dissociation reaction.

To gain a complete understanding of the defect chemistry, we will address four critical questions in the following: i) How does the dopant concentration, ii) the phase transition, and iii) the formation of a binary defect complex between the vacancy and the dopant affect the ionic conductivity? And, most importantly, iv) is the effect of acceptor dopants type-specific or is it possible to formulate general design rules? For

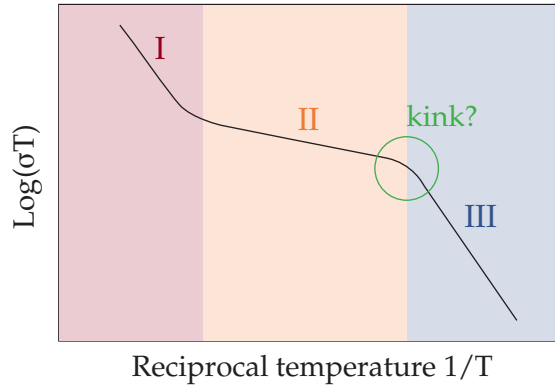


Figure 29: Schematic illustration of the ionic conductivity. A pronounced kink at the transition between stage III and II has been discovered in NBT [1]. Adapted from Reference [152].

this purpose, we study the conductivity in Mg- and Fe-doped NBT. Specifically, we investigate samples with 0.1 mol% up to 1.5 mol% Mg-dopant concentration on the B-site by employing impedance spectroscopy. Additionally, we develop an analytical model to extract all relevant macroscopic energetic contributions to explain the origin of the temperature-dependent change in the activation energies.

Similar to the idea of Yang *et al.* [153], the model includes a structural phase transition from the rhombohedral to the tetragonal symmetry. Experimental methods as well as results from X-ray diffraction, scanning electron microscopy, and Nyquist-plots will not be covered in this chapter and are fully presented in the original publication [363], in Reference [159], as well as in Chapter 2.

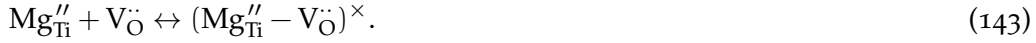
To complement the study, we will review the association energy by replacing Mg with Fe-dopants. Fe has a different relative charge compared to Mg and is suitable to comment on the influence of the dopant's nature. Finally, various vacancy-dopant configurations are studied to shed light on the concentration-dependent interaction between oxygen vacancies and dopants, qualitatively.

4.1 COMPUTATIONAL METHODS

We applied the projector augmented wave method [364, 365] in conjunction with the local density approximation (LDA) [247] to calculate vacancy-dopant association energies. A single \mathbf{k} -point and a plane wave energy cut-off of 600 eV were used for all relaxations. We chose a valence electron configuration as introduced in the main method section and a supercell with a total of 319 atoms. In the following, we investigated three different defect arrangements with two Mg dopants and one oxygen vacancy to mimic three different Mg concentrations. We varied the vacancy position relative to the closest Mg-dopant in each set while keeping the distance between the two dopants fixed. The sets themselves differ by an increasing Mg-Mg-distance, which ranges from the first nearest neighbor shell to the third nearest neighbor site, mimicking a change in the Mg concentration. Note that the $(2\text{Mg}_{\text{Ti}}'' - \text{V}_{\text{O}}'')$ complex is twofold negatively charged, implying that two additional electrons were added to the simulation cell to achieve the correct ionic charges.

4.2 AN ANALYTICAL MODEL

In the following, we derive a model to reproduce measured conductivities over a temperature range from 150 °C to 500 °C for differently Mg-doped samples. As mentioned in Section 2.6, introducing Mg-ions on the B-cation sublattice (which are regularly occupied by Ti) requires a simultaneous generation of positively charged oxygen vacancies to keep the entire system charge neutral. The formation of defect associates between the Mg-dopant and the oxygen vacancy leads to a reduced effective concentration of mobile charge carriers [151] such that the complex formation reaction reads as follows:



For this reason, we divide the total vacancy concentration into fractions of trapped and free species, where only free vacancies contribute to the total charge flow. Both free (f) and trapping (tr) Mg-dopants are considered to be immobile. The charge flow j_i of the species i is given by

$$j_{\text{Mg,tr}} = j_{\text{Mg,f}} = j_{\text{V}_{\text{O},\text{tr}}} = 0. \quad (144)$$

Thus, defect complexes act as internal sinks, decreasing the concentration of free oxygen vacancies. Generally, the amount of free vacancies is determined by the dissociation and association rates of the Mg-vacancy-complex. This means that $[\text{V}_{\text{O}}^{\bullet\bullet}]_f$ is temperature dependent, while the total concentration of vacancies, $[\text{V}_{\text{O}}^{\bullet\bullet}]_{\text{tot}}$, remains constant and constitute a conservative ensemble [150, 151].

In this model, we exclude other internal defect reactions, such as surface reactions, reduction of oxygen vacancies, unintentional Bi loss (we used a Bi-excess starting composition), as well as an electronic contribution by the formation of electron-hole pairs. Thus, for the defect concentrations, the following constraints apply:

$$[\text{Mg}_{\text{Ti}}'']_f = [\text{V}_{\text{O}}^{\bullet\bullet}]_f \quad (145a)$$

$$[\text{Mg}_{\text{Ti}}'']_{\text{tr}} = [\text{V}_{\text{O}}^{\bullet\bullet}]_{\text{tr}} \quad (145b)$$

$$[\text{V}_{\text{O}}^{\bullet\bullet}]_{\text{tot}} = [\text{Mg}_{\text{Ti}}'']_{\text{tot}} = [\text{Mg}_{\text{Ti}}'']_f + [(\text{Mg}_{\text{Ti}}'' - \text{V}_{\text{O}}^{\bullet\bullet})^{\times}] = C. \quad (145c)$$

We can calculate the free vacancy concentration from the equilibrium constant of the association reaction, K_{asso} , which is given by [140, 366],

$$K_{\text{asso}} = \frac{[(\text{Mg}_{\text{Ti}}'' - \text{V}_{\text{O}}^{\bullet\bullet})^{\times}]}{[\text{Mg}_{\text{Ti}}'']_f [\text{V}_{\text{O}}^{\bullet\bullet}]_f} = \frac{C - [\text{V}_{\text{O}}^{\bullet\bullet}]_f}{([\text{V}_{\text{O}}^{\bullet\bullet}]_f)^2} \quad (146a)$$

$$= \exp \left[\frac{-\Delta H_{\text{asso}}}{k_{\text{B}} T} + \frac{\Delta S_{\text{asso}}}{k_{\text{B}}} \right], \quad (146b)$$

where C is the constant dopant concentration, ΔH_{asso} is the association energy, and ΔS_{asso} represents the configuration entropy, taking into account the six possible orientations of the defect complex. The vacancy concentration is given by a quadratic equation, derived from Equation 146b, in which the association enthalpy is the relevant parameter. Using the diffusion coefficient, $D_{\text{V}_{\text{O},f}}^{\bullet\bullet}(T)$, for vacancy migration and

the Nernst-Einstein relation [142, 367] (Equation 147), we obtain a complete expression for the conductivity:

$$\sigma = \frac{D_{V_{O,f}} q^2 Z^2 [V_{O,f}]}{RT}, \quad (147)$$

with

$$D_{V_{O,f}}(T) = \frac{1}{6} a^2 Z \nu_0 \exp\left(\frac{\Delta S_{\text{mig}}}{k_B}\right) \exp\left(\frac{-\Delta H_{\text{mig}}}{k_B T}\right). \quad (148)$$

Here, the coordination number is $Z = 8$ and corresponds to the number of nearest oxygen neighbors. The attempt frequency ν_0 was assumed to be 1×10^{12} Hz [145], which is in the order of the Debye frequency. The hopping distance a amounts on average to 2.76 Å. ΔS_{mig} and ΔH_{mig} are the migration entropy and enthalpy respectively, q denotes the charge of the vacancies, and F the Faraday constant.

If we neglect ΔS_{mig} and take the remaining parameters ΔH_{asso} , ΔH_{mig} , and ΔS_{asso} as fitting numbers, we are not able to obtain a reasonable agreement between the experimental data and the model. From the orange curve in Figure 30, it is apparent that using a set of constant, temperature-independent parameters only leads to a hardly visible kink. Therefore, a model which is solely based on the dissociation of defect pairs does not provide a sufficient explanation for the ionic conductivity in NBT.

4.2.1 Phase dependency

Up to this point, we have ignored the phase transition from a rhombohedral to a tetragonal symmetry. Recent results from *ab initio* nudged elastic band calculations by Meyer and Albe [156] showed that the mobility of oxygen vacancies is not only path, but also phase-dependent. This observation could be a possible reason for the missing coincidence with experimental data when using the analytical model's constant kinetic parameters. Therefore, from now on, we will assume a region of phase coexistence [57] and use a smooth step-function, comparable to the Fermi-function, to tune the impact of the specific phase-dependent kinetic parameters. Although the model has been reduced to the macroscopic scale in this way, temperature-dependent microscopic structural modifications can be included by a broadening of the Fermi-like function. The steepness of the Fermi-like distribution, which is normally defined by the temperature, has been chosen such that the region of coexistence corresponds to experimentally measured phase fractions determined by Reference [57]. Using the Fermi-function instead of a sharp step function leads to

$$\Delta H_{\text{asso}} = \Delta H_t + (\Delta H_r - \Delta H_t) \cdot \left(1 - f\left(\frac{1}{T}\right)\right), \quad (149)$$

where ΔH_r and ΔH_t are the activation energies for the association in the rhombohedral phase and tetragonal phase, and f represents the Fermi-like function. In short, we aim at an effective expression for H_{asso} , which is determined by each component of the two-phase region. In fact, this resembles a G-closure problem known for disordered or heterogeneous media, where the G-closure is a set of effective tensor properties describing an anisotropic composite material. Mathematically, this problem is treated by homogenization theory, where effective equations are derived for

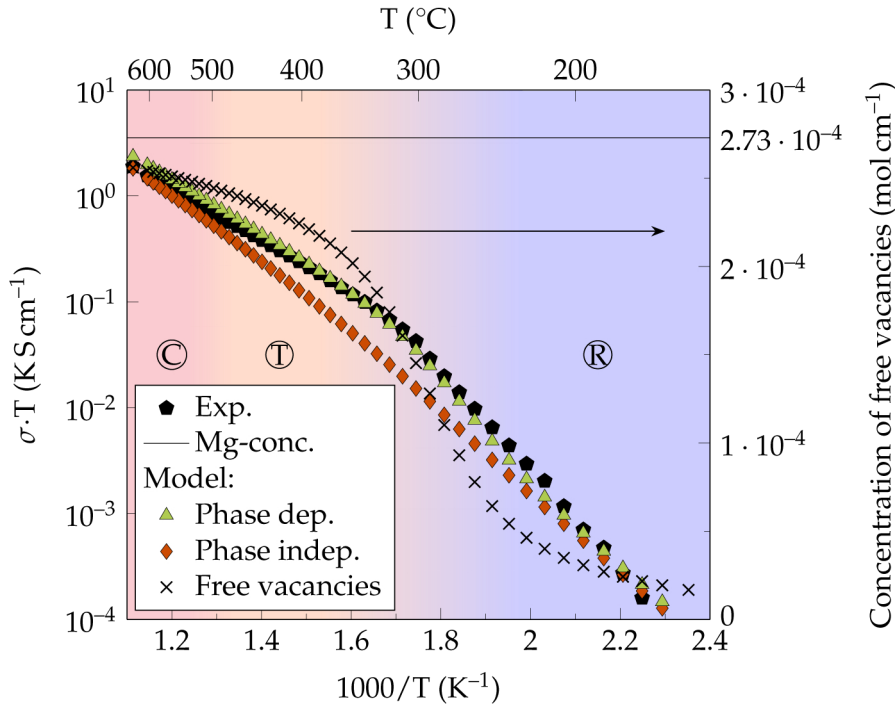


Figure 30: Conductivity model for 1% Mg-dopant concentration with phase dependent (light green, $\Delta H_{\text{asso,t}}=0.1$ eV, $\Delta H_{\text{asso,r}}=0.45$ eV) and phase independent (orange, $\Delta H_{\text{asso,t}}=\Delta H_{\text{asso,r}}=0.45$ eV) association energy and free vacancy concentration as a function of the temperature. The horizontal line represents the constant Mg-dopant concentration. Again, the background colors and the capital letters indicate the specific phase within the observed temperature range.

complex systems with rapidly varying and fine microstructures [368–370]. However, since this model is at significant risk of becoming far too complex, we will follow the minor resistance route and continue with the Fermi-like approach.

It is tempting to assume that an arithmetic or a harmonic mean, also known as the Series and Parallel model for multiphase materials [371], are suitable approaches for defining an effective conductivity within the range of phase coexistence. However, in the present case, these procedures do not lead to a satisfying description of the experimental results, which is probably caused by a statistical dispersion of the tetragonal structure within a rhombohedral matrix at the beginning of the phase transformation [372] (does not resemble a layered microstructure). In total, we have four independent parameters, namely $\Delta H_{\text{mig,t}}$, $\Delta H_{\text{mig,r}}$, $\Delta H_{\text{asso,t}}$, and $\Delta H_{\text{asso,r}}$, where t and r stand for the tetragonal and the rhombohedral phase respectively. In accordance to the results from density functional theory calculations by Meyer and Albe [156], migration energies are chosen identically for both phases, namely $\Delta H_{\text{mig,t}}=0.5$ eV and $\Delta H_{\text{mig,r}}=0.5$ eV. Since the DFT results suggest that association energies are much more sensitive to the type of phase being present, only $\Delta H_{\text{asso,t}}$ and $\Delta H_{\text{asso,r}}$ are considered as temperature (phase) dependent quantities. The best fit to the experimental data is obtained, if we choose $\Delta H_{\text{asso,t}}=0.1$ eV and a $\Delta H_{\text{asso,r}}=0.45$ eV, which is in the order of the DFT data. Figure 30 shows measured conductivities for 1% Mg concentration (black pentagons) in comparison to the model with phase dependent association energies (light green curve). The letters with the corresponding colored background indicate the thermo-

dynamically stable phase present in the specific temperature region. R represents the rhombohedral, T the tetragonal, and C denotes a cubic symmetry. In turn, the color gradient between two distinct arrangements displays a temperature region, where two phases coexist.

The model data is consistent with the experimental values. This implies that the pronounced kink observed in the conductivity curves is due to temperature-dependent (and therefore phase-dependent) association energies that vary in the temperature range of phase coexistence. With our choice of parameters, the agreement between the experimental data and the model is surprisingly good, considering the fact that octahedral rotations at vacancy sites lead to various structural reconstructions in different chemical environments [327]. However, the averaging over local configurations is a possible explanation for remaining deviations from the actual values. It is also instructive to inspect the number of free vacancies as predicted by the model. Figure 30 depicts the concentration of free vacancies at 1 % dopant concentration over the observed temperature range. Even at elevated temperatures, the amount of mobile charge carriers does not reach the dopant concentration. Thus, a certain amount of vacancies is still trapped, and a state of complete dissociation does not occur at any observed temperature.

A crucial test for the model is its capability to reproduce the conductivity of samples with varying Mg-contents. For this purpose, we will focus on Mg-concentrations of 0.5 % and 1.5 % respectively. We find that the association energies increase with decreasing dopant concentration. For 1.5 % Mg we obtain a best fit with $\Delta H_{\text{asso,t}} \approx 0$ eV and $\Delta H_{\text{asso,r}} = 0.39$ eV, while values of 0.51 eV and 0.55 eV describe the case of 0.5 % Mg-concentration. Note that the difference between energies of the rhombohedral and the tetragonal phase becomes smaller with decreasing concentration. Furthermore, these values sensitively depend on the chosen migration energies. Nevertheless, the general trend of increasing association energies with decreasing concentration remains true. The concentration-dependent association energies are possibly resulting from electrostatic and mechanical interactions caused by the size difference between the Mg-ions and the Ti-ions.

Figure 31 shows the fits as well as the measured conductivities for all three concentrations. For the case of 1.5 % and 0.5 % Mg-concentration the model predictions deviate from the experimental data in the high-temperature regimes, indicating that the phase transition alone does not entirely explain the concentration and temperature-dependent conductivity. Note that we excluded electronic contributions, which could still influence the overall conductivity at 0.5 % Mg to a certain degree. The same is valid for the high-temperature region of the 1.5 % Mg sample. In fact, it was shown by electromotive force measurements that the electronic contribution increases above 500 °C [1]. Although the migration energies should also be affected by higher dopant concentrations, the data analysis implies that the significant contribution stems from the concentration-dependent association. To prove this assumption, we calculated binding energies between a magnesium ion and an oxygen vacancy in the presence of a second magnesium ion by using density functional theory. Figure 32 shows the results of the *ab initio* calculation, where we simulate various defect Mg–vacancy arrangements with different Mg–Mg distances. The latter varies from the first nearest

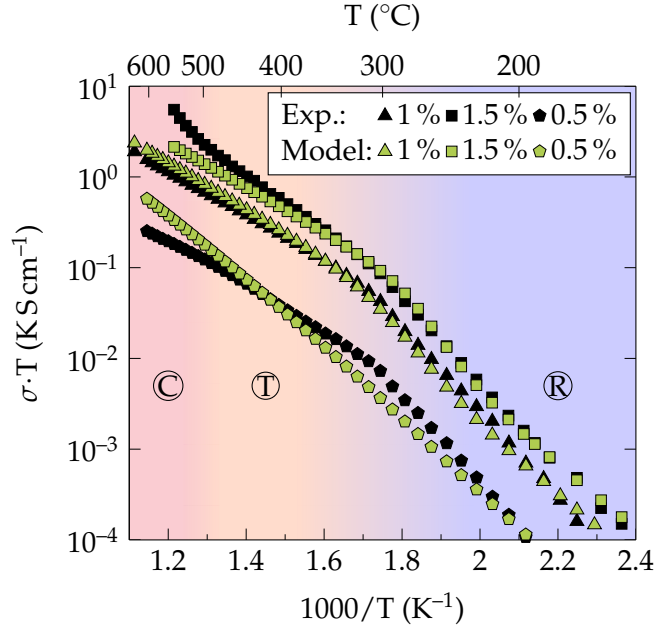


Figure 31: Phase dependent conductivity model with $\Delta H_{\text{asso,t}}=0$ eV and $\Delta H_{\text{asso,r}}=0.39$ eV for 1.5%, $\Delta H_{\text{asso,t}}=0.1$ eV and $\Delta H_{\text{asso,r}}=0.45$ eV for 1%, and $\Delta H_{\text{asso,t}}=0.51$ eV and $\Delta H_{\text{asso,r}}=0.55$ eV for 0.5% Mg-concentration. Background colors again specify the phases present at certain temperatures.

neighbor site up to the third neighbor shell. It can be seen that with decreasing distance between the Mg-ions, the association enthalpy becomes more and more short-ranged as assumed from the model fit.

We further experimentally replaced magnesium with iron, which should naturally change the stability of the complex. If we use the same model for the Fe-doped as for the Mg-doped NBT, we obtain $\Delta H_{\text{asso,t}}=0.5$ eV and $\Delta H_{\text{asso,r}}=0.57$ eV for the sample with 4%. We expect that most vacancies are trapped in defect complexes at lower concentrations, making the electrons the major charge carriers.

Both investigations emphasize the strong influence of the association enthalpy. A relationship between defect concentrations and effective diffusion properties was already indicated in literature [366, 373], where a defect lattice with a lattice constant of the mean defect-defect distance was proposed. However, the impact of this dependency is massive, and further investigations need to be done to understand the origin of this observation completely. Additionally, our simulations reveal that the association decreases with a decreasing distance between the dopants, which resembles a state far from the dilute limit. We expect that this reduction is caused by an interplay of mechanical and electrostatic interactions. Although we neglect electronic contributions to the conductivity, we cannot exclude a reduction reaction of the oxygen vacancy at higher temperatures completely. We will tackle this problem in Chapter 8 in detail.

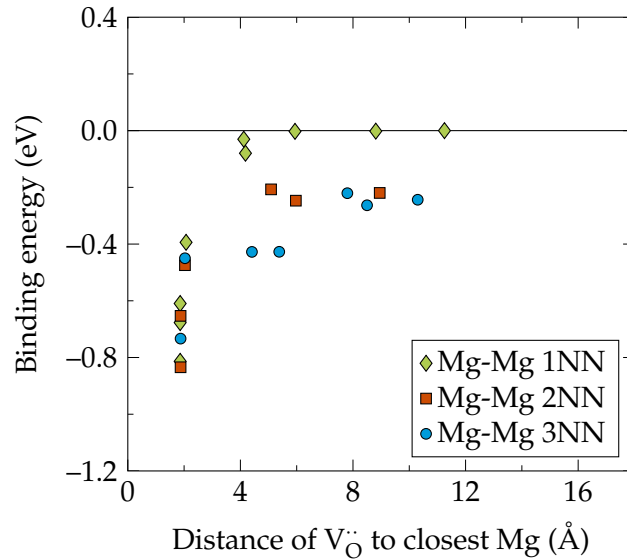


Figure 32: Binding energies for a defect associate in the presence of a second Mg-ion for different Mg-Mg distances, where 1NN means the first, 2NN represents the second and 3NN the third nearest neighbor shell.

4.3 THINGS TO REMEMBER

We have investigated the impact of B-site acceptor doping on the conduction behavior of NBT by using various Mg doping levels ranging from 0.1 mol % up to 1.5 mol %. We learned that NBT could either be used as an insulator, semiconducting material, or ionic conductor, depending on the defect concentration. A substantial vertical jump of the conductivity has been observed for a concentration change from 0.2 % to 0.5 %, where the conduction mechanism changes from being dominantly electronic to primarily ionic. Furthermore, Mg's replacement with Fe-ions verified that the critical concentration at which this jump occurs also depends on the dopant type.

An analytical defect chemistry model is used to reproduce the experimentally measured conductivities. By taking the above mentioned conditions into account, we assumed that the association energies are temperature dependent due to the coexistence of rhombohedral to tetragonal phases and that they depend on the dopant concentration, a good fit for experimental data is achieved. These results could also be helpful to gain a better understanding of the defect chemistry in more complex NBT-based solid solutions [157].

Since the oxygen vacancy mobility crucially depends on the dopant concentration, the latter must be carefully controlled during the processing. In conclusion, we find clear evidence that the temperature dependence of the ionic conductivity in doped NBT is the result of a delicate interplay of defect complex formation, phase transitions, and phase coexistence. However, the migration and association energies stem from a simple fitting procedure. *Is it possible to validate these quantities with more advanced techniques? Let us open a new chapter!*

Most of the results presented in this work rely on fundamental material properties, such as the elastic and dielectric constant. For instance, we have to use theoretically obtained material constants to consistently remove supercell artifacts of electrostatic or elastic origin [24, 316, 317]. In this chapter, we calculate these properties, which allow us to

- i) obtain necessary input parameters for subsequent calculations,
- ii) investigate the influence of different A-site orders and point groups on the electronic structure and mechanical constants,
- iii) benchmark the GGA exchange-correlation potential and DFT/DFPT in general.

Besides these elementary properties, we provide an overview on phonon dispersion curves, Born effective charges, interatomic force constants, and polarizations in polymorphic NBT (introduced in Section 2.5). In a few cases, we also perform a distortion mode analysis, which applies the formalism presented in Section 2.4.

5.1 COMPUTATIONAL METHODS

In the present chapter we use the codes VASP [209, 210] (finite difference) as well as density functional perturbation theory as implemented in the ABINIT package [217–220], which provides additional post-processing utilities. In the VASP set up, we chose a 40 atom cell, an energy cut-off of 800 eV, and a $4 \times 4 \times 4$ \mathbf{k} -point mesh for the calculation of phonon modes, the elastic constants, and the dielectric constants. In order to calculate the electronic band structure, we choose an $8 \times 8 \times 8$ \mathbf{k} -point mesh and the rhombohedral unit cell. In the case of the COHP-analysis, we use an energy cut-off of 600 eV and a Γ -point calculation. We use norm-conserving PBEsol pseudopotentials for our calculation with ABINIT and expand the plane waves up to an energy cut-off of 50 Ha. For more detailed information on the potential, we refer to Section 3.1.

We calculate the phonon band structure on a $4 \times 4 \times 2$ \mathbf{q} -point mesh, after optimizing the $P4/mmm$ 001-ordered structure with ten atoms on an $8 \times 8 \times 4$ \mathbf{k} -point grid. In contrast, we apply a $2 \times 2 \times 2$ mesh of special \mathbf{q} -points in the case of an orthorhombic $Pmc2_1$ 20 atom cell with an 001 A-site cation order, which was relaxed on an $8 \times 8 \times 8$ set of \mathbf{k} -points. Finally, we optimize the rhombohedral $R3$ and the cubic $Fm\bar{3}m$ 111-ordered 40 atom cell on a $4 \times 4 \times 4$ \mathbf{k} -point mesh and use the Γ -point only to determine interatomic force constants and Born effective charges.

5.2 ELASTIC AND DIELECTRIC TENSORS

We will start by comparing the elastic constants of different symmetries in Table 2. The orientation of the simulation cell can be deduced from Figure 48. If we include all components of the C_{ij} tensor (we calculated the tensor in the pseudo-cubic

	P4/MMM (A)	PMC2 ₁ (A)	R ₃ (PC) (A)	R ₃ (PC) (V)	R ₃ (V)	EXP.	I $\bar{4}$ 2M (V)
C ₁₁	316.99	190.33	166.10	119.62	225.95	153.9	257.67
C ₁₂	105.61	53.03	107.53	99.00	92.89	18.7	103.26
C ₁₃	136.61	88.80	107.63	98.99	41.84	52.1	122.75
C ₂₂	316.99	241.71	166.92	121.56	225.95	153.9	258.08
C ₂₃	136.61	111.95	107.76	99.09	41.84	52.1	122.57
C ₃₃	329.40	235.34	167.74	123.48	152.74	168.1	307.07
C ₄₄	80.89	89.07	81.17	75.25	19.51	82.3	91.46
C ₅₅	80.89	77.61	81.16	75.22	19.51	82.3	91.48
C ₆₆	91.79	31.31	81.18	75.29	66.53	67.6	91.19
\bar{C}_{11}	332.09	312.55	317.14	283.97	312.49	-	-
\bar{C}_{12}	118.37	129.17	121.00	110.68	121.41	-	-
\bar{C}_{13}	118.92	109.06	121.32	111.35	100.32	-	-
\bar{C}_{22}	332.09	346.72	317.68	285.21	312.49	-	-
\bar{C}_{23}	118.92	119.50	121.35	111.43	100.31	-	-
\bar{C}_{33}	356.10	347.14	317.92	285.79	252.62	-	-
\bar{C}_{44}	95.46	101.41	101.87	95.40	89.53	-	-
\bar{C}_{55}	95.46	102.05	101.96	95.60	89.53	-	-
\bar{C}_{66}	91.79	110.26	101.76	95.12	95.54	-	-

Table 2: Elastic constants in different symmetries of NBT. We follow the notation of Wu *et al.* [114] and denote clamped-ion tensors by a bar and relaxed-ion properties at fixed electric field boundary conditions without any bars. All values are given in GPa. The superscript signalizes whether we calculated the tensor with the help of ABINIT (A) or VASP (V). Note that the elastic constants, which have been calculated in the pseudo-cubic representation of the rhombohedral cell and are marked with a “pc”, have been used throughout this thesis. The experimental (single crystal) values have been adopted from Reference [374] and are measured at room temperature.

representation), we additionally obtain the results for an R₃ symmetry as listed in Table 3. From our calculations, we conclude that the elastic constants, especially C₁₁, C₂₂, and C₃₃, decrease in the less symmetric subgroups. The direct comparison of a P4/mmm and a Pmc2₁ structure is a representative example. We further deduce that the material’s stiffness decreases if the ions are allowed to relax (internal relaxation allows for a reduction of stress [114]). The difference between the R₃ elastic tensors calculated with ABINIT and VASP is remarkable. Although they are in the same order of magnitude, they differ particularly for C₁₁, C₂₂, and C₃₃. Possible reasons for this might be a different potential or slightly varying optimum lattice constant (see Appendix). In turn, the off-diagonal components of the two different matrices are in good agreement.

If we compare these values with experimental single crystal C_{ij} tensor components [374], we find a reasonable agreement to the theoretical values. Deviations from the

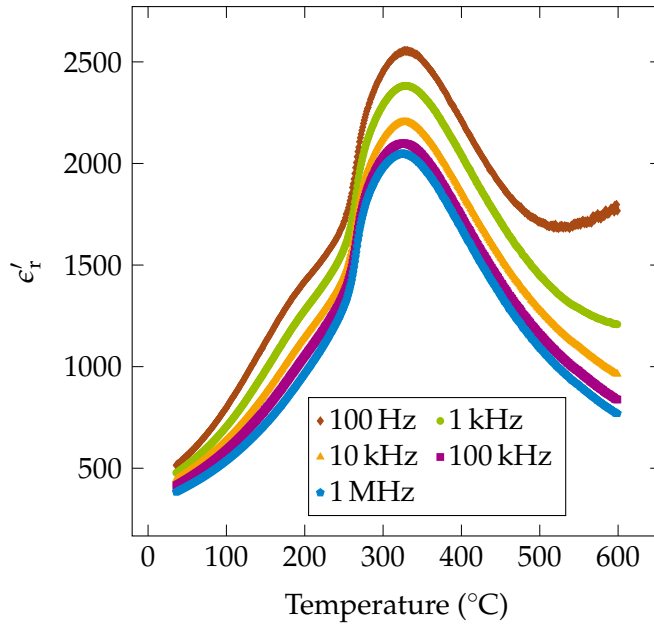


Figure 33: Temperature and frequency dependent permittivity ϵ'_r of NBT.

measured elastic constants have been expected since they have been obtained at room temperature and stem from a globally A-site disordered structure. However, our results differ from the report of Bujakiewicz *et al.* [375], who received values in the order of our clamped-ion elastic tensor and even larger. They further obtained a stiffer rhombohedral phase, while we observed higher elastic constants in the tetragonal phase. Compared to BaTiO_3 , NBT shows smaller C_{ij} -values on the main diagonal (except for C_{44}) but smaller components on the off-diagonal sites [114].

In the following, we investigate the dielectric tensor of NBT with a R_3 and a $\text{Pmc}2_1$ symmetry. The results are summarized in Table 4. We note that the $\bar{\epsilon}_{11}$ and the $\bar{\epsilon}_{33}$ component of the dielectric tensor are similar to BaTiO_3 , which are 6.20 and 5.79, respectively [114, 131]. Since the electronic dielectric tensor shows a sensitive dependency on the band gap, we probably include a systematic error by using a standard DFT approach [252].

Generally, if we allow for an additional strain relaxation ($\epsilon_{ij}^{(\sigma)}$), the tensor components increase. While using stress-free boundary conditions, the polarization might increase in the direction of the applied electric field [114].

If we compare the results of Table 4 with the temperature-dependent relative permittivity, obtained by Dr. Sebastian Steiner and shown in Figure 33, we find that our values are much smaller than in the experiment. Again, there are several possible reasons for this disagreement. On the one hand, we have to remember that the soft modes crucially depend on the cell volume (and we do not use the experimental lattice constant) [2]. On the other hand, we can not consider polar nano-regions or other structural features of NBT in a single supercell calculation.

	R ₃ (PC) (A)	R ₃ (PC) (V)	R ₃ (V)
C ₁₄	5.26	0.46	25.46
C ₁₅	-18.13	-18.14	0.46
C ₁₆	18.83	19.26	0
C ₂₄	18.58	18.84	-25.46
C ₂₅	-5.46	-0.95	-0.46
C ₂₆	19.45	21.70	0
C ₃₄	19.17	21.15	0
C ₃₅	-19.89	-22.35	0
C ₃₆	5.67	1.47	0
C ₄₅	0.12	0.08	0
C ₄₆	0.03	0.41	-0.46
C ₅₆	-0.17	-0.86	25.46
\bar{C}_{14}	8.21	7.82	5.03
\bar{C}_{15}	-12.36	-12.56	-3.84
\bar{C}_{16}	5.88	6.50	0
\bar{C}_{24}	5.60	6.88	-5.03
\bar{C}_{25}	-8.22	-7.83	3.84
\bar{C}_{26}	12.50	13.11	0
\bar{C}_{34}	12.29	12.64	0
\bar{C}_{35}	-5.81	-6.59	0
\bar{C}_{36}	8.29	8.01	0
\bar{C}_{45}	2.64	2.87	0
\bar{C}_{46}	-2.63	-2.81	3.84
\bar{C}_{56}	2.68	2.92	5.03

Table 3: Additional pseudocubic components of the elastic constant tensor in R₃ (GPa). We use the same notation as above.

	PMC2 ₁	R ₃
ϵ_{11}	59.32	63.49
ϵ_{12}	0.00	27.52
ϵ_{13}	0.00	-2.32
ϵ_{22}	130.85	64.09
ϵ_{23}	0.00	2.29
ϵ_{33}	13.08	12.70
$\epsilon_{11}^{(\sigma)}$	82.43	141.57
$\epsilon_{12}^{(\sigma)}$	0.00	62.88
$\epsilon_{13}^{(\sigma)}$	0.00	-37.30
$\epsilon_{22}^{(\sigma)}$	320.83	142.93
$\epsilon_{23}^{(\sigma)}$	0.00	36.89
$\epsilon_{33}^{(\sigma)}$	24.88	92.28
$\bar{\epsilon}_{11}$	6.57	6.65
$\bar{\epsilon}_{12}$	0.00	0.35
$\bar{\epsilon}_{13}$	0.00	-0.35
$\bar{\epsilon}_{22}$	7.06	6.66
$\bar{\epsilon}_{23}$	0.00	0.34
$\bar{\epsilon}_{33}$	6.74	6.67

Table 4: Dielectric tensor for NBT with R₃ and Pmc2₁ symmetry. All data has been obtained with ABINIT. Here, ϵ_{ij} is the relaxed-ion (fixed strain), $\epsilon_{ij}^{(\sigma)}$ denotes the free-stress relaxed-ion tensor, and $\bar{\epsilon}_{ij}$ represents the purely electronic dielectric tensor.

5.3 INFLUENCE OF SYMMETRY ON THE ELECTRONIC STRUCTURE

In chapter 10, we will intensively study the electronic structure of doped NBT and the resulting covalent bond strengths. Thus, it is instructive to initially deal with the influence of symmetry on the electronic band structure and to perform a COHP analysis in undoped NBT reference structures.

5.3.1 Band structures

Figure 34 depicts the band structures of the rhombohedral as well as the tetragonal 111-ordered configuration. In both cases, the oxygen contribution is predominant at the valence band maximum, while the titanium states are mainly observed in the conduction band. This is particularly apparent from the projected band structures (orbital and atom type) for Ti 3d and O 2p orbitals given in Figure 35. Since the atom- and orbital specific weights do not significantly change for the tetragonal structure, we only present the fat bands for the rhombohedral unit cell.

Compared to the Ti and O contribution to the band structure, the Bi character is considerably reduced and not shown here. However, the Bi 6s components can be

detected mainly at the valence band maximum, and a Bi 6p-character is predominant at the lower valence band edge and the conduction band minimum.

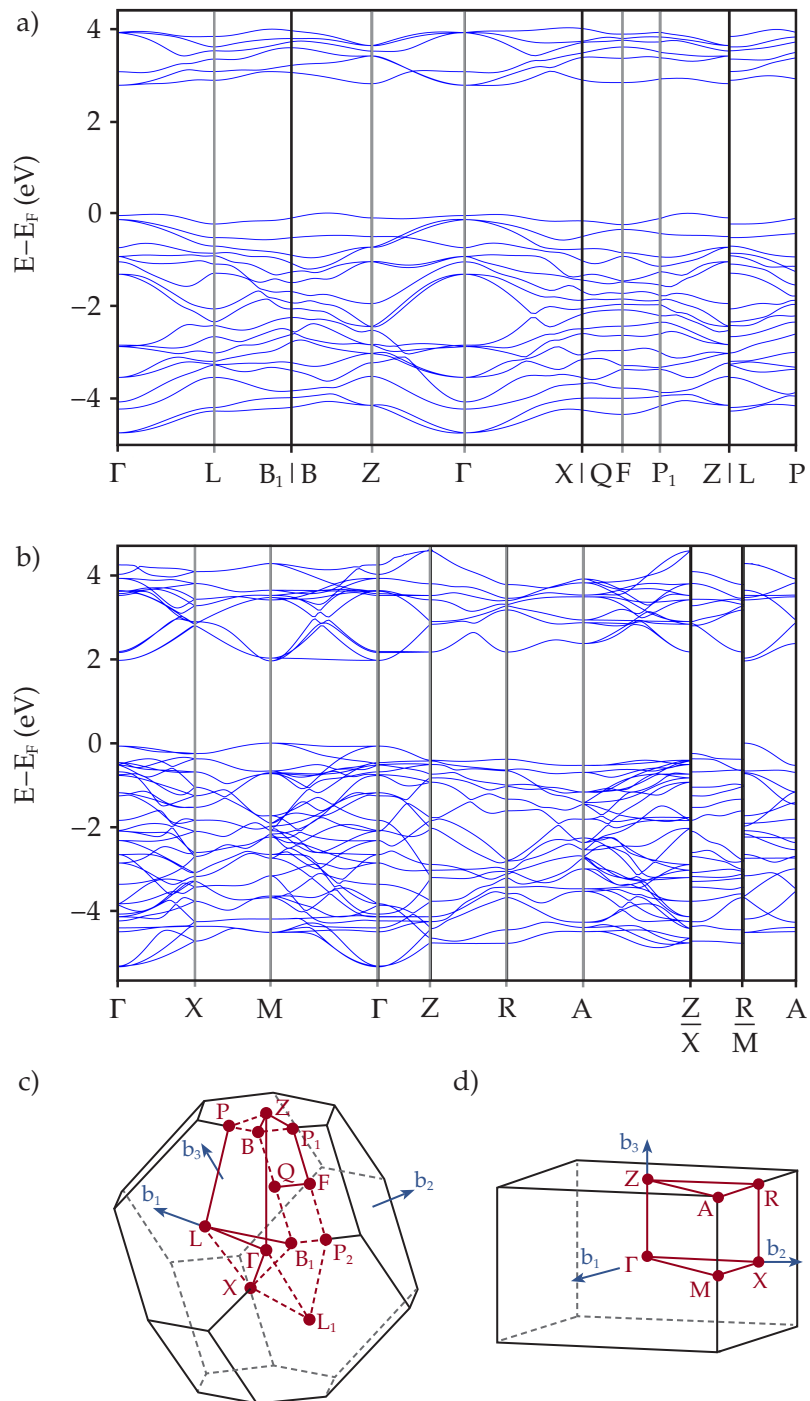


Figure 34: Electronic band structure (GGA) of the a) rhombohedral (with a transition between $(0.186, 0, 0)$ and Γ) and the b) tetragonal structure (transition between M and M) with a 111 cation order. The valence band maximum has been shifted to zero. In c) and d) we depict the k-point path through the rhombohedral and the tetragonal Brillouin zone, respectively. The k-point paths have been adapted from Reference [376].

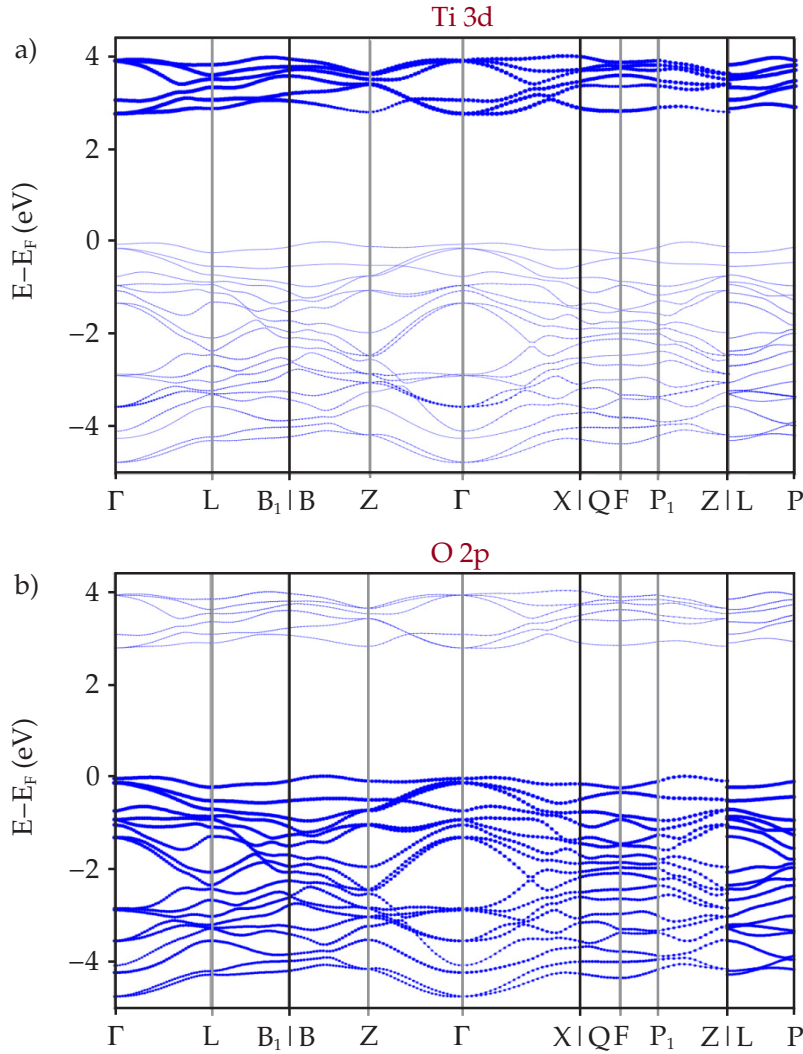


Figure 35: Projected band structure (fat band representation with GGA) of the R3 NBT unit cell for a) Ti 3d and b) O 2p states.

The rhombohedral band gap is 2.83 eV, which is close to the experimentally measured average of 3.3 eV. In turn, the band gap in the tetragonal structure resembles the one encountered in the high temperature, untilted cubic phase [2]. More precisely, the band gap shrinks down to 1.97 eV, which is a significant reduction by more than 1 eV. The band gap is slightly higher in a 001-ordered tetragonal structure (2.18 eV), but the band structure shows similar features and orbital characteristics in a fat band representation. Since the band structures for the 001-ordered structure are otherwise similar, they are not shown here.

The decrease of the band gap within the tetragonal structure is not a deficiency (at least not preliminary) of the GGA potential but rather a manifestation of a reduced octahedral tilt ($a^0b^0c^+$) and thus also a reduced hybridization between Bi, O, and Ti-orbitals [2]. In Figure 36, we demonstrate how the band gap changes with increasing amplitude of the Γ_5^- (anti-phase tilt mode) and the Γ_4^- mode (polar mode), as well as a superposition of both modes. Note that we use the $Fm\bar{3}m$ aristotype as a reference in 36a), 36b), and 36c), while we refer to the $R3m$ subgroup in Figure 36d). In the

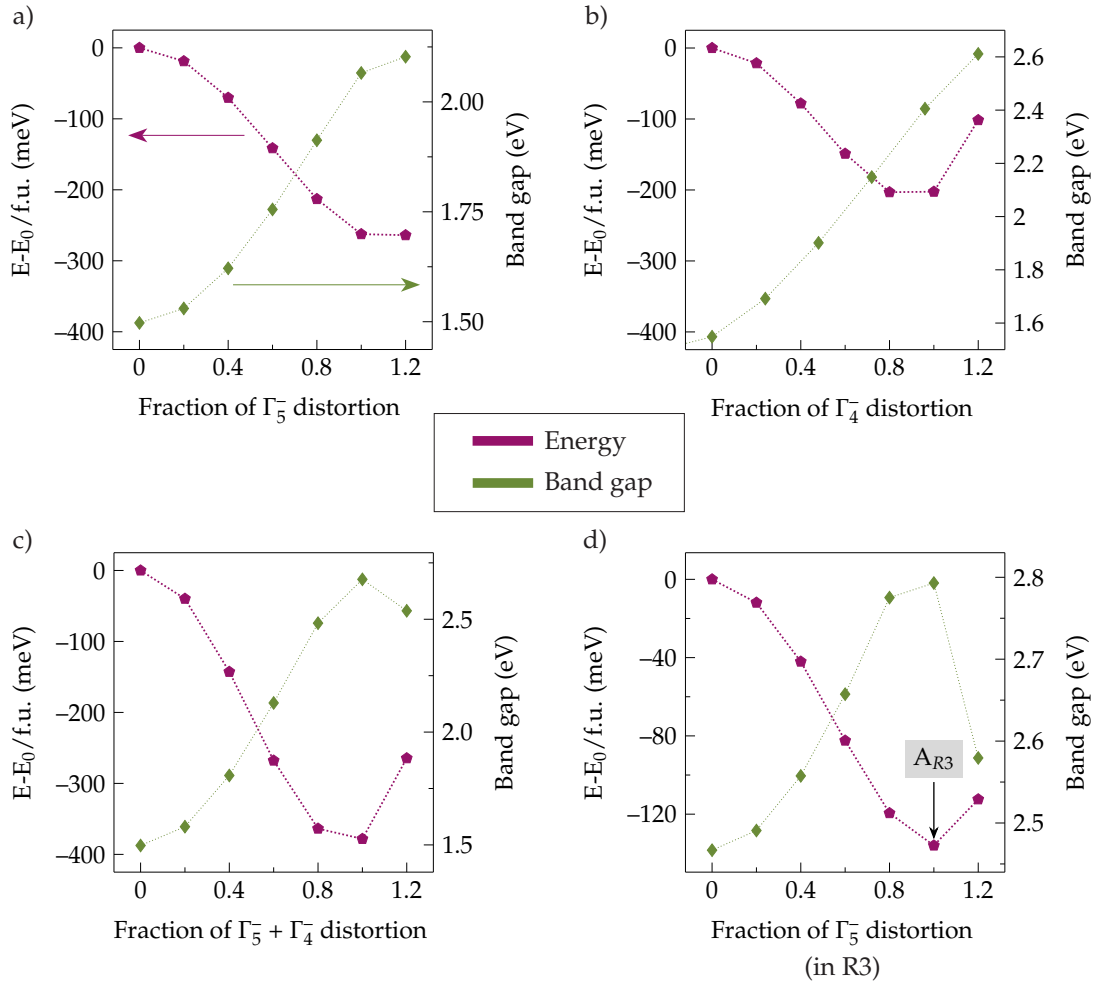


Figure 36: Energy and band gap size for several distortion amplitudes in 111-ordered NBT. The energy in Figure a), b), and c) is referenced to the energy of the Fm $\bar{3}$ m aristotype, while we choose E_0 to be the energy of the R3m structure in d). A fraction of 100% means that the equilibrium mode amplitude of the R3 hettotype has been reached. We marked this amplitude by A_{R3} in d).

latter case, we obtain the familiar R3 space group at a Γ_5^- mode fraction of 100% (marked as A_{R3} in Figure 36d). This means that we reach the equilibrium distortion amplitude for the 111-ordered rhombohedral unit cell.

Both the Γ_5^- and the Γ_4^- mode are depicted in Figure 37. If we solely introduce a Γ_5^- or Γ_4^- distortion of arbitrary amplitude, we observe a continuous increase of the band gap as well as a decrease in energy. However, if we introduce a superposition of both modes, the gap size immediately decreases again after reaching the equilibrium value (the opposite is true for the energy). We observe the same behavior if we successively raise the fraction of the Γ_5^- distortion in the presence of the Γ_4^- , Γ_2^- , and Γ_5^+ modes. Though the energy is sensitive to changes in the magnitude of the Γ_5^- distortion amplitude, the energy gain is reduced in the latter case.

Generally, we deduce from Figure 36 that although the tilt distortion contributes significantly towards increasing the band gap, the ions' polar displacement is also

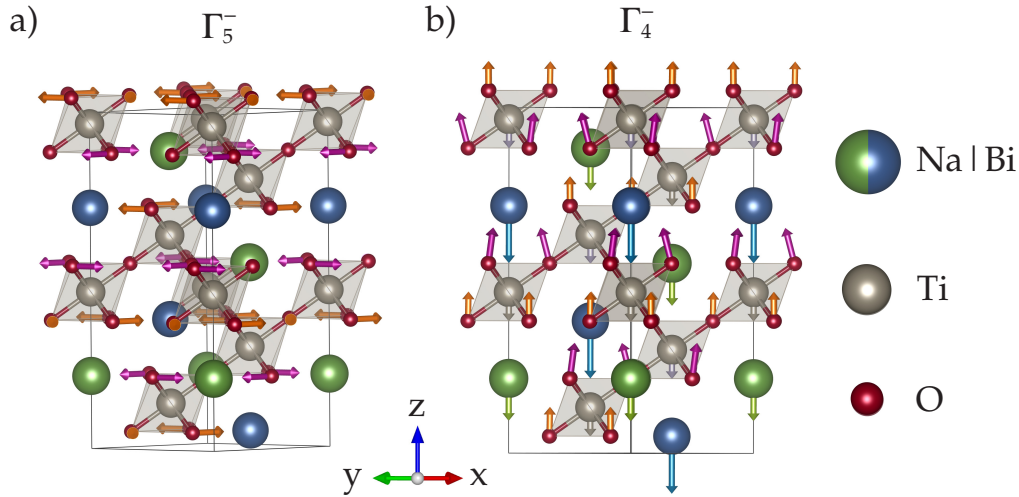


Figure 37: Visualization of the symmetry-adapted distortion modes Γ_5^- and Γ_4^- within the R₃ structure. Pink and orange arrows indicate two different oxygen positions.

essential.

One may ask, why the band gap for the R₃ structure (at 100 % in the R₃m hettotype) is lower than 2.83 eV in Figure 34. This is because we did not perform a whole band structure calculation for every distorted structure, but determined the energy difference between the valence band maximum and the conduction band minimum on a $8 \times 8 \times 4$ Γ -centered \mathbf{k} -point mesh in a structure containing 30 atoms. However, the exact band gap is indirect and located between (0.186,0,0) and the Γ -point at (0,0,0). A dependency of the band gap on octahedral tilting or strain has also been found in related materials such as perovskite oxysulfides or oxynitrides [377, 378]. These interrelations offer a possibility for band gap engineering.

5.3.2 Density of states and bonding analysis of bulk structures

Before qualifying the influence of dopants on the density of states, we first have to inspect the bulk densities. Again, we include the four polymorphs, which are primarily considered in the present thesis. These are the 111-ordered rhombohedral (R₃, 38a), tetragonal ($I\bar{4}2m$, 38d), cubic ($Fm\bar{3}m$, 38c), and the 001-ordered orthorhombic structure ($Pmc2_1$, 38b). In Figure 38 all spin up and spin down components are symmetric such that we present only the spin up component. However, Figure 38a results from a spin-polarized calculation, while the density of states in Figure 38b), 38c), and 38d) have been deduced from a spin-non-polarized calculation. This means that the energies do not change if we switch to a non-polarized version in the bulk structures and explains the different scales on the y-axis.

At first sight, the density of states of all symmetries appears to be similar. In all cases, we have a substantial Bi 6s contribution at -10 eV, which additionally overlaps with oxygen states. A second and relatively small contribution can be found in the upper valence band, as already pointed out by Gröting [2] for the cubic aristotype. Again, the Bi 6p states are primarily at the lower valence band and in the conduction band.

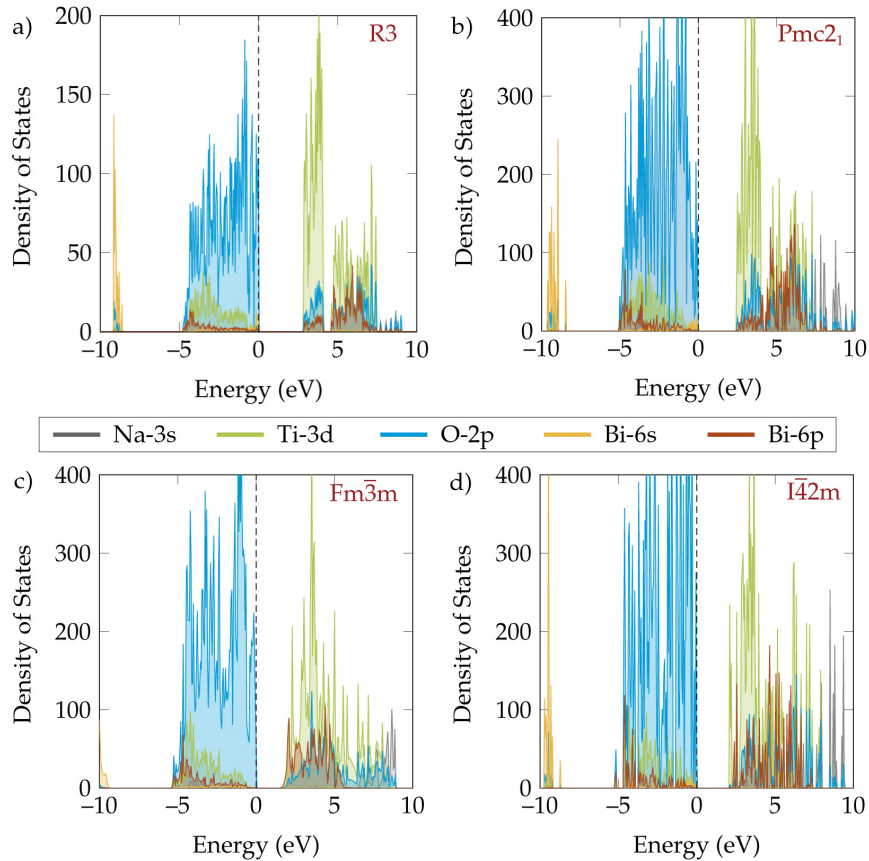


Figure 38: Density of states for GGA calculations and the different bulk structures of a) R3, b) $Pmc2_1$, c) $Fm\bar{3}m$, and d) $I\bar{4}2m$ symmetry.

Especially in the cubic structure (Figure 38c), we find a large amount of Bi 6p states at the conduction band minimum such that we might even have a p-p rather than a p-d transition.

The contribution of Na is relatively small in the regions of interest (valence and conduction band edges) such that we neglect them in the following discussion.

In the bulk structures, the O 2p states are energetically lower than the transition metal Ti d states such that the deep states have a predominantly p-character with a slight admixture of the d-levels. In turn, the anti-bonding bands, resulting from the hybridization of Ti and O, mainly consist of a combination of d-states [379].

The displacement of the Bi-ions from their ideal cubic lattice position leads to a symmetry allowed overlap between O 2p, Bi 6s, and Bi 6p orbitals. This increases the amount of Bi 6s states directly below the Fermi level and implies the formation of a stereo-chemical active lone pair (see Section 2.5.3).

To compare the bonding character and strength in the different bulk symmetries, we will analyze the pCOHPs as well as the IpCOHPs (see Section 3.13). As in the case of the density of states analysis, we compare our results with a calculation on a larger \mathbf{k} -point mesh. Although the curves are smoother and a tetrahedron method instead of Gaussian smearing could be used for the \mathbf{k} -point integration, the critical features remained the same. Thus, we rely on the Γ point calculations in the following. The

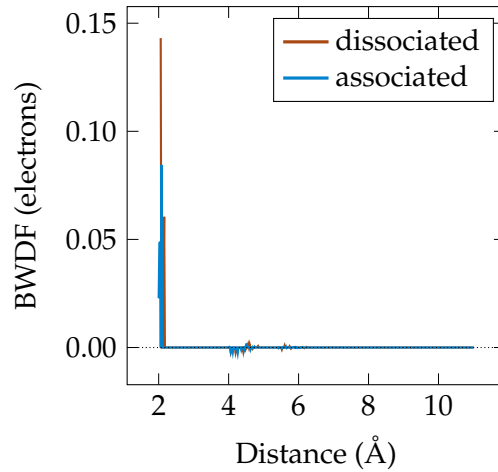


Figure 39: Bond-weighted distribution function for a Mg dopant in a R3 matrix. The transition between positive and negative BWDF is helpful to define a bond length cutoff [362]

charge spilling amounts to approximately 1% such that our basis set is considered to be sufficient. In every covalent bonding analysis below, we concentrate only on the interactions between an atom of type i with the nearest neighbors of type j . This is justified by the BWDF in Figure 39 for a Mg-doped R3 structure as a representative example for all bonding analyses in doped and undoped NBT. An attractive interaction between Mg and oxygen can only be observed for the first nearest neighbor shell.

In Figure 40 we present the COHPs for the 111-ordered tetragonal (111-T) and cubic (111-C), as well as the 001-ordered orthorhombic structure. Figure 40a) shows the bonding Ti-O interaction in the range between 0 eV and -6 eV. For all three bulk structures, the IpCOHP is similar, which can also be deduced from Table 5. A relatively stable environment corresponds to the observations of Woodward [36] that the interactions between the B-site and the oxygen are stronger than the A-O interactions. Furthermore, the former hardly change, even in the presence of octahedral tilts. Moreover, no destabilizing bonds can be found at the Fermi energy.

In turn, the Bi-Ti interactions in Figure 40c) are significantly smaller than the Ti-O contributions. We only find for the 001-order structure stabilizing bonding contributions directly at 0 eV. However, if we substitute one Na with a Bi atom, essentially generating a Bi-excess, we receive a similar result (not shown).

The Bi-O interactions are depicted in Figure 40b) and show a large anti-bonding contribution at the Fermi energy for the tetragonal and the orthorhombic structure. This indicates a reduced covalent bond between Bi and oxygen if no A-site off-center displacement is present within the structure.

Figure 40d) compares the Bi-O COHPs in a 111-ordered rhombohedral Fe-doped NBT structure for two Bi ions, located opposite to each other and between two Fe-dopants, if a vacancy is introduced near the dopants (associated) or within the surrounding matrix (dissociated). We see that the amount of states crucially depends on the direction of the ferroelectric distortion with respect to the vacancy position. Although we analyze defective structures in detail in the following chapters, we already present Figure 40d) to emphasize that the lone-pair effect is a stabilized anti-bonding interac-

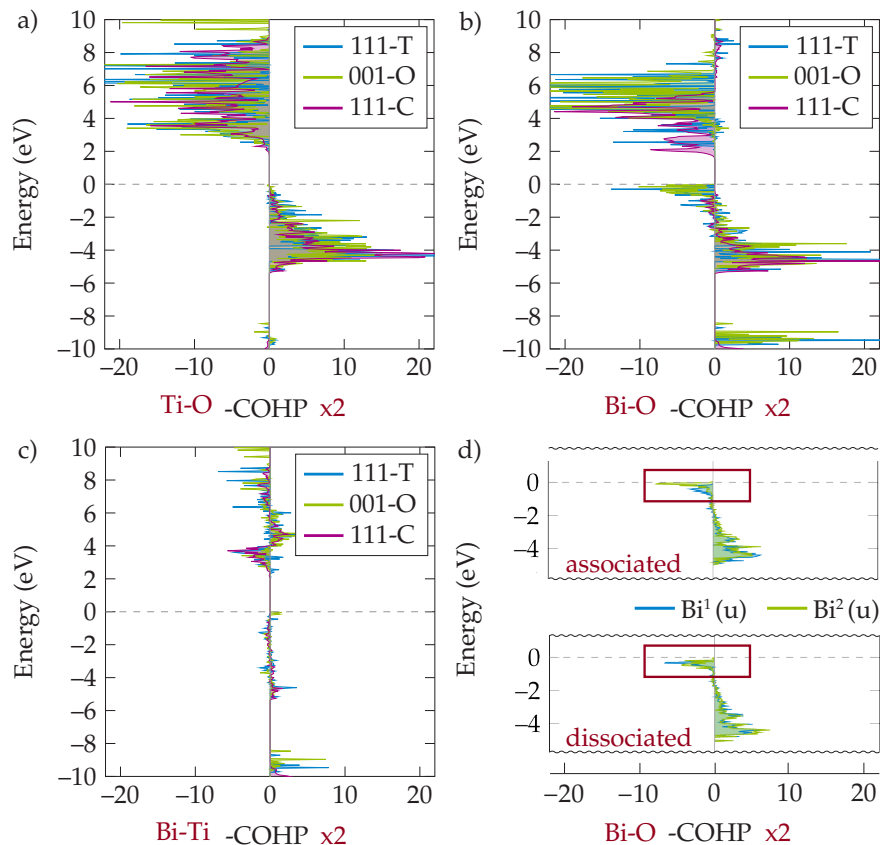


Figure 40: Crystal orbital hamiltonian population for a) Ti-O, b) + d) Bi-O, and c) Bi-Ti interactions. Figure a), b), and c) compare the tetragonal (T), cubic (C), and orthorhombic (O) bulk structures, while d) depicts the Bi-O interaction in a Fe-doped rhombohedral supercell with an associated and a dissociated $\text{Fe}_{\text{Ti}'}\text{-V}_{\text{O}}\text{-Fe}_{\text{Ti}'}$ defect cluster. Two different Bi-O interactions (in both cases the Bi ions are located between the Fe-dopants) are shown, illustrating that the bonding strength depends on the direction of the A-site displacement. Note that all COHP values have been multiplied by two.

tion [135, 136].

Table 5 summarizes the calculated average IpCOHPs/bond for Ti-O, Bi-O, Bi-Ti, and Ti-Ti. We notice that, as seen from the pCOHPs, the average values are similar in all symmetries and that the IpCOHPs of the Ti-Ti bonds are almost negligible. That is, interatomic d-d bonding can only be achieved by coupling of Ti 3d and O 2p orbitals. However, we want to emphasize the decrease of the Ti-O IpCOHPs with increasing Bi-O interaction. This can be explained by a competition of the Bi-O σ - and the Ti-O π -bonds about the same oxygen orbitals such that strong Bi-O bonds reduce the electron density in B-O π -orbitals (inductive effect) [36, 380]. A covalent interaction between the A-site cation and oxygen might strengthen the B-O bond if the electrons stem from high-energy bands. Any change of these anion and cation orbital overlaps will alter the covalent bonding interaction [2, 36].

This interplay becomes particularly evident if we visualize the charge density of a structure with Bi-excess with respect to the undisturbed bulk charge distribution in the 111-ordered rhombohedral symmetry. The additional Bi atom in Figure 41 is sur-

	TI-O	BI-O	BI-TI	TI-TI
111-C	-4.01	-0.82	-0.34	-0.04
111-T	-3.81	-1.0	-0.33	-0.04
111-R	-3.73	-1.11	-0.31	-0.04
001-O	-3.76	-1.12	-0.31	-0.05

Table 5: Average IpCOHP per bond (eV/bond) in the 111-ordered tetragonal, cubic, and rhombohedral, as well as 001-ordered orthorhombic bulk structures.

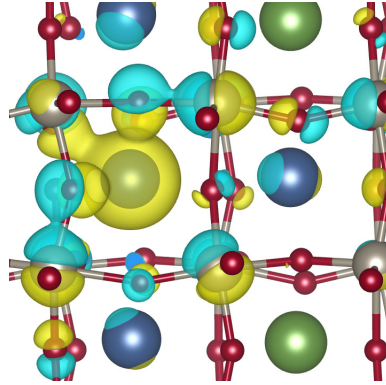


Figure 41: Charge density difference between a Na-deficient (Bi-excess) and a undisturbed bulk NBT structure. Yellow clouds show positive and blue negative charge differences.

rounded by a yellow sphere, indicating the charge introduced by the substitution of Na. However, this substitution not only increases the amount of charge on the A-site, but also on three of the nearest oxygens. Simultaneously, we observe a decrease in the covalent bonding interaction between Ti and O (blue clouds mark charge depletion). The excess Bi adopts a similar ferroelectric displacement as the regular Bi ions, with a slightly reduced absolute amplitude. This leads to the same chemical bonding environment in terms of IpCOHPs. Since the Ti ions move away from the oxygen ions close to the lone pair cation Bi^{3+} , we further induce a slight intra-octahedral displacement on the surrounding B-sites [381].

We do not identify any intercorrelation between Na-O and B-O covalent bonds. Even if we introduce a Na-vacancy, the change in the surrounding bonds is negligible. The analysis of the IpCOHP value for the average Na-O bond yields -0.26 eV/bond, which is weaker than the average Bi-O equivalent (see Table 5). This is in contrast to the suggestion of Dawson *et al.* [382] that strong Na-O bonds cause a higher oxygen vacancy formation energy in a Na-layer (or at least $4\times\text{Na}$ configuration) compared to a Bi-layer ($4\times\text{Bi}$ configuration).

5.4 PHONON DISPERSION CURVES

In this last chapter, we focus our attention on the dynamic properties of some bulk structures. In particular, we will deal with the phonon dispersion curves and the projected phonon density of states. We will specifically focus on the transition between a high symmetric $P4/mmm$ structure to a lower symmetric Pmc_21 configuration.

Phonon spectra allow for a detailed analysis of the instabilities in crystals as well as their origin [31]. Chapter 2 provides an in-depth explanation of the theory of ferroelectricity and how we describe lattice dynamics in terms of modes. Thus, at this point, we emphasize that negative frequencies are a clear indication of lattice instabilities and the presence of soft modes, which condense at the phase transition [107].

Let us first consider the $P4/mmm$ aristotype. Figure 42 depicts the phonon dispersion curves (Figure 42a), the projected phonon density of states (Figure 42b) and the atom type dependent contributions to the phonon displacements at the Γ -point (Figure 42c).

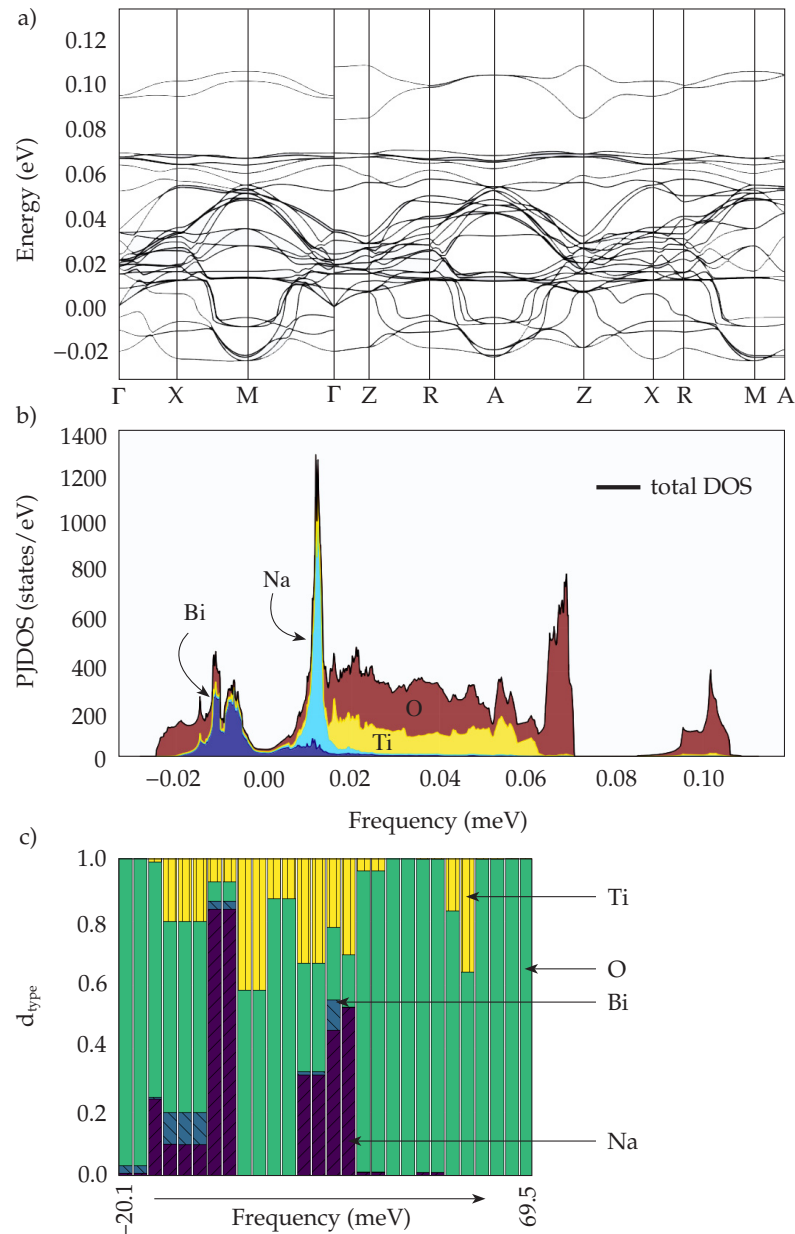


Figure 42: Phonon dispersion curve (a), projected phonon density of states (b) and atom type dependent contributions to the phonon displacements at the Γ -point in a $P4/mmm$ structure.

In contrast to BaTiO₃ [92, 130, 131], we observe various unstable modes along the given paths within the Brillouin zone. However, similarities such as the flat modes between the M-, the X-, and the Γ -point exist. In BaTiO₃, this has been ascribed to the destabilizing Ti-O interaction and a chain-like instability in real space within a Ti-O chain and small correlations between different Ti-O chains. That is, a cooperative atomic displacement along Ti-O is necessary to induce a polar distortion. In turn, an almost equally flat dispersion curve has been observed in CaTiO₃ along R-M [92], which is an indication for an antiferrodistortive instability (coupled rotation of corner-connected oxygen octahedra [131]) and implies a weak coupling between oxygen atoms in different lattice planes or a mutual compensation between other interplane interactions [131]. Indeed, if we visualize the phonon band structure in a fat band representation (not shown), we identify a prevailing oxygen contribution at these points. The most unstable eigenvector at the Γ -point is the Γ_5^- -mode, which is depicted in Figure 45.

The projected phonon density of states is shown in Figure 42b) and demonstrates that, on the one hand, oxygen crucially contributes to soft and hard modes and, on the other hand, that NBT is characterized by an A- and B-site instability. Moreover, Figure 42c) verifies that oxygen has the largest contribution to the phonon displacements at Γ and that Na's relative contribution exceeds the one of Bi. The latter might be related to the higher mass of Bi.

If we perform the same calculation on a structure with Pmc2₁ symmetry, we obtain the results presented in Figure 43. Since no modes appear at negative frequencies, the Pmc2₁ structure is the ground state of the 001-ordered NBT. Especially at the Γ -point, we observe similar characteristics compared to the P4/mmm parent. Additionally, the oxygen motion extensively contributes to the high-frequency modes, while A- and B-site displacements prevail at lower frequencies.

5.5 POLARIZATION IN Pmc2₁

In the next step, we will discuss the polarization in 001-ordered NBT with a Pmc2₁ symmetry. Figure 44a) shows the energy of the system with respect to the amplitude of the polar Γ_5^- mode in a structure where all other symmetry-adapted distortion modes of the Pmc2₁ structure are condensed. These other modes are the $a^0a^0a^+$ in-phase tilt M_2^+ , the $a^-a^-a^0$ anti-phase tilt referred to as M_5^- , the M_3^+ - (Jahn-Teller distortion), and the Γ_1^+ -mode. All modes are visualized in Figure 45. The latter possess only small amplitudes, and we will not dwell on these distortions [2]. Figure 46 verifies the dominance of the tilt and polar distortions over the M_3^+ - and Γ_1^+ -mode. It further demonstrates that the P4/mmm parent structure is unstable and that even at 50 K the mode amplitudes rapidly converge to their ground state (identified by the black dots) and subsequently fluctuate around these equilibrium values in an *ab-initio* molecular dynamics simulation. Despite the initially substantial increase of the polar mode amplitude, the in-phase and the anti-phase tilt prevail in Pmc2₁ [2].

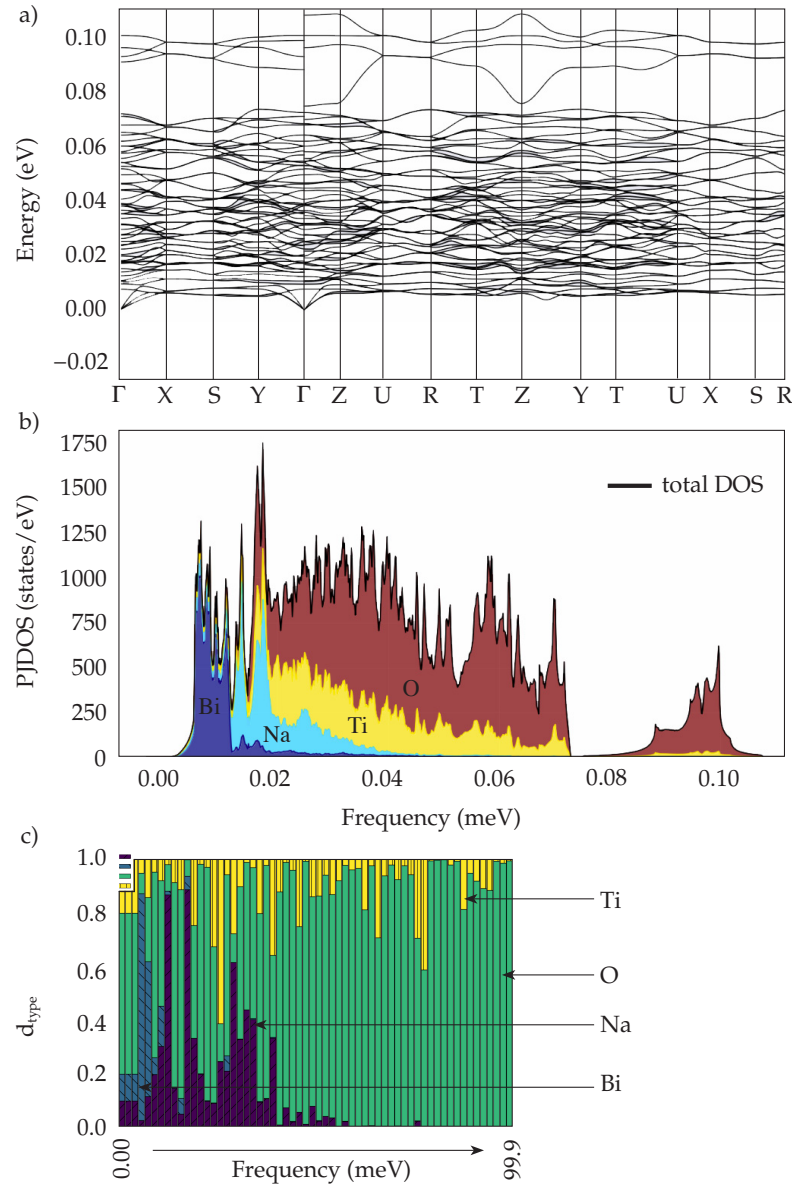


Figure 43: Phonon dispersion curve (a), projected phonon density of states (b) and atom type dependent contributions to the phonon displacements at the Γ -point (c) in a Pmc₂₁ structure.

The shape of the energy curve with respect to the distortion mode amplitude demonstrates that this structure shows characteristics in-between a (hybrid) improper ferroelectric [97] and a proper ferroelectric. From Gröting [2], we know that a transition between these two types of ferroelectrics is volume dependent. Although the polar and the tilt modes already become slightly pairwise cooperative at the given volume (a sign for proper ferroelectricity, see Figure 47), we still observe a typical shift of the polar mode double well to lower energies in the presence of the two tilt distortions. The latter is a clear indication for hybrid improper ferroelectricity and shows that the improper coupling terms dominate (see Figure 44) [2].

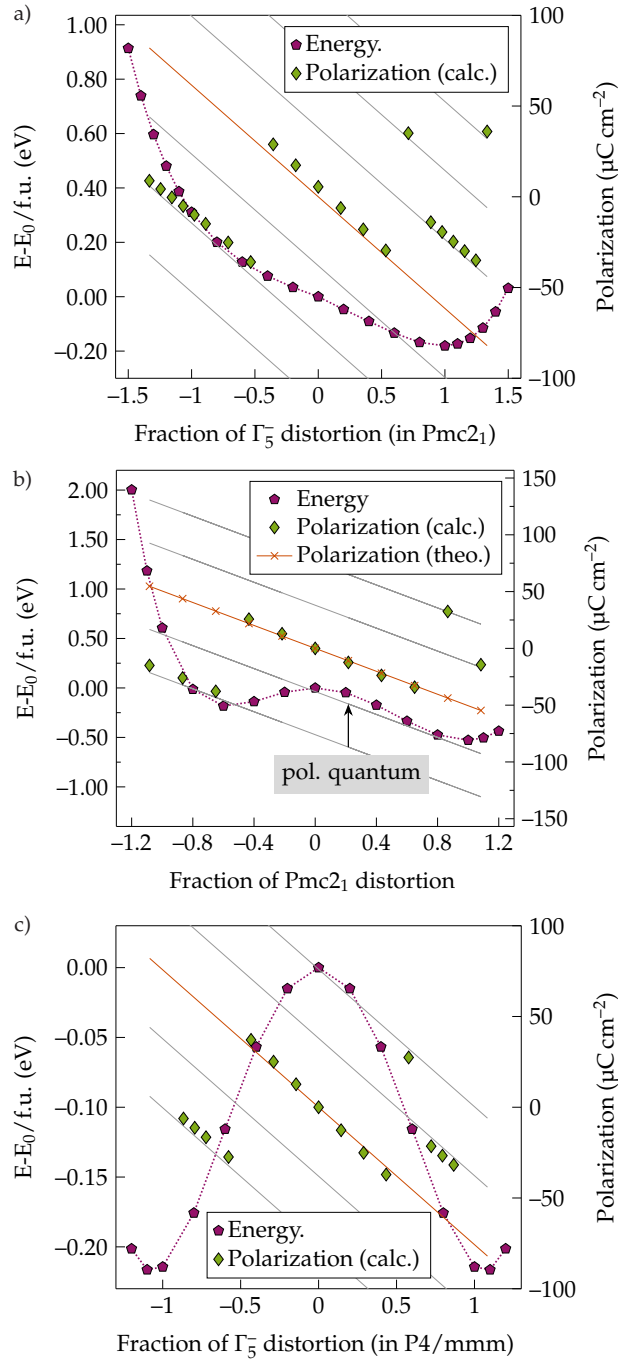


Figure 44: Spontaneous polarization and energy as a function of mode distortion amplitudes. In a), we modified the distortion amplitude of the Γ_5^- -mode such that a full Pmc2₁ symmetry at 100% is obtained. In c), we perform the same calculation but use a P4/mmm high symmetry structure as a reference. In b), we manipulate all modes present in the Pmc2₁ ground state simultaneously. The light gray lines depict the polarization lattice, while the orange line represents the main polarization branch. The distance between the branches denotes the polarization quantum as indicated by the black arrow.

We calculated the polarization in two different ways, as presented in Chapter 3. On the one hand, we use the Berry-phase approach, and on the other hand, we apply Equation 94. If we study the polarization in closer detail, we note that the values ob-

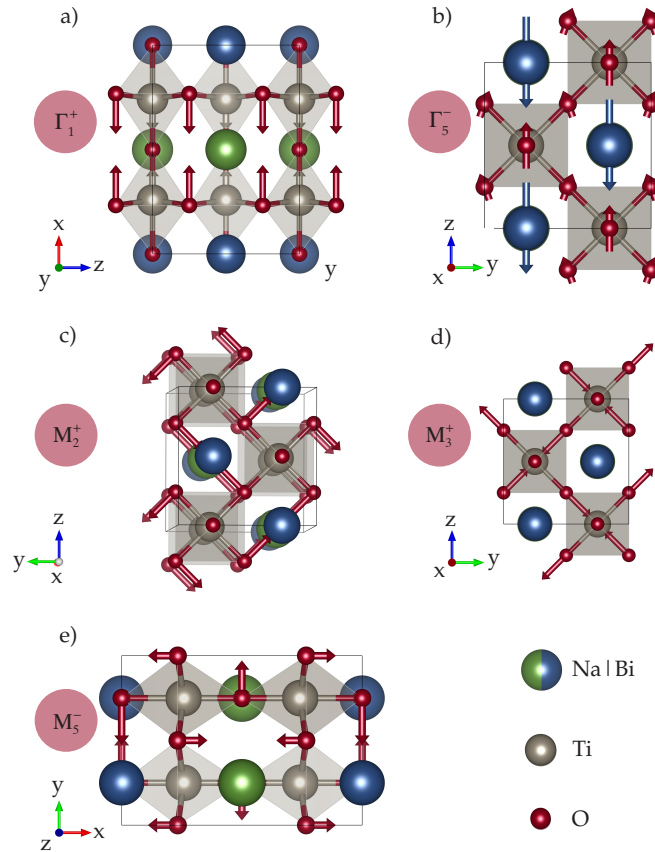


Figure 45: Visualization of the symmetry-adapted modes within a $Pmc2_1$ structure

tained by the Berry phase approach jump between different branches. These branches are indicated by the light grey lines in Figure 44 and display the polarization lattice, which has been determined using Born effective charges. Remember that the distance between the branches is the polarization quantum and that the bulk polarization is multi-valued [295].

Our calculation demonstrates what has been pointed out by Spaldin [295] concerning the calculation of the spontaneous polarization: While extracting the spontaneous polarization in a particular subgroup, it is essential to calculate the polarization at intermediate distortions to ensure not to switch branches and obtain misleading results. The real solution at a Γ_5^- distortion of 100% can be extracted from the orange branch. We note that this polarization is much larger than the experimentally measured remnant polarization in NBT, which amounts to $38 \mu\text{C cm}^{-2}$ [19, 27]. This value even increases, if we vary the amplitude of Γ_5^- in the otherwise undisturbed $P/4\text{mmm}$ parent phase, as illustrated in Figure 44c). Instead, if we modify all symmetry-adapted distortion modes simultaneously, we receive a value of approximately $55 \mu\text{C cm}^{-2}$. For comparison, the calculated polarization in $R3c\text{-CaTiO}_3$, generated by “artificial heteroepitaxy”, amounts to $44 \mu\text{C cm}^{-2}$, while PbTiO_3 possesses a polarization of $78 \mu\text{C cm}^{-2}$ [383]. A possible explanation for this deviation is that a global $Pmc2_1$ structure with a 001 A-site cation order does not reflect the average configuration in an actual sample. Thus, we can only determine material properties, which partially contribute to the overall behavior of NBT.

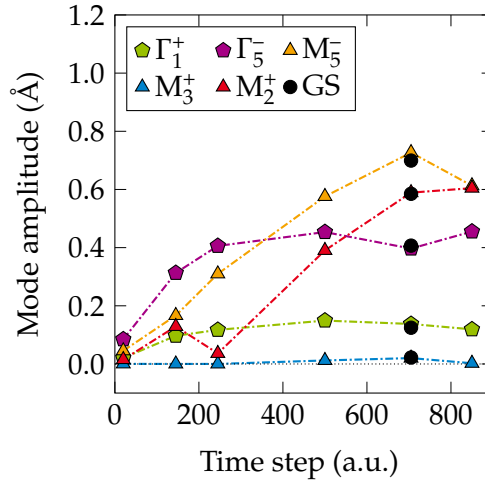


Figure 46: Development of symmetry-adapted distortion modes of the $Pmc2_1$ structure. We use the high symmetry $p/4mm$ parent as a reference structure and perform an *ab-initio* molecular dynamics simulation at 50 K.

5.6 BORN EFFECTIVE CHARGES AND INTERATOMIC FORCE CONSTANTS

5.6.1 Born effective charges in a $P4/mmm$ structure

In 1994 Resta [297] assumed that Born effective charges are “most badly” needed to understand the ferroelectric instability in perovskite oxides. These effective charge tensors describe the macroscopic polarization, which has been generated by a rigid displacement of a sublattice in a vanishing electric field [297, 384] and are well-defined quantities to assess the covalent bonding character in a material [121]. In the following, we will summarize the Born effective charges of the 001-ordered parent structure $P4/mmm$.

As in the case of $BaTiO_3$ and $KNbO_3$, we see a reduction of the Born effective charge components when we reduce the symmetry to $Pmc2_1$ [121]. Ghosez *et al.* [121] showed that especially Ti and the O_{\parallel} component (parallel displacement with respect to B-O bond) decrease significantly in a lower symmetry structure, while the values for the A-site and O_{\perp} are almost unchanged. They further stated that the anisotropy of the Ti environment along the Ti-O chains is the most relevant factor.

In Table 6 we can find the Born effective charges of for the individual lattice sites in $P4/mmm$, which are additionally shown in Figure 48. In contrast to $BaTiO_3$ or $SrTiO_3$, we have two or three different tensor components instead of only one in $Pm\bar{3}m$. Except for Na, we observe large anomalous charges at least in one specific direction. For instance, we obtain values between 4.07 and 5.88 for Bi, although the nominal ionic charge amounts to 3+. This further reveals the substantial covalent bonding contribution between Bi and oxygen and, in particular, explains the increase of the Born charges in xx - and yy -direction (O_{\perp}) and the sensitivity towards atomic displacements. For comparison, Pb shows an anomalous charge of 3.9, indicating that Z^* increases quasilinear with the nominal charge in this compound [121]. In contrast, the Born effective charges of Ti in $BaTiO_3$, obtained by a linear response calculation, is 7.25. The exact value slightly deviates depending on the model used to determine

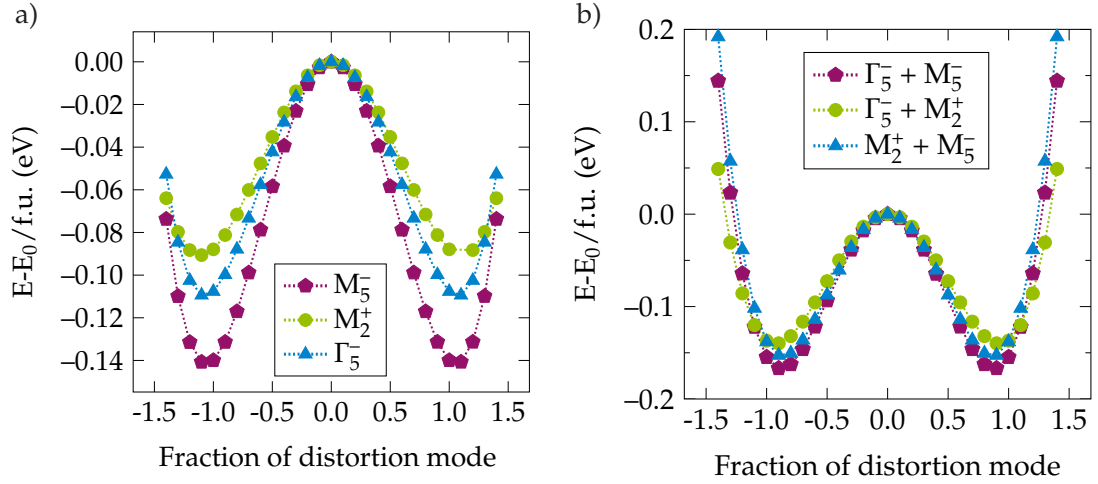


Figure 47: Energy-distortion curves for several symmetry-adapted distortion modes in $\text{Pmc}2_1$.

	xx	yy	zz
$\text{Bi}^{(3+)}$	5.88	5.88	4.07
$\text{Na}^{(1+)}$	1.17	1.17	1.48
$\text{Ti}^{(4+)}$	6.98	6.98	7.44
$\text{O}_1^{(2-)}$	-5.79	-2.46	-2.13
$\text{O}_2^{(2-)}$	-3.14	-3.14	-4.11
$\text{O}_3^{(2-)}$	-1.38	-1.38	-7.82

Table 6: Born effective charges of different atoms in the P_4/mmm structure. The atoms are labeled according to Figure 48. The superscript denotes the nominal ionic charge of the specific atom type.

this property. However, they can be found in a range between 7.26 to 7.51. For O_\perp and O_\parallel values of -2.15 and -5.71 have been reported [121, 128, 385]. Thus, we conclude that the A-site has a small influence on Z_B^* , but significantly affects the O_\perp and O_\parallel components of oxygen atoms sitting in a Bi- or Na-layer. We do not observe such an anomaly for oxygen atoms which are located in-between two A-site layers or in the case of a 111-ordered NBT structure. Interestingly, O_\parallel of the third oxygen becomes exceptionally large (-7.82), while O_\perp even decreases below the nominal ionic charge of -2. We notice the opposite behavior for the third oxygen. This suggests that a covalent interaction with Bi slightly decreases, and the negligible covalent interaction with Na increases the Ti-O interaction. We explained this interrelation between Bi, Ti, and O in the context of the COHP analysis (see Chapter 6).

5.6.2 Interatomic force constants

With the help of interatomic force constants, we identify energetically favorable long- and short-range couplings between different atom types and rationalize the presence

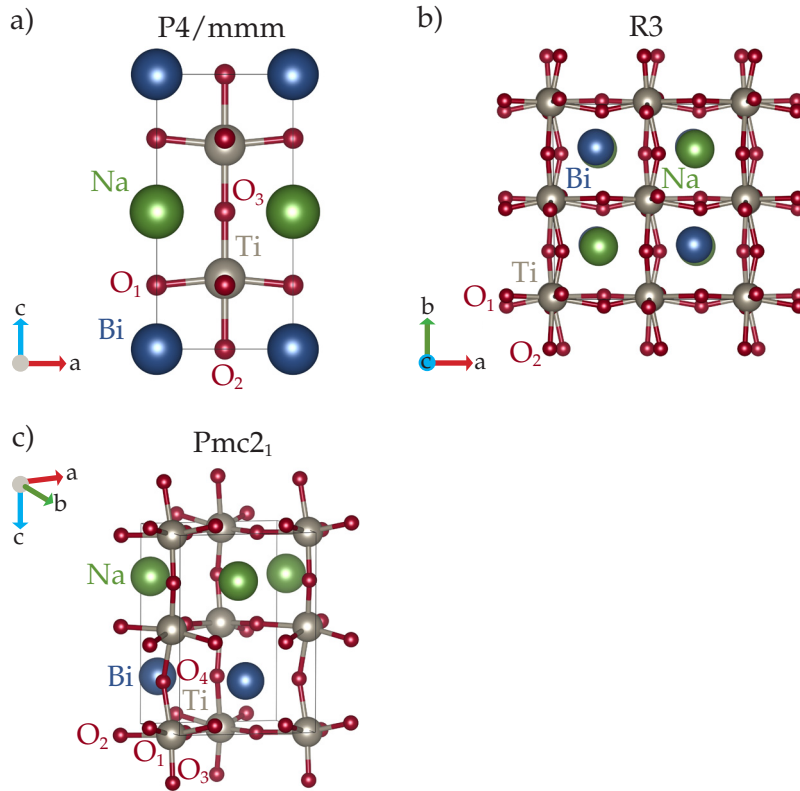


Figure 48: Lattice sites in a $P4/mmm$, a $Pmc2_1$ and a $R3$ structure. The atoms in a) are labeled in accordance to Table 6.

of unstable phonon branches [131]. The concept of ICFs has been introduced in Chapter 2. Before we discuss any results, we remind the reader that negative values represent stable interactions, while positive IFCs correspond to unstable and therefore destabilizing interactions. We report the IFCs in local coordinates, where we distinguish between longitudinal and transverse contributions with respect to the bonding direction of two atoms.

In turn, the self-force constant, which denotes the force acting on an atom upon a rigid off-site displacement, is always positive. Thus, only cooperative motions can decrease the energy of the system and lead to ferroelectric instabilities [131]. It is known that the self-force constant and the off-diagonal coupling of oxygen on nearest neighbor sites affects the frequency of the antiferrodistortive mode [131]. However, in the following, we only report on the diagonal elements and compare them between different phases.

Table 7 summarizes the self-force constants as representatives of a high symmetric 001 -ordered as well as a low symmetry 001 - and 111 -ordered configuration. Indeed, all constants in both structures are positive. The high symmetry $P4/mmm$ parent shows lower self-force constants, indicating that the tetragonal configuration is generally unstable. If we compare these values with other familiar representatives of the perovskite family, we deduce that Bi has a lower self-force constant than Ba in $BaTiO_3$ (especially yy and zz), but a higher one than Ca in $CaTiO_3$ [92]. The low on-site force constant in $CaTiO_3$ has been associated with a significant amount of A-site instabil-

	xx	yy	zz
Bi-Bi (P_4/mmm)	0.086	0.035	0.035
Na-Na (P_4/mmm)	0.011	0.011	0.012
Ti-Ti (P_4/mmm)	0.126	0.125	0.114
O ₁ -O ₁ (P_4/mmm)	0.204	0.043	0.037
O ₂ -O ₂ (P_4/mmm)	0.051	0.202	0.050
O ₃ -O ₃ (P_4/mmm)	0.089	0.146	0.038
Bi-Bi ($Pmc2_1$)	0.102	0.105	0.091
Na-Na ($Pmc2_1$)	0.035	0.024	0.021
Ti-Ti ($Pmc2_1$)	0.210	0.213	0.195
O ₁ -O ₁ ($Pmc2_1$)	0.180	0.064	0.061
O ₂ -O ₂ ($Pmc2_1$)	0.215	0.062	0.064
O ₃ -O ₃ ($Pmc2_1$)	0.243	0.066	0.042
O ₄ -O ₄ ($Pmc2_1$)	0.137	0.071	0.094
Bi-Bi (R_3)	0.106	0.118	0.109
Na-Na (R_3)	0.030	0.030	0.623
Ti-Ti (R_3)	0.212	0.191	0.194
O ₁ -O ₁ (R_3)	0.210	0.065	0.057
O ₂ -O ₂ (R_3)	0.194	0.061	0.078

Table 7: Total self-force constants for P_4/mmm , $Pmc2_1$, and R_3 . The values are given in Ha/bohr² in the corresponding local coordinate system. That is, xx represents the \parallel and yy as well as zz denote the \perp component.

ity in the polar displacement [92]. Na possesses the smallest and, in contrast to Bi, almost isotropic self-force constant.

For both, the A-A and the B-B interaction, NBT lies between the two cases of predominantly B-site ($BaTiO_3$) and a prevailing A-site ($CaTiO_3$) ferroelectricity. Thus, the inspection of the self-force constant nicely demonstrates which has already been assumed from the Goldschmidt tolerant factor [43]: The B- and the A-site crucially contribute to the development of a ferroelectric distortion (while in the 001 structure the A-site contribution to the unstable phonons is larger than the contribution of Ti) [2]. Our results further support the findings of Ghosez *et al.* [131], who states that the self-force constant is primary dependent on the differences of A-O and B-O interactions.

Since all investigated structures have less symmetry than the cubic aristotype $Pm\bar{3}m$, and we additionally have two different atom types on the A-site, a stringent notation of the single IFCs for all interactions is not constructive. Thus, we decided to visualize and comment on the most critical interatomic interactions as a function of the distance for three distinct structures, namely $P/4mmm$, $Pmc2_1$, and R_3 .

Figure 49 shows the ICFs for a Ti_0 - Ti_1 interaction in the P_4/mmm structure. We plotted the total IFC as well as the dipole-dipole (DD) and the short-range (SR) con-

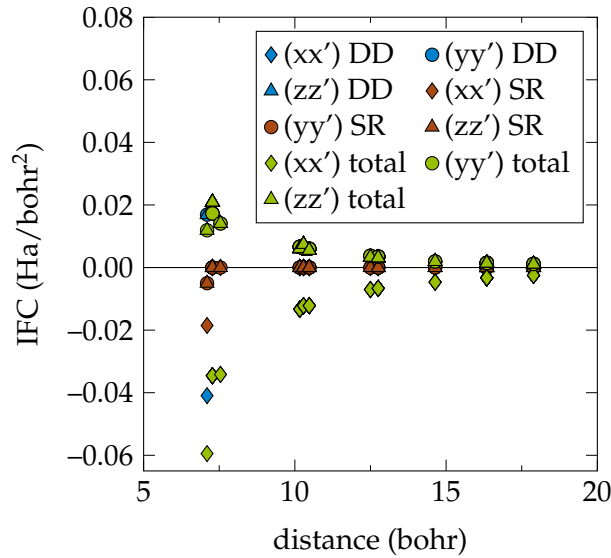


Figure 49: Interatomic force constants for a Ti-Ti interaction as a function of distance in a $P4/mmm$ structure. The green signs denote the total interatomic force constant, which is a sum of a dipole-dipole (DD) and a short-range (SR) term.

tribution for all interatomic interactions. Naturally, the interatomic constant between two Ti-atoms decreases rapidly as a function of the distance and approaches zero slightly below 20 bohr. We observe a largely negative IFC for the \parallel component of the Ti-Ti interaction. The strong coupling is a combination of the relevant DD-and SR-interaction and has been attributed to the chain-like instability in $BaTiO_3$. However, the transversal force component is only one-third of the longitudinal and positive. On the one hand, this signifies a weaker coupling between different Ti-O chains and, on the other hand, an overall anisotropic coupling [130]. Although our results resemble the behavior of $BaTiO_3$ and $CaTiO_3$ [92, 130, 131], NBT shows a slightly higher coupling transversal to the Ti-O bond direction.

We observe a similar trend for the Bi_0-Bi_1 and the Bi_0-Na_0 interaction, which is for Bi again slightly larger and for Na slightly lower in comparison to $BaTiO_3$. Likewise, the Bi-Ti interaction leads to a more repulsive longitudinal and a more positive transversal force on the nearest neighbor than for the classical perovskite oxides [92]. Instead, if we take a closer look at Figure 50d), we note that, in contrast to an equivalent Ba-O coupling, the contribution of a Bi-O interaction is not negligible for a ferroelectric distortion. Figure 50d) is a representative example of a Bi-O coupling. However, we identify an increase by approximately 0.01 Ha/bohr^2 in the case of the longitudinal force component for O_2 and a drastic reduction (approximately 50%, depending on the direction) for both \perp and \parallel directions in the case of O_3 . This is reasonable since we detect a significant Bi and O contribution for the unstable phonon branches at Γ or the Z-point. The former significantly contributes to the Γ_5^- mode. We further assume that this coupling might be smaller with a $2 \times Bi / 2 \times Na$ (111 order) configuration around the oxygen.

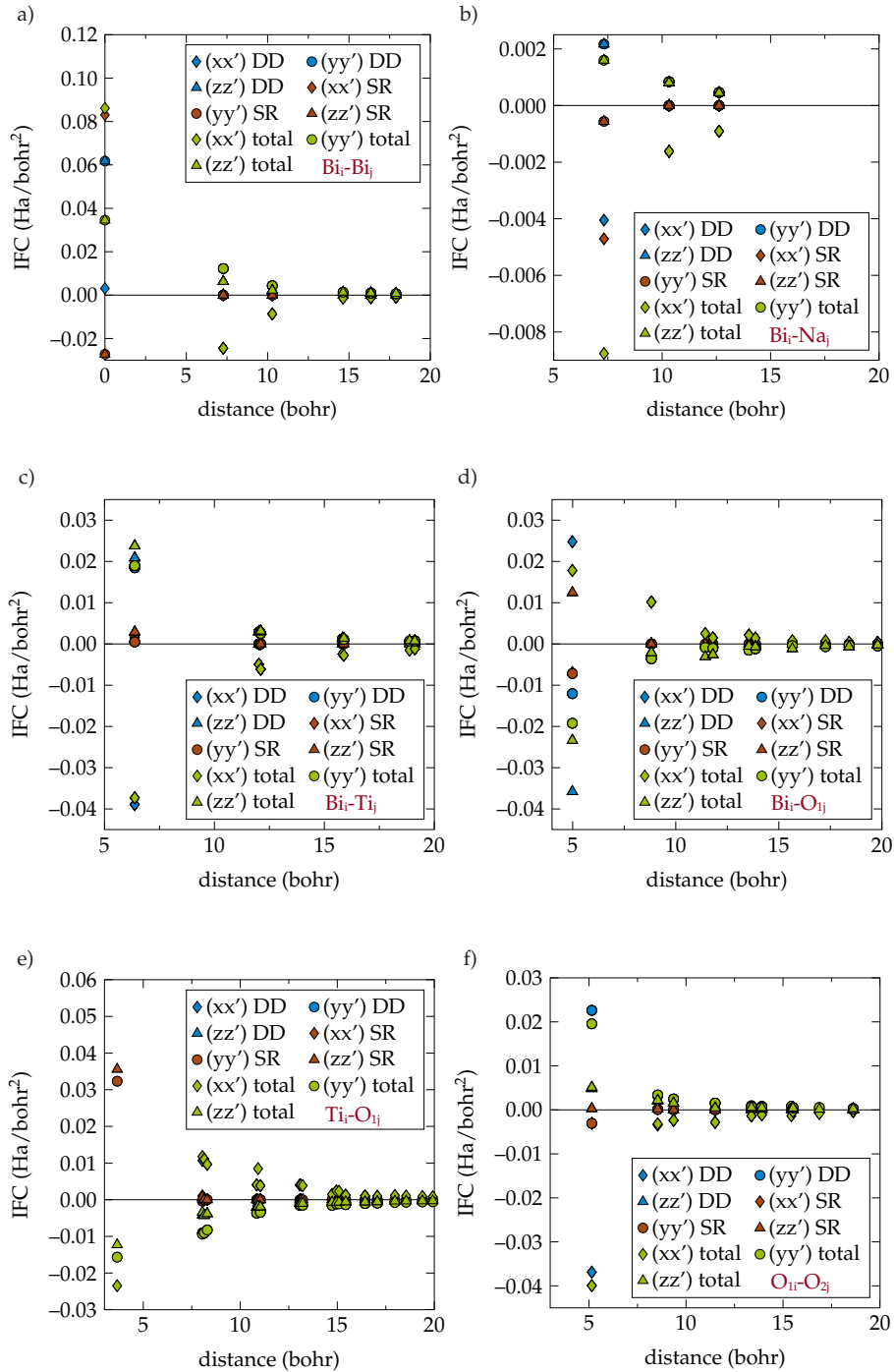


Figure 50: Interatomic force constants as a function of distance in a P_4/mmm structure. The green signs denote the total interatomic force constant, which is a sum of a dipole-dipole (DD) and a short-range (SR) term.

In the case of Ti-O_{\parallel} , we observe a stable coupling on the first neighbor site. For higher neighbor shells, this interaction becomes positive until it decreases continuously to zero at large distances (see Figure 50b). This is surprising since such behavior has not been detected for BaTiO_3 , where the destabilizing DD and the stabilizing SR contributions almost compensate each other, leading to a decoupling of Ti and oxygen dis-

placements [130]. However, in NBT, the SR-part overcompensates the DD-interaction, resulting in an overall repulsive IFC. The yy' and the zz' components remain negative at all distances and closely resemble the chemistry in BaTiO_3 [92]. In contrast to the case of Bi-O, we detect an increase of the longitudinal force for Ti-O₃ and a decrease for Ti-O₂ with almost unaffected transversal components.

The IFC for an O-O coupling is shown in Figure 50f). Again, the stable and unstable interactions increase the respective magnitude in BaTiO_3 [92]. The large DD-contribution primarily causes these. Both the longitudinal and transverse IFC decrease for an O₁-O₂ interaction, while they are relatively similar for all other interactions amongst the oxygen atoms. The IFC of Na with Ti or O is generally lower than those observed for Bi (not shown in Figure 50). While for Na-Ti the xx' component is repulsive (approximately -0.01 Ha/bohr^2), yy' and zz' are slightly destabilizing. The opposite has been detected for a Na-O coupling.

We conclude the present chapter by briefly comparing the results obtained for $P4/mmm$ lower symmetry structures such as $Pmc2_1$ and $R3$. Generally, unstable coupling terms lead to low symmetry structures, as already mentioned in the context of self-force constants (see Figure 52a) and Figure 52b) for comparison). Especially the coupling between Bi and the oxygen, which is located in the Bi-layer, shows a sizable stable interatomic coupling. The Ti-O₄ IFCs in the $Pmc2_1$ structure (Figure 52c), see Figure 48 for atomic labels) become increasingly similar to the B-O interaction in BaTiO_3 , which has already been discussed above. All other Ti-O coupling terms become repulsive, at least on the first neighbor.

If we turn our attention towards the 111-ordered $R3$ structure, we observe that the A_i-A_j and the A_i-B_j IFC do barely change. This becomes particularly clear if we compare Figure 52f) with Figure 49. While the longitudinal Na-O interaction in Figure 52c) is still relatively small and positive, the longitudinal Bi-O interaction in Figure 52d) becomes negative for the nearest symmetry equivalent O₂ instance. In contrast, we only obtain approximately -0.006 Ha/bohr^2 for O₁. Interestingly, the Ti-O₂ interaction has a positive longitudinal IFC of 0.012 Ha/bohr^2 , but the Ti-O₁ coupling provides a \parallel component of -0.081 Ha/bohr^2 . This might be a result of the different bond lengths and, therefore, bond strengths between oxygen and titanium. From He *et al.* [386], we know that n-type doping increases Ti's self-force constant and thus reduces the ferroelectric instability. This might also affect the polar distortion in Bi-excess NBT.

5.7 THINGS TO REMEMBER

This chapter provides a general overview of essential properties in 001- and 111-ordered NBT. To a large extend, these properties have been used to calculate the electrostatic and mechanical interaction between defect images at the periodic boundary. We included an in-depth comparison of the interatomic force constants, polarization, and phonons with other common perovskite oxides, which, to the author's knowledge, are not available in current literature. However, in each section of this chapter, we faced computer simulations' limitations describing a globally disordered system accurately. As already emphasized by Resta [31], the relatively flat energy landscape composed of the cubic aristo- and the lower symmetry hettotypes, makes the compu-

tation of material properties a highly challenging task. This includes a careful choice of the physical approximation, and all other “numerical technicalities”, for instance, the basis set (especially if “computationally unfriendly atoms” such as oxygen are involved). But more importantly, we could not include A-site disorder, phase and grain boundaries, or consider ordered nano-regions in a disordered matrix. Nonetheless, we found a reasonable agreement for the lattice constants in the rhombohedral 111-ordered structure, large spontaneous polarizations and can, to some extent, explain the anomalous large Born effective charges and lattice instabilities at negative frequencies.

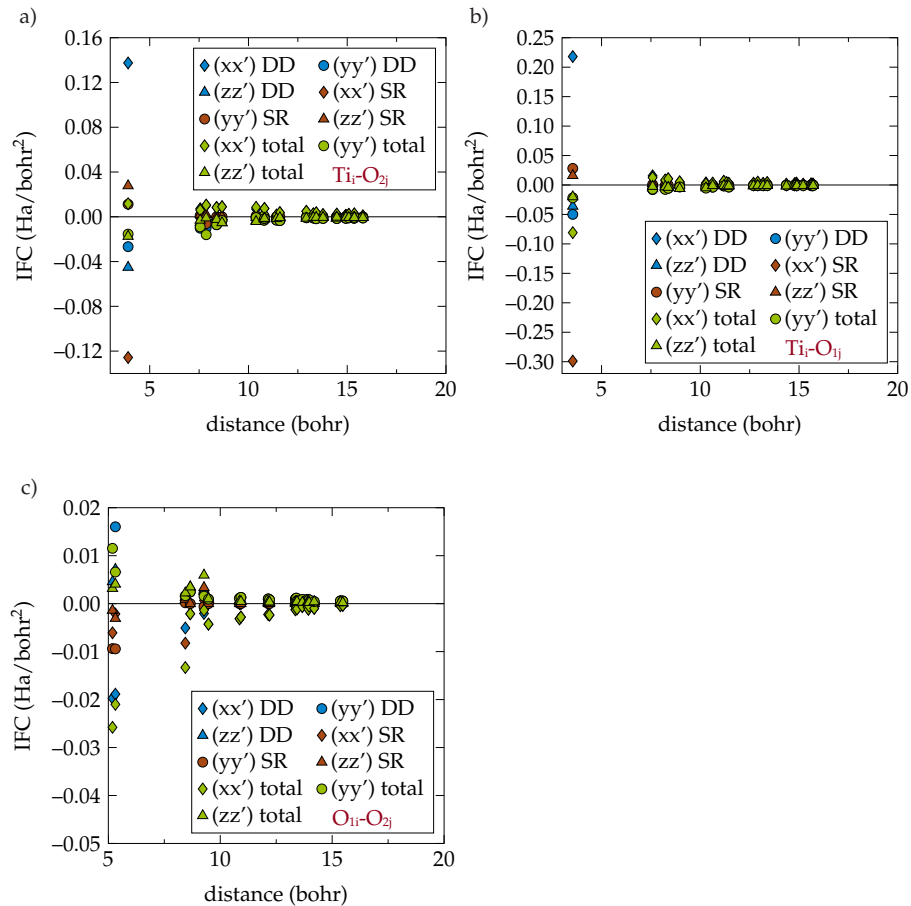


Figure 51: Interatomic force constants as a function of distance in a R₃ structure. The green signs denote the total interatomic force constant, which is a sum of a dipole-dipole (DD) and a short-range (SR) term.

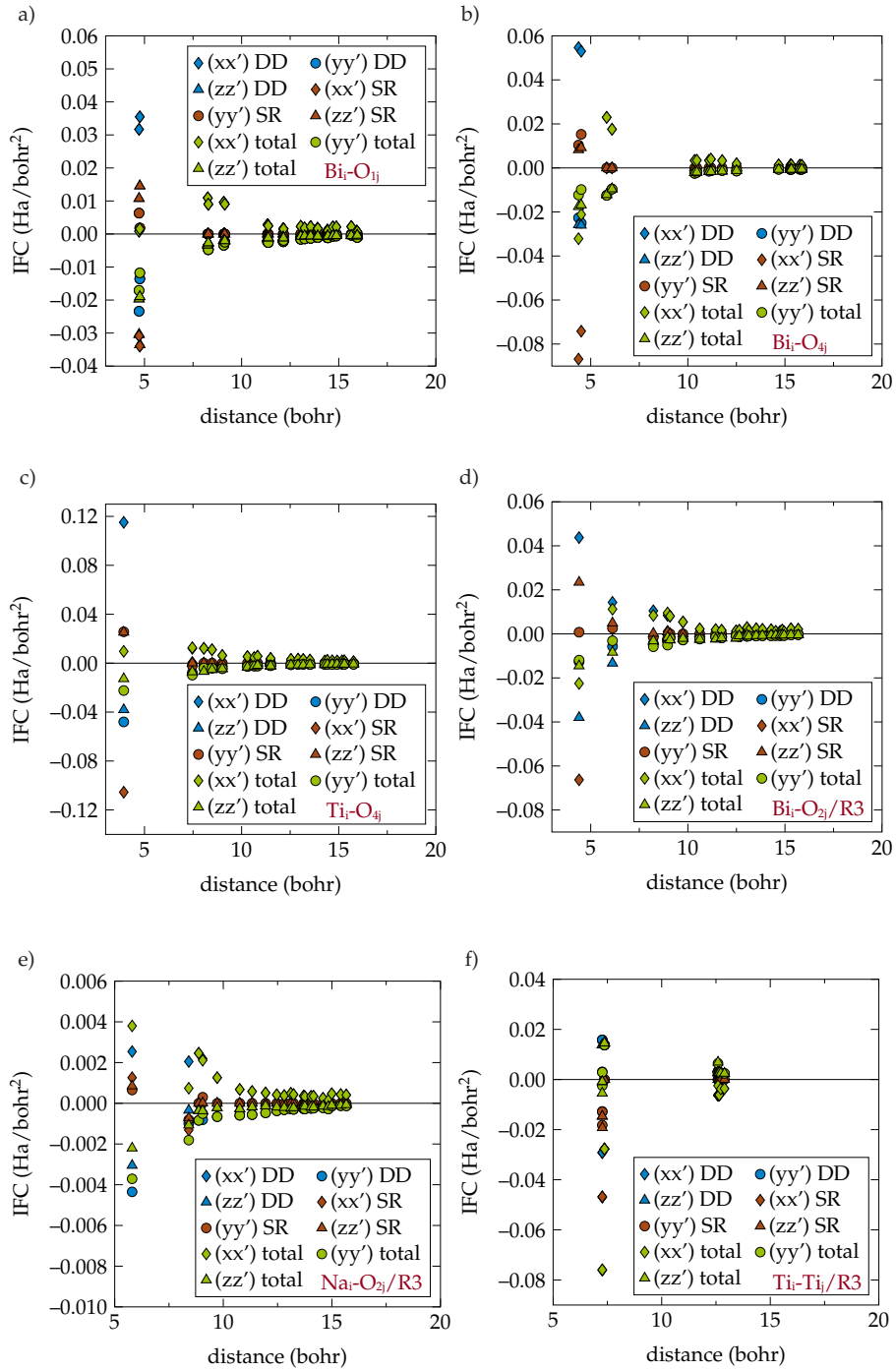


Figure 52: Interatomic force constants as a function of distance in a Pmc2_1 (a-c) and R_3 (d-e) structure. The green signs denote the total interatomic force constant, which is a sum of a dipole-dipole (DD) and a short-range (SR) term.

All impedance spectroscopy measurements in the following chapter have been obtained by Dr. Sebastian Steiner [159] of the nonmetallic-inorganic materials division of the Technical University in Darmstadt and are used with his permission.

In the last chapters, we have learned that the conductivity depends on a delicate interplay between the dopant type and the dopant concentration. Furthermore, the introduction of Mg, Fe, and Al, inevitably involves the formation of defect associates (see Equation 10) between the acceptor dopant and the oxygen vacancy. However, we have little knowledge of energetics, relaxation processes, chemical bondings, and electronic structure changes after introducing a dopant. These physical responses are essential to optimize the defect chemistry in NBT, following the principle “doping by design” [18]. Thus, in the words of Walsh *et al.* [18], we investigate in the following the “defect tolerance” of doped NBT, which is “encoded in the basic genetics and thermodynamics of the host material”. Firstly, we will focus on the vacancy characterization as the mobile charge carrier in different model scenarios (varying chemical and structural environments). We will quantify binding and migration energies, observe local structural rearrangements, and evaluate the model of Chapter 4. For this purpose, we heavily rely on Sections 2.6, 3.9, and 3.11. All in all, this investigation enables us to qualify point defect behavior and presents new insights to model the macroscopic behavior of NBT and NBT-based solid solutions.

6.1 COMPUTATIONAL METHODS

As pointed out in Section 2.3, NBT is characterized by a rich and challenging polymorphism, phase coexistence regions, and topological disorder, leading to deviations of the local from the global structure [2, 57, 73, 153]. In the same section, we explained in detail how we tackled this problem computationally.

In the following, we will concentrate on the rhombohedral 111 -ordered (R_3) and the orthorhombic ($Pmc2_1$) structure, where the A-site cations are arranged in a 001 fashion, and describe the defect chemistry in these ordered configurations. However, we must not forget that the experimentally proven disorder on the A-site sublattice leads to different local chemical environments. Thus, we have to consider absolute values in this, and the following sections as “subset solutions”.

Both symmetries describe the ground state structures of the chosen A-site orders and remain stable after introducing single defects or even defect associates. In contrast, cubic and tetragonal 111 -ordered arrangements develop an antiphase tilt similar to the $a^-a^-a^-$ pattern in the R_3 structure after introducing the defect associate. We will discuss this issue in the following sections in greater detail and only partially consider the tetragonal structure. For the advocates of a global Cc structure, we refer to

Reference [382], in which the authors demonstrate the similarities between the chemical bonds in R_{3c} and Cc. Thus, we assume that the results are equivalent or show the same trend in both structures.

In our studies, we noticed that the standard DFT is a highly competitive method in the case of NBT such that we used the calculation setup addressed in section 3.1. We rely on the supercell approach to allow for disproportionation (polymorphous local environments for the same atom type) in all calculations. Thus, we use an appropriately flexible cell to permit symmetry breaking. We use a simulation cell containing 320 atoms in the defect-free state, which corresponds to 64 formula units of Na_{0.5}Bi_{0.5}TiO₃. The wave function is expanded in plane waves up to a kinetic energy cutoff of 600 eV. We replace the integral over the Brillouin zone by sums on a 2×2×2 Γ -centered mesh of special \mathbf{k} -points for the examination of binding energies and use a Γ -point calculation in more complex simulations. The latter are, for instance, dopant clusters, solid solutions, or doping by a natural off-stoichiometry. However, differences in the energies are in the range of 0.5 meV per formula unit, and all important features of the electronic structure are correctly reproduced (gap size, bandwidths, local properties [387]).

After introducing the defects into the lattice, we solely relax the atomic positions while fixing the volume and the shape of the simulation cell to the equilibrium GGA bulk value. We do not employ any symmetry constraints during the minimization of the lattice energy to remove any limitations on the relaxation of the ions (P1 space group) [36].

In Section 3.9.3, we described that the size-dependent interaction between defect images could strongly influence the energy and the aperiodic charge density in a charged supercell calculation. We encounter this issue in the case of an isolated Al/Fe dopant and the presence of a twofold positively charged vacancy. We suggest that, Al³⁺ and Fe³⁺ are the preferred formal charge states, leading to a positive net charge of the simulation cell (see Chapter 8 for a more detailed discussion). However, in the present chapter, we circumvent expensive corrections by concentrating solely on the same charge state's energy differences.

The binding energies or association energies are determined by the energetic minimum of the oxygen vacancy with a gradually increasing distance to the dopant. We choose an oxygen vacancy at approximately 11 Å as a reference. The reason for this specific choice will become clear in the remainder of this chapter. The migration barriers are determined by NEB calculations (see Section 3.11).

6.2 BINDING ENERGIES IN DIFFERENT MODEL SCENARIOS

As mentioned in the short introduction of this chapter, we initially deal with the electrostatic interactions between the oxygen vacancy and an acceptor dopant. We will preliminarily investigate how different local relaxation patterns around the defect associate influence the binding energy. In the first part, we will focus on the oxygen polyhedral relaxation after introducing a defect associate and compare the results to the isolated vacancy. As the long-range ordering of oxygen octahedral tilts is also coupled to the surrounding cations' displacements, we further examine the amount

and consequences of the cation off-site displacement [2, 64, 388].

6.2.1 Defect association leads to a local displacement disorder

Figure 53a) shows the distribution of tilt angles after the relaxation process. The absolute tilt angle is given in the axis-angle representation for the oxygen octahedron rotation. The dashed lines represent the two prevailing octahedral rotations of the $a^-a^-a^-$ bulk structure, illustrating that they are almost but not totally symmetric. After minimizing the forces in the doped structure, we obtain a distribution of tilt angles within the whole structure. In all defective supercells, a few tilt angles are noticeably larger than the bulk angles.

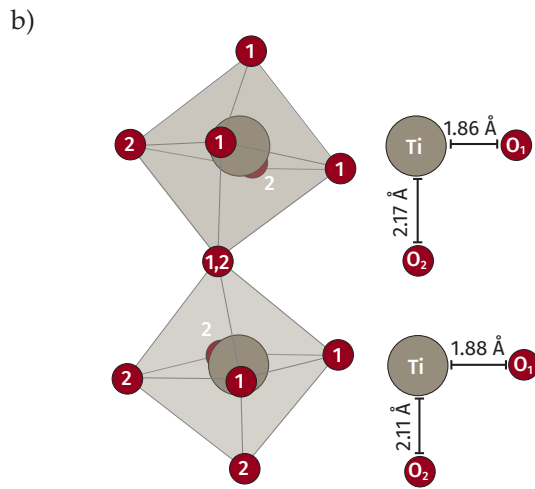
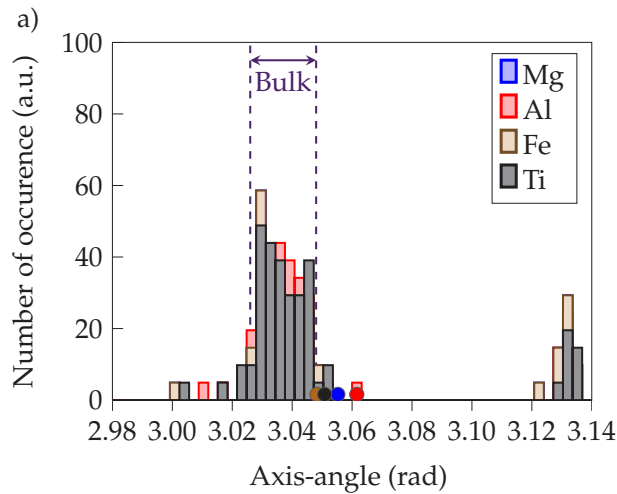


Figure 53: a) shows the distribution of octahedral tilt angles after introducing a dopant-vacancy complex or an isolated vacancy. The circles describe the rotation of the dopant octahedron in an axis-angle representation. Figure b) depicts two different oxygen vacancy positions on the first neighbor shell of a dopant in the R3 symmetry for both tilt directions.

However, these tilts do not belong to the dopant octahedra, which are indicated by the circles at the bottom of the graph. Although they do not significantly differ from

the bulk values, they can be found at the tail of the distribution for every investigated dopant type. Al shows the largest deviation, shortly followed by Mg, Ti, and Fe. The strong similarity between Fe and Ti can be related to d-electrons in both systems and a similar size. Nevertheless, the small difference between the polyhedral tilt around the varying dopant types suggests that the size or charge of the B-site cation has no significant influence on the change of the tilt angle.

Choi *et al.* [389] observed the formation of an anti-phase tilt even in STO after introducing an oxygen vacancy into the structure. This shows that even in cubic host lattices, the $a^-a^-a^-$ tilt seems to be the optimal arrangement around the vacancy. Thus, it is reasonable that there is hardly any driving force to destroy a preferred tilt pattern in NBT.

Conceptually, this reminds of the antiferrodistortive (AFD) instabilities along the R-M line of the Brillouin zone, which corresponds to planar instabilities in real space rather than isolated ones [92, 131, 390]. A single local distortion can not destroy the long-range order of the remaining structure. The results further demonstrate a cooperation between the polar and the anti-phase tilt in the R₃ host lattice and that they are not entirely independent at the equilibrium volume [2].

Interestingly, such a restriction has not been observed in $\text{Na}_{1-3x}\text{Bi}_x\text{NbO}_3$, where A-site vacancies significantly distort the long-range correlation of the oxygen octahedra network. This shows that the effect of defect dipoles and the presence of single A-site vacancies on the chemical surrounding is different [388]. However, note that since every Bi substitute introduces two vacancies on the Na-site, the total defect concentration exceeds the number of defects that can be reasonably treated in a DFT approach. Furthermore, the results have been obtained for x larger than 0.1, making it difficult to compare both scenarios at the same defect levels.

Another possible reason for the stability of the anti-phase tilt mode in the presence of a defect dipole can be the symmetry-conforming property of point defects [391, 392]. The symmetry-conforming property states that when the equilibrium is reached, the symmetry of the short-range order distribution of point defects has to follow the crystal symmetry [391, 392]. We learn two things from this property in the context of NBT. First, we deduce different defect probabilities on the two inequivalent oxygen positions of the R₃ structure (see Figure 53b). These will be explored in the next section in greater detail. Secondly, we expect that the defect associate's dipole moment favorably aligns to the direction of the spontaneous polarization in the bulk phase. The preference for a collinear alignment of both polarization vectors, the bulk and the defect dipole polarization, has already been analyzed in a systematic study about dipole reorientations in doped and tetragonal PbTiO_3 by Erhart *et al.* [147]. We suggest that this polarization alignment restricts the oxygen octahedral tilt relaxation directly at the dopant site in NBT, leading to small deviations from the ideal tilt angle only. Although the bonding direction does not coincide with the direction of the spontaneous polarization in the R₃ space group ([111]-direction), a severe local reduction of the tilt amplitude (towards a cubic octahedral arrangement) would exacerbate it even more. Figure 54 schematically shows two possible arrangements for a defect associate between an oxygen vacancy and a dopant in rhombohedral 111-ordered NBT. From these illustrations, we understand that case 54a) should be energetically

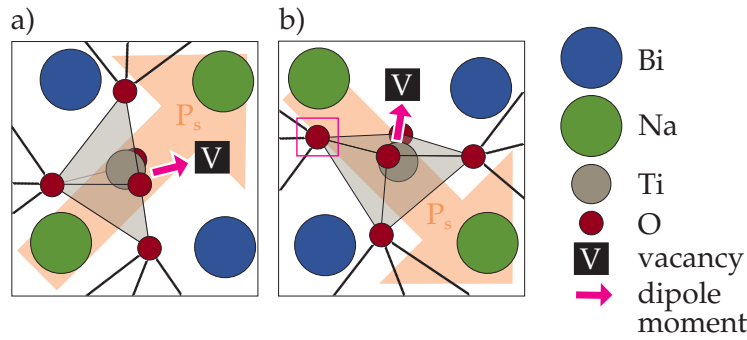


Figure 54: Relationship between the defect dipole and the spontaneous polarization for two different vacancy positions in a R3 host symmetry. Figure a) shows a vacancy at a distance of 1.88 \AA away from the dopant. In Figure b) the vacancy has been introduced at an oxygen position with an original bond length of 2.11 \AA .

avored. If we would generate a vacancy on the position marked by a pink square in Figure 54b), we would obtain an anti-parallel orientation.

Figure 55 shows the ionic displacements as a function of the distance from the acceptor dopant in the R3 supercell of NBT. In total, we selected three representative model scenarios to discuss the effect of a defect dipole, an almost dissociated defect pair, and a dopant-vacancy cluster on the structural relaxation processes. Since the displacement distribution is similar for all dopant types, we restrict our presentation to Fe only.

In cases where the vacancy resides on the nearest neighbor position of a single dopant (Figure 55a), the largest displacement amplitudes can be found at the dopant itself, as well as the O and the Bi ions in close vicinity to the dopant. Nevertheless, we observe deviations from the undisturbed bulk structure even at regular lattice sites in the neighborhood of the defect associate. Based on the DFT data, we suggest an impact radius around the defect between 12 \AA and 13 \AA . Note that this does not exclude long-range dipole-dipole interactions above this radius. We further note that not all O ions on the defective octahedra are displaced by the same amplitude, which is consistent with the stability of the long-range $a^-a^-a^-$ oxygen tilt ordering. The small tilt disorder did not lead to a complete disruption of the global anti-phase oxygen octahedron tilt pattern (no *complete* disturbance of the long-range order). Instead, if the defect pair is almost dissociated (Figure 55b), the displacements of the nearest bismuth and oxygens are less pronounced. Only the off-site motion of one Ti close to the vacancy is especially noticeable. This suggests that the A-site displacement disorder is more distinct in the presence of a defect dipole and less pronounced for isolated oxygen vacancies. At this point, we might deduce that a local A-site disorder is beneficial for the oxygen vacancy from an energetic perspective. Below, in the context of association energies, we will learn more about the A-site disorder. Precisely, we analyze how this disorder and the orientation of the defect associate are related, and how the A-site displacement influences the association energy of the defect pair. We further examine how the A- and B-sites are covalently interrelated with the oxygen sublattice.

A reduction of the A-site displacements can also be observed for a defect cluster

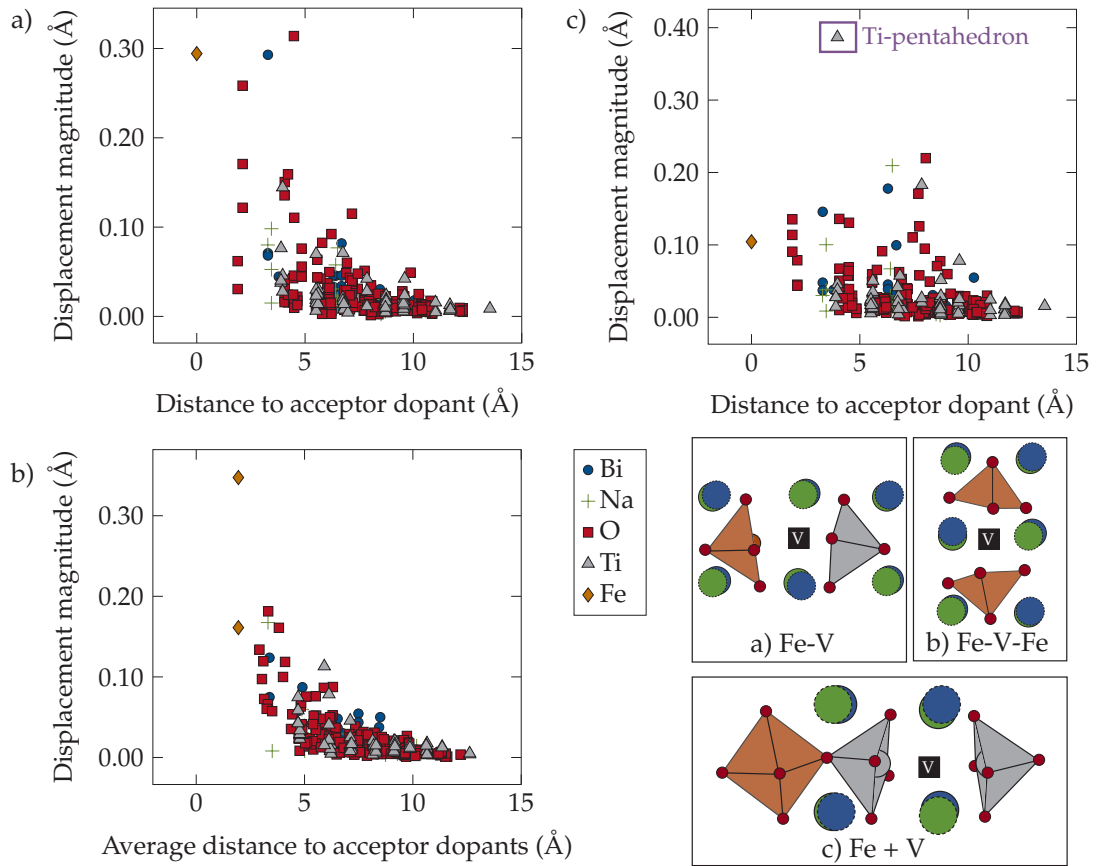


Figure 55: Ion displacements upon introducing a $(\text{Fe}_{\text{Ti}}'-\text{V}_{\text{O}})'$ defect associate in a), a $(\text{Fe}_{\text{Ti}}'-\text{V}_{\text{O}})'-\text{Fe}_{\text{Ti}}'^x$ defect cluster in b), or a higher-order defect pair with a Fe_{Ti}' dopant and an oxygen vacancy V_{O} in c). The insets on the lower right side schematically illustrate the exact arrangements.

out of two Fe acceptor dopants and an oxygen vacancy (Figure 55c). Here, the ionic displacement is plotted as a function of the average distance to both dopants. The observed reduction might be related to the two partially compensating defect dipole moments such that the resulting net dipole is less coupled to the bulk polarization. This extinction occurs if the oxygen vacancy resides in the middle of both dopants. We will explain this idea in more detail below.

From the distribution of the tilt angles and the ionic displacements, we deduce that the relaxation is *not* completely confined to the nearest neighbors of the dopant but extends beyond the bonding length. This reminds of a “butterfly effect” [393], where a “defect driven symmetry breaking” forms extended regions with a changed polarization (coupling between the local defect dipole with the bulk ferroelectric) and non-local elastic fields [388, 393, 394]. Put simply, a single dopant affects the nearest neighbors, which initiate a displacement on the second neighbor shell and so on. The amplitude of this off-site displacement reduces with an increasing number of neighbor shells until the difference to the regular host pattern becomes negligible. These ionic displacements, caused by the dopant, the oxygen vacancy, and the formation of a defect associate, locally change the polarization and, therefore, the host’s properties.

Remember Figure 44, where we saw that already a change of 20 % in the amplitude of the polar mode could change the polarization by about $12 \mu\text{C cm}^{-2}$. Although these calculations have been performed in the $\text{Pmc}2_1$ structure, these results give us a sense of how much the local polarization can change with deviations from the equilibrium host pattern in NBT. The driving force for atomic displacements is not solely long-range dipole-dipole interactions but rather unfavorable bonding environments in an interconnected oxygen polyhedra network.

Since there is hardly any difference between the extent of defect-induced off-site displacements for all three dopant types, the dopant's size or charge does not have a decisive influence on its impact radius. This correlates with the observation of similar conductivities for all three dopant types at medium concentrations in the range between 1 % and 1.5 % in Figure 17. This range approximately reflects the dopant concentration used in the supercell of the present calculations.

6.2.2 Energy lowering by the formation of defect associates

Figure 56a) compares the energy between a structure with a vacancy residing at x to a configuration, where the vacancy is located at approximately 11 \AA . This is the farthest reference point in our setup. We use the dopant cation position as the origin and determine all defect coordinates in the unrelaxed supercell.

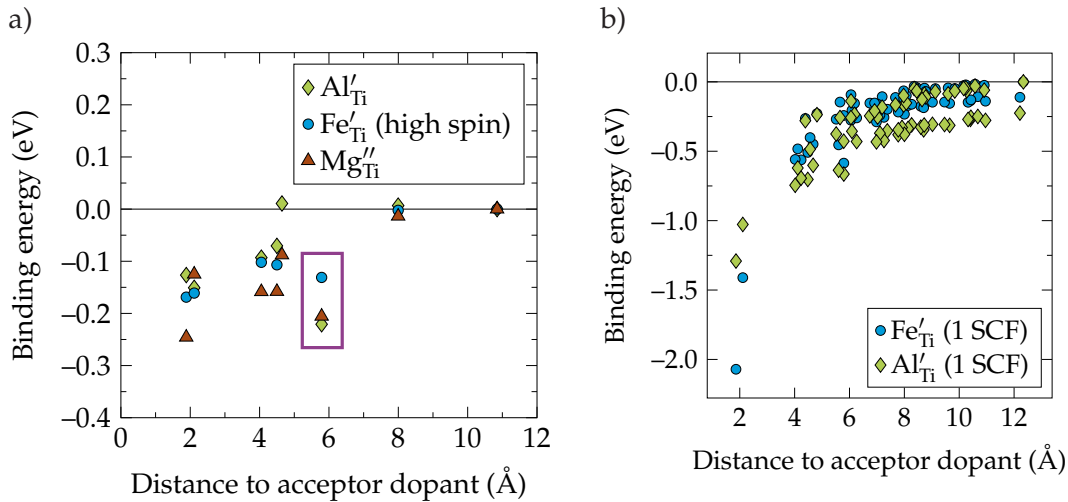


Figure 56: Binding energy between the oxygen vacancy and a) an acceptor dopant (Mg, Al, and Fe) on the B-site after relaxation and b) an acceptor dopant (Fe and Al) after a single self-consistent cycle (no relaxation of the ions) in the R_3 structure.

In all three cases, Al-, Fe-, and Mg-doped NBT, we observe a tendency to form defect associates. If the vacancy is located on the first nearest neighbor shell, we receive an average energy gain of about -0.15 eV for all dopant types. However, although the vacancy positions and the A-site order remains equal for all dopant types, we recognize slightly different trends and structural preferences for different acceptor species. We start in the first coordination shell, where the oxygen vacancy has been generated either at approximately 1.87 \AA (V_O^1) or 2.14 \AA (V_O^2) as shown in Figure 53b). First, Al-doped and Fe-doped NBT show rather similar association energies of approximately

0.15 eV for both oxygen positions, despite a small energy difference amounting to approximately 0.02 eV. A larger deviation can be observed for Mg with association energies of 0.25 eV and 0.12 eV, respectively. The calculated association energy between Mg and the oxygen vacancy is approximately half of the value obtained by Meyer *et al.* [156], which can be related to a different exchange-correlation potential (LDA) or a symmetry constrained relaxation procedure.

If we again consider the symmetry-conforming property of the last section [391, 392], the deviation between the association energies for V_O^1 and V_O^2 can be related to the different orientation of the defect dipole moment with respect to the spontaneous polarization of the host lattice. Since the dipole moment is generally more significant in the case of Mg (higher defect charge), the “alignment effect” becomes more obvious than for Fe- or Al-dopants. Indeed, in Fe-doped NBT, we notice only a minor deviation between the two oxygen vacancy positions, which are much smaller than half of the energy difference in Mg-doped NBT. Interestingly, we observe the opposite for Al-doped NBT, where a vacancy at the O_2 -position seems to be preferred.

To find an explanation for this inverse trend, we studied the average bond length, the volume of the defective polyhedron, and the coordination of the dopant. If we take a closer look at the final, relaxed positions of the different vacancy positions, we identify that similar rearrangements take place. Furthermore, the average bond length in the irregular square pyramid (henceforth, we will loosely call this a pentahedron) is comparable for both nearest-neighbor vacancy sites.¹ The adjacent oxygen atoms relax slightly toward the vacancy as a result of their Coulomb attraction. All dopant types move toward the oxygen atom opposite to the oxygen vacancy irrespective of the initial (bulk) polar displacement, decreasing the oxygen dopant bond compared to the remaining oxygen neighbors.² However, this effect is larger if the vacancy is generated at O_2 since the dopant induced and the natural polar displacement are superimposed. Otherwise, the volume and the average bond length are larger, and the average coordination of the defective polyhedron is slightly smaller for a vacancy on O_2 . Hence, this position should be energetically less favorable as it is in Mg- and Fe-doped NBT. The only difference we can observe in Al-doped NBT is a slightly larger relaxation of the neighboring oxygen ions toward the oxygen vacancy at O_2 . This might outweigh all other “geometrical frustrations”, although the difference is not significant and more statistic is needed for a conclusive statement.

After noticing that the association tends to be position-dependent, while the average bonding lengths and polyhedral volumes are not significantly altered, it might be a good idea to return to the Bi^{3+} and Na^+ displacements.

¹ The average bond length within a dopant pentahedron amounts to 1.89 Å for Al, 1.98 Å for Fe, and 2.05 Å for Mg.

² The shortest dopant-O bond shrinks by about 14.38% (vacancy at O_2) or 5.04% (vacancy at O_1) for Al-doped NBT and by approximately 9.65% (vacancy at O_2) or 0.19% (vacancy at O_1) for Fe-doped structures. In Mg the bond to O_2 is reduced by 5.91% (vacancy at O_1), while the one to O_1 is expanded by 3.53% (vacancy at O_2). These values refer to the equilibrium bulk Ti-O bond length.

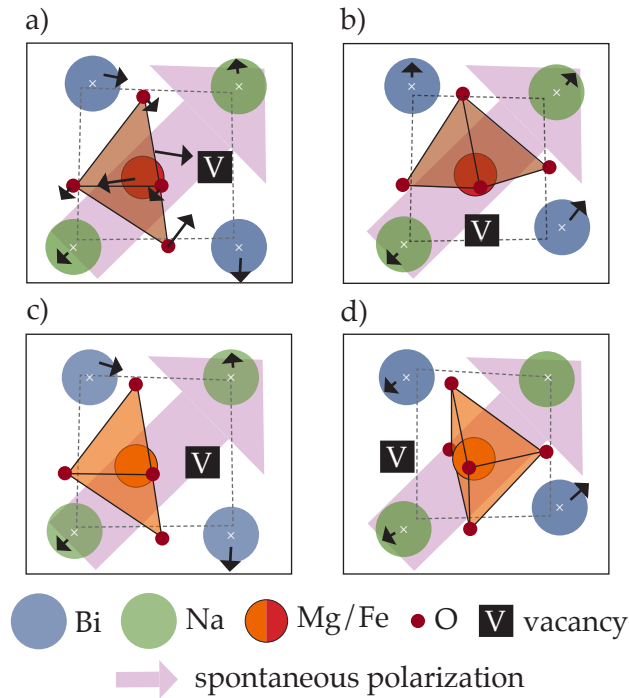


Figure 57: A-site cation displacement caused by acceptor doping or oxygen non-stoichiometry. Figures a) and b) describe different oxygen vacancy configurations with an Fe acceptor dopant on the B-site. Figure c) and d) depict a second set of two different Mg-vacancy associates, leading to off-site displacements on the A-site sublattice. A detailed description of the ionic displacements can be found in the main text. Blue ions represent Bi, while green ions describe Na cations. The corners of the dashed polygon indicate the original positions of the A-site cations, while the white crosses are the centers of the displaced Na- and Bi-ions. We mark the displacements of the ions upon relaxation by black arrows. For clarity, we included the displacements of the dopant and the oxygens in Figure a) only. However, they are analog in the other scenarios. The big, violet arrow in the background specifies the direction of the spontaneous polarization in the R3 host symmetry and the V on the black square defines the position of the oxygen vacancy.

In Figure 57a), 57b), 57c), and 57c) we see four different dopant-vacancy associates for two different acceptor dopants, namely Fe and Mg. A comparison between Figure 57a) and Figure 57c) clearly shows the qualitative similarity in the host lattice's structural response upon acceptor doping, regardless of the dopant type. The black arrows on the A-site indicate the direction of the Bi^{3+} and Na^+ relaxation and show that in comparison to the regular A-site off-centering, the displacement amplitudes of Bi^{3+} in the host lattice are either reinforced (57b) and 57d)) or weakened (57a) and 57c)). The displacement magnitude of the upper left Bi in Figure 57d) is relatively small such that we suggest an overall strengthening of the regular off-centering. Thus, different oxygen vacancy positions involve various A-site rearrangements, which can compensate for the local perturbation more or less. This leads to scattering in the energy for vacancy positions on neighbor shells.

Indeed, at approximately 6 \AA (third neighbor shell, marked by a violet rectangle in Figure 56), we observe a similar structural environment compared to 1.87 \AA , which explains the noticeable drop in the energy-distance curve. This position is equally favorable in Mg-doped samples but not energetically more stable than an associate

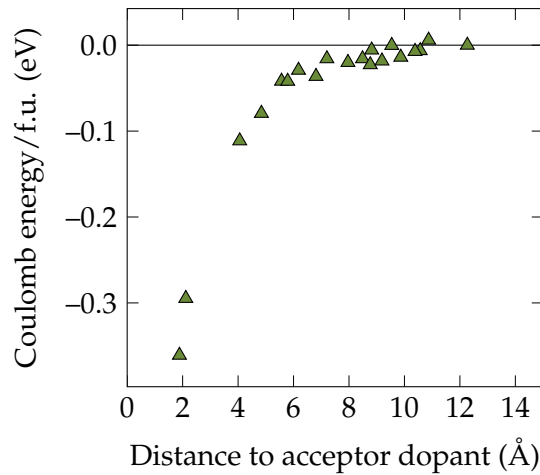


Figure 58: Coulomb energy of the (unrelaxed) supercell as a function of the distance between an oxygen vacancy and a Mg-dopant.

on the first neighbor shell. We relate this to a reduced Coulomb interaction, which is an important driving force for defect association [366]), with an increasing distance.

We can understand this reduction from Figure 58, where the electrostatic energy per formula unit for various dopant-vacancy distances is depicted. In this exemplary calculation for a Mg acceptor dopant, we use the ions' nominal charges and refer to the unrelaxed structure. The same trend as in Figure 56 can be observed, showing that the electrostatic energy decreases non-linearly with the distance to the dopant.

Interestingly, the drop at 6 Å is less sharp in Fe-doped NBT and even leads to an energy gain in the case of Al doping. The latter indicates that the nearest neighbor defect associate is less favorable in Al-doped NBT than a higher-order associate [366]). The difference between Mg and Fe might be explained by a higher formal oxidation state (3+) of Fe compared to Mg, which, in consequence, results in a smaller defect charge (1-). However, since Al carries the same formal charge as Fe, the change in Coulomb interaction should not be the only factor for the energy decrease in the case of Al-doped NBT. Considering that Al is the smallest dopant, the energy gain could be related to the dopant's elastic interaction with the host lattice. This assumption would confirm the observations of Kilner *et al.* [152], who proposed that the elastic strain energy introduced by the dopant and caused by a size mismatch between host and dopant cations can dominate over the Coulomb interaction. It would also explain the slightly larger octahedral tilt relaxation depicted in Figure 53a). Another possibility to explain the difference between Al and Fe might be varying covalent contributions, which would mainly result from the presence of occupied transition metal d-orbitals. We will analyze the covalent and the elastic contribution in greater detail in the subsequent chapters.

After exceeding 8 Å, which corresponds to the fourth neighbor shell, the association energy has already been substantially reduced. It should be noted that the choice for a suitable reference configuration is limited by the simulation cell size and therefore does not necessarily represent the case of entirely negligible defect interaction. Nevertheless, Figure 56 shows that the binding energies converge to zero at high distances,

justifying our choice.

To qualify the effect of local ionic relaxations on the association, we calculate the energy for several oxygen vacancy positions, performing a single self-consistent step. That is, we fix the ions on their ideal bulk positions and relax the electronic system for this fixed set of nuclei positions only. Such simplifications drastically reduce the computational effort and give an idea of the potential energy surface for this specific configurational subspace. Figure 56b) shows the final energy-distance curve, where we used the same conventions as in Figure 56a). The first and most striking difference compared to Figure 56a) is the magnitude of the association energy, which increases by almost 2 eV in the case of Fe and by more than 1 eV in Al-doped samples. Note that the total energies are reduced after relaxing the structure. This shows that local strain relaxations or even compensations significantly contribute to the mobility of the oxygen vacancy [139]. Furthermore, they are the result of a delicate interplay between long- and short-range interactions [107]. In general, both datasets can be divided into two curves representing the two different oxygen vacancy positions in the structure. Interestingly, we can also detect a local minimum around 6 Å for the unrelaxed configurations, even if it is less pronounced.

6.3 A-SITE DOPING DOES NOT LEAD TO THE FORMATION OF DEFECT ASSOCIATES

Since we discuss a possible Bi^{3+} substitution by an Al acceptor dopant in the context of NMR measurements, we present the association energies for A-site Al-doped NBT in Figure 59.

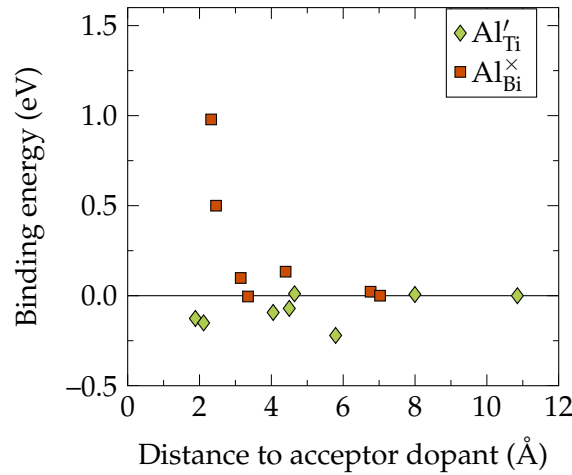


Figure 59: Binding energy between an oxygen vacancy and an Al dopant on the A-site (regular Bi^{3+} site) in comparison to an Al dopant on the B-site in the R_3 structure.

The replacement of a regular Bi^{3+} by an Al^{3+} dopant is called isovalent doping (see Chapter 2) and does not lead to any net charges and therefore to no charge compensating oxygen vacancies. The energy distant curve demonstrates that a first-order associate is energetically unstable and that the absolute repulsive short-range interaction is higher than a possible association to an Al dopant on a regular Ti^{4+} -site. An

investigation of the local relaxation process reveals that large oxygen displacements are necessary to prevent the formation of a high amount of free volume inside the structure. In the case of small defect distances, which is particularly unfavorable, Al is tetrahedrally coordinated. With increasing distance between the vacancy and the defective A-site, we detect a deformed octahedral environment. We conclude that, especially for isovalent doping with a non-transition metal, elastic strain significantly affects the thermodynamics in doped NBT.

6.4 DOPANT CLUSTERS CHANGE THE DEFECT BINDING ENERGY

In physical samples, the doping can exceed the dilute level such that defect dipoles can interact with each other. In the following, we will present the dopant-vacancy interaction for a defect cluster containing two acceptor dopants of the same species. These calculations are important for the analysis of the covalent bonding character in NBT and will serve as a representative example of high doping concentrations. It simultaneously constitutes the limiting case in our A-site ordered simulation cells. We already showed the effect of a second Mg-dopant in 111-ordered NBT in Figure 32 of Chapter 4. Thus, in the following, we will concentrate on Al- and Fe-acceptor dopants.

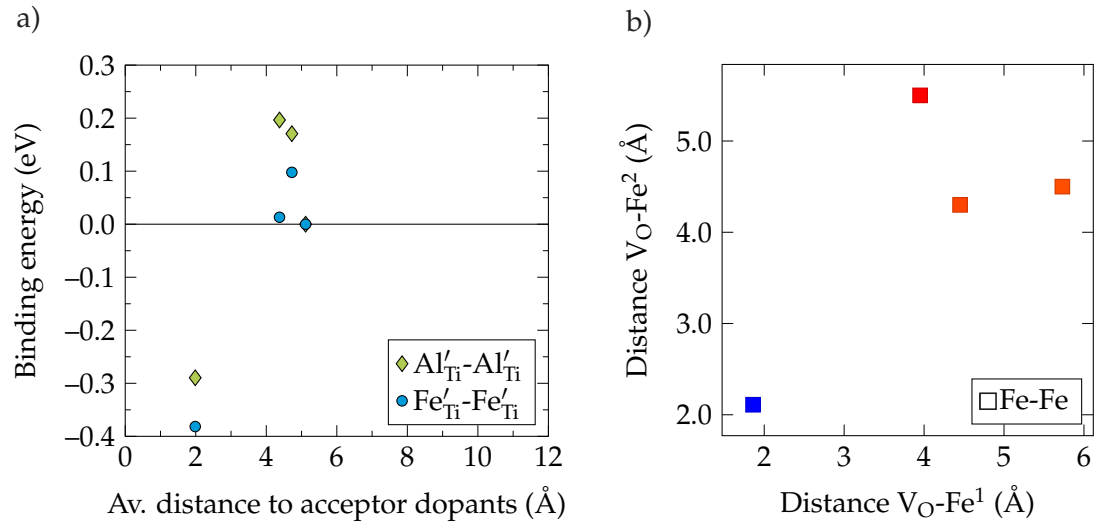


Figure 60: Figure a) shows the binding energy between an oxygen vacancy and a first neighbor Fe_{Ti}' cluster in an R₃ structure with respect to the average distance between the oxygen vacancy and the dopants. Figure b) shows the same results for Fe-doped NBT in a scatter plot, where blue represents low and red high energies.

In Figure 60a) we present the energy-(average) distance curve for an Fe_{Ti}'-Fe_{Ti}' and an Al_{Ti}'-Al_{Ti}' first neighbor cluster. Note that our reference energy is the configuration where the oxygen vacancy occupies the lattice site with the largest distance to the dopants. Since this reference structure does not necessarily constitute a configuration where the defect association is negligible, we must treat the binding energy in Figure 60 with caution. Nevertheless, we can assess the rate of change in the energy with increasing distances from this data set. As in the case of Mg (Figure 32, 1NN) and

as observed by Merkle *et al.* [366], the spacial range of defect association decreases with increasing dopant concentration and even shows a slight repulsive character at about 4 Å. The same data is shown in Figure 60b) as a scatter plot for Fe-doped NBT, where blue represents low and red high energies. In this representation, we do not average out any critical information on interatomic distances and show that the result is unaffected.

Absolute association energies in the range of 0.3 eV and 0.4 eV, which is almost twice as large as for isolated dopants, demonstrate the large Coulomb contribution to the defect association. Note that the presence of a defect cluster leads to a considerable size restriction such that we are limited to rather small distances. However, our data suggest that the defect association should be significantly reduced beyond 6 Å.

Although we obtain the same trend for increasing distances for both dopant types, the association in Al-doped NBT is slightly lower, and the repulsive interaction is slightly larger compared to Fe-doped structures. Again, this can be caused by Al and Fe's size difference, as already explained above. A more detailed analysis of the structural relaxation reveals that, compared to an isolated dopant, similar rearrangements take place. The A-site cations, in particular Bi^{3+} , move away from the vacancy, leading to a local displacement disorder. The main difference between Al and Fe is the slight compression of the coordination polyhedra around the Al dopants.

At this point, we will take the opportunity to shortly describe various possible configurations of two first and second neighbor dopants used throughout the thesis. These are either associated with an oxygen vacancy or dissociated (see Figure 61a). Note that an oxygen vacancy is present in all model scenarios irrespective of the distance between the single defect instances.

In the case of Fe, we additionally investigated the dependency of the energy on the spin arrangements at the dopant site (ferromagnetic vs. antiferromagnetic). The results are depicted in Figure 61b). We reference the data to the energy of the second configuration in the respective spin state. The energy difference between both spin variants is negligible and the total energy shows a local minimum in this particular arrangement.

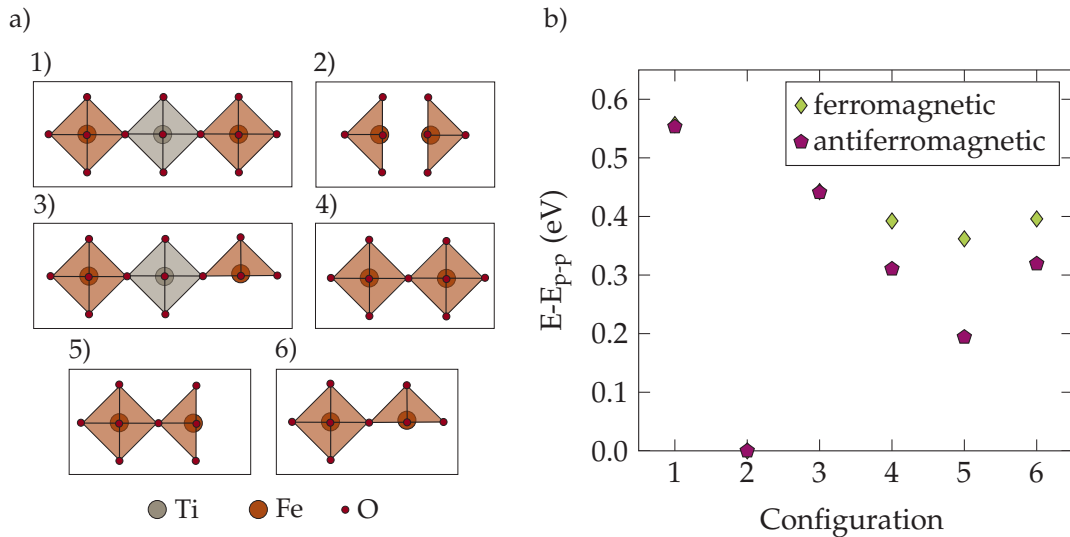


Figure 61: In a) six different dopant cluster configurations are shown schematically for the example of an Fe-doped NBT structure. All simulation cells contain two Fe'_{Ti} dopants and one V_{O} defect. In b) the energy difference between an ferromagnetic and an antiferromagnetic order is shown for the configurations in a). All energies are referenced to the energy of configuration two in the respective spin state. Note that in this configuration each Fe'_{Ti} ion is coordinated by an oxygen pentahedron (specified as p-p) and the energy difference between the ferromagnetic and the antiferromagnetic variation is negligible.

We deduce from Figure 61b) that the actual spin arrangement is only relevant in the case of a first neighbor dopant cluster, where an oxygen atom connects the two Fe dopants (configurations 4, 5, and 6). In this configuration, the energy difference between ferromagnetic and antiferromagnetic arrangements amounts to approximately 0.2 eV. A distinction between ferro- and antiferromagnetic arrangements is irrelevant for all other cases, probably due to the large distance between the two dopants. Especially in the second configuration, the interatomic spacing is too large for a d-d-orbital interaction between the Fe'_{Ti} dopants. Since we are specifically interested in the second configuration, we will exclusively use the ferromagnetic arrangement. However, we have to remember that we might include a systematic error of up to 0.2 eV in our data.

6.5 OXYGEN VACANCY PINNING CAUSED BY NATURAL BI NON-STOICHIOMETRY

Since process-related Bi vacancies can often not be avoided, we will shortly quantify the defect association between an oxygen vacancy and a threefold negatively charged bismuth vacancy.

Figure 62 demonstrates that the association between both vacancies can even exceed the interaction between a dopant and an oxygen vacancy and decreases continuously with increasing distance. Note that in this setup, we are also limited by the simulation cell size.

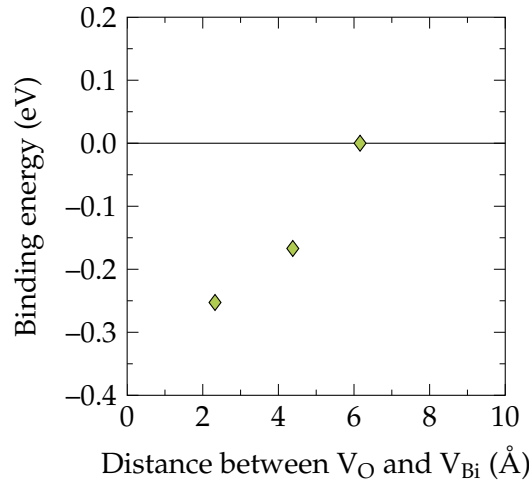


Figure 62: Binding energy between an oxygen vacancy (V_O) and a bismuth vacancy (V_{Bi}''').

Besides an outward relaxation of the neighboring oxygens, we observe a displacement of the host Ti ions toward the Bi-vacancy. The latter is not restricted to the neighboring Ti ions but reduces substantially for higher coordination shells. However, our results suggest that Bi-vacancies can trap oxygen vacancies in close vicinity, which contrasts with the results of Meyer *et al.* [156]. They observed a global minimum on the second neighbor shell and attributed this to an unfavorable mechanical interaction. In turn, they strongly support the findings of Zhang *et al.* [395], showing that A-site vacancies increase the activation barrier for oxygen vacancy migration, especially if the missing A-site ion is Bi^{3+} . In addition, Levin *et al.* [388] observed a modulation of the oxygen displacements in the presence of A-site vacancies in Bi-substituted $NaNbO_3$. This leads to a local reduction of the tilt amplitude and is therefore comparable to a replacement with Ba on the same A-site (see experimental measurements to NBT-6BT in Chapter 2 and the next section).

6.6 THE EFFECT OF NBT-BT SOLID SOLUTIONS ON DOPANT-VACANCY ASSOCIATIONS

In the introductory section, we learned that NBT-based solid solutions are of primary interest for most practical applications. Thus, in the following, we will investigate a subset of possible configurations, where we substitute either Na^+ (Ba'_{Na}) and Bi^{3+} (Ba'_{Bi}) or solely two Bi^{3+} by Ba^{2+} . This corresponds to a concentration of approximately 3%, if we consider the whole A-site sublattice as valid defect sites. We additionally introduced a $Fe'_{Ti}-V_O$ defect associate into the structure, which is located at a fixed position inside all investigated R_3 host supercells.

A vast number of possible configurations have been generated with the help of the superlattice program [396]. This method applies a combinatorial structure-generation approach for atomic substitutions. The structures are categorized by their Coulomb energy, using the formal charge state of the ions in the crystal. We use the same terminology and choose nine high and nine low Coulomb structures. For comparison, we randomly select four additional configurations.

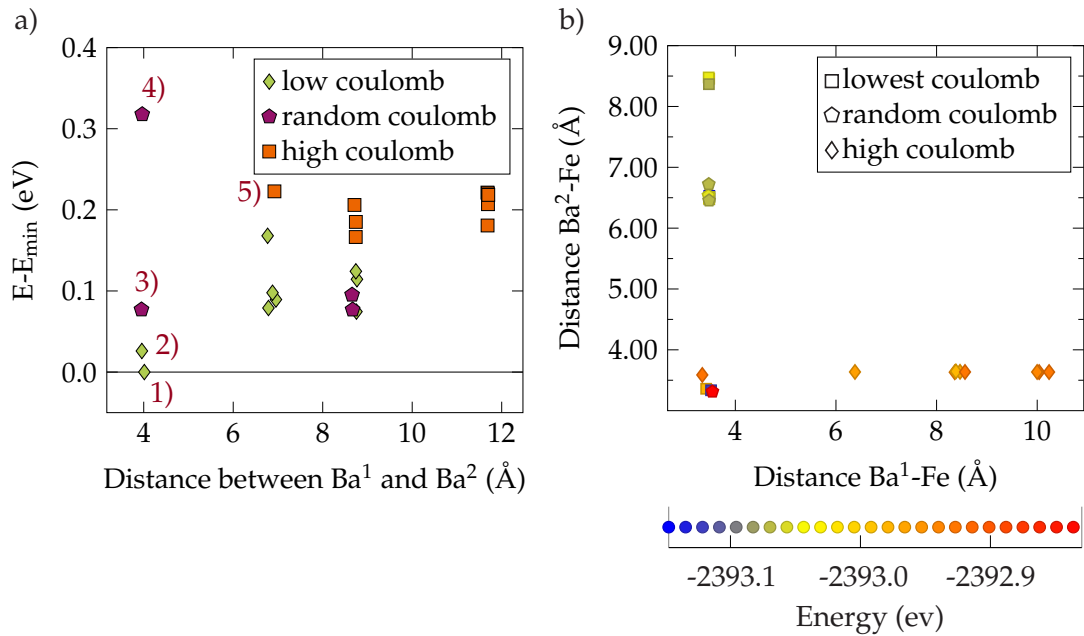


Figure 63: Energies for a Fe-oxygen associate in a NBT-3BT solid solution with different Ba distributions. Figure a) shows the energy with respect to the distance between the two Ba ions. The energy is referenced to the minimum energy configuration. The five numbers mark the five configurations, which we will describe in greater detail in the main text. Figure b) provides a different view on the same data. Here, we plotted the energy encoded by the color gradient over the distance between Fe and the two Ba ions.

Figure 63 depicts the energy for several NBT-3BT configurations containing a first-order $Fe'_{Ti}-V_{\dot{O}}$ associate. Our results confirm that the rough estimate of the supercell program provides an accurate classification of the energies in this solid solution model. Although we can not cover the whole parameter space, even with a fixed dopant-oxygen associate, almost all “high Coulomb” test cases possess higher energies than the configurations of the other subsets. There is only one exception at approximately 4 Å of the randomly chosen defect structures.

If we consider both graphs in Figure 63 in greater detail, it is challenging to formulate universal design rules. In most cases, the energy not only depends on the distance between the two Ba^{2+} ions or the distance between Ba^{2+} and Fe^{3+} but also on the exact lattice site they occupy. This becomes particularly noticeable around 4 Å in both figures, where we observe a considerable spread compared to the energies of the whole data set.

To illustrate the sensitivity of the energies with respect to the local chemical and structural environment, we will take a closer look at the exact ionic arrangements in the four configurations at 4 Å, and one “high coulomb” configuration at approximately 7 Å. For clarity, we schematically draw the five different configurations, which are analyzed in Figure 63a), in Figure 64.

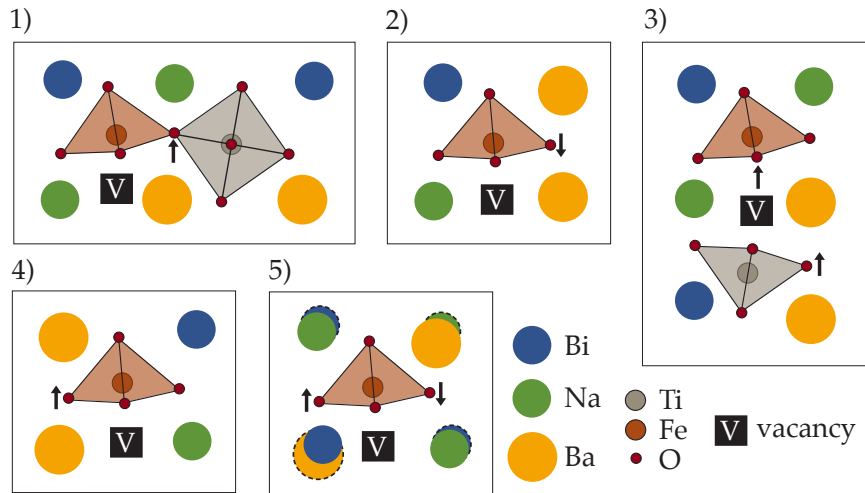


Figure 64: Five different NBT-3BT configurations with a Fe-oxygen associate. These configurations correspond to the energies which are marked by a number in Figure 63a). If needed, we used a dashed line to indicate atoms in the foreground. The small arrows at the edges of the coordination polyhedra of Ti or Fe denote a change in the tilt angle. For clarity, we did not draw any oxygen ions. However, their presence and displacement has been taken into account by the tilt of the coordination polyhedra.

Similarly to pure NBT, we observe a weakening or an enhancement of the natural pseudo-Jahn-Teller distortion³ of the A-site cations. Mostly this displacement is accompanied by a small outward relaxation away from the positively charged oxygen vacancy. However, we observe additional effects, which are predominantly caused by the large size of Ba^{2+} . For comparison, Ba has an ionic radius of 1.61 Å, the one of Bi amounts to 1.17 Å, and the radius of Na is about 1.39 Å [397]. The small arrows at the coordination polyhedra indicate a reduction of the tilt angle (configurations 2, 3, 4, 5). We notice a slight increase in the tilt angle only in the first structure. Furthermore, a Ba-displacement toward the center of the AO_{12} polygon (similar to cubic aristotype), locally changes the amplitude of the polar mode. Yang *et al.* [160] reported that a 2% Ba doping in $\text{NB}_{0.49}\text{T}$ is enough to increase the cell volume (larger than in Ca or Sr doped equivalents), and Gröting [2] demonstrated that the anti-phase tilt (Γ_5^- mode) decreases for increasing volume. Our calculations show that this tendency can be observed on the local scale, even if it is relatively small.

In configuration 4, the lower Ba^{2+} replaces a regular Bi^{3+} , which reduces the A-site off-center displacement and increases the free volume in this specific arrangement even more. This might be one reason for a higher energy. In configurations 1, 2, and 3, we observe the exact opposite. Here, Ba^{2+} replaces a Bi^{3+} , which would typically relax away from the vacancy, such that the presence of Ba^{2+} seems to be energetically favorable. If we solely substitute Bi^{3+} , we observe a similar behavior with respect to the tilt angle and the local expansion. The maximum energy difference between the

³ The hybridization between the empty Ti d orbitals with the filled oxygen p orbitals leads to a huge amount of electronic configurations, which are nearly degenerated. A spontaneous distortion removes this pseudo-degeneracy such that the pseudo-Jahn-Teller effect is assumed to be the source for instabilities in high-symmetry configurations. A spontaneous break of the symmetry leads to an added covalence in the distorted state and a gain in energy. For a C_3 point group symmetry the distortion is along the 111 axis, resulting in three short and three long Ti-O bonds [44, 138, 381, 386].

tested configurations amounts to 0.1185 eV. Nevertheless, we always have to keep in mind that these site-specific relaxations are less pronounced in an A-site disordered structure.

Since we are primarily interested in the kinetics of oxygen vacancies, we present the association energies in different model scenarios in Figure 65.

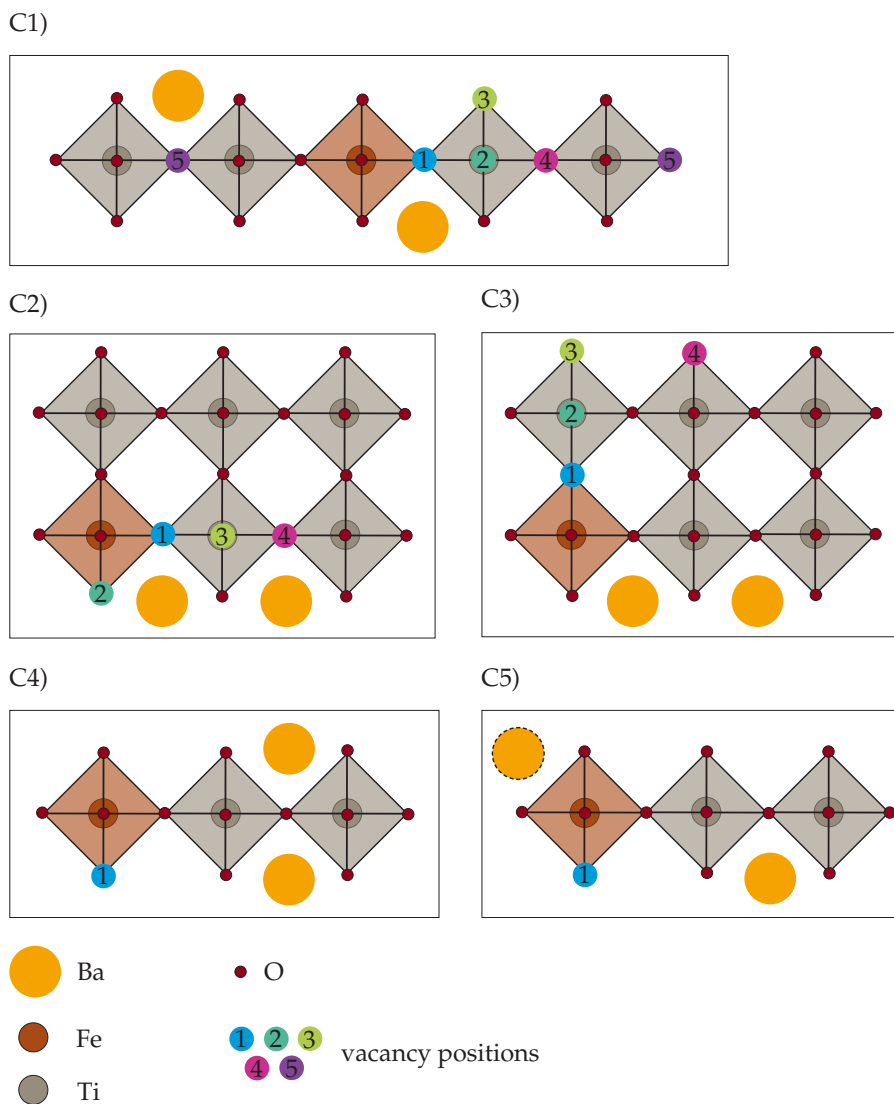


Figure 65: Five different NBT-3BT configurations containing a Fe dopant and an oxygen vacancy for the calculation of association energies. The dashed line at the upper left Ba^{2+} in C5 indicates, that this ion is located in the foreground. The light grey polyhedra in configuration C1 imply periodic images. The colored circles represent various oxygen vacancy positions, which are marked according to their distance to the Fe acceptor dopant. Note that we neglect any octahedral tilts and A-site ions (apart from Ba) in this scheme, although we performed the calculation in the R₃ host lattice.

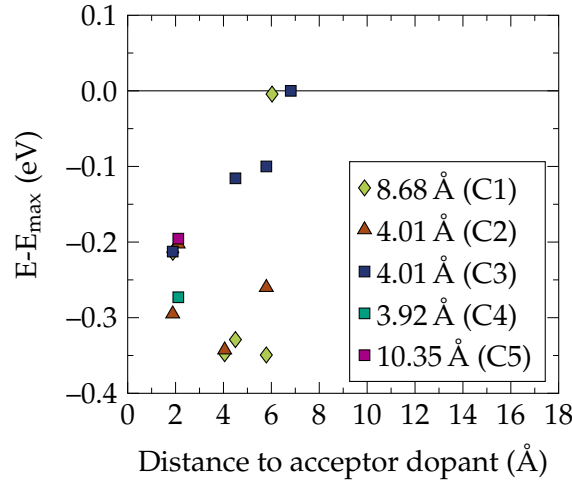


Figure 66: Binding energies between a Fe dopant and an oxygen vacancy in the model structures depicted in Figure 65. The energies are referenced to the maximum energy obtained from all configurations.

In Figure 66, we depict the association energy of a Fe dopant and an oxygen vacancy in NBT-3BT structures, which are shown schematically in Figure 65. Generally, the association energy slightly increases in the presence of Ba ions, suggesting higher defect association energies in the presence of 3% BT. However, this increase depends on the distance between the Ba substituents and the distance between the vacancy and the two Ba ions, respectively. Naturally, we also have to consider the different effective charges of the two Ba ions, namely Ba_{Na}^{\cdot} and Ba_{Bi}' . If the positively charged vacancy resides close to Ba_{Na}^{\cdot} , we notice an increase of the energy.

From Li *et al.* [115] we know that a reduced Bi-O covalence causes a local polarization distortion, leading to variations in the local electric effects. From our study above and recent literature [148, 391], we further know that defect dipoles preferentially align parallel to the overall spontaneous polarization, as far as this is consistent with the host symmetry. Since the defect dipole can not align with the spontaneous polarization in the [111]-direction, we can assume that the local polarization distortion favors defect associate formation.

We further recall Section 6.2, where we saw that: Firstly, the association was most pronounced in areas with high ionic displacements (see Figure 56 and 55). Secondly, the association scatters around an average value in a globally topological disordered structure (see Figure 70 below). Based on this limited data set, we can assume that the percolation of these disordered regions is the reason for an abrupt, non-linear increase of the ionic conductivity with rising dopant concentration.

Figure 67 illustrates both the case of low and high defect concentration. The defective polyhedron has been drawn explicitly, while a grey background indicates the host structure. In turn, a blue circle represents the impact radius of the defect dipole. From this reduced representation of a grain, we deduce that only a network of distorted regions can lead to high ionic conductivities and, therefore, increase the oxygen vacancies' mobility.

Recently, Yang *et al.* [398] proposed a model of large and conductive NBT grains submerged in an isolating small-grained matrix. They assume that the percolation of the large grains constitutes the threshold for a conducting phase, analogous to

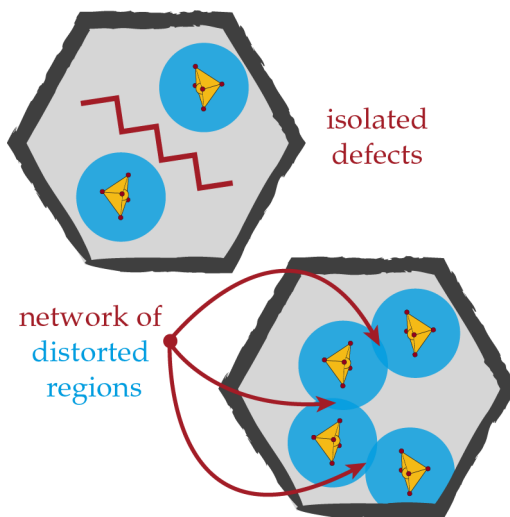


Figure 67: Schematic illustration of two grains with a different defect concentration. The first grain illustrates the case of low defect concentrations, where the impact radii do not overlap. Instead, the second grain shows a network of topological distorted regions, which facilitates the migration of oxygen vacancies.

the overlapping impact radii. However, highly topical ^{18}O diffusion measurements of our experimental partners showed that an inhomogeneous insertion of dopants into the bulk structure is not expected [399]. Hence, the model of non-conducting, small grains is unlikely. Nevertheless, both ideas are inherently related: A high ionic conductivity is induced by a “synergistic effect from the defect chemistry and the microstructure” [398]. However, we consider much smaller length scales and a homogeneous diffusion of dopants into all grains.

A comparison between the datasets C2 and C3 reveals that the local elastic strain field caused by the Ba ions should be localized. If the oxygen vacancy moves perpendicular to lattice plane in which the Ba ions are incorporated, we observe a similar defect association compared to the Fe-doped NBT sample. We further notice a substantial increase of electron density at the oxygen close to the Ba^{2+} ion and opposite to the first vacancy position. In turn, if the vacancy migrates parallel to this plane, we even gain a small amount of energy until the energy rises again at larger distances. This is mainly in the vicinity of the second Ba ion. The only exception is the second vacancy position in the C2 case. Although the vacancy is on the first neighbor shell, the energy is approximately 0.1 eV larger. A comparison to the vacancy-free NBT-6BT structure reveals that the electron holes are delocalized within the whole supercell expressed by small ionic displacements throughout the structure. However, the displacements should be negligibly small at the supercell boundaries to avoid elastic defect-defect image interactions caused by lattice periodicity [400]. This might be one reason for the observed energy difference.

Since the structural degrees of freedom are huge (although we still have not reached the commonly preferred 6% BT within the solid solution) and the calculations are expensive, we have to rely on this relatively small subset solution. Without being exhaustive, we will mention at this point that $(\text{Na}_{0.5-x}\text{K}_x)\text{BT}$ with $x=0.03$ behaves

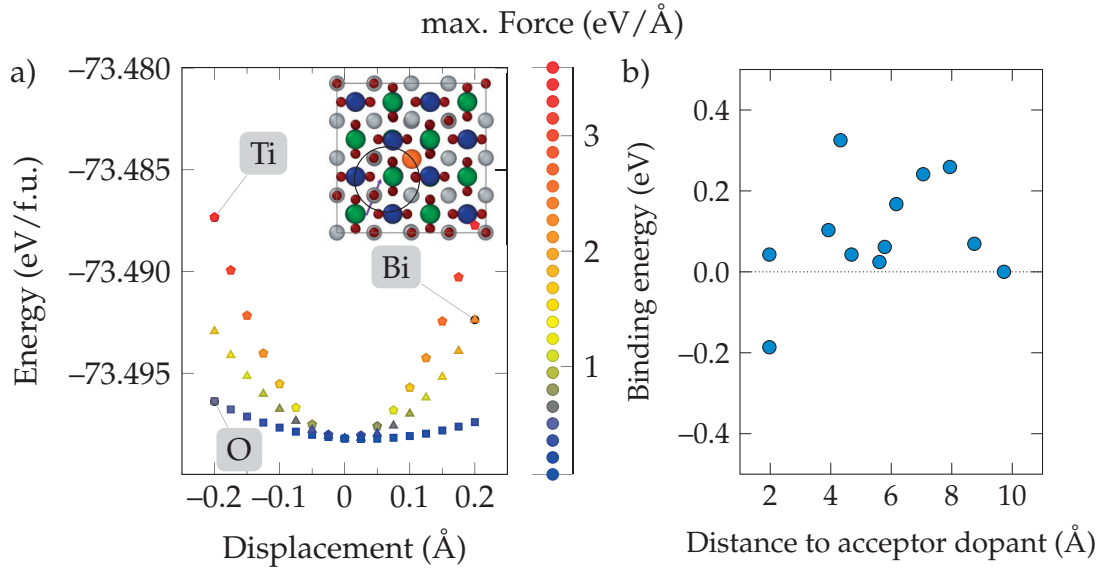


Figure 68: Figure a) shows the energy with respect to a cooperative displacement of either O, Ti, or Bi. The inset in b) demonstrates that the maximum force, which is indicated by the (scaled) arrow, is not located at the defect associate. The orange atom defines Mg, the blue atoms represent Bi atoms, Na and O atoms are green and red, respectively. Figure b) shows the binding energy of a Mg dopant and an oxygen vacancy in a 111 -ordered tetragonal structure with a global $a^0b^0c^-$ tilt pattern. All energies are referenced to the configuration at approximately 10 \AA .

similarly to NBT-3BT. As proposed by Woodward *et al.* [36], this can be related to the increasing volume around the A-site cation.

6.7 INFLUENCE OF LATTICE SYMMETRY ON THE DEFECT THERMODYNAMICS

6.7.1 Tetragonal structure

We start with the influence of the lattice symmetry by investigating the energy-distance curve for a $\text{Mg}_{\text{Ti}}''\text{-V}_{\text{O}}^{\bullet\bullet}$ defect pair in a 111 -ordered tetragonal structure with a global $a^0b^0c^-$ tilt pattern. As mentioned above, this structure is unstable with respect to the anti-phase tilt even, in a supercell containing 320 atoms. However, if we permit local tilting, we obtain the results shown in Figure 68a). Note that in these simulations, the maximum atomic force is about 0.1 eV \AA^{-1} , which is beyond our convergence criteria.

Although a first neighbor associate seems favorable, we observe fluctuations of the same order of magnitude at larger distances. Even at the same dopant-vacancy distance, the energy varies by more than 0.2 eV . We attribute this difference to distinct Bi-displacement patterns around the oxygen vacancy. However, at this moment, it is uncertain if these relaxation patterns are a computational artifact or if the displacive disorder is coupled to a reduced octahedral tilt [388] in the tetragonal phase. Figure 68b) shows the energy with respect to a cooperative displacement of either O, Ti, or Bi. The energies change by less than 0.02 eV per formula unit in the given range and are almost symmetric. This suggests that the energies might not drastically change

for different atomic residual forces.

The inset in Figure 68b) further demonstrates that the ion with the maximum force is not located at the defect center. We can assume that the equilibrium structure has not yet been reached but that the structure oscillates around a given minimum. A detailed investigation of the relaxation process further reveals that small displacements are spread throughout the whole supercell, which contradicts the more local character of the defect associate at least with respect to strain relaxation processes.

If we fix the ions entirely at their prescribed positions in R3 and vary the Γ_5^- anti-phase tilt amplitude gradually, we obtain the results shown in Figure 69. The energy of the vacancy decreases until the amplitude reaches 100%, which is equal to the equilibrium tilt displacement in the undisturbed bulk phase. If we exceed this value, the energy starts to increase again. This behavior does not change if we change the charge state of the oxygen vacancy. Here, V_O^\times denotes the neutral charge state. On the one hand, this explains the tendency to develop a global $a^-a^-a^-$ tilt pattern (defect induced strain field) during the calculation of defective tetragonal structures in the case of NBT or a local anti-ferrodistortive oxygen-octahedron rotation in SrTiO_3 [389]. This suggests that the amount of octahedral tilting and the cation off-site displacements are critical for defect association. On the other hand, it explains the comparably marginal tilt relaxation directly at the dopant-vacancy defect associate and indicates that a reduced tilt angle is not the only reason for an increased association in partially Ba^{2+} substituted NBT. The polarization distortion in the host lattice around the defect is equally important.

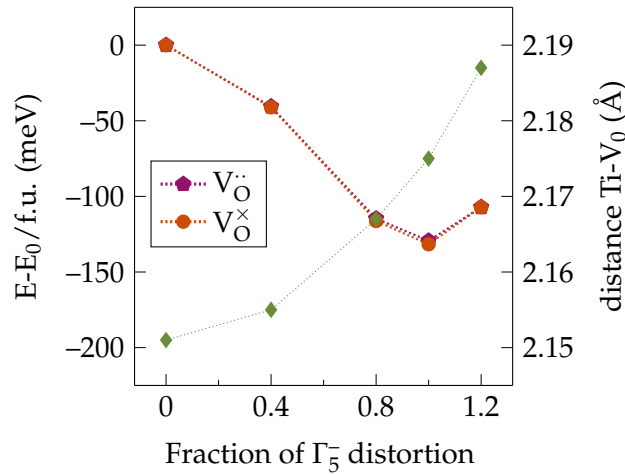


Figure 69: Energy of an oxygen vacancy in a 111-ordered structure with varying Γ_5^- mode amplitude (violet and orange) referenced to the energy of the structure with vanishing tilt displacement. At 0% the structure has R3m symmetry, while at 100% the structure is characterized by the R3 space group. The green curve depicts the distance between the Ti and the adjoining vacancy.

6.7.2 Cubic structure

Figure 70 depicts the binding energies of an oxygen vacancy to an Mg-or Al-dopant in initially 111 -ordered, cubic NBT, where we applied the same conventions as in Figure 56. We use the word “initially” to emphasize the development of a global A-site and tilt disorder after relaxation. Although the A-site off-displacements occur along the $[111]$ -direction as in the R3 hettotype, they are generally uncorrelated. Likewise, we partially observe the manifestation of anti-phase octahedral rotations. However, these patterns are rather short-ranged and alternate with in-phase rotations such that the structure has a global tilt disorder. We already explained the formation of octahedral tilts in the case of tetragonal NBT above. This argumentation is equally valid in the cubic configuration.

For both dopant types, we observe a distribution of binding energies at the same distances. This shows that the exact energy crucially depends on the local A-site arrangement, the tilt distortion, and how much the coordination polyhedron is deformed. The more distinct the local $a^-a^-a^-$ -pattern and the less deformed the polyhedron, the lower is the energy of a specific ionic configuration. From the data in Figure 70b), we find an even higher defect association than in the rhombohedral space group. The highest binding energy is reached at 4.4 \AA and amounts to -1.0 eV . This demonstrates again that defect associates on higher neighbor shells are preferred in Al-doped NBT independent of the host symmetry. In turn, the association energy in Mg-doped NBT is on average -0.2 eV . Although we are faced with a much larger energy scatter than in the R3 structure, the values are less ambiguous compared to the tetragonal example above, see Figure 68. However, at this point, we emphasize that these conclusions are based on a small database owed by the enormous technical difficulties to relax defective NBT structures which are not the ground state structure.

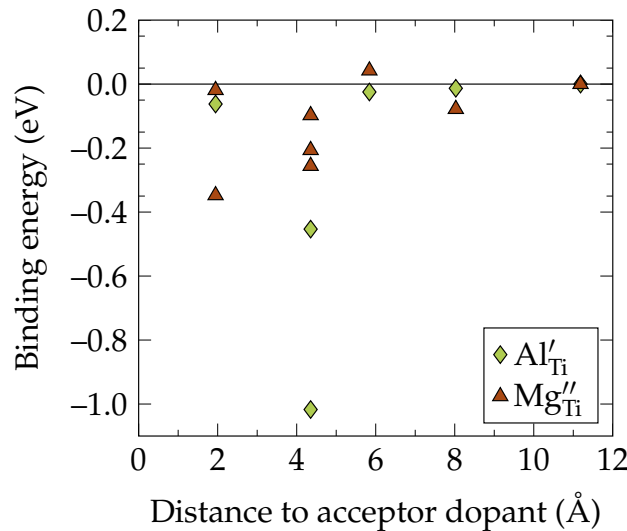


Figure 70: Binding energy in an initially cubic NBT host structure for Al- and Mg-doped NBT.

6.7.3 Orthorhombic structure

In the 001-ordered orthorhombic $Pmc2_1$ structure, we have to distinguish between a vacancy in a Bi-layer, in a Na-layer, or between these two layers. The latter is also known as cis-configuration [2, 382]. Several studies showed that vacancies are particularly favored in the Bi-layer and that the migration within this layer is almost effortless and barrier-free [156, 372, 382]. For this reason, we show Figure 71 as an introduction of the structures, which we will use below and demonstrate that the structures follow the same trend as in recent literature. The energies of vacancies in the Bi-layer are always smaller compared to vacancies introduced in the Na-layer. For Mg, we additionally tested the position in between the two A-site planes, which turned out to be even lower in energy than V_O^{Bi} . We observe comparable relaxation patterns, irrespective of the dopant type. Additionally, the difference between the dopant-specific coordination polyhedra are negligible for all tested configurations (V_O^{Bi} , V_O^{Na} , V_O^m).

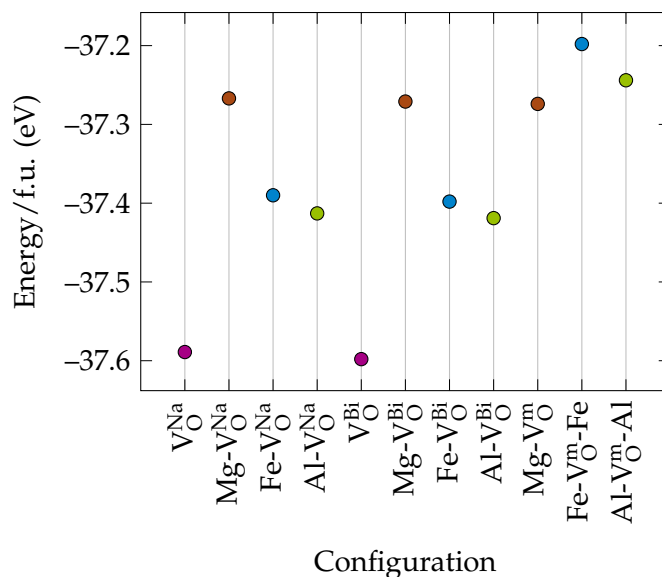


Figure 71: Energies of different dopant-oxygen associates in a 001-ordered orthorhombic structure. The superscript at the vacancy describes the A-site layer in which the vacancy has been generated (m stands for oxygen atoms between the Na- and Bi-layer).

6.8 MIGRATION BARRIERS IN A R3 HOST LATTICE

Until now, we intensively studied the association between the oxygen vacancy and an acceptor dopant. However, to understand the unexpected high ionic conductivity in NBT, fundamental knowledge about the mobility of oxygen vacancies is equally important. Here, we present the migration energies for different acceptor dopants (Mg, Fe) and an isolated, charged oxygen vacancy (V_O^\bullet) in Figure 72a) and the migration energies for a vacancy in the vicinity of a first-order cluster in Figure 72b). Unfortunately, the images in Al-doped NBT did not converge at all, and several images in Figure 72b), identified by pink marks, still have maximum ionic forces beyond 0.01 eV \AA^{-1} . In the latter case, this is less severe since we are primarily interested

in the saddle point configuration (which is converged) to determine the migration barrier.

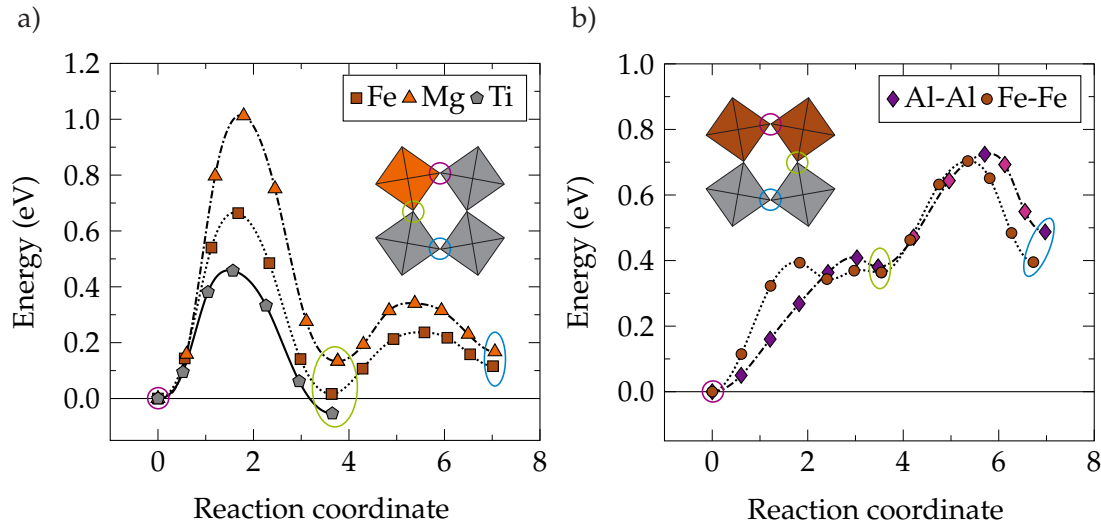


Figure 72: Migration energies in acceptor doped NBT with an R₃ host lattice for a) isolated acceptor dopants as well as a single vacancy (denoted by the ion which occupies the lattice site surrounded by the orange coordination polyhedra), and b) for a first-order dopant cluster. The insets schematically show the exact oxygen vacancy position inside the structure. The pink data points for the Al dopant cluster mark structures, which could not be completely relaxed toward the force criteria of 0.01 eV \AA^{-1} . Since we used CI-NEB, we are mainly interested in the saddle point configuration, which is sufficiently converged.

Except in the case of a single vacancy (referred to as Ti in Figure 72) we investigated the diffusion along one edge of a dopant coordination octahedra and, in the next step, away from the defect center. The reader can follow the migration path in the small insets in Figure 72a) and Figure 72b). Let us first concentrate on Figure 72a), from which we can draw three major conclusions.

Firstly, the migration barrier around an acceptor dopant is higher than in the host lattice, which agrees with the results of Schie *et al.* [140] in SrTiO₃. The vacancy position marked in green is energetically lower than a vacancy position surrounded by Ti ions. This indicates a tendency to form defect associates with the investigated acceptor dopants.

Secondly, Mg shows the highest migration energy around the dopant cation, which is approximately 0.4 eV higher than in Fe. This supports the trends observed in Figure 56. The second barrier is even 0.01 eV smaller than the equivalent in the Fe-doped structure. The latter reveals that the influence of the dopant type drastically reduces with increasing distance such that there is already hardly any difference between Mg and Fe-doped NBT on the second neighbor shell. Nevertheless, they are both smaller than the bulk value, even if we assume anisotropic migration barriers in the host lattice as reported by Meyer *et al.* [156].

Thirdly, we see that the energy difference between the oxygen vacancy positions around the dopant (site preference) depends on the dopant type and is smaller compared to doped PbTiO₃ (0.43 eV [148]). As mentioned by Erhart *et al.* [148], this can influence the redistribution of defect dipoles in the presence of oscillating fields (fatigue). The migration energies of the present study are given in Table 8.

	$E_M^{1.1}$	E_M^2	$E_M^{1.2}$
undoped	0.46	-	-
Mg	1.01	0.21	-
Fe	0.67	0.22	-
Fe-Fe	0.4	0.34	0.03 (0.37)
Al-Al	0.41	0.35	-

Table 8: Migration barriers for different acceptor dopants in a R_3 host lattice. $E_m^{1.2}$ accounts for the second maximum for the first order Fe cluster along the first path, starting at zero. The number in brackets is the energy of the image with respect to zero, while 0.03 eV refers to the migration barrier with respect to the local minimum at 0.34. All energy barriers are given in eV.

Generally, the calculated barrier heights are smaller than those found by Meyer *et al.* [156] for undoped NBT (LDA, 320 atoms) and by He *et al.* [401] for Mg-doped NBT (GGA, 120 atoms). However, the migration of an isolated vacancy is in good agreement with the results of Zhang *et al.* [395], who used a core-shell model and received a barrier height of 0.43 eV in the 111-ordered NBT structure. This migration energy was the lowest for all tested A-site orders, showing that although a rocksalt A-site arrangement is the energetically least stable one [2], it provides the highest diffusion rates.

Similar deviations have been recorded for oxygen vacancy diffusion in SrTiO_3 , where migration barriers between 0.60 eV and 0.98 eV have been deduced from experiments. In turn, calculated values fluctuate around 0.35 eV and 0.9 eV, depending on the simulation setup. It turned out that especially the exchange-correlation functional, the size, and the shape of the simulation cell are responsible for these large deviations in recent literature [402]. Zhang *et al.* [402] demonstrated that increasing simulation cell sizes drastically reduces the error of the data, irrespective of the used functional and the charge state of the vacancy. ⁴ In SrTiO_3 , they attributed these finite size effects to long-range relaxations, which are restricted by periodic boundary conditions in small simulation cells.

We also observed a striking and unexpected size dependency for $\text{Mg}_{\text{Ti}}''\text{-V}_{\text{O}}\ddot{\text{O}}$ defect associates in NBT with a $1\times 1\times 2$ and a $1\times 2\times 2$ supercell, which might be caused by a constraint relaxation procedure. However, the errors in SrTiO_3 have already been significantly reduced by using a cell with 320 atoms. This simulation setup has been used as a default in the present thesis such that our results are assumed to be reasonable and only slightly affected by size effects. Additionally, we quantified the interaction energy of a periodic defect lattice with the help of ANETO [320], using the elastic constants, the residual stress, and the periodicity vectors. Chapter 9 will deal with this interaction in greater detail. However, note that this interaction energy is rather small. In Mg-doped samples, we receive a value of less than -0.03 eV.

⁴ The charge state has less influence on the migration barrier if no Hubbard U-term has been used. In this case, the excess charge is delocalized within the supercell structure, which is more pronounced in large supercells. Instead, the migration barrier for neutral oxygen vacancies increases if a GGA+U functional is used.

We turn our attention to Figure 72b), where we investigated the migration of an oxygen vacancy in the vicinity of a first-order acceptor dopant cluster. The first thing to be noticed is again the similarity between the two dopant types Fe and Al. Although the final energy is lower in Fe-doped NBT, the migration energies (see Table 8) are almost identical. Both dopant clusters show a decreased barrier along a defective octahedron and an increased barrier toward the bulk structure, if we compare the results with Figure 72a). A closer look at the fifth image in the Fe-doped structure reveals a local energy minimum which might be caused by a simultaneous optimization of the Fe-O-Fe and the Bi-O bond length. While in the fourth image, the Bi-O bond is even smaller, the average Fe-O-Fe is increased. For the sixth image it is the exact opposite.

Finally, we also tried to calculate the migration energy of an oxygen vacancy through a Ba-Ti-Ba triangle (see Section 2.6) in a Fe-doped NBT sample. However, as in the Al-doped sample, we could only converge four out of seven images along the MEP. The forward and backward migration barrier along one edge of a Fe coordination polyhedra amounts to 1.11 eV and 2.84 eV, respectively. Although these may be preliminary results, they suggest an increase of the barrier height in the presence of Ba²⁺ ions.

Again, we remind the reader that the flat energy landscape in NBT and NBT-based solid solutions leads to a global A-site disorder, which might decrease the conductivity of oxygen vacancies. A study of He *et al.* [401] indicates an increase of the activation barrier and a simultaneous decrease of the conductivity, using a pseudo-random A-site ordering and *ab-initio* molecular dynamics simulations.

6.9 AB-INITIO VS. MODEL VS. EXPERIMENT – DOES IT MATCH?

6.9.1 Comparison with the macroscopic defect model

If we compare the results of this chapter with the association and migration energies of Chapter 4, we see that although the averaged DFT values are generally smaller than the fitted values, they are in the same order of magnitude. For instance, the model predicts an association energy of 0.39 eV at 1.5% Mg doping concentration, while our DFT data indicates that the effective association energy is between 0.15 eV and 0.25 eV. The fitted $\Delta H_{\text{asso,t}}$ was zero at the same concentration, which, if we can rely on the DFT calculations, is reflected by the fluctuating association energy. Suppose we use the average of the two calculated Mg migration energies in Table 8 (0.6 eV). In that case, we are close to the migration energy which we used in the model (0.5 eV) as a fixed parameter. Thus, the model can reproduce experimental results while it simultaneously delivers useful thermodynamic information. However, in the case of Fe-dopants, the model returned an association energy of 0.57 eV in the rhombohedral phase at 4% doping concentration. Considering that ΔH_{asso} should decrease with increasing doping concentration, that the DFT values are much smaller, and that the Arrhenius plots show the same trend for Mg and Fe at higher doping concentrations, this is a relatively high value and should be questioned. The contradiction between the model and *ab-initio* results suitably documents the multidimensional nature of oxygen vacancy migration [35, 152], which can not be captured by a simple fitting

procedure with global and site unspecific parameters. However, it provides a straightforward solution to determine the most relevant factors, which are concentration and phase transition dependent oxygen vacancy trapping.

6.9.2 Comparison with the experiments

Impedance spectroscopy measurements showed that NBT is a prevailing Type III (electronic) conductor at low concentrations. The formation of defect associates in Al- and Fe-doped NBT could be proven with NMR [166] and EPR [21, 22] at low dopant concentrations. From our DFT calculations, we could also confirm a thermodynamic driving force for defect association. In Figure 18, we have seen that all doped samples transform into a Type I conductor at higher concentrations, which is related to a dissociation of the defect pair. Especially Fe- and Mg-doped NBT behave similarly, although Fe-doped samples have slightly lower conductivities than the Mg-doped equivalent. From a defect chemical perspective, this difference can be either caused by a higher oxygen vacancy concentration in Mg-doped NBT (if we assume a complete incorporation of the dopants into the NBT host lattice) or by a different interaction strength between the dopant and the oxygen vacancy. This interaction is composed of long- and short-range electrostatic and elastic components. In the present chapter, we mainly concentrated on the short-range relaxations and long-range Coulomb interactions. Until now, we learned that although the concentration of oxygen vacancies is highest in Mg-doped NBT, the binding energy exceeds the one of Al- and Fe-doped NBT. The latter effectively reduces the ionic conductivity.

We could further observe that the binding energy of an oxygen vacancy and a dopant cluster is relatively short-ranged, emphasizing the concentration dependency of the defect association. Finally, we showed that there are indications for a stabilized defect associate in a solid solution with BaTiO_3 as well as higher migration barriers for oxygen vacancy migration. We suggest that this is strongly related to the A-site disorder around the defect pair. All in all, both *ab-initio* and experimental results correspond to each other such that our calculations can provide a plausible explanation of the observed trend. However, there are still various open questions about defect states, long-range elastic interactions, and covalent contributions. We will consider them in the next chapter to gradually uncover the ionic conductivity mechanisms in NBT.

6.10 THINGS TO REMEMBER

In this chapter, we used DFT to determine defect association energies and migration barriers of doped NBT. We learned that:

- All investigated dopant types (Mg, Al, Fe) show a preference to associate with an oxygen vacancy (see Section 6.2.2 and “association” in Figure 73).
- The association energy can be increased by the addition of BaTiO_3 (at least for certain configurations) or the formation of a first-order dopant cluster (see Section 6.6).
- The defect association seem to strongly depend on the tilt modes in the structure (see Section 6.7).

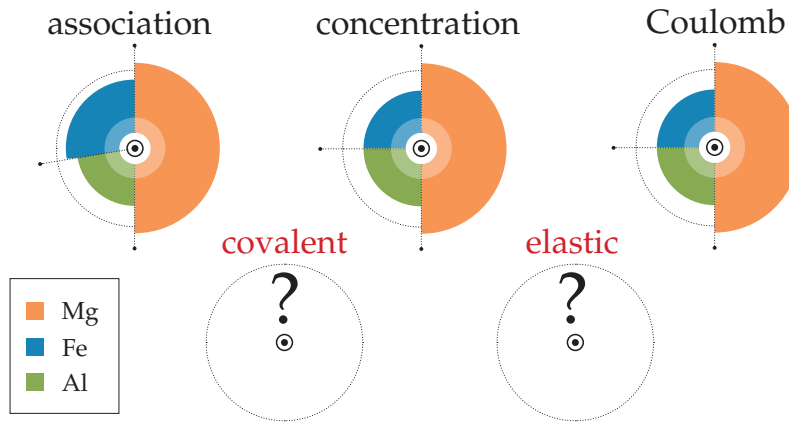


Figure 73: Summary of the different charge compensating oxygen vacancy concentration and the Coulomb interaction in Mg-, Al-, and Fe-doped NBT. Will will discover the influence of covalent and elastic interactions in the following chapters.

- The computational instability of the cubic and tetragonal phase upon the generation of an oxygen vacancy confirms the observations of He *et al.* [401]. They state that the global A-site disorder (configurational entropy) significantly contributes to the stabilization of the cubic perovskite structure in NBT (see Section 6.7).
- For the theoretical concentration of oxygen vacancies the following rule applies: $[V_{\text{O}}^{\cdot\cdot}]_{\text{Mg}} > [V_{\text{O}}^{\cdot\cdot}]_{\text{Al}} = [V_{\text{O}}^{\cdot\cdot}]_{\text{Fe}}$ (see “concentration” in Figure 73).
- For the Coulomb contribution to the association energy the subsequent order is valid: $E_{\text{Mg}}^{\text{C}} > E_{\text{Al}}^{\text{C}} = E_{\text{Fe}}^{\text{C}}$ (see “Coulomb” in Figure 73).
- The migration barrier is highest in Mg-doped NBT, decreases in Fe-doped NBT, and is lowest in undoped NBT. Despite the calculation of the association energies, the determination of migration energies is another method to confirm an attractive interaction between diluted acceptor dopants and oxygen vacancies (see Section 6.8).

Note that Figure 73 is primarily a visual guide for the reader and is used to explain tendencies from the above analysis. It does not represent exact percentages. We will explore the two missing contributions in the following chapter.

The results of the following chapter were obtained in close collaboration with Dr. Pedro Groszewicz from the institute of physical chemistry (NMR spectroscopy) and Dr. Sebastian Steiner (impedance spectroscopy) of the nonmetallic-inorganic materials division of the Technical University in Darmstadt and are used with their permission. They have been first published in Reference [166].

Until now, we analyzed the thermodynamic driving force to form defect associates in acceptor doped NBT. We further shed some light on the impedance spectra of differently doped NBT and NBT-based solid solutions and presented recent NMR measurements on Al-doped NBT. However, in the latter case, the observed resonances could not be assigned unambiguously to structural patterns in NBT, which is essential to track the formation of associated defects between Al^{3+} and oxygen vacancies and to understand their impact on functional properties. Thus, so far, we can only speculate about the fate of Al in NBT. Inspired by the idea of “smarter Crystallography” [4] (see Section 3.12 of Chapter 3), we combine in the present chapter ^{27}Al NMR spectroscopy and *ab-initio* calculations to characterize the local structure around aluminium dopants, to eliminate uncertainties about the formation of associates, and to find the unique fingerprint of the defect pair in the NMR spectra. We demonstrate how this powerful combination of techniques allows us to derive the complete range of chemical environments occupied by Al^{3+} in perovskite oxides. This knowledge allows us to better rationalize the electric conductivity for samples with varying aluminum content and opens a new possibility for the investigation of structure-property relationships in these materials. Although the following analysis serves primarily as a benchmark to interpret experimentally observed NMR peaks for Al-doped NBT, it is equally relevant for NKBT-xBA solid solutions. A review of the experimental results can be found in Section 2.6.10.

7.1 COMPUTATIONAL METHODS

In this chapter, we use density functional theory computations to calculate the ^{27}Al chemical shift in structural models of aluminum-doped NBT. Worthwhile emphasizing in this context and the basis for the evaluation of the chemical shift data is the Gauge-Including Projector Augmented Wave (GIPAW) method, which was first introduced by Pickard and Mauri [346] and further transferred to non-norm-conserving pseudopotentials by Yates *et al.* [347]. This technical evolution allows using a plane-wave basis set within periodic boundary calculations to predict the desired chemical shielding tensor from structural models under well controllable circumstances [344, 347]. We used the GIPAW formalism as implemented in the Vienna *Ab-initio* Simulation Package [209, 210, 403, 404] by de Wijs *et al.* [351] and the generalized-gradient approximation in the Perdew-Burke-Ernzerhof parameterization [211]. A brief discussion of the theoretical background is given in Section 3.12 of Chapter 3.

For all calculations, we use a plane wave energy cut-off of 700 eV. Sums on a Γ -centered $3 \times 3 \times 3$ k-point mesh have been used to approximate integrals over the Brillouin zone. The convergence of the calculated NMR values concerning the energy cut-off and the k-point mesh has been carefully carried out, leading to an absolute maximum difference of around 0.1 ppm. This deviation is expected to be reasonable, considering the general spread of the experimental data.

For all structural models with defined aluminum and oxygen vacancy arrangements, a cell composed of 160 atoms has been used. The supercell size has been chosen such that the Al-substituents are sufficiently separated from their periodic images. Note that we initialized all calculations by using an optimized lattice constant instead of the experimental one. However, a calculation with a hydrostatically strained structure demonstrates that the general trend remains valid despite minor variations. A more detailed description of the different structural motifs follows in the upcoming sections.

Recent studies demonstrated that the minimization of atomic forces before the actual calculation of chemical shifts is crucial for comparison with experiments and to resolve structural peculiarities [344, 347]. For this reason, atomic positions have been relaxed until atomic forces are below a threshold of $0.01 \text{ eV } \text{\AA}^{-1}$ for all studied cases. Moreover, we compare the influence of two different relaxation protocols. Firstly, we relaxed the atomic positions while keeping the cell shape fixed. Secondly, we do not apply any constraint neither on the atomic positions nor the cell shape. However, the volume remained constant in both approaches.

In analogy to the experimental procedure, where measured chemical shifts are referenced to a well-known system, a similar practice has become established in literature for computed values [344]. Generally, we compare experimental results of chemical shift values (δ_{iso}) with the calculated isotropic chemical shielding (σ_{iso}). Several compounds have to be analyzed to reduce inaccuracies. For this purpose, we chose Al_2O_3 [188] as a representative Al^{3+} source during the synthesis of NKBT- x BA, followed by $\text{Bi}_2\text{Al}_4\text{O}_9$ [405], the thermodynamic most stable phase in the Al_2O_3 - Bi_2O_3 phase diagram [406], and $\text{Y}_3\text{Al}_5\text{O}_{12}$ (YAG) [407], as a further example of an aluminum-containing oxide with different Al environments.

The calculated values of σ_{iso} for different aluminum sites in these reference substances are plotted against the experimental δ_{iso} data in Figure 74, along with a linear regression curve. Although originally a slope of one was expected to relate experiment (δ_{iso}) and calculation (σ_{iso}), recent studies report partly significant deviations from this optimum. Inappropriate exchange-correlation potentials or inaccurate structural models have been regarded as the main reasons for this variance [344]. In the present case, the mapping between experimental and theoretical data does not change regardless of the fitting procedure (constrained or optimal fit). We decided to use the latter in the current analysis.

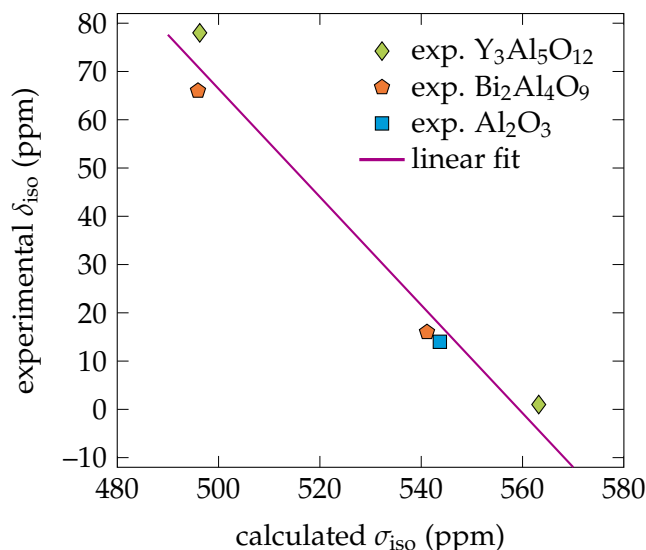


Figure 74: Reference curve to relate computed σ_{iso} and experimental δ_{iso} values. For this purpose chemical shifts of $\text{Bi}_2\text{Al}_4\text{O}_9$, $\text{Y}_3\text{Al}_5\text{O}_{12}$, and Al_2O_3 have been calculated.

7.2 ASSIGNMENT OF CHEMICAL SHIFTS TO STRUCTURAL MOTIFS BY DFT

After completing the reference procedure, we are able to investigate several structural models of Al-substituted NBT. These different configurations, which are depicted in Figure 75 are particularly helpful to assign ^{27}Al NMR peaks to specific atomic arrangements in chemically disordered NBT and reflect the high sensitivity of NMR data to the local geometry. Three cases have been investigated, where aluminum occupies either the A-site (Al_{Bi} - Figure 75a,b), is incorporated on a single B-site (Al'_{Ti} - Figure 75c,d) or forms a cluster with a second Al^{3+} on an adjacent B-site ($\text{Al}'_{\text{Ti}}\text{-Al}'_{\text{Ti}}$ - Figure 75e,f,g). For the latter, the chemical shift of both Al sites are listed. Additionally, these three coordination environments have been analyzed with the presence of an oxygen vacancy on the nearest neighbor site, representing a defect associate (Figure 75b,d,f,g).

As it remains an ongoing challenge to simulate chemically disordered materials as NKBT-xBA using reasonable system sizes (see Chapter 3), we benefit from the following two simplifications: First, we assume that potassium will only cause a volume expansion of the structure, and, consequently, calculations have been done solely for Al-substituted NBT. Second, we calculate each Al environment's chemical shift for two different A-site cation orders rather than a disordered structure. On the one hand, we choose the rock salt cation order (111-order - Figure 75h), where the ground state structure appears with R_3 symmetry. On the other hand, we use the layered cation order (001-order - Figure 75i), where the energetically most favorable arrangement leads to a $\text{Pmc}2_1$ symmetry.

In the first case considered, Al replaces the A-site cation (Figure 75a,b). Due to the similarity of their charge state ($3+$), we will solely substitute the Bi atoms by Al in the following study. We found a chemical shift of -8 ppm when Al occupies a regular

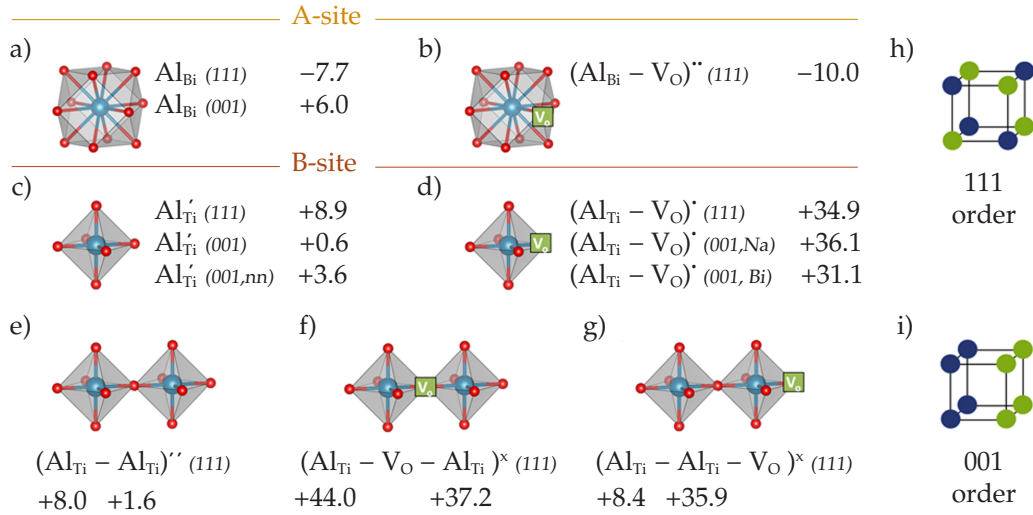


Figure 75: Different local environments of Al^{3+} and their theoretically obtained chemical shift values.

A-site in a 111 cation ordered system ($\text{Al}_{\text{Bi}} (111)$). This value supports the hypothesis that the negative chemical shift obtained for NKBT-7BA corresponds to an Al^{3+} surrounded by an oxygen cubododecahedron.

If an oxygen vacancy is associated to the A-site ($\text{Al}_{\text{Bi}} - \text{V}_{\text{O}}'' (111)$), the computed chemical shift further decreases to -10 ppm, which might be related to the fact that two signals are resolved in this region of the spectrum. When changing to a 001 cation order ($\text{Al}_{\text{Bi}} (001)$), the chemical shift increases to 6 ppm. This difference demonstrates the influence of the cation ordering on the NMR data. Conceivably, individual cation orders' contribution cannot be resolved in the NMR spectra, and a distribution of chemical shift values is expected.

Next, we will look onto the results obtained for different Al'_{Ti} configurations. The chemical shift in the 111 order ($\text{Al}'_{\text{Ti}} (111)$) amounts to 8 ppm. Thus, the assignment of the main spectral component at 8 ppm to Al'_{Ti} is strongly supported by the calculations. A different charge state of the simulation supercell (equivalent to a different charge state of the defect), which can be controlled by the number of electrons during the calculation, does not alter the chemical shift value significantly. A deviation of 1.5 ppm has been extracted for the structural model $\text{Al}''_{\text{Ti}} (111, \text{charged})$. Instead, the formation of an Al'_{Ti} defect in a globally 001-order structure leads to a chemical shift of 0.6 ppm, a fact that reinforces the significant effect of the A-site ordering on the chemical shift values of both the B-site and the A-site. Thus, the broad distribution of the B-site resonance might be a consequence of both topological disorder on the A-site (occupied by Bi^{3+} , Na^+ and K^+) as well as a distribution of oxygen octahedral tilts and their coupled cation motion [64, 201]. A similar effect has been observed in $^{47,49}\text{Ti}$ NMR spectra of the closely related NBT-xBT solid solution and has been attributed to the distribution of local environments [408].

A comparison to the experimental values confirms that the 001-order should only exist on the short-range scale and shows that a 111-ordered structure most closely resembles the actual structure or is prevalent at the local scale. Good comparability of

the 111-ordered system to experimental results has already been observed for other properties [76, 80] and the short-range character of the 001-order has also been suggested from negligible migration barriers for oxygen vacancies in pure Bi-layers [156].

We have also evaluated the effect of dopant-vacancy associates in Al_B configurations. Regardless of the cation order, calculations repeatedly delivered values in the vicinity of 40 ppm for all Al'_{Ti} environments considered. Such values lie in the AlO_5 range of the chemical shift scale (see Figure 19). For the 111-order, a chemical shift of 35 ppm has been computed. This value changes little if a 001-order is considered, resulting in a chemical shift of 36 ppm for Al'_{Ti} (001,Na), which denotes a V_{O} inside the Na-layer, and a shift of 31 ppm, if the vacancy is introduced into the Bi-layer. Interestingly, the chemical shift already returns to the AlO_6 range if the oxygen vacancy is located in the next neighbor shell (Al'_{Ti} (111,NN)). This shows that although small distortions are present, we can clearly distinguish associates on different coordination shells by NMR.

For completeness, we examined additional structural models containing an Al'_{Ti} point defect. First, we not only relaxed the atomic positions but also the shape of the simulation cell. This procedure should resemble the local configurations in solid-solution structures, where a higher concentration of Al is present than the diluted case. However, the difference only amounts to 0.33 ppm, such that small local geometrical changes do not significantly impact the resulting chemical shift. Secondly, we tested the influence of potassium indirectly by straining the simulation cell hydrostatically up to 2%. The difference compared to the equilibrium volume of bulk NBT equals to 2 ppm. These calculations demonstrate that the influence of a volume expansion has a more substantial contribution to the ^{27}Al chemical shift than other structural distortions.

We can also investigate the effect of a larger Al concentration (e.g., 6% instead of 3% for the supercell) by assuming the presence of a small cluster, consisting of two Al atoms on adjacent B-sites. In case no vacancy is found in close vicinity of the cluster (Figure 75e), chemical shift values of 8 ppm and 1.5 ppm have been computed for both Al^{3+} ions. These values have been expected for the occupation of a regular B-site. In turn, the generation of a vacancy inside the dopant cluster results in two adjacent pentahedra. In this arrangement both aluminum sites display chemical shift values equal to 43.9 ppm and 37.2 ppm, which are both in the AlO_5 range (see Figure 19).

In a further arrangement (Figure 75g), the oxygen vacancy is connected to a single Al dopant of the cluster. This results in an Al-centered octahedron and a defective Al-centered pentahedron. Consequently, chemical shift values of approximately 8 ppm and 36 ppm have been computed for the cluster, which match the AlO_6 as well as the AlO_5 range of the ^{27}Al chemical shift scale. Therefore, one may conclude that Al-cluster produce results that are comparable to the isolated models, showing only slight variations as compared to Al'_{Ti} .

All in all, these calculations demonstrate that there is a unique fingerprint for each local environment in the perovskite structure. Examples are the occupation of the A-site

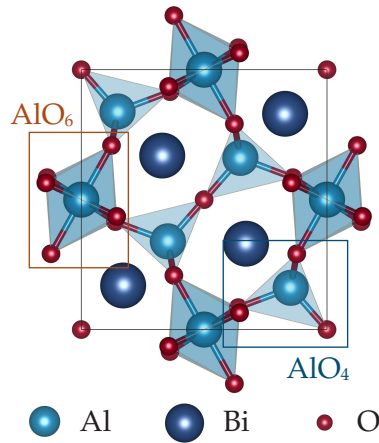


Figure 76: Structure model of $\text{Bi}_2\text{Al}_4\text{O}_9$.

($\delta_{\text{iso}} \sim -8$ ppm), the B-site ($\delta_{\text{iso}} \sim 10$ ppm) and associated defects between aluminum and V_{O} with a chemical shift between 35 ppm and 40 ppm. Even more interesting is the fact that resonances around 70 ppm have only been computed for aluminum in a tetrahedral coordination environment (AlO_4), as for the reference substances $\text{Bi}_2\text{Al}_4\text{O}_9$ or YAG (Figure 74), which is shown in Figure 76

7.3 PREDICTIONS ABOUT THE FORMATION OF DEFECT ASSOCIATES

DFT calculations predict a chemical shift between 35 ppm and 40 ppm for an $(\text{Al}_{\text{Ti}}-\text{V}_{\text{O}})'$ defect associate, corresponding to the AlO_5 region of the ^{27}Al NMR spectrum. Only small signals are present in this spectral region and only for samples with an aluminum content below 0.25 %. According to impedance measurements, these compositions exhibit a relatively high resistivity and a predominantly electronic conductivity. The onset of ionic conduction is observed between NBT-0.3Al and NBT-0.5Al, where no significant signal is observed. Hence, we may conclude that hardly any defect association occurs within the benchmark system of acceptor-doped NBT- x Al ($x \geq 0.5$ %), which is consistent with the non-linear increase of the conductivity with a rising acceptor dopant concentration. However, we do observe two ^{27}Al NMR signals (i.e. $\delta_{\text{iso}}=19$ ppm and $\delta_{\text{iso}}=70$ ppm) that have been previously attributed to associated defects in the literature [195, 197]. Thus, before excluding nearest neighbor associates' formation, we carefully analyze these previous reports in light of our new findings.

We start this analysis with the signal at $\delta_{\text{iso}}=19$ ppm. This resonance is located at the border between the AlO_6 and the AlO_5 region. A similar chemical shift in Al-substituted MgSiO_3 has been recorded by Stebbins *et al.* [195] and interpreted as an $(\text{Al}_{\text{Si}}-\text{V}_{\text{O}})'$ defect.

Likewise, as already mentioned, the high C_Q value of 4.6 MHz might be another indication for a defect associate. Indeed, the structural distortion caused by $(\text{Fe}_{\text{Ti}}-\text{V}_{\text{O}})'$ has been used to identify defect associates in hard PZT by means of EPR spectroscopy [177]. Both the zero-field splittings (ZFS) [176] in EPR and the quadrupolar coupling constant C_Q in NMR are measures of the distortion around the dopant, which the association with oxygen vacancies might significantly increase.

Alternatively, Lima *et al.* [197] argued that the formation of associated defects in Sr²⁺-substituted LaAlO₃ perovskites lead to resonances in the range of 70 ppm.

Although this seems contradictory since this specific range of chemical shift is related to AlO₄ coordination environments rather than an AlO₅ coordination shell, a signal in the vicinity of 70 ppm is present for all analyzed samples and is quite pronounced in NBT-4Al. However, both the AlO₄ and the AlO₆ ($\delta_{\text{iso}}=19$ ppm) resonance also appear in the ³QMAS spectra of NKBT-7BA (Figure 22), NKBT-6BA, and NBT-4Al, and their intensity increases notably at higher Al concentrations. If we assume that these two resonances indicate defect associations, this chapter's observations and Chapter 4 would be contradictory. As a reminder, in Chapter 4 we concluded that the binding energy successively declines with increasing dopant concentration. Instead, in this chapter, our results points toward an increasing contribution of defect associates at the same dopant content. Let us find out if there is another reasonable explanation for the AlO₄ and the AlO₆ peak.

We already addressed the possibility of secondary phases contributing to the NMR spectrum, especially if the solubility limit is approached. The solubility limit of BiAlO₃ in NBT-based perovskites is reached at roughly 8%, and secondary phases might be detected [169, 409]. Yang *et al.* [20] demonstrated the presence of Al-rich phases by secondary electron microscopy on polished surfaces already at 7% Al concentration. Furthermore, the Al₂O₃-Bi₂O₃ phase diagram shows numerous phases that could be formed during the formation of the Al-modified NBT and Bi₂Al₄O₉ is highly favorable [406].

Interestingly, the ³QMAS spectrum of Bi₂Al₄O₉ (not shown here) shows two differently coordinated Al-sites in a 1:1 ratio [405]. While the octahedral site exhibits a δ_{iso} equal to 16 ppm and a C_Q equal to 4.8 MHz, the tetrahedral site shows a δ_{iso} of 66 ppm and a C_Q of 5.2 MHz [405]. These values suggest that the two undefined resonances are better described by the appearance of Bi₂Al₄O₉ rather than the formation of defect associates.

The attentive reader might argue that although the latter explanation is consistent with the results of Chapter 4, they do not comply with the assumptions of a strong defect interaction as proposed by Yang *et al.* [20]. No sign of a significant nearest neighbor association has been observed at high concentrations in the present study. In turn, DFT predicts a small but non-negligible thermodynamic driving force for defect association between an oxygen vacancy and an Al acceptor dopant in NBT (see Chapter 6), which is in line with the fact that Al-doped systems behave analogously to Fe- and Mg-doped NBT [1, 19, 21].

This apparent contradiction may be resolved if one considers oxygen vacancies on the second or third neighbor shell instead of the first coordination sphere of the Al³⁺. A comparison between the chemical shift values for a vacancy on the first and the second neighbor shell (Figure 75g) showed that second neighbor shell configurations for associated defects closely resemble the isolated case (i.e., a regular B-site). Thus, defect associations between Al³⁺ and an oxygen vacancy on a higher-order neighbor shell would be consistent with the present NMR spectra and, therefore, conceivable. Such a higher-order association does not imply that oxygen vacancies are completely free but rather that they are more loosely bound. Examples for an association be-

tween a dopant and a vacancy on a second neighbor shell and the importance of long-range interactions have already been reported for doped ceria [410].

We do not find any evidence for an associate in NKBT- x BA, which was at first contrary to our expectations. From the knowledge of NBT- x BA solid solutions [20], we assumed a reduced dielectric loss due to the formation of defect associates. However, from the latest impedance spectra on NKBT- x BA samples (see supplemental of Reference [166]), we must admit that the conductivity even results in an increased conductivity compared to NBT- x BA. Thus, the absence of defect associates is not only a consequence of an unfavorable first neighbor arrangement, but primarily caused by the introduction of potassium.

Despite the small size of the Al^{3+} cation, DFT calculations demonstrate that besides forming a secondary phase, the A-site can be occupied as well. A good match between computed and measured chemical shift values in the range from -5 ppm to -10 ppm has been found. The presence of two signals in the A-site range of the chemical shift (δ_{iso} equal to -5 ppm and -9 ppm) suggests the presence of two quite distinct A-site environments, which might be explained by an oxygen vacancy on the first coordination shell around the A-site (if we compare the experiments with the DFT calculations in the 111-ordered structure).

However, since Al^{3+} preferentially replaces Ti on the B-site at lower concentrations, we may explain the occupation of the A-site due to a saturation effect for Al substitution on the B-site. Based on the signal area in the spectrum of NKBT-7BA, one can estimate that 5% of all Al^{3+} cations are found on the A-site and 90% on the B-site. This is equivalent to a total B-site occupancy of only 6%. Interestingly, this is the amount of aluminum in NKBT-6BT, a sample for which the Al_{Bi} configuration is absent. Consequently, aluminum concentrations higher than 6% will inevitably lead to the occupation of the A-site or the formation of secondary phases, for instance, $\text{Bi}_2\text{Al}_4\text{O}_9$. It is also consistent with the solubility limit of 8% of Al^{3+} in NKBT-BA solid solutions.

7.4 THINGS TO REMEMBER

In contrast to many other trivalent dopants investigated in recent literature and contrary to the calculation of binding energies in NBT, directly associated defect complexes between Al^{3+} and oxygen vacancies are only detectable for samples with Al contents below or equal to 0.1%. This explains the low ionic conductivity in those samples, which is even lower than in pure NBT. The absence of nearest neighbor associates for compositions with $x \geq 0.5$ has a significant impact on the current understanding of oxygen vacancy migration (less trapping) and hardening effects (should not be substantial) in Al-doped NBT and supports the model of a non-linear increase of the ionic conductivity for rising acceptor dopant concentrations. We further have to redefine the concept of defect association in these samples, including the dopants' interaction range. Another surprising observation is the occupation of the A-site by Al with increasing BA concentration. Although Al preferentially substitutes Ti on the B-site, a replacement of Bi on the A-site should be taken into consideration, especially at BA concentrations equal or higher than 7%.

We could further demonstrate that a secondary $\text{Bi}_2\text{Al}_4\text{O}_9$ phase is ubiquitous and

forms at much lower aluminum content than previously reported, leading to a resonance around 70 ppm and a shoulder at 19 ppm. This secondary phase becomes more pronounced with increasing Al concentration.

Finally, we were able to demonstrate that the combination of ^{27}Al NMR spectroscopy and DFT calculations is a powerful tool to investigate defect interactions on the local scale, even at low dopant concentration.

So far, we intensively studied the formation of dopant-vacancy associates according to Equation 32. However, we have not addressed different charge states of the associate or investigated whether electrically active and localized defect levels exist in the band gap. Since most of the defects studied in this thesis can have different charge states, there are at least two reasons for analyzing under which conditions a charge transition can occur. Firstly, a different charge state can alter the electrostatic interaction within a defect associate, which will be explained in detail below and which is of major concern in the present chapter. Secondly, analytical models, such as the one developed in Chapter 4, will never predict the charge state of a defect and associated therewith the actual defect equilibrium (charge compensation). That is, if, for instance, a $(\text{Fe}_{\text{Ti}}-\text{V}_{\text{O}})^{\cdot}$ interacts with an electron, the amount of oxygen vacancies needed for charge compensation will be halved. For this reason, we will calculate the charge transition states for all studied dopant-vacancy associates to verify or model assumptions and to exclude any electronic contribution to the visible kink in the semi-logarithmic Arrhenius representation (see Figure 17). To put it in the words of Walsh *et al.* [18], we will investigate “if the generated electrons or holes will be eliminated by structural rearrangements and if charge carriers survive such compensation, whether they will be localized or delocalized”.

An almost pressure independent bulk conductivity in Mg- and Sr-doped $\text{NB}_{0.49}\text{T}$ suggests that electronic charge compensation mechanisms hardly contribute to the overall conductivity [158]. Only in Bi-excess samples, an increasing electronic conductivity has been found, making non-stoichiometry a valuable tool to modify electric properties and to utilize NBT in diverse practical applications [411, 412]. However, electrons might occupy electrically active and localized defect sites [413] such that electrons contribute to the temperature-dependent defect association without becoming the dominant charge carrier. This is analogous to trapping of electronic charge either on a defect associate or an isolated defect, which might change the effective concentration of oxygen vacancies available for migration (the effective diffusion coefficient depends on the total non-stoichiometry when internal association reactions occur [414]). Indeed, density functional theory calculations in a rhombohedral 111-ordered structure showed that the migration energy of a neutral oxygen vacancy is doubled compared to the twofold positively charged instance [156, 415].

In the following, we first investigate the stability of the twofold positively charged vacancy in the polymorphic, undoped NBT. To qualify the difference between the two coexisting phases within the medium temperature regime (see Chapter 4 for more details), we will compare the results obtained in the rhombohedral and the tetragonal phase. Subsequently, we deal with the vacancy-dopant associate formed in magnesium doped NBT. In this particular case, we compare the results, which have been obtained with the GGA exchange-correlation functional, with a hybrid

calculation. Finally, a comparison with Al- and Fe-doped NBT follows in the third part of this chapter. The choice of different dopant types allows to investigate the influence of several ionic sizes and differently charged defect associates, including various available valence electron states (s, p, and d-orbitals).

8.1 COMPUTATIONAL METHODS

In all total energy calculations, we used a plane wave energy cut-off of 600 eV, a single \mathbf{k} -point, and a supercell with a total of 319 atoms for the simulation of the dopant-vacancy complex. As already mentioned above, we do not impose any symmetry constrained onto the wave function or the charge density during relaxation to prevent high symmetry solutions and allow for lattice distortions [416]. Due to the self-interaction-error in common density functional approaches [246, 254], we verified our results by performing hybrid calculations of the thermodynamic defect states of Mg-doped NBT in the 111-ordered rhombohedral structure. However, instead of using the standard HSE06 [258, 259] setting, we use an exact exchange fraction of 0.08 and a screening parameter of 0.2. Compared to the default value of 0.25, a reduced exact exchange fraction has been found to be particularly useful in certain perovskite structures [6]. Furthermore, this parameter set reproduces well the band gap and leads to an acceptable pseudocubic lattice constant of 3.9 Å in the rhombohedral structure (experimentally a value of 3.88 Å has been determined [159]). The linearity of the hybrid potential with these input variables has been tested and verified (see Appendix).

Two different polymorphs of NBT have been chosen as a host structure to qualify the local structure's influence on the charge state of the vacancy. These two configurations are expected to coexist at temperatures around 300 °C, namely the 111-ordered rhombohedral structure ($a^- a^- a^-$ anti-phase tilt pattern) and the 111-ordered tetragonal structure ($a^0 a^0 a^+$ in-phase tilt pattern). For the latter, we additionally investigate the 001-ordered structure, not only to distinguish between different phases but also to extract the influence of the local cation order on the charge state of the vacancy. Remember that global disorder is challenging to implement in supercells suitable for *ab-initio* calculations. We have to investigate the influence of symmetry by performing separate simulations with defined cation arrangements.

The thermodynamic transition levels have been deduced from the defect formation energies according to Equation 97. In contrast to the previous chapter, where we solely dealt with structures of the same charge state, we will now compare formation energies in differently charged supercells. We already explained the challenge of determining accurate formation energies in charged supercells in Chapter 3. In this study, we followed the approach of Kumagai *et al.* [316], which is based on the correction scheme first proposed by Freysoldt *et al.* [304] and equally described in detail in Section 3.9.3 of Chapter 3. The main problem of the Freysoldt approach in the context of doped NBT was the failure of this method for relaxed structures. However, as we learned in Chapter 6, relaxation around the dopant is critical to optimize the local bonding environment and reduce energy significantly.

Figure 77a) shows an example for the Freysoldt method in a relaxed Fe-doped NBT. Instead of reaching a plateau halfway between the defect associate at approximately

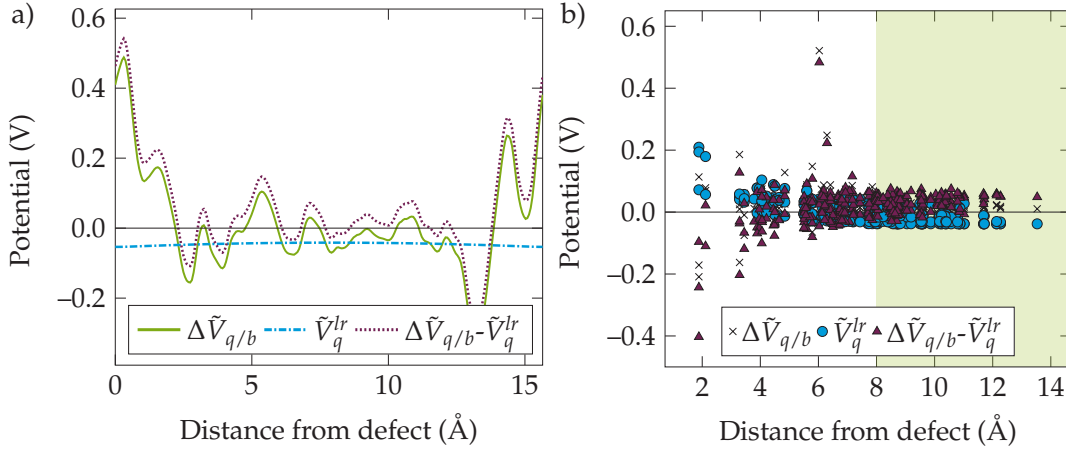


Figure 77: Visualization of the charge correction scheme of Freysoldt *et al.* [304] and Kumagai *et al.* [316]. For an explanation of the symbols see Chapter 3 and the main text.

o Å and its image at about 15.1 Å, we observe a rapidly varying shape of the potential. Thus, the macroscopically screened Coulomb potential fits not even close to the calculated electrostatic potential in the cell. In turn, if we use the approach of Kumagai *et al.* [316] in Figure 77b), we avoid this problem, although we used relaxed supercell structures. Note that we use the theoretical dielectric constant in each correction scheme ¹ to consistently remove the supercell artifacts [24, 316, 317]. The absolute total charge corrections are generally small and do not exceed 0.03 eV, which is mainly due to the high dielectric constant of NBT (see Chapter 5)[18, 308]. Since we are mainly concerned with the transition energy between two different charge states q and q' (see Equation 97), we do not intend to discuss the absolute formation energies which depend on the chemical environment, in greater detail.

8.2 THE ISOLATED OXYGEN VACANCY WANTS TO STAY POSITIVE

In the following, we discuss the charge state of an isolated vacancy in the rhombohedral structure with a 111 cation order. Remember that there are two different vacancy positions in the 111-ordered rhombohedral structure as a result of the Ti off-center displacement along the 111-direction. These two positions are illustrated as yellow dots in the structures of Figure 78. Figure 78 shows the transition states for both positions. We indicated the average experimental band gap and the GGA band gap by red arrows on the left side of the diagram. As seen above, density functional theory calculations underestimate the band gap, where the deviation amounts to approximately 0.5 eV. The transition level between the twofold positively charged vacancy and the neutral defect is located at a Fermi energy of 2.21 eV with respect to the valence band maximum. The absence of any transition to a single positively charge state at all Fermi energies indicates the instability of this electronic configuration. If we take a look at the second vacancy position, we observe an upward shift in the thermodynamic transition level energy of about 0.1 eV compared to the first position. Despite

¹ We use the ion-clamped dielectric constant for unrelaxed and the relaxed-ion dielectric constant for relaxed supercells.

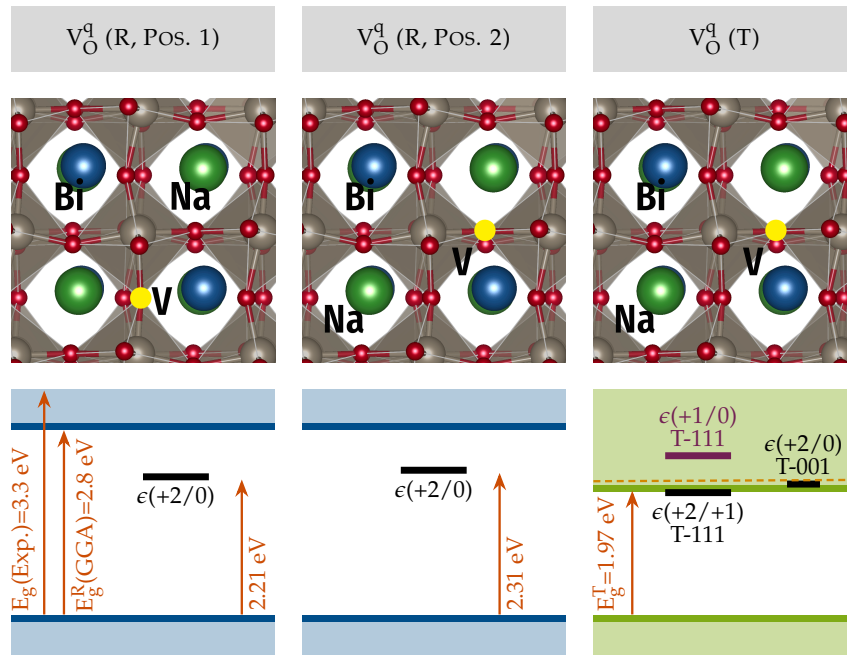


Figure 78: The first and second panel show the transition energies for two oxygen vacancy positions in the rhombohedral 111-ordered structure. The third panel depicts the transition states of an isolated vacancy in a structure with a tetragonal symmetry and two different cation orders. Note that the band gap in the 001-cation order is increased to 2.18 eV, as indicated by the dashed line. In all cases, q represents the charge state of the defect, and the calculations are performed with GGA.

this small increase in energy, the general defect chemistry remains the same such that the transition state is still relatively deep. Thus, we will only show the results of one oxygen vacancy position in the following. Similar results have been obtained from transition level calculations of mono oxygen vacancies in BaTiO_3 . However, the charge transition level has been found to be closer to the conduction band edge [417].

An analysis of the displacement vectors shows that the largest structural relaxations are spatially constrained to the nearest neighborhood for every tested charge state. Interestingly, their magnitudes differ, most noticeable in the case of Bi. Whereas Bi displaces only slightly in the positively charged vacancy case, larger relaxations can be observed towards the singly charged and the neutral vacancy. We draw this displacement schematically in Figure 79a) and Figure 79b) analog to Figure 57 of Chapter 6. We see that Bi strongly relaxes into the free volume if we add electrons to the system. This relaxation is constrained in the case of a positively charged oxygen vacancy. Equally noteworthy is the difference in the displacements of the adjoining Ti-ions. In both charge states, only one Ti-ion shows a pronounced off-center relaxation. If we take a look at the charge difference between two supercells containing either a V_{O}^{\cdot} or a $V_{\text{O}}^{\cdot\cdot}$ (Figure 80), we see that the additional charge is not solely localized on the vacancy site, but rather at the adjoining Ti neighbors and the first neighbor Bi. One additional electron leads to a donor spin-up state close to the conduction band minimum, which is a mixed state with Bi (mostly 6p but also 6s orbitals), Ti 3d, and O 2p contributions. At the same time, the spin-down state is resonant in the conduction

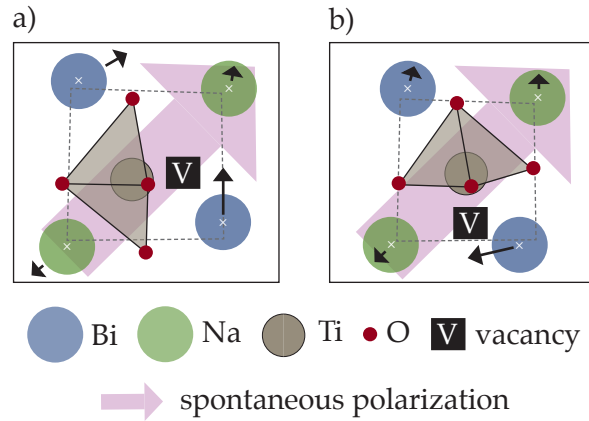


Figure 79: Figure a) and b) show two different positions of a neutral oxygen vacancy of undoped NBT, leading to various A-site displacements. Blue ions represent Bi, while green ions describe Na cations. The corners of the dashed polygon indicate the original positions of the A-site cations, while the white crosses are the centers of the displaced Na- and Bi-ions. The black arrows mark the displacements upon relaxation, while the big, violet arrow in the background specifies the direction of the spontaneous polarization in the R3 host symmetry. We defined the position of the oxygen vacancy by a V on a black square.

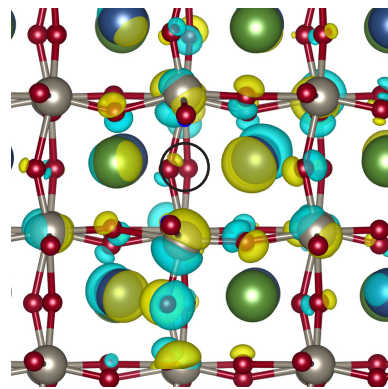


Figure 80: Charge density difference between a V_{O} and a $V_{\text{O}}^{\cdot\cdot}$ defect. Blue denotes a depletion and yellow an increase of electronic charge.

band. The same applies for the V_{O}^{\times} charge state, however with an increased Bi 6p proportion in the gap state, such that the spin-down state occurs at the same energy as the spin-up state.

In the neutral charge state, the gap state is shifted to lower energies such that it becomes an even deeper state. Figure 81 shows the density of states for different charges of the oxygen vacancy (f and g) or a defect associate (a-e). We will investigate the latter below in detail.

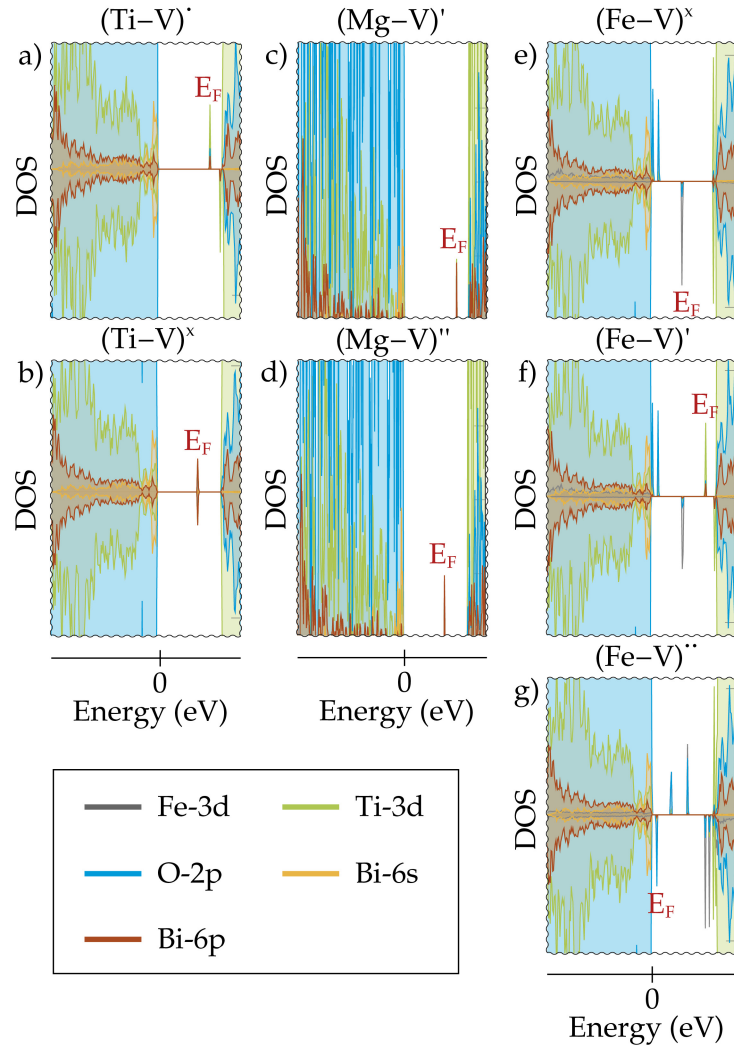


Figure 81: Density of states for different charge states of the defect complex. The investigated supercells contain a $(\text{Fe}_{\text{Ti}}\text{-V}_{\text{O}})^{\text{q}}$ associate (a-c), a $(\text{Mg}_{\text{Ti}}\text{-V}_{\text{O}})^{\text{q}}$ associate (d-e), or an isolated oxygen vacancy $\text{V}_{\text{O}}^{\text{q}}$ (f and g). The energies are referenced to the valence band maximum and the highest occupied state is marked as the Fermi energy, E_F .

Figure 82a) depicts the partial density of states in undoped NBT. We visualize the results of the V_{O} structure on the left-hand side and present the charge densities for a $\text{V}_{\text{O}}^{\times}$ calculation on the right-hand side. We deduce that both charge distributions share common features and that the only difference between both charge states is the amount of charge trapped at the oxygen vacancy and a neighboring Bi site. Thus, without any structural modifications and additional U-value on the Ti atoms, we do not obtain a polaronic state, which is localized at the Ti neighbors of the vacancy. In the case of $\text{V}_{\text{O}}^{\times}$, we do not observe defect states in the band gap since the bonding, and the anti-bonding state are resonances in the conduction band [149].

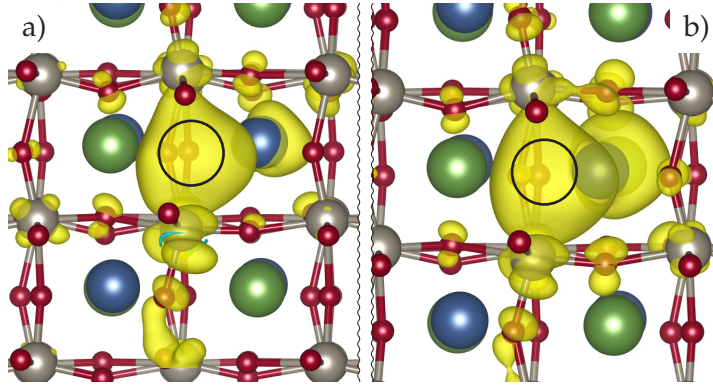


Figure 82: Band decomposed charge density for defect states in undoped NBT. Figure a) shows the structure with V_O and b) a cell with V_O^x . The defect states are ordered according to their appearance in the density of states in Figure 81, starting close to the valence band maximum. The black circle indicates the position of the oxygen vacancy.

The attempt to manipulate the occupation matrix of the Ti 3d orbitals by adding an excess electron into a specific d-state did not succeed. This procedure facilitates the polaron formation and verifies that the system is not trapped in a local energy minimum. We used the occupation-matrix-control program [418], which is an open-source extension of the VASP code [209, 210].

After constraining the occupation matrix and relax the structure according to the prescribed electron density, we allow the system to either maintain this electronic configuration or find another energetic minimum in a second step. Although we investigated only a subset of all possible electron configuration, neither of them was more stable than the original, unconstrained solution or led to the formation of a polaron. This is in contrast to SrTiO_3 or caria [149, 400, 419, 420], where polaron and oxygen vacancy complexes are energetically favorable. A possible reason might be a U-value of zero on the d orbitals of Ti. However, adding a U-term in NBT results in a hardly increasing band gap with a significant change of the remaining electronic structure. Another reason might be the strong coupling between the Bi 6s and the O 2p states. Such a coupling was the reason for an absence of self-trapped polarons in PbTiO_3 [421].

If we introduce the vacancy into the tetragonal structure with a 111-cation order, we observe two striking differences compared to the rhombohedral structure (see right panel of Figure 78). Firstly, the band gap decreases in the tetragonal phase, which has been discussed in the previous chapter. Secondly, the single positively charged state becomes energetically stable only at the conduction band edge. Additionally, the transition state to a neutral oxygen vacancy is resonant in the conduction band. These findings resemble the defect chemistry in SrTiO_3 [149, 389]. However, a variation of the cation arrangement to 001 reverses this order again such that the charge state changes from +2 to 0. In this case, the transition level is located at a Fermi energy of 2.1 eV and therefore also shortly below the conduction band minimum at 2.18 eV.

Since the transition in both symmetries is located at high Fermi energies, it may be assumed that a change in the charge state of the vacancy is not the main reason for a

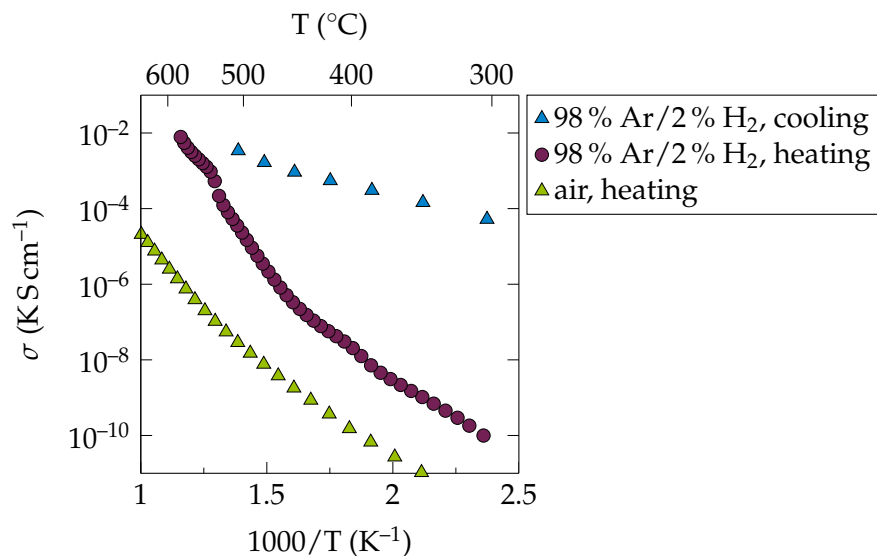


Figure 83: Arrhenius plot for NBT under reducing conditions.

variety of migration or association energies with increasing temperature. However, an electronic contribution could be conceivable in highly reducing conditions, where the Fermi level lies near the conduction band edge. Such conditions might even lead to a high electronic conductivity in the tetragonal phase of NBT when the oxygen vacancy becomes a donor. Indeed, an increasing conductivity under reducing conditions has also been observed experimentally, as shown in Figure 83. The impedance measurements have been performed by Dr. Sebastian Steiner from the nonmetallic-inorganic materials division of the Technical University in Darmstadt and are reprinted with his permission. An enhanced electronic contribution most probably causes this increase in bulk conductivity.

8.3 THE CHARGE STATE OF A VACANCY-DOPANT ASSOCIATE – THE VACANCY WINS

In the following, we investigate the influence of an additional dopant on the charge transition states. We start with the Mg-doped system. For completeness, we examined a first-order defect associate and a second-order complex with a vacancy on a neighboring octahedra. Both tested oxygen vacancy arrangements lead to similar results such that we will concentrate on the configuration where the dopant and the vacancy are immediate neighbors and, similarly to the case of the single vacancy, discard all other positions for the moment.

In Figure 84, we see that the charge state of the vacancy is almost independent of the presence of the dopant since the charge transition energy only marginally changes compared to an isolated oxygen vacancy. Note that a twofold positively charged vacancy, whereas a twofold negatively charged state represents a neutral vacancy such that the dopant has almost no influence on the transition level. If we take a look at the defect associate in the tetragonal phase, we notice that also in this configuration, the interaction between the defects hardly changes the transition states. However, as already observed in the isolated vacancy case, the single nega-

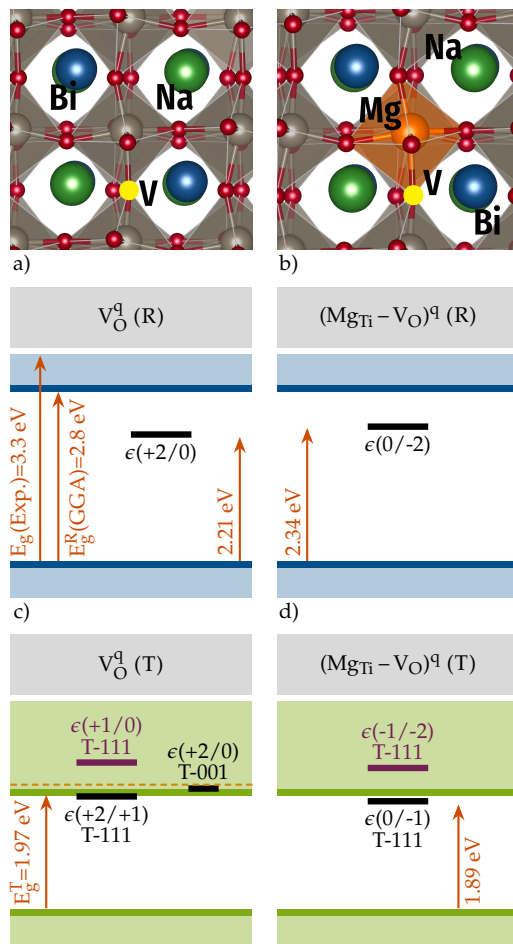


Figure 84: Comparison of the thermodynamic transition states between a single vacancy (V_O)^q in a) and c) and the ($Mg_{Ti}-V_O$)^q associate in b) and d) in the rhombohedral and tetragonal cell (GGA).

tively charged defect state is located close to the conduction band minimum.

To exclude an artificial error by choosing a semi-local exchange-correlation potential for the Ti-3d electrons, we recalculated all doped configurations using the hybrid functional with the parameter set in the methods section of this chapter. The results are illustrated in the right panel of Figure 85. As the conduction band minimum is shifted to higher energies by employing the hybrid potential, the transition level from a neutral to a negatively charged state of the defect complex is similarly increased. Consequently, the relative positions between the transition level and the conduction band edge remain almost identical. For this reason, we assume that the GGA-potential accurately describes the defect chemistry. Moreover, the good approximation of the GGA band gap indicates a suitable approximation of the physics by a standard DFT calculation. This assumption is supported by recent findings of Varignon *et al.* [3], who demonstrated that a polymorphous description of various perovskite structures can be obtainable by GGA-calculations. Even if they used a meta-GGA approach, a standard GGA potential seems to be equally sufficient in NBT.

The density of states for charged defects are an additional excellent demonstration of the similarity between an isolated vacancy and a ($Mg_{Ti}-V_O$)^q associate. In Figure 81d) and Figure 81e) (non-spin-polarized calculation), we generate a band gap state by adding electrons to the supercell, which again is formed by Bi 6s/6p, O 2p, and Ti 3d

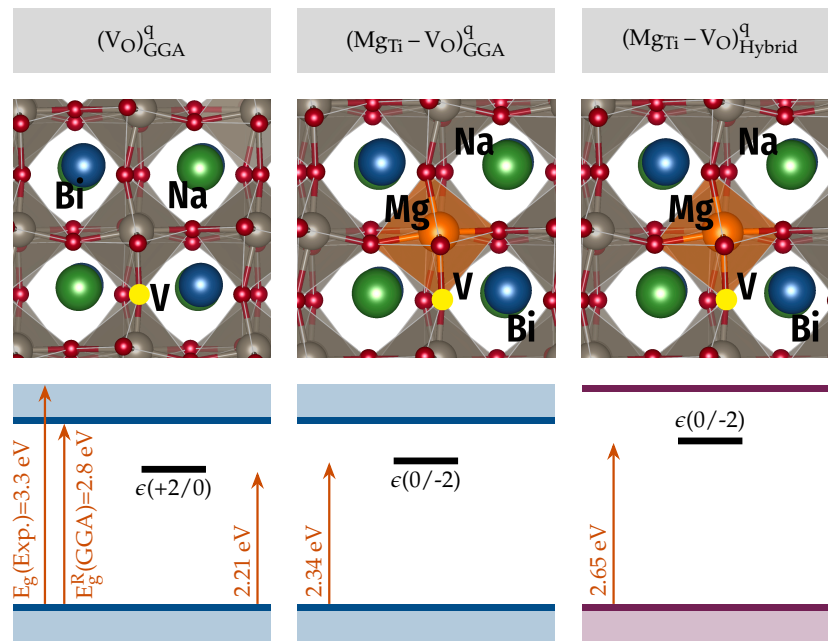


Figure 85: Comparison of the thermodynamic transition states between a single vacancy $(V_O)^q$, first panel) and the $(Mg_{Ti}-V_O)^q$ associate in the rhombohedral phase, calculated with GGA and a hybrid potential. The charge state of the complex is indicated by q . Note that the charge transition of the vacancy from +2 to 0 and of the complex from 0 to -2 describe comparable defect chemical reactions.

states. Moreover, the band gap state decreases in energy with an increasing amount of excess electrons.

Even strain hardly changes the thermodynamics of the defect associate. Figure 86 illustrates that the transition state from zero to -2 is almost unaffected if we apply 2% compressive hydrostatic strain and is only slightly shifted to lower energies under 2% tensile strain. Note that we use another form to present the transition levels to guarantee clarity. Since we do not include the chemical potentials in Equation 95, the formation energy values are only relative to each other. The determination of absolute values would require calculating several boundary phases of the NBT system.

In the next step, we change the dopant type from Mg to Al and Fe. We assume that the four tested cases $(V_O)^q$, $(Al_{Ti}-V_O)^q$, $(Fe_{Ti}-V_O)^q$, and $(Mg_{Ti}-V_O)^q$ are representative for different local environments, where not only the size of the dopant but also the highest valence orbitals vary. We restrict this analysis to the case of the rhombohedral structure, the ground state at low temperatures.

Figure 87 shows that Fe-doped NBT has two transition states inside the band gap. The charge transition level from +1 to zero is close to the middle of the band gap. This can explain the increased electronic conductivity at low Fe-dopant concentrations, as observed in the previous chapter. A second transition level is visible at 2.32 eV, where the charge state changes from zero to -2. This charge transition corresponds to the formation of a neutral oxygen vacancy.

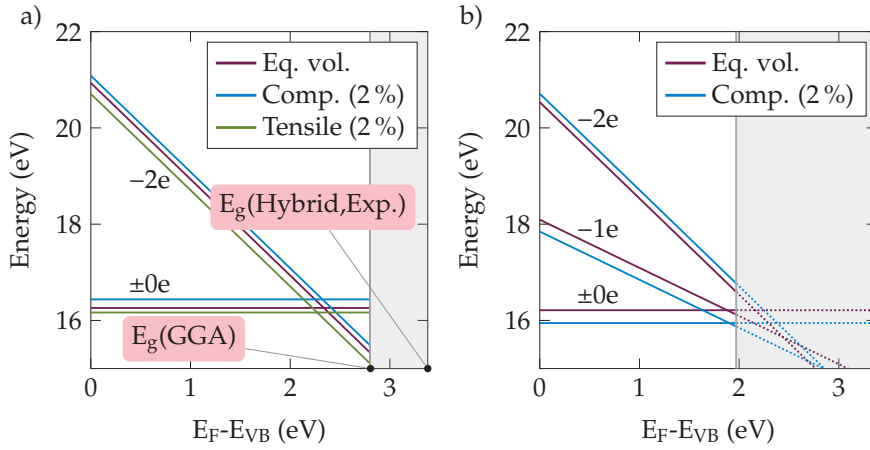


Figure 86: Comparison of thermodynamic transition states in Mg-doped NBT, containing a $(\text{Mg}_{\text{Ti}}-\text{V}_{\text{O}})^{\text{q}}$ associate (GGA). Figure a) displays the result obtained in a rhombohedral cell, while b) depicts the transition states in the tetrahedral structure. The tetrahedral structure under tensile strain was not stable. The intersection points mark the transition level. For a comment on the absolute values of the formation energies, see main text.

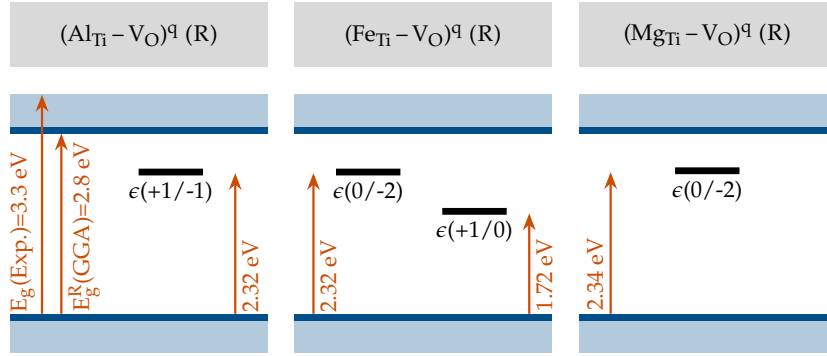


Figure 87: Comparison of the thermodynamic transition states between the $(\text{Al}_{\text{Ti}}-\text{V}_{\text{O}})^{\text{q}}$ (first panel) and the $(\text{Fe}_{\text{Ti}}-\text{V}_{\text{O}})^{\text{q}}$ associate (second panel), calculated with GGA in the rhombohedral NBT structure. As in the cases before, q describes the charge state of the defect associate.

From the Fe dopant's occupation matrices, we confirm that the additional electrons or holes do not significantly alter the absolute occupancy of the d-orbitals. Hence, the effective charge at the dopant hardly depends on the formal charge [422–424]. However, the occupancy of the single orbitals depends on the supercell charge. For instance, the addition of one electron to the Fe-doped system leads to a slight reduction of all d occupancies, except for one spin-down state with a prevailing xy and xz contribution in the eigenvector. In contrast, if we add a hole to the supercell (energetically most unstable charge state), we observe on the one hand a reduction of the spin-up occupancies, especially in two d orbitals with a dominant z^2 and $x^2 - y^2$ (the σ -bonds in the O_h point symmetry) character. In these orbitals, the electron occupancy is decreased by almost half. On the other hand, to preserve a constant charge density, one eigenvalue of the spin-up density matrix increases to 0.94. We assume that the occupancy increase results from an electronic charge transfer from the surrounding oxygen and primarily from the oxygen opposite to the vacancy. In Figure 88a) and Figure 88b), we present the band decomposed charge density of $(\text{Fe}_{\text{Ti}}-\text{V}_{\text{O}})^{\text{q}}$

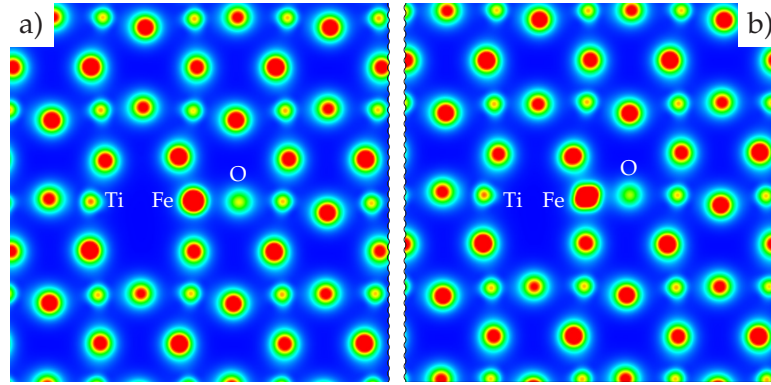


Figure 88: Band decomposed charge density for Fe-doped NBT with an excess a) electron or b) hole. Red means a high charge density, while blue represents low charge densities. Note that this is a 2D section through the crystal, which contains the dopant-vacancy associate. Thus, we have to consider intrinsic deviations of the charge density on the oxygen sites, which are caused by the anti-phase pattern in the rhombohedral 111 -ordered structure.

and $(\text{Fe}_{\text{Ti}}-\text{V}_{\text{O}})'$, respectively. First, we validate the preference for certain orbitals even in a low symmetry environment by visualizing the partial charge density around the Fe-dopant in the electron deficient supercell or generally around the B-site ions. Secondly, we confirm a slight decrease of the charge density on the oxygen opposite to the vacancy in Figure 88b).

Let us revisit Figure 81 and, in particular, Figure 81a), Figure 81b), and Figure 81c). In contrast to Mg-doped or undoped NBT, we count more than one band gap state upon changing the supercell's charge state. Although they are unexceptionally a mix of Ti, Bi, O, and Fe states, the O 2p and the Fe 3d contributions are predominant. For instance, the introduction of one additional electron causes the formation of two band gap states, a deep one in the middle of the gap and a shallow acceptor state at the valence band maximum. The latter has a significant oxygen contribution and is probably a dangling bond hybrid, while the former is assumed to be a crystal field resonance [422]. A further increase of the supercell charge leads to a third band gap state close to the conduction band minimum, which is primarily caused by Ti 3d states.

Let us now take a look at the defect states' squared wave function in Figure 89a) since this provides a comprehensive summary of the individual points we talked described so far. Indeed, the first hybrid state within the band gap is σ -like (dominant z^2 and $x^2 - y^2$ character) and shows a large charge density localized on the ligand oxygen atoms. Instead, the second hybrid state has a high weight on the Fe-dopant and strongly reminds on the xz , xy , and yz (π -type) orbitals in a cubic crystal field. This explains the increase of d-state occupancy for orbitals with a prevailing xy and xz contribution in the eigenvector, as mentioned above.

All band gap states are occupied such that an increase of the anti-bonding crystal field resonance (2. density peak) while maintaining a constant charge around the Fe-dopant leads to a significant decrease of the Fe-contribution in the deep bonding levels (which are additionally shifted to higher energies) [422, 425]. The third elec-

tronic band gap state, which appears after adding a second electron to the system, is a hybrid state with a large Ti, a moderate Bi and O, and a small Fe contribution. If we visualize the band decomposed charge density for this state, we confirm that a large amount of charge density is localized at the Ti adjacent to the Fe-dopant as well as the oxygen vacancy (π -type). In turn, a smaller magnitude of defect density resides at second neighbor B-sites. However, besides the recognizable Bi character, we observe a relatively high charge density directly at the oxygen vacancy site.

In summary, we see that the addition of one excess electron leads to an electron polaron on the iron site. In contrast, a second electron is trapped at the oxygen vacancy. In principle, the formation of an electron polaron on the Ti-site would also be possible, which, however, could only be revealed by applying a U-parameter correction to the Ti d-states.

In turn, if we introduce a hole, we increase the amount of band gap states even more. However, in this case, the character of the peaks that lie deep in the band gap is predominantly O-type, while those close to the conduction band are primarily composed of Fe states. We can verify this by visualizing the square of the defect wave functions for all defect states in Figure 89b) again. Although the first three defect states are similar at first sight, we find that only the second and the third one probably originate from a broken σ -bond. In contrast, the first one has an evident π -bonding character with a small but noticeable contribution of the Bi.

The fourth state is more localized on the Fe-dopant, with an almost balanced contribution of all d-states. It should be mentioned that only the first band gap state is occupied such that peaks two and three are ligand holes. This corresponds to our observation above, where we learned that we have a substantial reduction in d orbital occupancies with a dominant z^2 and $x^2 - y^2$ (σ -like bonds). We might describe this electron configuration as d^5L , where L denotes the hole in the oxygen 2p orbitals [426]. Similar results have been reported by Liu *et al.* [427], who investigated $\text{Li}_x\text{FeSiO}_4$. They showed that instead of having an unfavorable formal oxidation state of Fe^{4+} , two hole polaronic O-states form inside the gap. However, if an electron occupies these states, they “rejoin the reservoir in the valence band”.

Similar to the case of an isolated vacancy, we tried to manipulate the occupation matrix of the Fe d-orbitals. Depending on the charge state of the simulation cell, we either reduced or increased the electron density in one specific d-state. If we add an electron, we consistently end up with the same solution we received in the unconstrained simulation. We did not generate a second polaron on a neighbor Ti since we could not stabilize such an electronic configuration in undoped NBT (see above) with our computational setup. Furthermore, even in undoped SrTiO_3 [149], the formation of complex consisting of a V_O^{2+} and two polarons was less stable than a (V_O^{1+} + polaron) defect.

However, if we introduce a hole into the supercell, we obtain a further possible electronic configuration with an energy difference of 24 meV/fu with respect to the unconstrained value. In this case, the unoccupied defect states are predominantly of Fe-type with a smaller O- and Ti-contribution, located in the upper half of the band gap. The square of the wave function for the energetically deeper state resembles

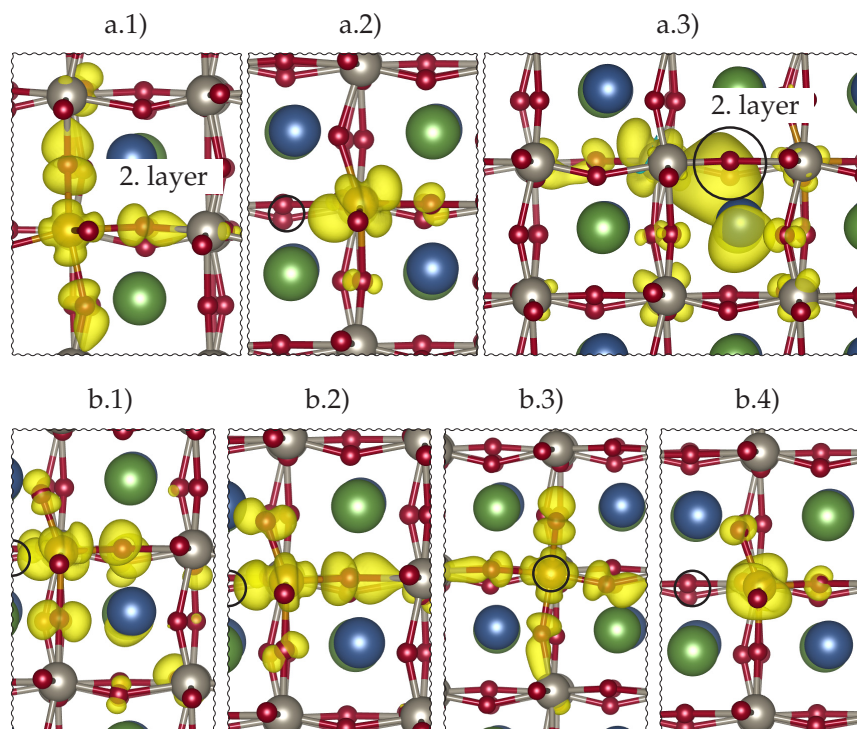


Figure 89: Band decomposed charge density for defect states in Fe-doped NBT with an excess a) electron or b) hole. The defect states are ordered according to their appearance in the density of states in Figure 81, starting close to the valence band maximum. The black circles indicate the position of the oxygen vacancy.

Figure 89b.4), while the second state closely resembles Figure 89b.3) and is close to the conduction band minimum.

In Al-doped NBT we observe a charge transition state from +1 to -1 at approximately 2.32 eV. Remember that this corresponds to the two-fold negatively charged associate in the Mg-doped sample and is comparable to the defect chemistry observed in Mg-doped NBT and the second state in Fe-doped NBT. However, this transition state occurs at even higher Fermi energies, such that, under ambient conditions, we do not expect any changes of the oxidation states. Interestingly, we could not find any defect states in the gap for Al-doped NBT, although Al- and Mg-doped NBT have several common features (which might be related to their valence electron configuration). A look at the charge density difference between a structure with an $(Al_{Ti}-V_O)'$ and a structure with an $(Al_{Ti}-V_O)'$ defect associate reveals that there is an increasing amount of charge at the adjacent Ti compared to the Mg-doped structure. This might lead to a defect state, which is resonant in the conduction band.

Generally, the comparison between these three different dopant types showed that the presence of occupied d-orbitals at the valence band maximum seems to be an essential requirement for shifting the charge transition levels inside the band gap and inducing several defect states within the gap. Otherwise, the defect states are either resonant in the conduction band or are located close to the conduction band minimum with a predominantly Ti and Bi character. Depending on the Fermi level, these states might induce n-type conductivity or operate as electron traps.

8.4 THINGS TO REMEMBER

In the present chapter, we investigated electronic properties for a set of four different oxygen vacancy environments in NBT, including three dopants with varying size and valence electrons ($(\text{Fe}_{\text{Ti}}-\text{V}_{\text{O}})^{\text{q}}$, $(\text{Al}_{\text{Ti}}-\text{V}_{\text{O}})^{\text{q}}$, and $(\text{Mg}_{\text{Ti}}-\text{V}_{\text{O}})^{\text{q}}$). We further studied the influence of the symmetry on these results in the undoped supercell. Although we observe charge transition states of a pure vacancy in the band gap of rhombohedral and tetragonal NBT, these states occur at high Fermi energies. They can even be resonant in the case of tetragonal symmetry, where the band gap shrinks due to a reduced oxygen octahedral tilt. Hence, we conclude that these charge transitions will not contribute to the electronic conductivity at ambient conditions. Only under strongly reducing conditions may electrons either impact the mobility and association of the oxygen vacancies or contribute to the electronic conductivity in the tetragonal phase. We learned that the introduction of a defect associate in Al- or Mg-doped NBT does not change the electronic properties compared to the isolated oxygen vacancy. The primary effect of these dopants is to increase the total oxygen vacancy concentration and to form defect associates [166, 363]. However, we suggest that the defect association and dissociation are hardly affected by electron trapping at the defect site. The only exception is the multivalent Fe-dopant, where the charge transition from +1 to zero occurs at a value close to half of the calculated band gap. Particularly, we saw that polaronic hole states on the oxygens could not be excluded and, if mobile, can contribute to the electronic conductivity. Such an increased electronic conductivity should be visible in impedance measurements, at least at small doping concentrations. Finally, we demonstrated that a standard GGA calculation is sufficient to investigate the charge transition levels in NBT, such that we can avoid complex hybrid calculations.

LONG-RANGE STRAIN FIELDS – THE ELASTIC EFFECT OF VACANCIES

So far, we extensively examined the long-range electrostatic interactions between extrinsic and intrinsic defects and short-range distortions in the form of local relaxations in NBT. We could verify the favored defect charge state and even prove the presence of defect associates at low concentrations in Al-doped NBT employing DFT calculations as well as NMR measurements. However, we could not explain from Coulomb interactions why the conductivity continuously decreases if the Al-dopant concentration increases (see Figure 18). As discussed in Chapter 6, the formal oxygen vacancy concentration and the Coulomb interaction should be the same as in the case of Fe-doped NBT. The only difference is the size of the dopant, the long-range elastic interaction, and the amount and type of the valence electrons, which might alter the short-range electrostatic interactions. In the following section, we first investigate the long-range elastic effects of isolated oxygen vacancies as well as dopant-vacancy associates. Besides, we determine if the defect-induced long-range strain fields are superior to the electrostatic interactions. A profound understanding of these effects offers the opportunity to control defect concentrations in the bulk by elastic fields [327] or to evaluate the influence of strain fields (e.g., by grain boundaries) on the bulk conductivity. Elastic interactions might be further the decisive factor to explain the premature formation of secondary phases in Al-doped NBT. Additionally, we assess how the charge state of the defect or defect associate impacts the elastic effect since the volume changes around individual defects depend on both the size mismatch of the dopant and the charge transfer mechanisms [323].

This chapter heavily relies on Section 3.10, where we extensively described the concept of the elastic dipole tensor and relaxation volumes. These properties are related to the macroscopic change (volume and shape in the case of asymmetric defects with a distinct orientation) upon the formation of the defect [428]. However, the elastic dipole tensor can also be understood as the strain derivative of the defect formation energy [428].

9.1 COMPUTATIONAL METHODS

To calculate the relaxation volumes and the elastic dipole tensor, we relaxed the structures until the residual forces are smaller than or equal to $0.001 \text{ eV \AA}^{-1}$. Subsequently, we calculated the elastic dipole tensor by applying Equation 117 and used the code ANETO [320] to determine the relaxation volume and the interaction energy between the periodic images of the defects. Again, we rely on the theoretically obtained elastic constant tensor to consistently calculate all the present section properties. See Chapter 5 on how these values have been obtained.

In the case of charged supercells, we correct the residual stress tensor by using the correction proposed by Bruneval *et al.* [311] and summarized in Section 3.10. This correction requires complicated calculations of the absolute deformation potential (ADP).

Meanwhile, there are alternatives available to determine the ADP, for instance, using a neutral group to guarantee a neutral simulation cell. However, we use the method of Li *et al.* [339, 340], who derived a formula to calculate the hydrostatic ADP for cubic symmetries on the basis of symmetry-adapted linear combinations of spherical harmonics with $l_{\max}=6$.

Although we calculated the ADP for a cubic 111-ordered system, we used the obtained results for the correction of the 111-ordered rhombohedral structures. According to Table 5, the anion p and cation d coupling changes if we decrease the symmetry from cubic to rhombohedral (see Chapter 10). However, the differences in covalent bonding strengths are limited. Thus, the calculated ADPs for the valence and the conduction band serve as upper boundaries and should not distort our results.

We used deep Ti-core levels in the evaluation of Equation 120 such that \bar{a}_c and \bar{a}_v become independent of the exact choice of the core level [336, 339, 340]. As a result, we obtain an ADP for the valence band of 2.087 eV and -1.112 eV for the conduction band, respectively. Note, that these values perfectly reproduce the trend observed by Li *et al.* [339, 340] in a series of IV-IV, III-V, and II-VI semiconductors. There \bar{a}_v is generally positive and decreases with increasing p-d coupling, while \bar{a}_c is negative and decreases with increasing ionicity [336].

9.2 ELASTIC DIPOLE TENSOR AND RELAXATION VOLUMES

We will start by summarizing relaxation volumes, the components P_{ij} of the symmetric elastic dipole tensor, and the mechanical interaction energy in Table 9 and Table 10. Note that all values have been calculated in the pseudo-cubic representation.

We first consider a single vacancy in a 111-ordered rhombohedral structure. The relaxation volumes for the two oxygen positions in Figure 53a) differ and amount either to approximately -4.3 \AA^3 or lies in the range between -0.65 \AA^3 and -0.69 \AA^3 . This can be related to the position dependent relaxations, as illustrated in Figure 57a)(O_1) and in Figure 57b) (O_2) for the neutral vacancy. In this charge state, we observe a major difference between the Bi close to the vacancy site. If we do not apply any correction to the stresses obtained by our DFT calculation, we receive values of 15.33 \AA^3 for a V_{O} configuration and 29.78 \AA^3 for a V_{O}^{\cdot} defect respectively. Neither the sign nor the large magnitude seems reasonable, especially if we compare them to the neutral oxygen vacancy.

Except for the oxygen vacancy on O_1 , where P_{22} and P_{33} are comparable to the corresponding components in SrTiO_3 [327], we obtain an anisotropic elastic dipole tensor with non-vanishing off-diagonal components (also related to the simulation cell's pseudo-cubic orientation). For both oxygen positions, most of the main diagonal components are negative, which meets our expectations and shows that the vacancy is an overall negative dilatation center. Thus, a vacancy should be a preferred defect under compressive stress. Depending on the stress state at grain or phase boundaries, vacancies can get trapped or depleted in these areas. An accumulation of charge carriers at the grain boundary would result in the formation of space charges, contributing to a change in the dielectric polarization as suggested by Li *et al.* [115] in $(\text{Bi}_x\text{Na}_{1-x})_{0.94}\text{Ba}_{0.06}\text{TiO}_3$. However, this remains to be shown.

For the vacancy at O_2 , the relaxation volume is relatively small and could decrease if

	$\Delta\Omega_R$ (\AA^3)	P_{11} (eV)	P_{22} (eV)	P_{33} (eV)	P_{12} (eV)	P_{13} (eV)	P_{23} (eV)	E_{INT} (eV)
$V_{\text{O}}^{\times}(\text{O}_1)$	-4.333	-2.817	-2.882	-2.945	0.491	0.908	1.140	0.0056
$V_{\text{O}}^{\cdot}(\text{O}_1)$	-4.313	-2.804	-2.869	-2.932	0.491	0.908	1.140	0.0055
$V_{\text{O}}^{\cdot\cdot}(\text{O}_1)$	-4.294	-2.791	-2.856	-2.919	0.491	0.908	1.140	0.0055
$V_{\text{O}}^{\times}(\text{O}_2)$	-0.686	1.940	-0.671	-2.638	2.074	-0.944	0.023	-0.0168
$V_{\text{O}}^{\cdot}(\text{O}_2)$	-0.667	1.953	-0.658	-2.625	2.074	-0.944	0.023	-0.0168
$V_{\text{O}}^{\cdot\cdot}(\text{O}_2)$	-0.647	1.966	-0.645	-2.612	2.074	-0.944	0.023	-0.0168
$\text{K}_{\text{Na}}^{\times}$	-6.687	-4.400	-4.417	-4.522	0.666	0.627	0.609	0.0098
$\text{Ba}_{\text{Bi}}^{\cdot}$	-4.926	-3.284	-3.248	-3.292	0.850	0.827	0.839	0.0064
$\text{Ba}_{\text{Na}}^{\cdot}$	-11.624	-7.551	-7.794	-7.843	1.624	1.628	1.549	0.0327
$(\text{Al}_{\text{Tl}}-\text{V}_{\text{O}})^{\times}$	5.605	1.307	5.469	4.405	-0.052	1.363	-0.456	-0.0133
$(\text{Al}_{\text{Tl}}-\text{V}_{\text{O}})^{\cdot}$	5.625	1.320	5.482	4.418	-0.052	1.363	-0.456	-0.0133
$(\text{Al}_{\text{Tl}}-\text{V}_{\text{O}})^{\cdot\cdot}$	5.616	1.314	5.476	4.412	-0.052	1.363	-0.456	-0.0133
$(\text{Al}_{\text{Tl}}-\text{V}_{\text{O}}-\text{Al}_{\text{Tl}})^{\times}$ (1)	9.607	7.374	2.187	9.604	0.330	-0.753	-0.032	-0.0378
$(\text{Al}_{\text{Tl}}-\text{Al}_{\text{Tl}}-\text{V}_{\text{O}})^{\times}$ (2)	11.844	12.392	7.573	3.662	1.928	-0.207	0.034	-0.0443
$(\text{Al}_{\text{Tl}}-\text{Al}_{\text{Tl}}+\text{V}_{\text{O}})^{\times}$ (3)	10.751	8.137	4.354	8.956	1.172	2.771	0.658	0.0056
$(\text{Al}_{\text{Tl}}-\text{V}_{\text{O}}^{\text{Bi}})^{\times}$ (001)	4.783	2.058	8.385	1.249	4.676	0.331	0.986	-0.0083

Table 9: Relaxation volumes and elastic dipole tensor for doped an undoped NBT. O_i specifies the oxygen which has been removed to generate the oxygen vacancy, as presented in Figure 53a). 2NN stands for second neighbor shell, 001 refers to the 001 A-site cation order with an orthorhombic host lattice (if not stated otherwise, we used an 111-ordered rhombohedral structure), and (1), (2), or (3) represent the vacancy positions according to Figure 72b). Note that the relaxation volume is the trace of the relaxation volume tensor.

	$\Delta\Omega_R$ (\AA^3)	P_{11} (eV)	P_{22} (eV)	P_{33} (eV)	P_{12} (eV)	P_{13} (eV)	P_{23} (eV)	E_{INT} (eV)
(Mg _{TI} -V _O) [×] (1×1×1, O ₂)	-1.8757	-4.476	1.361	-0.627	1.235	0.851	1.331	-0.2774
(Mg _{TI} -V _O) [×] (1×1×2, O ₂)	-1.030	-4.011	1.411	0.546	1.328	0.930	1.469	-0.0864
(Mg _{TI} -V _O) [×] (1×2×2, O ₂)	-2.452	-5.279	0.801	-0.414	0.343	0.719	1.616	0.0430
(Mg _{TI} -V _O) [×] (2×2×2, O ₂)	-2.545	-4.147	0.552	-1.482	1.360	1.153	0.987	-0.0203
(Mg _{TI} -V _O) [×] (O ₁)	-3.955	-6.744	1.438	-2.584	0.651	0.146	3.448	-0.0558
(Mg _{TI} -V _O) [×] (O ₁ to O ₂)	-9.706	-11.016	-5.375	-2.972	5.088	1.106	3.971	-0.0254
(Mg _{TI} +V _O) [×] (2NN)	-7.003	-8.534	-0.983	-4.453	1.048	1.646	1.475	-0.0474
(Mg _{TI} -V _O) [×] (001)	-5.024	-5.811	-0.835	-5.635	3.900	-0.881	-0.368	-0.0108
(Fe _{TI} -V _O) [×]	-5.165	-4.171	-2.245	-3.886	2.788	1.652	0.975	0.0088
(Fe _{TI} -V _O) [·]	-5.145	-4.158	-2.232	-3.873	2.788	1.652	0.975	0.0088
(Fe _{TI} -V _O) ^{··}	-5.125	-4.145	-2.219	-3.860	2.788	1.652	0.975	0.0088
(Fe _{TI} -V _O) [·]	-5.154	-4.164	-2.238	-3.880	2.788	1.652	0.975	0.0088
(Fe _{TI} -V _O -Fe _{TI}) [×] (1)	-1.648	-0.765	-3.836	1.313	0.010	0.080	-0.079	-0.0252
(Fe _{TI} -V _O -Fe _{TI}) [×] (1 to 2)	-4.958	-2.435	-3.448	-4.008	2.133	0.664	0.969	0.0074
(Fe _{TI} -Fe _{TI} -V _O) [×] (2)	-1.895	2.606	-2.033	-4.354	2.616	0.517	0.445	-0.0419
(Fe _{TI} -Fe _{TI} +V _O) [×] (3)	-5.070	-2.860	-6.038	-1.216	2.118	3.222	1.090	-0.0062
(Fe _{TI} -V _O) [×] (001)	-5.923	-6.306	-2.522	-5.649	3.934	0.166	0.929	-0.0123

Table 10: Relaxation volumes and elastic dipole tensor for doped an undoped NBT. O_i specifies the oxygen which has been removed to generate the oxygen vacancy, as presented in Figure 53a). 2NN stands for second neighbor shell, 001 refers to the 001 A-site cation order with an orthorhombic host lattice (if not stated otherwise, we used an 111-ordered rhombohedral structure), and (1), (2), or (3) represent the vacancy positions according to Figure 72b). Labels such as (1 to 2) describe a saddle point configuration. Different cell sizes are indicated by annotations of the type (2×2×2). The latter is the regular supercell size used in this thesis (320 atoms). Note that the relaxation volume is the trace of the relaxation volume tensor.

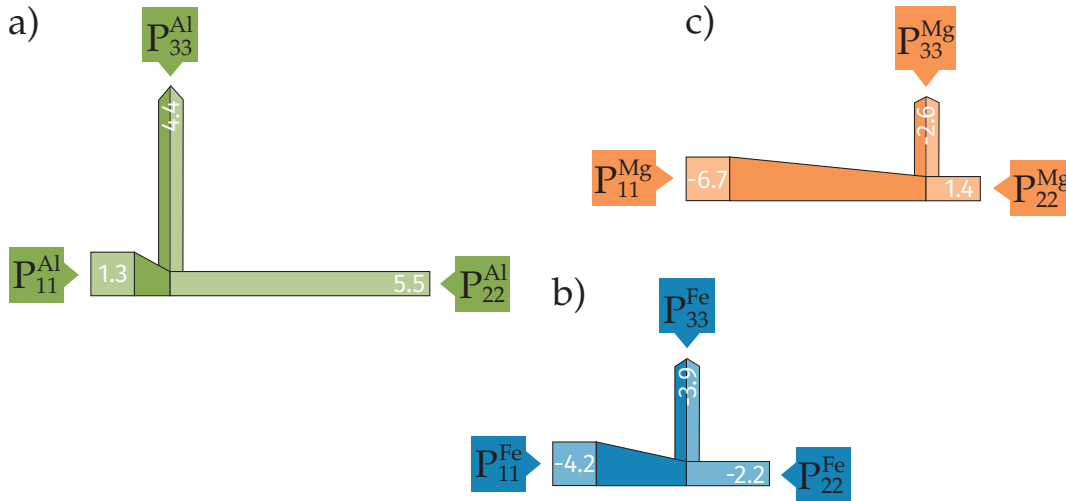


Figure 90: Main diagonal components (P_{11} , P_{22} , and P_{33}) of the elastic dipole tensor for Mg-, Al-, and Fe-doped NBT. Note the anisotropy of this property.

we average over all defect orientations. This would make it tremendously difficult to control the defect concentration by external strain fields [327].

We continue with defect associates between an oxygen vacancy and the acceptor dopants Al, Mg, and Fe, which are of particular interest in the present thesis. Since we are interested in the elastic “net effect” of the whole defect associate, we neglect the cases of isolated dopants.

Al shows a positive relaxation volume as well as positive components P_{ii} . This is counterintuitive since Al is the smallest acceptor dopant. The relaxation volume even increases if we introduce a second acceptor dopant. As far as long-range elastic distortions are considered, the formation of a secondary phase with increasing dopant concentration is plausible solely from the relaxation volume increase. This is in direct contrast to Fe-doped NBT and is probably the major cause for their different behavior with increasing dopant concentration. It also explains the association between a first-order dopant cluster and an oxygen vacancy, if we compare the configuration $(\text{Al}_{\text{Ti}}-\text{V}_{\text{O}}-\text{Al}_{\text{Ti}})^{\times}$ with the $(\text{Al}_{\text{Ti}}-\text{Al}_{\text{Ti}}+\text{V}_{\text{O}})^{\times}$ arrangement. In the former case, the relaxation volume is smaller.

The anisotropy of the elastic dipole tensor might pave a way to control the defect associate’s orientation by external strain fields [327, 429].

In contrast to Al-doped NBT, we observe a negative relaxation volume as well as primarily negative P_{ii} components (especially P_{11}) of the elastic dipole tensor for Mg-doped NBT. Hence, we expect a similar but more pronounced dependence of associate concentrations on external elastic fields as in the case of a pure vacancy. Again, we notice a difference between the two possible oxygen positions, however, less pronounced. This indicates a dependency of the elastic properties on the orientation of the defect dipole. Interestingly, a “second neighbor” configuration leads to a larger absolute relaxation volume, which is probably an additional reason (besides the Coulomb interaction) for a strong defect associate. It further explains why Mg shows similar



Figure 91: Comparison between the relaxation volume of a defect dipole and the ionic radii of the dopant in Mg-, Al-, and Fe-doped NBT.

conductivities compared to Al- and Fe-doped NBT, although the oxygen vacancy concentration should be twice as high (if all Mg-ions are incorporated into the host lattice).

An iron dopant leads to the largest negative relaxation volume and a less anisotropic elastic dipole tensor, at least on the main diagonal. However, the same general trend as in Mg-doped NBT can be observed. A possible explanation for a deviating absolute magnitude can be either the size difference between Fe and Mg or the presence of a magnetic moment on the Fe-lattice site. The latter seems to be a decisive factor in metals [430]. Contrary to Al, a first-order cluster reduces the absolute magnitude of the relaxation volume from -5.145 \AA^3 to -1.648 \AA^3 and seem to promote the accumulation of Fe-dopants. Figure 90 summarizes the main components (P_{11} , P_{22} , and P_{33}) of the elastic dipole tensor for Mg-, Al-, and Fe-doped NBT and clearly visualizes the anisotropy of this property.

Figure 91 contrasts the relaxation volume ($\Delta\Omega_r$) of a defect dipole in Mg-, Al-, Fe-doped NBT with the ionic radii of the dopant species. The ionic radii have been determined from Reference [397]. The reciprocal relationship between the ionic radii of the dopant and the absolute relaxation volume is especially noticeable. The larger the ionic radius, the smaller the absolute relaxation volume. Furthermore, if the ionic radius is larger than the size of Ti (0.61 \AA [397]) the relaxation volume becomes negative. Instead, if the dopant is smaller than Ti, it becomes positive.

Generally, the atomic displacements hardly vary with respect to the charge state of the associate and amount to approximately 7% of the average bulk Ti-O bond length of 2.0 \AA . This explains the slight difference between the relaxation volume of defect complexes with varying charge states. A comparison between a higher-order and a first-order defect associate reveals a further driving force for a strong defect association in Mg-doped NBT. Table 11 lists the differences in the relaxation volumes between different dopant-vacancy associate configurations. We emphasize that these differences depend on exact oxygen vacancy position within a neighbor shell (O_1 and O_2). In Al-doped NBT, we see almost no difference in the relaxation volumes for oxygen vacancies, located on the first neighbor shells. A small difference for Fe-and

	ALUMINUM	IRON	MAGNESIUM
$O_{1,3NN} - O_{1,1NN}$	0.92	-0.70	-0.94
$O_{1,2NN} - O_{1,1NN}$	0.30	-1.44	-2.37
$O_{2,3NN} - O_{2,1NN}$	0.10	-2.16	-2.81
$O_{2,2NN} - O_{2,1NN}$	-0.54	-2.55	-3.23

Table 11: Difference of relaxation volumes of vacancy-dopant associates on various neighbor sites in \AA^3 . The differences are with respect to the first neighbor site. The subscript 1 or 2 depicts the two inequivalent oxygen positions in the R3 structure.

Mg-doped NBT can only be observed for the O_1 position on the third neighbor shell. However, in case of O_2 , we observe an increase in the absolute relaxation volume for the second and third neighbor shell. More precisely, it shows that the dissociation is most unfavorable in the case of Mg, since the absolute relaxation volume increase is largest, if the vacancy is successively removed from the immobile Mg dopant. Since these calculations have only been performed once, we can not provide any statistics. However, the trend is unambiguous.¹

We can also use the relaxation volume to quantify the effect of A-site substituents. The results for K_{Na}^\times , Ba'_{Bi} , and Ba_{Na} (without any oxygen vacancies) are given in Table 9. Similar to the other defects, the off-diagonal components are rather small and positive in all three cases (pseudo-cubic representation). The almost direction-independent elastic dipole tensor components on the main diagonal are particularly noticeable. This contrasts with the other defects, where we observe a distinct anisotropy even for an isolated vacancy on O_2 . Equally interesting and the most striking result is that all three relaxation volumes are negative, despite the large ionic radii of Ba or K. Since the centering of the Ba and K ions within the A-site polyhedron results in a locally reduced polarization, a substitution with these ions mimics the decrease of the polar mode amplitude in a compressed simulation cell [2]. Therefore, it resembles the response toward a compressive external strain field. Further comparing the elastic effect of Ba'_{Bi} with the data of Ba_{Na} suggests that Ba is more likely to replace Bi than Na.

If we use an orthorhombic host lattice and incorporate a defect associate such that the oxygen vacancy resides in the Bi-layer, we do not observe significant changes in the relaxation volumes. Although the absolute P_{ii} values are in most cases larger, they show a similar trend and sign.

A “size effect” study has been performed for Mg-doped NBT, which shows that the relaxation volume and the elastic dipole tensor are not converged for small system sizes, even with a $1 \times 2 \times 2$ supercell (160 atoms). We further see that the interaction energy E_{int} is most substantial in a $1 \times 1 \times 1$ cell and decreases with increasing system size, but not consistently.² Since E_{int} hardly depends on the charge state, the inclusion

¹ Note that the difference for Al- and Fe-doped NBT has been obtained by comparing two calculations of the same charge state. Thus, despite the ill-defined stresses in charged supercells, the difference is meaningful.

² Remember that we have to subtract $\Delta E = 0.5 E_{int}$ from the total energy of the supercell.

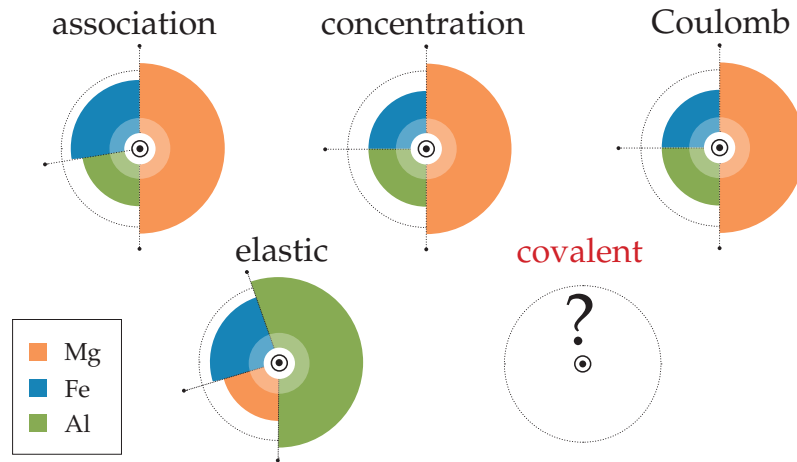


Figure 92: Summary of the different charge compensating oxygen vacancy concentration, the Coulomb, and the elastic interaction in Mg-, Al-, and Fe-doped NBT.

of the interaction energy between two neighbors of the periodic defect array does not change the exact position of the charge transition level above.

9.3 THINGS TO REMEMBER

Contrary to our expectations, we obtained a positive relaxation volume and a predominantly positive elastic dipole tensor for Al (positive dilatation center), while we detect the opposite for Fe and Mg dopants (negative dilatation center). Although a distortion of the dopant can lower the electronic energy, this lowering has to compete with an increase of the structural energy [44]. In Al-doped samples, this competition is lost at approximately 2%. At this concentration the amount of secondary phases increases continuously, as they are energetically more favorable than randomly distributed point defects. Furthermore, the difference between the relaxation volume of a second-order and a first-order defect associate is comparably small. This suggests a lower driving force for defect association from an elastic point of view. Thus, in Al-doped NBT, the elastic contribution seems to be the decisive factor for an early formation of secondary phases and becomes increasingly important for the remaining dopant types at higher concentrations. We do not identify a pronounced dependency of the A-site order of NBT on the mechanical response, at least not for the three acceptor dopants Mg, Al, and Fe. Figure 92 summarizes the results of the present thesis up to this chapter, including different oxygen vacancy concentrations, Coulomb, and elastic interactions. Thus far, Mg-doped NBT shows a dominant attractive interaction between the oxygen vacancy and the dopant. While Al- and Fe-doped NBT behave comparably in the previous chapters, we observe a high elastic contribution in the present chapter with a tendency to form either higher-order associates or even secondary phases. In the next chapter, we will focus on the last contribution: covalent bonds.

COVALENT BONDING CONTRIBUTION TO THE STABILITY OF DEFECT ASSOCIATES

In the previous Chapters, we emphasized the importance of atomic arrangements (point symmetries) in the vicinity of defects [360, 379]. These are affected by both the electronic structure of the ions and lattice stresses [44]. In this final chapter, we will take a closer look at the short-range electrostatic interaction between the different dopants and their surrounding, focusing on the covalent bonding contribution. We will see that these interactions are a natural consequence of local relaxation processes, leading to small but detectable variations on the total energy landscape. However, are they large enough to influence the defect association remarkably?

To answer this question, we quantify bond strengths using integrated COHPs, which are essentially pairwise contributions to an effective one-particle energy [355, 360]. This analysis widens the defect chemical picture beyond a predominantly Coulomb interaction. For a detailed introduction to these concepts, the reader is referred to Section 3.13. Since this chapter requires knowledge of the bulk properties, we encourage the reader to review Section 5.3. In Section A.1, we present a short analysis of the crystal field splitting in the R3 space group, which is optional but a helpful supplement for the following discussion.

10.1 FIGHTING AGAINST CHARGE LOSS: REHYBRIDIZATION OF FE-O QUANTUM STATES

Let us first investigate the changes in the electronic structures upon doping. If we introduce a Fe-dopant and an oxygen vacancy into an R3 host lattice, we notice a reduction of the band gap at the Γ -point by the formation of dangling bonds. These defect states are closely attached to the conduction band minimum in the associated as well as the dissociated case and are a mix of a Fe-, a Ti-, an O-, and a small Bi-contribution. However, for an associated dopant pair, these states are more pronounced and reach further into the band gap. Figure 93a) is an example for the structure containing a $\text{Fe}'_{\text{Ti}}\text{-V}\ddot{\text{O}}$ associate.

A further contribution of Fe 3d orbitals can be observed at around -6 eV. These states mainly stem from the interaction between Fe and the surrounding oxygens, forming a non-regular polyhedral environment (as already discussed above). A small Bi component can be observed as well. Additionally, a small but noticeable Fe 3d density can be found in the region between -5 eV and 0 eV with a slight increase at the Fermi level. This results from the interactions with the oxygen ligands and neighboring Bi. At the lower bound of this valence band, we also observe a Fe 4s contribution (not included in Figure 93), which most likely couples with O 2p and Bi 6p states.

The analysis of the pCOHPs and IpCOHPS shows that, as in the case of a Ti-Ti bond, the Fe-Ti covalent interaction is not particularly strong (IpCOHP/bond is about

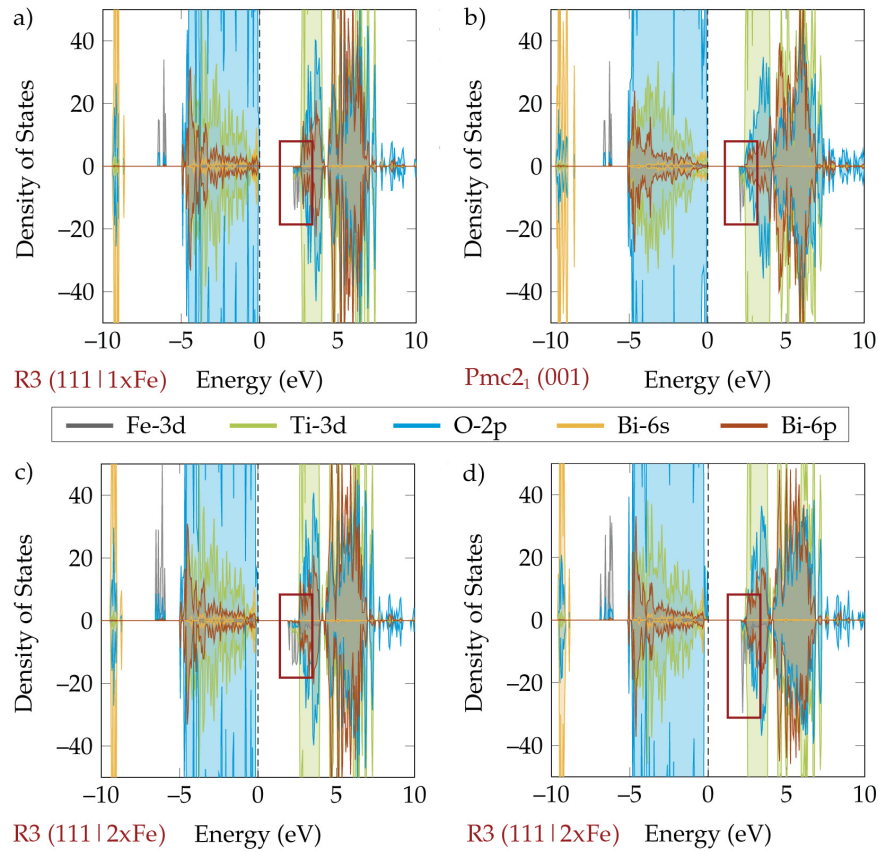


Figure 93: Density of states for different Fe-doped structures. Figure a) shows the density of states for a structure containing a $\text{Fe}'_{\text{Ti}}-\text{V}_{\text{O}}$ associate in a R3 host lattice, b) depicts a $\text{Fe}'_{\text{Ti}}-\text{V}_{\text{O}}$ associate in a $\text{Pmc}2_1$ matrix, and c) and d) illustrate a $\text{Fe}'_{\text{Ti}}-\text{Fe}'_{\text{Ti}}$ cluster with an associated and a dissociated oxygen vacancy, respectively.

-0.013 eV/bond). Although we observe an on-site hybridization of Fe 3d and Fe 4p states, which normally leads to more extended orbitals, we do not have a significant B-site d-d coupling [413]. The IpCOHP value for Fe-Bi (-0.013 eV/bond) and Fe-O (-2 eV/bond) is almost half of the Ti-O and Ti-Bi equivalents. The only difference between the IpCOHPs for a associated and a dissociated $\text{Fe}'_{\text{Ti}}-\text{V}_{\text{O}}$ defect pair is at most -0.25 eV per bond. Interestingly, a higher bonding strength is observed for the pentahedral coordination environment. In the latter case, this leads to a pronounced anti-bonding spin up contribution (Figure 94c) at the Fermi energy, caused by a smaller average Fe-O bond length and, associated therewith, a higher interatomic orbital mixing.¹ In turn, for a Ti-O covalent bond, no destabilizing anti-bonding contribution can be found at E_{F} .

Likewise, the average IpCOHP values for Bi-O bonds are almost unaffected by the dopant and the vacancy. An example for a COHP curve of a Bi-O band is given in Figure 40a) for two different Bi ions in the same Fe-doped 111-ordered rhombohedral

¹ The Mulliken charge for Fe decreases from 1.84 in the dissociated case to 1.78 for a dopant-oxygen associate. We further obtain an average Mulliken charge of 1.45 for Bi, 0.94 for Na, 1.4 for Ti, and -0.87 for oxygen. However, if the bond length between the B-site cation and oxygen decreases, the charge around the oxygen may increase up to -1.02 simultaneously.

structure with and without a vacancy attached to the dopants. We see that the amount of anti-bonding states at E_F depends on the relaxation of Bi after introducing a defect associate: A relaxation, which enhances the displacement caused by the ferroelectric instability, does not significantly alter the energy or the amount ² of anti-bonding states at the Fermi level (high covalent inter-atomic bonding contribution leads to a more significant splitting of the states and thus to a higher density at E_F [137]). In turn, a more noticeable change can be observed when the Bi relaxes opposite to the ferroelectric distortion. As a result, the amount of anti-bonding states at 0 eV decreases and the magnitude of low energy bonding states increases simultaneously. The reduction of these anti-bonding states might be the result of a decreasing Bi 6s and Bi 6p intra-atomic hybridization, which is a result of the lone pair effect (remember that the lone pair effect is a stabilized anti-bonding interaction [135, 136]). Such a decrease leads to a smaller splitting between the bonding and the anti-bonding states. A centering of the A-site cation also increases the effective coordination ³ to the neighboring oxygen ions such that this relaxation leads to a shrinkage of the average Bi-O bonding distance.

Figure 94d) illustrates the Ti-O interaction in a rhombohedral structure for a fivefold coordinated Ti close to a vacancy. A comparison between 94d) and 40a) demonstrates two things: Firstly, Ti has a relatively stable bonding environment in different NBT polymorphs. Secondly, this constant bonding environment does not seem to depend on the coordination polyhedra, such as the octahedra in 40a) or the pentahedron in 94d). The only exception are the absolute COHP values at about -4 eV, which most probably result from the introduction of a vacancy on the first neighbor shell.

This short analysis indicates that the structural relaxation process results in an optimal, almost unchanged bonding environment. The same result can be deduced from the eigenvalues of the density matrix, which hardly change if we compare the associate with the dissociated defect pair. Instead of reducing the valence electron concentration and to “get rid of the anti-bonding states” [360] in the presence of an oxygen vacancy, structural relaxations lead to an even higher amount of destabilizing states at E_F in the case of a Fe-dopant. This charge compensation process reminds of a self-regulating response in transition metal oxides upon a perturbation. This means that a local rehybridization counterbalances the charge loss on the cation site. Such self-regulating processes are often observed in materials with a strongly coupled anion and cation sublattice, enabling the exchange of charge carriers [422, 424].

Interestingly, if we introduce a second Fe-dopant to form a $Fe'_{Ti}-Fe'_{Ti}$ cluster, which is associated or dissociated to a vacancy, we observe similar trends in the density of states as shown in Figure 93. The band gap states are closely attached to the conduction band minimum and deeper in energy for the associated oxygen vacancy. However, we obtain the opposite behavior for the Fe-O COHPs in Figure 95. If the oxygen vacancy and the Fe-dopants form a first-order associate, the amount of anti-bonding states at the Fermi level decreases, which slightly stabilizes this configuration. Both

² Fluctuations even occur in the bulk structure.

³ The effective coordination in a polyhedra is given by $\sum_i \omega_i$ with $\omega_i = \exp[1 - (l_i/l_a)^6]$, where l_i is the bond length i and l_a can be formulated as $l_a = \frac{\sum_i l_i \exp[1 - (l_i/l_{min})^6]}{\exp[1 - (l_i/l_{min})^6]}$.

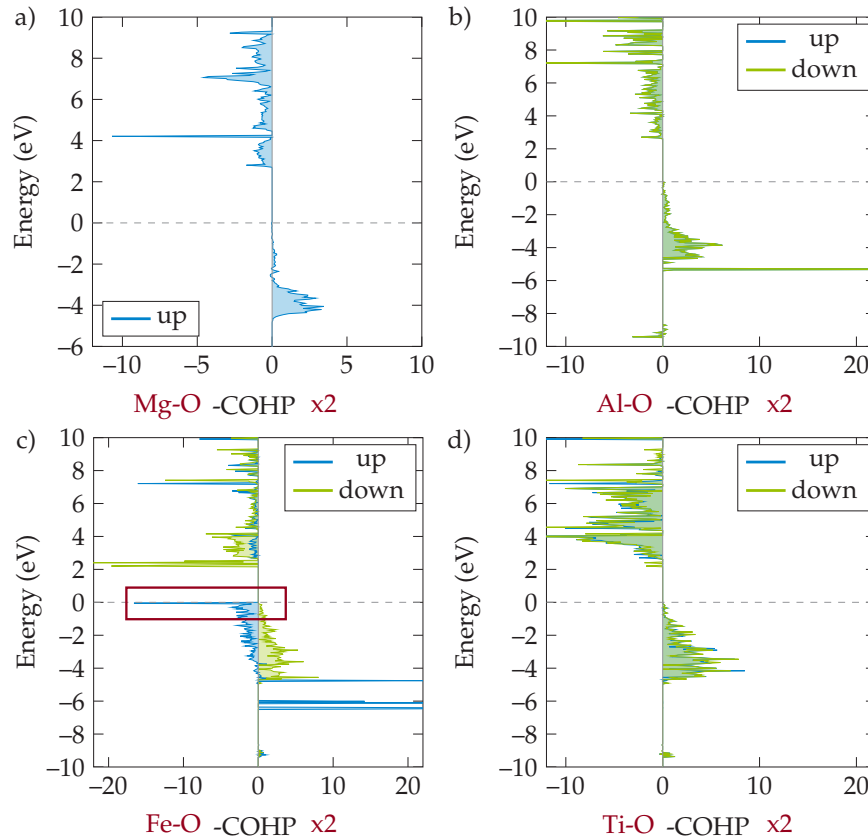


Figure 94: Crystal Orbital Hamiltonian Population (COHP) for a Dopant-oxygen bond in a a) Mg-doped, b) Al-doped, and c) Fe-doped 111-ordered rhombohedral structure. Figure d) shows an example for a Ti-O bond in a R_3 host lattice. Note that we multiplied the COHPs by two for clarity.

dopants form an almost monomorphous environment in terms of covalent bonding strength and orbital occupation, which additionally closely resembles the isolated case. The enhanced anti-bonding contribution in Figure 95d) is probably associated with the increased spin up O 2p density at the valence band maximum Figure 93d). Although we can not completely exclude a destabilization of the covalent bonds by the formation of a $\text{Fe}'_{\text{Ti}}-\text{V}'_{\text{O}}-\text{Fe}'_{\text{Ti}}$ associate, we note for this specific case that the interatomic covalent interaction does not solely explain the pronounced concentration dependency in acceptor doped NBT. Thus, we assume that predominantly long-range dipole-dipole interactions modify the association and dissociation behavior between an oxygen vacancy and a dopant with increasing dopant concentration.

10.2 A SOLID SOLUTION WITH BaTiO_3 STABILIZES THE Fe-V DEFECT ASSOCIATE

In the following, we estimate the effect of a solid solution with BaTiO_3 on the stability of a $\text{Fe}'_{\text{Ti}}-\text{V}'_{\text{O}}$ associate. For this purpose, the volume of the supercell has been successively increased. Additionally, for the sake of completeness, we investigate the behavior of NBT under decreasing volume. The band gap at Γ increases slightly with larger volumes and decreases with smaller lattice parameters. We further observe

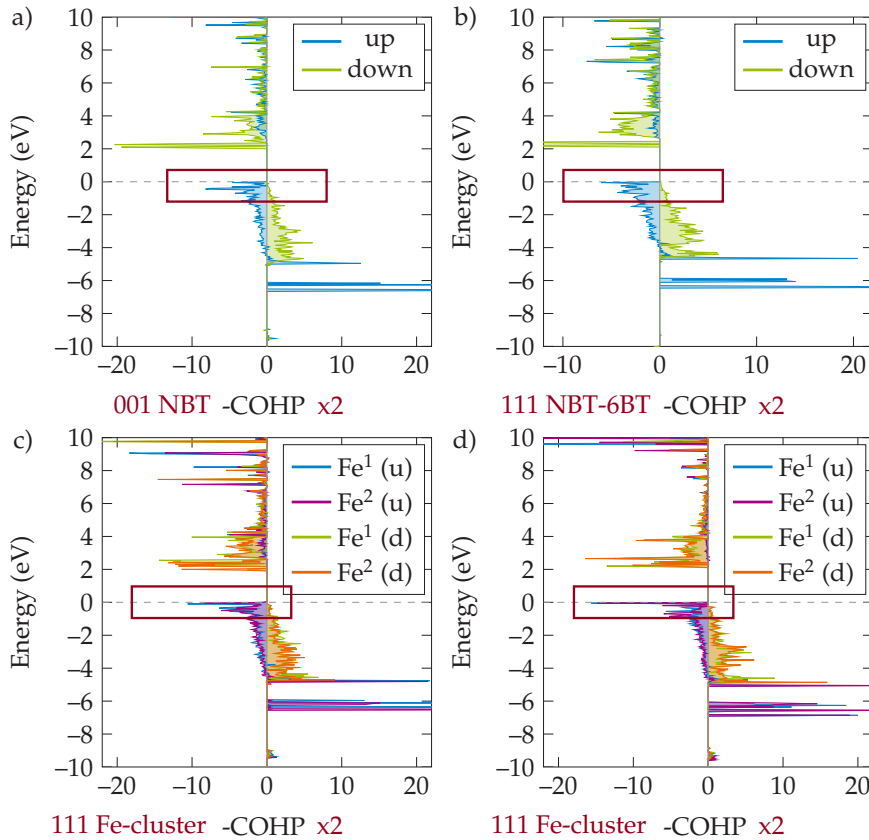


Figure 95: Crystal Orbital Hamiltonian Population for Fe-doped NBT in a) 001-ordered orthorhombic structure, a b) 111-ordered rhombohedral NBT-6BT, and in a 111-ordered rhombohedral structure containing a $\text{Fe}'_{\text{Ti}}\text{-Fe}'_{\text{Ti}}$ cluster with c) an associated and d) a dissociated oxygen vacancy.

that the contribution of Fe 3d states at the valence band maximum depends reciprocally on the bond length and, therefore, on the cell's volume. The Bi 6s density shifts slightly upwards for increasing volume and vice versa. This can be a result of a decreasing lone pair effect.

In general, all covalent bonds between Fe, Ti, Bi, and O weaken for more considerable interatomic distances, leading to a declining number of anti-bonding states at the Fermi level and, therefore, stabilizing the defect associates. This locally stabilizing defect configuration could be a decisive difference between Fe-doped NBT and Fe-doped NBT-based solid solutions. Remember that in the latter case, ionic conductivity first prevails at dopant concentrations equal to and above 2 %.

If we replace two of the eight A-site cations by Ba^{2+} , we observe a general increase in the B-O bond length. This is most pronounced close to the Ba^{2+} ions, but the deviation of the average Fe-O bond does not exceed 0.03 Å. The formation of a solid solution with BaTiO_3 has a similar effect compared to a volume increase and can be reduced if the two Ba^{2+} ions are located close to the oxygen vacancy on regular Bi^{3+} sites. In this arrangement, the Ba^{2+} ions replace two Bi^{3+} , which displace from the dopant as a result of their ferroelectric distortion and are loosely bonded to the Fe-

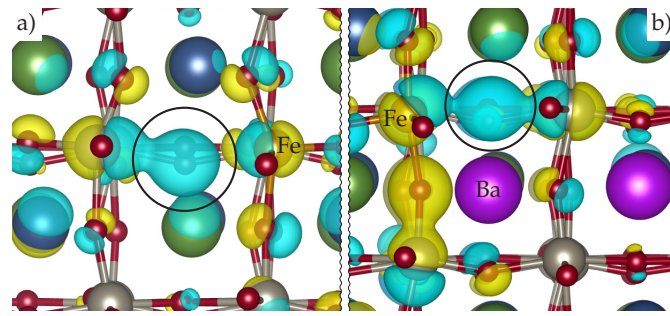


Figure 96: Comparison of the charge density between a) a Fe-doped NBT and b) a Fe-doped NBT-BT structure. Both structures are referenced to a doped cell without an oxygen vacancy. A blue charge cloud represents a decrease and a yellow cloud an increase of charge density.

dopant. Thus, the influence of the Ba^{2+} ions on the Fe-O anti-bonding contribution is marginal. However, if we replace two Bi^{3+} opposite to the vacancy and closer to Fe, the adjacent Fe-O bond expands, and the amount of anti-bonding states at the Fermi energy reduces (see Figure 95b) or is shifted towards lower energies. This illustrates again the “triangular relationship” between Fe, O, and Bi.

Although the Fe-O covalent bonds become slightly stronger if a Ba^{2+} substitutes Bi^{3+} on the nearest neighbor site (inductive effect [380]), we observe a decrease of electron density in anti-bonding states. This might be caused by a negligible covalent contribution (orbital overlap) of the Ba^{2+} .⁴

Additionally, we see in Figure 96 that the positive charge (blue) from the oxygen vacancy is centered between two B-sites if a Ba^{2+} ion is located on a first neighbor Bi^{3+} site. Instead, if no Ba^{2+} is present, we see a clear preference for the B-site, which was initially closer to the now removed oxygen ion.

Instead, if we replace a Na^+ and a Bi^{3+} by two Ba^{2+} to remain charge neutrality, the stabilizing effect is hardly reproducible. For that reason, it can be assumed that a stabilization of the local bonding environment can only be realized if Ba^{2+} occupies Bi^{3+} sites, which additionally have a sufficient covalent bond to the B-site cation in question. Note that this conclusion is solely based on the covalent bonding analysis and does not include long-range electrostatic interactions, which can compensate for these local instabilities. We should remember that a Ba'_{Bi} defect is effectively negatively charged, which brings a second Coulomb interaction into play.

10.3 ELECTRONIC CONDUCTIVITY DUE TO SHALLOW DOPANT-OXYGEN STATES?

In the following subsection, we investigate the chemical environment for Al-, and Mg-doped NBT, starting with Al. The band gap at the Γ -point is close to the band gap calculated with the GGA functional for the bulk R_3 structure. This shows that the vacancy alone does not cause a significant energy reduction of the neighboring Ti 3d states, neither for A-site nor B-site substitution. However, the slight reduction of the band gap is more pronounced if an O_1 with a slightly smaller Ti-O bond length is removed as depicted in Figure 53. Thus, the dangling bonds are assumed to be

⁴ The Mulliken charge of Ba^{2+} is on average 2.01, which resembles the formal ionic charge states.

primary resonant within the host electronic bands.

The main contribution of Al in the overall density of states can be found at energies between -5 eV and -6 eV, where Al and O 2p orbitals overlap. It is relatively small compared to the other elements, such that the density of states plot hardly distinguishes from the bulk electronic structure and is not shown here.

Also, in the case of Al, the covalent contribution seems to be non-negligible. The effective coordination in an irregular pentahedron is close to ideal and amounts to approximately 4.7.⁵ If we analyze the IpCOHPs and the pCOHPs to understand the chemical environment around the dopant, we find that the IpCOHPs of Al-Bi, Al-Ti, and Al-O are generally larger compared to the Fe-doped structure. For instance, the Al-O bond's average IpCOHP is about -5.13 eV/bond, which is contradictory at first sight. However, if we examine the pCOHPs in greater detail, we recognize that these bonding states lie at low energies rather than at the Fermi level, where electronic conductivity would take place. In this upper energy window, we observe only non-bonding states (see Figure 94b). The Ti-O and Bi-O bonds are comparable to the Fe-doped sample, indicating that appropriate relaxations can compensate for a perturbation caused by a substitutional atom. The fact that Al dopants show larger IpCOHPs for the oxygen bonds agrees with the results of the Chapters 6 and 9. It indicates the formation of higher-order associates at lower and secondary phases at higher concentrations, respectively. It also means that the loss of an oxygen bond is more detrimental in the case of Al-dopants compared to Fe- or Mg-dopants.

For Mg-doped NBT, the band gap at Γ is equal to the bulk value, and no gap states appear upon the incorporation of Mg. As already mentioned above, the average Mg-O bond length and the effective coordination exceed the respective values in Al- or Fe-doped NBT. While the Bi-O and the Ti-O bonds are again stabilized against extrinsic doping, the interaction of Mg with the surrounding Bi, Ti, as well as O (IpCOHP amounts to -0.97 eV/bond) is weakened compared to the other dopant types. Furthermore, no bonding or anti-bonding contribution is found directly at the Fermi level (see Figure 94a).

For Fe-doped and undoped NBT, we learn that a sizeable interatomic distance hinders a direct d-d coupling between B-site orbitals. However, interatomic bonding is feasible by a coupling of O 2p orbitals into d electron states. If the overlap between the transition metal and the oxygen orbitals becomes strong, the 3d electrons might become itinerant [37, 380]. In turn, if we introduce Mg- or Al-dopants into the supercell, we locally disturb the coupling between B-site 3d and oxygen 2p orbitals. Thus, Mg and Al can act as charge scattering defects, effectively reducing the mobility of electrons [18].

Let us remember the experimental results of Figure 18 and concentrate on the concentration range before oxygen vacancies "take over" and we observe predominant electronic conduction. Here, we see an initial increase of the electronic conductivity at low Fe-doping contents. At the same time, we notice a decrease in Mg- and Al-doped NBT. This observation fits perfectly with the theoretical findings. The latter shows

⁵ The Mulliken charge of Al is 1.4, which is almost half of the formal charge state 3.

that we have a reduced band gap (2.25 eV) and additionally a B-site dopant, which bridges the Ti vacancy via covalent bonds to the adjoining oxygens at the Fermi level.

In any case, we exclude deep band gap states in an otherwise impurity-free doped NBT sample with the applied computational parameters. It might be possible that a different U parameter for Fe would lead to a complete splitting of defect states from the conduction band edge such as in the case of bulk anatase [431]. However, since there is no experimental evidence, we do not assume any deep states (at least in a Fe^{3+} charge state), which might even develop into an intermediate band at higher doping concentrations.

10.4 A-SITE ORDER HARDLY INFLUENCES COVALENT BONDING CONTRIBUTION

If we compare the density of states between the doped $\text{Pmc}2_1$ host lattice and a doped R3 structure, a seemingly reduced intra-atomic hybridization of Bi 6s and Bi 6p states can be observed. Figure 93b) shows the density of states for a Fe-doped 001-ordered supercell as a representative example. This shows that the on-site coupling is more pronounced in samples with a corporate $\langle 111 \rangle$ -displacement.

Particularly in the case of Fe-doping, we further notice a declining Bi 6p contribution in the shallow band gap states attached to the conduction band edge. Interestingly, the IpCOHP values for the characteristic Bi-O and Ti-O bonds are almost identical to the 111-ordered rhombohedral structure, irrespective of small local variations. Also, the average bond lengths at the A- and the B-site are comparable. The only difference between an oxygen vacancy in the Na-layer and an oxygen vacancy in the Bi-layer has been detected in the IpCOHP s of the dopant-O and dopant-Bi interaction. While the IpCOHP for the dopant-O bond slightly increases for an oxygen vacancy in the Bi-layer, the opposite is true for the dopant-Bi bond. A more intense bonding analysis in the Fe-doped supercell reveals that the amount of anti-bonding states at the Fermi level decreases in the presence of a vacancy inside the Bi-layer. This can result from a reduced Bi-O overlap (see Figure 95a) and is similar to the effect of a Ba'_{Bi} substitution. It also shows once more the delicate interplay between Bi, O, and dopant covalent bonding contributions.

10.5 THINGS TO REMEMBER

In this chapter, we used DFT to determine the electronic structure of doped and pristine NBT. We further studied the covalent contribution to the occurring defect association and learned that:

- For the covalent contribution (B-O bond) to the association energy, we obtain:

$$E_{\text{Al}}^{\text{Cov}} > E_{\text{Ti}}^{\text{Cov}} > E_{\text{Fe}}^{\text{Cov}} > E_{\text{Mg}}^{\text{Cov}}.$$
- For the amount of destabilizing anti-bonding states, we found: $N_{\text{Fe}}^{\text{antib.}} > N_{\text{Al,Mg}}^{\text{antib.}}$
- A high covalent bonding contribution, in combination with a small size, is a reasonable explanation for the preference of higher-order associate with an oxygen vacancy (full octahedron vs. pentahedron).

- The covalent bonding contribution is almost independent of the A-site order, if we compare the 111-ordered rhombohedral with the 001-ordered orthorhombic structure.
- A small Fe-doping content increases the electronic conductivity by decreasing the effective band gap and raising the amount of covalent bonding states at the Fermi level.
- An increasing amount of destabilizing anti-bonding states in Fe-doped NBT upon the formation of a $\text{Fe}'_{\text{Ti}}-\text{V}_{\text{O}}$ associate is a consequence of a self-regulating response.
- We assume that different Coulomb and elastic interactions (short- and long-range) are the prevailing factors concerning the formation of defect associates.

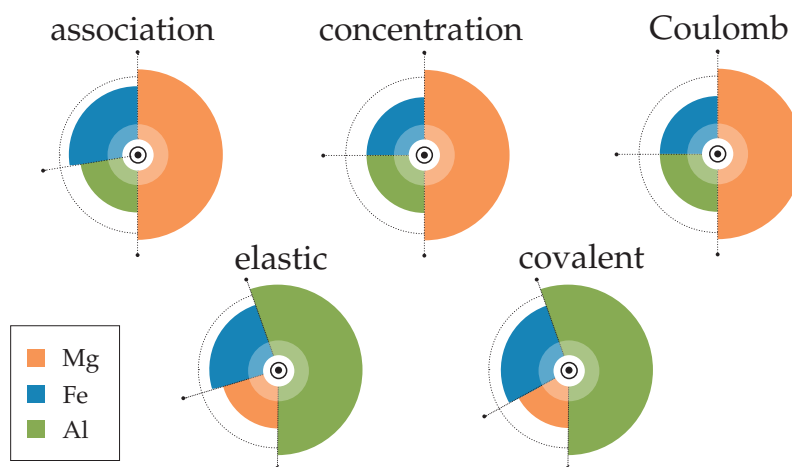


Figure 97: Summary of the different charge compensating oxygen vacancy concentration, the Coulomb, the elastic, and the covalent interaction in Mg-, Al-, and Fe-doped NBT.

Finally, Figure 97 depicts all discussed interaction types between the oxygen vacancy and the acceptor dopant that contribute to the results in Figure 56 and the experimentally observed conductivity. Again, these figures are a visual guide for the reader and do not represent exact percentages but rather tendencies. The strength of the dopant-oxygen bond is highest in Al-doped NBT, making the nearest neighbor associate energetically unfavorable. Until now, we saw that there are numerous effects, either increasing or decreasing the association with an oxygen vacancy. For instance, if we assume that all acceptor dopants are incorporated into the lattice, the number of introduced oxygen vacancies is the largest in Mg-doped NBT. However, the electrostatic interactions are equally high, reducing the benefit of a higher oxygen vacancy concentration. Also the relaxation volumes become larger for higher-order associates, leading to an even higher defect association. In total, we obtain similar ionic conductivities, regardless of the formal charge state and dopant type, until the formation of secondary phases in Al-doped NBT sets in.

Part III

CONCLUSIONS



SUMMARY

Motivated by the need for next-generation conductors, we investigated the defect chemical properties of the promising lead-free NBT [1, 19]. We provide a fundamental understanding of how acceptor doping affects the electronic structure and the local bonding topology in several NBT hettotypes.

For this purpose, we performed first-principles calculations based on the density functional theory approach.

Acceptor doping introduces high ionic conductivities, which increase non-linear with the doping concentration. Hence, the emphasis of this study is on the oxygen vacancy as an “active element”, leading to “added functionality” [432].

We extensively studied the rhombohedral 111-ordered hettostucture and further provide insight into higher-temperature phases, such as tetragonal configurations or orthorhombic 001-ordered systems. Large parts of this study are based on a critical comparison between experimental impedance and NMR-spectroscopy measurements (both acquired by our experimental collaborators) with the results of supercell *ab-initio* calculations. Besides determining defect association energies between B-site acceptor dopants and oxygen vacancies, we also included a detailed discussion about covalent bonding interactions and the relaxation volumes of defective supercells. Thus, we have built a solid foundation to analyze the defect chemistry of NBT concerning ionic, covalent, and elastic interaction forces and are equipped to answer the questions of Chapter 1:

- **Do acceptor dopants and oxygen vacancies form thermodynamic stable defect associates? How large is the association enthalpy, the migration barrier, and what characterizes a defect associate? Which role does the dopant concentration play, and how do substituents on the A-site change the bonding energy?**

The acceptor dopants, Fe, Al, and Mg form stable defect associates with an oxygen vacancy at low defect concentrations. The equilibrium between associated and dissociated defects is an integral part of the macroscopic conductivity model, which we used in Chapter 4. In this chapter we showed that the temperature dependence of the ionic conductivity in doped NBT is the result of a delicate interplay of defect complex formation, phase transitions, and phase coexistence. Only the introduction of phase-dependent thermodynamic parameters allowed the reproduction of experimental results.

The total energy decreases if the oxygen vacancy resides close to the acceptor dopant, independent of the dopant type. The differences in association energies are notable but not significant such that we assume an average value of -0.2 eV. Especially in the R3 configuration, we observe a strong dependency of the defect interaction on the local relaxation pattern. A comparison to the cubic and the tetragonal symmetries showed that a global topological disorder on the A-site sublattice and a variation of oxygen octahedral tilts leads to a huge scatter

of the association energies. Moreover, the formation of defect clusters locally reinforces the association but simultaneously leads to an increasing short-ranged interaction.

Despite the difference in the dopants' size and electron configuration, all dopants displace from their regular lattice site upon the formation of an adjacent oxygen vacancy. This displacement is largest for Al (0.36 Å) and decreases with increasing dopant size to 0.30 Å in Fe-doped and 0.22 Å for Mg-doped NBT, respectively. Likewise, we do not observe large oxygen octahedral tilt distortions within the defective samples. We assume that the stability of the oxygen sublattice is caused by the limited coupling between the polar and the tilt mode in R_3 , although we know that these lattice modes are not completely independent [2]. The driving force for local relaxations are thus Coulomb and defect-compensating covalent interactions.

The initially reduced ionic conductivity in NBT-BT systems can not be conclusively answered. The amount of decisive degrees of freedom is high, such that we could at least generate and investigate a subset of all possible solid solution configurations. Depending on the local atomic arrangement, we observed a slightly increased association compared to pure NBT.

In the context of our COHP analysis in Chapter 10, we further deduced that for some of the Fe-doped configurations, the destabilizing anti-bonding states at the Fermi level are reduced. However, this might not be the most relevant factor, in particular, if non-transition metal dopants are used and remains to be shown.

From Li *et al.* [115] we learned that a reduced Bi-O covalence causes a local polarization distortion, leading to variations in local electric effects. From our study and recent literature [148, 391], we further learned that defect dipoles preferentially align parallel to the overall spontaneous polarization, as far as this is consistent with the host symmetry. In the R_3 host symmetry, we observed that this dipole alignment is unsatisfactory, since the direction of the spontaneous polarizations does not coincide with the orientation of the chemical bonds. If we combine this information, we can assume that a local polarization distortion favors defect associate formation. A percolation of such depolarized regions with increasing defect concentration could be the reason for the abrupt, non-linear increase of the ionic conductivity.

In general, assuming A-site chemically disordered samples, the main factors for increasing or decreasing ionic conductivities should be Coulomb interactions and size effects, which are caused by a mismatch of B-site ionic radii. This is supported by NMR spectroscopy, suggesting the formation of higher-order associates or formation of secondary phases as a compromise between Coulomb attraction and the generation of large free volume and under-bonding. However, the numerous effects, which either increase or decrease the association with an oxygen vacancy, lead to similar ionic conductivities, regardless of the formal charge state.

The migration energy around the dopant lies between 0.6 eV and 1.0 eV. It is therefore generally larger than the bulk value. This barrier can be decreased in the presence of a first-order dopant cluster as shown for the cases of Al and Fe.

- **What influence does the lattice symmetry have on the electric properties and the formation of defect associates?** The present thesis primarily deals with defects within a 111-ordered rhombohedral host lattice. On the one hand, this polymorph represents the low-temperature average structural pattern. On the other hand, R₃ is the computationally most stable superlattice after introducing an isolated defect or an associated defect pair. We demonstrated that the system's total energy continuously decreases with the increasing amplitude of the anti-tilt mode.

The most critical impact of the lattice symmetry on the electronic properties is the shrinkage of the band gap in the tetragonal phase. This phenomenon can be largely attributed to the oxygen octahedral tilt mode rather than numerical approximations. The A-site order has almost no effect on the band gap size.

We further observed large scatterings in the total energies for defective tetragonal and cubic structures, obstructing a conclusive statement about defect association in these systems.

- **Does any phase coexistence significantly alter the conductivity in NBT?** During the time of this thesis, we could not perform a detailed analysis on how phase boundaries or interfaces between differently A-site ordered regions affect the ionic conductivity in NBT. However, we showed in Chapter 4 that the phase coexistence between the rhombohedral and the tetragonal phase contributes to the noticeable kink in the ionic conductivity.
- **Which lattice sites will be occupied by the acceptor dopant? How does the association energy change if the dopant is located on the A-site?** We have shown in Chapter 7 that Al first occupies the B-site. Only at concentrations equal to or higher than 7% will the A-site be filled as well. However, the occupancies remain below the amount of B-site substitutions, and the formation of secondary phases increases simultaneously with the BA content in the Na_{0.5}Bi_{0.5}TiO₃-BiAlO₃ solid solution.
- **What is the preferred charge state of the dopant?** The preferred charge states of the dopants are Mg²⁺, Fe³⁺, and Al³⁺. The vacancy is preferentially two-fold positively charged. In Chapter 8, we calculated the charge transition states of defect associates between a dopant and an oxygen vacancy. Although charge transition levels are present within the band gap of rhombohedral and tetragonal NBT, they appear at relatively high Fermi energies. Thus, we assume that only under strongly reducing conditions may electrons impact the mobility or association of the oxygen vacancies and therefore the effective concentration of free charge carriers. The only exception is the Fe-doped system, where the charge transition occurs at a value comparable to half of the calculated band gap. The latter and a d-p coupling to the host lattice could be responsible for the increased electronic conductivity at low defect concentrations. In this case, an electronic contribution to the mobility of the oxygen vacancies would be conceivable, at least at small doping concentrations.
- **Do we have defect states in the band gap? If we do have defect levels, are they electrically active?** The presence of defect states depends on the charge state of the dopant. If we introduce Mg²⁺, Fe³⁺, or Al³⁺ together with an oxygen

vacancy into an R_3 host lattice, we do not observe a deep or shallow defect state inside the band gap. We see a small amount of unoccupied electron density of states closely attached to the conduction band minimum only in Fe-doped NBT. If we change the supercell's charge state, we induce a defect state in the upper half of band gap for Mg-doped and undoped NBT. Instead, Al-doping results in defect levels, which are resonant in the conduction band. For Fe-doped structures, we observed a self-regulating-response [422] for electron or hole addition. That is, the charge around the Fe-dopant remains more or less constant. Also, in this case, we found defect states within the band gap, for instance, an anti-bonding crystal field resonance for one excess electron. This state is localized and has a polaronic character. A second additional electron is located predominantly at the vacancy site. In general, all defect states are hybrid states, composed of Ti-, O-, Bi-, and for Fe-doped samples, Fe-orbital contributions. This mix is a natural consequence of reduced symmetry.

- **What impact does the delicate balance of short- and long-range interaction have on the defect chemistry? Can we quantify the mechanical interaction between defects? If we can, are they superior to electrostatic interaction?** Employing a COHP analysis, we showed that the covalent bonding should not be a decisive factor for defect association, as already mentioned in the first question. The vacancy generation hardly changes the average $I_p\text{COHP}$ value due to the compensating displacements of the dopant and the surrounding oxygen atoms. Al-doped NBT shows the most significant contribution, resulting from deep bonding states.

To quantify the elastic response of NBT upon doping, we calculated the relaxation volume for different doping concentrations, dopant types, and A-site orders in Chapter 9. Contrary to our expectations, we receive a positive relaxation volume and a predominantly positive elastic dipole tensor for Al (positive dilatation center). In turn, we detect the opposite for Fe and Mg dopants, which indicates a negative dilatation center. The difference between relaxation volumes of second and first order associates comply with the results of Chapter 6 in the case of Mg and Fe. However, in Al-doped NBT, the short- and long-range elastic contribution seems to be a destabilizing factor, leading to an early formation of secondary phases. With increasing dopant concentration, we observe a similar trend for Mg- and Fe-doped NBT.

- **What are the limitations for DFT-based defect analysis in NBT?** As mentioned above, we are currently limited by the size of computationally feasible supercells regarding computational time and CPU hours. In this thesis, we faced the following challenges:
 - i) A size restriction induces artificial interactions between periodic defect images of elastic and electronic origin and complicates the investigation of different doping concentrations. However, the latter is crucial to investigate the defect chemistry at the dilute level.
 - ii) Advanced approximations (GW or Hybrid) are hardly useable in large cells, although they are known to be band gap openers and consequently

facilitate an accurate classification of band gap defect states [254].

- iii) We face the problem of mimicking a globally disordered structure with locally ordered nano-regions. Likewise, a rhombohedral and tetragonal phase coexistence is not feasible. Thus, we need to separately investigate the conductivity in several configurations to access material behavior under realistic conditions. However, even in this more heuristic approach, we faced extensive stability and convergence problems upon defect formation.

One strategy to circumvent a complete screening of all polymorphic structures is to develop an interatomic potential suitable for large-scale molecular dynamics simulations. This would allow for both high scalability and a detailed analysis of tilt dynamics at the phase transition. We will discuss this point in the next chapter, where we provide a short outlook for possible further research topics in the field of NBT and NBT-based solid solutions.

OUTLOOK

From the various findings of this work, we propose the following research questions for continuing the study on NBT in the future.

- From Qiao *et al.* [433] we learned that $\text{Ba}_{0.01}\text{Bi}_{0.5}\text{Na}_{0.49}\text{TiO}_3$ shows a relatively stable permittivity over a wide range. This composition suggests that Ba^{2+} occupies the regular Na^+ sites and becomes a donor. To understand this phenomenon, we need to understand how donor doping, as in Nb-doped NBT [17, 19], influences the electronic structure.
- Do we observe similarities between Fe and other d-orbital dopants, especially if they provide a different amount of d-valence electrons?
- Does a positive relaxation volume in Al-doped NBT lead to a stabilized defect associate in NBT-BT systems?
- Do we obtain the same results if we perform statistics for the calculations presented in the present thesis? Do we reach the same minimum structure from slightly different starting points on the total energy landscape? The occupation matrix control calculations showed that small deviations in the electronic structure are possible, even if the total energy has hardly changed.
- Even if we are limited by size, we can generate grain and phase boundary models to qualify the defect thermodynamics and kinetics in distorted lattices. Furthermore, we do not yet know which surprises are waiting in NBT superlattices (“interface engineering” [10]) with other perovskite family members. For instance, an epitaxial heterostructure between SrTiO_3 and PbTiO_3 induces improper ferroelectricity and leads to a large and almost temperature-independent dielectric constant [10, 434].

Many interesting computational studies related to ionic conductivity in NBT become feasible if we can increase the system size by simultaneously reducing the computational resources. As already mentioned at the end of the last chapter, molecular dynamics simulations would be the best-suited approach to reach this goal. Such simulations would include the effect of finite temperatures as well as disorder, decrease finite-size effects, and allow for calculating statistical averages in realistic conditions. However, an essential input of molecular dynamics simulations is a reliable interaction potential, which is desperately needed for NBT due to a challenging quantification of the involved parameters. How can we generate such potentials, and most importantly, what are the benefits of large-scale and temperature-dependent calculations?

- Recently, there is a huge collaborative effort to generate effective schemes for second-principles lattice dynamical models [435, 436]. These effective models are based on first-principles data sets, providing a physical meaning to the

fitting constants of a Taylor-like series of the total energy with respect to a reference structure. Unfortunately, the generation of these model potentials are still in an early stage, and no standardized fitting procedure is available.

Furthermore, despite the inclusion of all atomic degrees of freedom as well as homogeneous strain, the described fitting approach is restricted to a constant topology as bond breaking during the simulation is prohibited by a low-order expansion around a reference state. However, we see great potential in this technique to reveal lattice kinetics or find ground state structures, which may have been overlooked in density functional theory calculations.

During our studies, we tried to develop an effective potential for 001-ordered NBT, starting with the $P4/mmm$ cubic high symmetry structure as a reference with Multibinit [437]. Since NBT features different polar as well as tilt distortions (including spontaneous strain), chemical and displacive disorder, we could not define a stable parameter set in the given time frame [2].

- If a suitable interatomic potential would be available, we could investigate the effect of extended defect clusters or vacancy ordering on the ionic conductivity [438, 439]. We could further study elastodiffusion [321, 440] or investigate the dipolar interaction between a defect sublattice to rationalize the enormous concentration dependency of the conductivity in NBT [366].

Part IV

APPENDIX

A.1 CRYSTAL FIELD SPLITTING IN THE R₃ STRUCTURE

We are prone to think of an O_h crystal field splitting if we talk about d-orbitals in extended systems. That is, the degenerate d states split into doubly degenerate e_g (x²-x² and z² orbitals) states as well as triply degenerate t_{2g} states (xy, xz, and yz orbitals). The exact energetic order depends on the charge transfer energy, which is the position of transition metal d orbitals with respect to ligand states, as well as the competition between Coulomb and covalent interactions [379].

In the crystal, these d-states can interact with symmetry equivalent orbitals of the surrounding oxygen ions, forming bonding, antibonding, and non-bonding states according to the scheme in Figure 98.

Especially noteworthy are the non-bonding oxygen π-states of t_{1g}, t_{1u}, and t_{2u} directly at the Fermi level. However, the situation changes, if we consider structures with lower symmetry space groups. In this case, the irreducible representations of the higher symmetry group become reducible, leading to a splitting of the energy levels in the subgroup [442].

Let us consider the example of the R₃ hettotype, in which the transition metal (Ti or Fe in this work) has a C₃ point symmetry. To determine the symmetry of states within R₃, we have to find the irreducible representations of the low symmetry group, which are included in the l-dimensional matrix representation of the full rotational group for every symmetry element C_k. For this purpose, we have to calculate the character, $\chi_{\text{reducible}}^{(2)}$, for all symmetry operations of R₃ for an irreducible representation $\Gamma^{(2)}$ of the full rotational group, using [442]:

$$\chi^{(l)}(\alpha) = \frac{\sin[(l + 0.5)\alpha]}{\sin[0.5\alpha]}. \quad (150)$$

Here, α is the rotation angle and l denotes the angular momentum, which is 2 for d-orbitals. Since $\Gamma^{(2)}$ is reducible, we have to decompose this representation by applying the reduction formula [442]

$$a_j = \frac{1}{h} \sum_k N_k \chi^{(\Gamma_j)}(C_k) \chi_{\text{reducible}}^{(2)}(C_k), \quad (151)$$

where N_k is the coefficient in front of the class C_k, h represents the order of the group ($\sum_k N_k$), and a_j is a non-negative integer, describing how many times the irreducible representation Γ_j is contained in the reducible representation. If we carry out this procedure and we further use subduction tables provided by the Bilbao Crystallographic Server [222–224], we can see that for the transition metal d orbitals the t_{2g} states can be decomposed into two irreducible representations with a and e symmetry and the e_g orbitals reduce their symmetry to e (see Figure 99).

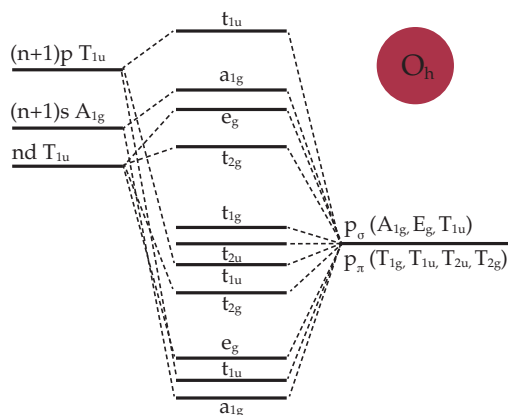


Figure 98: Schematic energy-level diagram for a regular octahedral environment (O_h point group) around a d^0 transition metal. Adapted from References [138, 441].

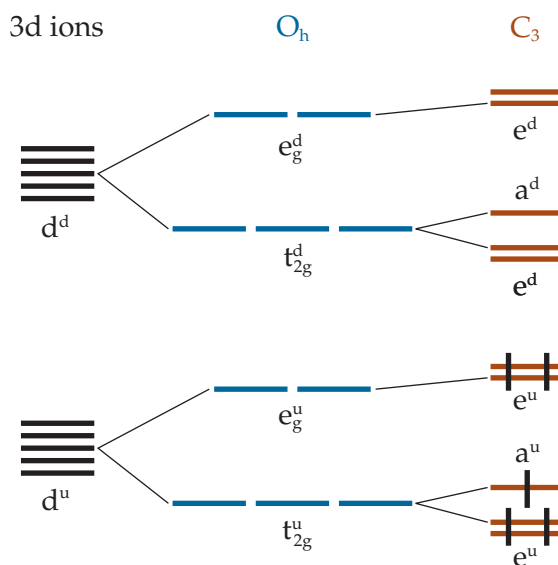


Figure 99: Schematic energy-level diagram for a C_3 point symmetry. The lowercase letters u and d denote the spin up and spin down state, respectively. Note that we do not reproduce the exact energy scale in this schematic picture for visualization purposes. Adapted from Reference [416].

In turn, the transition metal s orbitals, which have an a_{1g} symmetry in the O_h supergroup, are characterized by an a irreducible representation of the C_3 subgroup, while the p orbitals (t_{1u}) split into a and e states. The oxygen π and σ states can be described by $(4a + 4e)$ and $(2a + 2e)$ irreducible representations, respectively. From Mazin *et al.* [443] and McGarvey *et al.* [444] we additionally know that a linear combination of xy , xz , and yz leads to an state with symmetry a in a rhombohedral field,

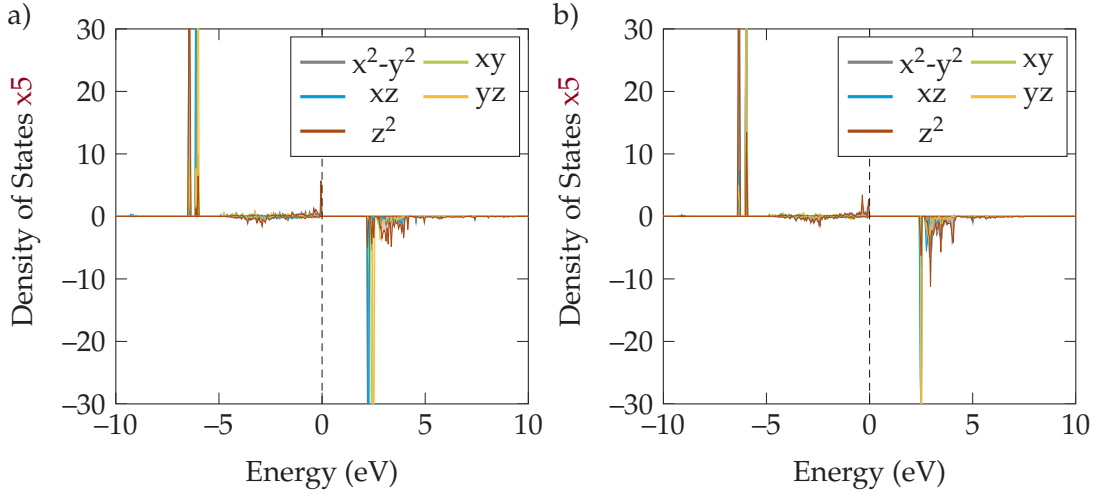


Figure 100: Density of states ($\times 5$) for the d-orbitals in Fe-doped NBT with a a) associated and b) dissociated $\text{Fe}_{\text{Ti}'}\text{-V}_{\text{O}}$ defect pair.

which can also be written as $z^2 - r^2$, if z is parallel to the $[111]$ -direction. Thus the five d_t orbitals are given by [444]

$$a = d_0 \quad (152)$$

$$e_{\text{low}}^1 = ad_{+2} - bd_{-1}, \quad e_{\text{low}}^2 = ad_{-2} + bd_{+1} \quad (153)$$

$$e_{\text{up}}^1 = ad_{+2} + bd_{-1}, \quad e_{\text{up}}^2 = ad_{-2} - bd_{+1}, \quad (154)$$

where up and down specifying the upper and lower orbitals of symmetry e . Formally, we say that we have locally a new basis of orbitals, which are proper linear combinations of spherical harmonics with coefficients that are primarily influenced by the octahedral rotations and A-site displacements [3, 442]. Inspired by the study of Trimarchi *et al.* [416], we use the eigenvectors of the occupation matrices as a suitable representation of the d-orbitals.

The order of the states, as implied in Figure 99 in NBT, can be verified by the density of states of a Fe-doped sample with a dissociated (Figure 100b) or associated (Figure 100a) $\text{Fe}_{\text{Ti}'}\text{-V}_{\text{O}}$ defect pair. In the case of Fe, the d states lie deeper than the O 2p-states, leading to an increased d-character at lower energies in occupied electronic states.

In the dissociated as well as the associated case, the second peak at approximately -6 eV is mainly a combination of the xy , xz , and yz combination. A slight deviation from the ideal C_3 crystal field is obvious since Fe is not a regular lattice site but an impurity (loss of translational symmetry [387]). If we further introduce a vacancy on one side of the distorted coordination octahedra, we might even end up with C_1 point symmetry (rather than a C_4 for a perfect square pyramid) with a distribution of bond lengths to the adjoining oxygen ions.

If we neglect for a short moment the electronic states at the conduction band minimum, we observe an increase of the Fe d-character directly at the top of the O 2p-bands below the Fermi level in Figure 100a). This might be caused by a larger hybridization between O 2p and Fe 3d orbitals and is crucial for our discussion [37]. However, at this point, we want to emphasize the fact that a reduction of the site

symmetry involves orbital interactions, which are restricted in the high symmetry structure. For instance, the transition metal s and p orbitals couple via intraatomic hybridization or interatomic covalent bonds [380] to other electronic states. Furthermore, the non-bonding states at the Fermi level become bonding or anti-bonding.

A.2 CAN WE COMPARE THE DENSITY OF STATES OF FOR SEVERAL SYMMETRIES AT THE Γ -POINT?

To verify that we can compare structures of different NBT polymorphs at the Γ -point, we perform a representative band unfolding with the help of the open-source code BandUp [445, 446]. In this example calculation, we try to access an effective primitive cubic cell band structure from a supercell calculation, including a Γ_5^- anti-phase tilt distortion (which has a high amplitude in R_3).

Essentially, we used the structure of Figure 36a) at 100%. During the unfolding procedure a wave vector \mathbf{K} of the supercell unfolds onto the wave vector \mathbf{k}_i of the primitive cell with the unfolding vector $\mathbf{G}_{\mathbf{k}_i \leftarrow \mathbf{K}}$:

$$\mathbf{k}_i = \mathbf{K} + \mathbf{G}_{\mathbf{k}_i \leftarrow \mathbf{K}} \quad (155)$$

For all wave vectors in the set $\{\mathbf{k}_i\}$, the eigenstates of the primitive cell, $|\Psi\rangle_{m,\mathbf{k}_i}$, have the same eigenvalue as the eigenstates of the supercell, $|\Psi\rangle_{n,\mathbf{K}}$. The result is presented in Figure 101, where the color bar represents the weight $\delta N(\mathbf{k}_i, \epsilon_j)$. This weight represents the number of primitive cell band crossings in the interval $(\epsilon, \epsilon + d\epsilon)$ of the (\mathbf{k}, ϵ) space, averaged over all symmetry equivalent \mathbf{k}_i wave vectors. For more details see References [445, 446]. In short, we observe that both representations agree well at the Γ -point, suggesting that we should include the most crucial features at the $(0, 0, 0)$ reciprocal lattice point.

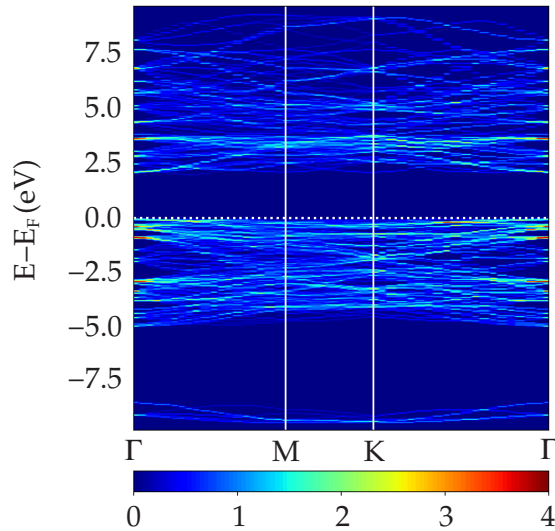


Figure 101: Band unfolding of a Γ_5^- distorted supercell. The color bar represents the weight $\delta N(\mathbf{k}_i, \epsilon_j)$ (see main text).

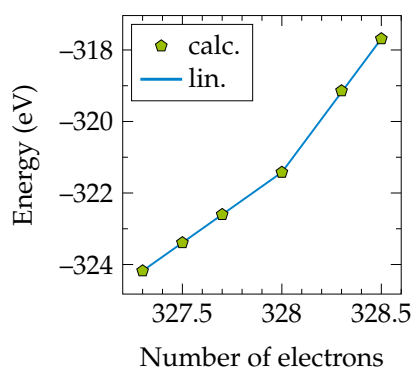


Figure 102: Linearity of the hybrid potential with an exact exchange fraction of 0.08 and a screening parameter of 0.2.

A.3 LINEARITY OF THE HYBRID POTENTIAL

Figure 102 validates the linearity of the hybrid potential with an exact exchange fraction of 0.08 and a screening parameter of 0.2, which has been used in chapter 8. The slope of the total energy as a function of the electron number is piecewise constant. A discontinuity is only observed at an integer number of electrons [250]. This linearity is necessary to avoid artificial energy minima at fractional occupations of the atomic orbitals. The latter might lead to an unphysical behavior and has been observed with the less complex LDA and GGA approaches.

A.4 STRUCTURAL PARAMETERS

Table 12 lists the lattice parameters of the most important and frequently analyzed pristine structures in the present thesis. These are the high symmetry as well as the ground state structures with a 111 A-site cation order and a 001 A-site arrangement, respectively. Note that the reason for differences between relaxed ABINIT and VASP structures is not solely code related but also caused by a slightly deviating Na-potential as indicated in Chapter 3.

SPACEGROUP	CODE	ORDER	a	b	c	α	β	γ	V
(-)	(-)	(-)	(Å)	(Å)	(Å)	(°)	(°)	(°)	(Å ³)
225 (Fm $\bar{3}$ m)	VASP	111	7.78731	7.78731	7.78731	90.0	90.0	90.0	472.23959
225 (Fm $\bar{3}$ m)	ABINIT	111	7.70144	7.70144	7.70144	90.0	90.0	90.0	456.78907
146 (R $\bar{3}$)	VASP	111	5.50887	5.50887	13.82739	90.0	90.0	120.0	363.40929
146 (R $\bar{3}$)	ABINIT	111	5.44398	5.44398	13.55169	90.0	90.0	120.0	347.82204
123 (P ₄ /mmm)	VASP	001	3.89477	3.89477	7.83130	90.0	90.0	90.0	118.79481
123 (P ₄ /mmm)	ABINIT	001	3.84933	3.84933	7.74567	90.0	90.0	90.0	114.77023
26 (Pmc ₂)	VASP	001	7.82862	5.46394	5.59224	90.0	90.0	90.0	239.20868
26 (Pmc ₂)	ABINIT	001	7.75104	5.38822	5.47689	90.0	90.0	90.0	228.73852

Table 12: Structural parameters for various NBT structures. Here, a, b, and c are the lengths, α , β , and γ are the angles, and V is the volume of the cell. The column "order" refers to the A-site cation order.

DECLARATION

Hiermit versichere ich, dass die vorliegende Dissertation selbständig und nur unter Verwendung der angegebenen Quellen und Hilfsmittel angefertigt wurde. Ebenso wurden alle Daten, die aus einer Kollaborationen hervorgingen, als solche kenntlich gemacht. Diese Arbeit hat in gleicher oder ähnlicher Form noch keiner Prüfungsbehörde vorgelegen, ein Promotionsversuch wurde von mir bisher nicht unternommen.

Darmstadt, March 2021

Leonie Koch

BIBLIOGRAPHY

- [1] M. Li, M. J. Pietrowski, R. A. De Souza, H. Zhang, I. M. Reaney, S. N. Cook, J. A. Kilner, and D. C. Sinclair. "A family of oxide ion conductors based on the ferroelectric perovskite $\text{Na}_{0.5}\text{Bi}_{0.5}\text{TiO}_3$." In: *Nature Materials* 13.1 (2014), pp. 31–35.
- [2] M. Gröting. "Ab-initio Calculations of the Relaxor Ferroelectric $\text{Na}_{1/2}\text{Bi}_{1/2}\text{TiO}_3$ and its Solid Solutions." PhD thesis. Technische Universität Darmstadt, 2013. URL: <http://hdl.handle.net/2268/237381>.
- [3] J. Varignon, M. Bibes, and A. Zunger. "Origin of band gaps in 3d perovskite oxides." In: *Nature Communications* 10.1 (2019), p. 1658.
- [4] C. Martineau, A. Cadiau, B. Bouchevreau, J. Senker, F. Taulelle, and K. Adil. "SMARTER crystallography of the fluorinated inorganic–organic compound $\text{Zn}_3\text{Al}_2\text{F}_{12}(\text{HAmTAZ})_6$." In: *Dalton Transactions* 41.20 (2012), pp. 6232–6241.
- [5] J. S. Centre. "JURECA: Modular supercomputer at Jülich Supercomputing Centre." In: *Journal of large-scale research facilities* 4.A132 (2018).
- [6] J. He and C. Franchini. "Screened hybrid functional applied to 3d0 \rightarrow 3d8 transition-metal perovskites LaMO_3 (M=Sc–Cu): Influence of the exchange mixing parameter on the structural, electronic, and magnetic properties." In: *Physical Review B* 86.23 (2012).
- [7] C. Domínguez et al. "Length scales of interfacial coupling between metal and insulator phases in oxides." In: *Nature Materials* 19 (2020), pp. 1182–1187.
- [8] R. D. King-Smith and D. Vanderbilt. "First-principles investigation of ferroelectricity in perovskite compounds." In: *Physical Review B* 49.9 (1994), pp. 5828–5844.
- [9] K. Uchino. "Glory of piezoelectric perovskites." In: *Science and Technology of Advanced Materials* 16.4 (2015), p. 046001.
- [10] E. Bousquet, M. Dawber, N. Stucki, C. Lichtensteiger, P. Hermet, S. Gariglio, J.-M. Triscone, and P. Ghosez. "Improper ferroelectricity in perovskite oxide artificial superlattices." In: *Nature* 452.7188 (2008), pp. 732–736.
- [11] F. El-Mellouhi, E. N. Brothers, M. J. Lucero, and G. E. Scuseria. "Modeling of the cubic and antiferrodistortive phases of SrTiO_3 with screened hybrid density functional theory." In: *Phys. Rev. B* 84 (11 2011), p. 115122.
- [12] A. J. Bell and O. Deubzer. "Lead-free piezoelectric – The environmental and regulatory issues." In: *MRS Bulletin* 43.8 (2018), pp. 581–587.
- [13] In: *Official Journal of the European Union* L174.54 (2011), p. 88.
- [14] In: *Official Journal of the European Union* L197.55 (2012), p. 38.

- [15] T. Ibn-Mohammed, I. Reaney, S. Koh, A. Acquaye, D. Sinclair, C. Randall, F. Abubakar, L. Smith, G. Schileo, and L. Ozawa-Meida. "Life cycle assessment and environmental profile evaluation of lead-free piezoelectrics in comparison with lead zirconate titanate." In: *Journal of the European Ceramic Society* 38.15 (2018), pp. 4922–4938.
- [16] J. Rödel, W. Jo, K. T. P. Seifert, E.-M. Anton, T. Granzow, and D. Damjanovic. "Perspective on the Development of Lead-free Piezoceramics." In: *Journal of the American Ceramic Society* 92.6 (2009), pp. 1153–1177.
- [17] M. Li, L. Li, J. Zang, and D. C. Sinclair. "Donor-doping and reduced leakage current in Nb-doped $\text{Na}_{0.5}\text{Bi}_{0.5}\text{TiO}_3$." In: *Applied Physics Letters* 106.10 (2015), p. 102904.
- [18] A. Walsh and A. Zunger. "Instilling defect tolerance in new compounds." In: *Nature Materials* 16.10 (2017), pp. 964–967.
- [19] F. Yang, M. Li, L. Li, P. Wu, E. Pradal-Velázquez, and D. C. Sinclair. "Defect chemistry and electrical properties of sodium bismuth titanate perovskite." In: *Journal of Materials Chemistry A* 6.13 (2018), pp. 5243–5254.
- [20] F. Yang, P. Wu, and D. C. Sinclair. "Suppression of electrical conductivity and switching of conduction mechanisms in 'stoichiometric' $(\text{Na}_{0.5}\text{Bi}_{0.5}\text{TiO}_3)_{1-x}(\text{BiAlO}_3)_x$ ($0 \leq x \leq 0.08$) solid solutions." In: *Journal of Materials Chemistry C* 5.29 (2017), pp. 7243–7252.
- [21] S. Steiner, I.-T. Seo, P. Ren, M. Li, D. J. Keeble, and T. Frömling. "The effect of Fe-acceptor doping on the electrical properties of $\text{Na}_{1/2}\text{Bi}_{1/2}\text{TiO}_3$ and $0.94(\text{Na}_{1/2}\text{Bi}_{1/2})\text{TiO}_3-0.06\text{BaTiO}_3$." In: *Journal of the American Ceramic Society* 102.9 (2019), pp. 5295–5304.
- [22] E. Aksel, E. Erdem, P. Jakes, J. L. Jones, and R.-A. Eichel. "Defect structure and materials "hardening" in Fe_2O_3 -doped $[\text{Bi}_{0.5}\text{Na}_{0.5}]\text{TiO}_3$ ferroelectrics." en. In: *Applied Physics Letters* 97.1 (2010), p. 012903.
- [23] N. W. Thomas. "Crystal structure–physical property relationships in perovskites." In: *Acta Crystallographica Section B* 45.4 (1989), pp. 337–344.
- [24] C. Freysoldt, J. Neugebauer, and C. G. Van de Walle. "Fully *Ab Initio* Finite-Size Corrections for Charged-Defect Supercell Calculations." In: *Physical Review Letters* 102.1 (2009).
- [25] Y. Guo, J. Robertson, and S. J. Clark. "The effects of screening length in the non-local screened-exchange functional." In: *Journal of Physics: Condensed Matter* 27.2 (2015), p. 025501.
- [26] URL: <https://www.marketsandmarkets.com/Market-Reports/piezoelectric-devices-market-256019882.html> (visited on 04/16/2020).
- [27] P. K. Panda. "Review: environmental friendly lead-free piezoelectric materials." In: *Journal of Materials Science* 44.19 (2009), pp. 5049–5062.
- [28] T. Ibn-Mohammed, S. C. L. Koh, I. M. Reaney, D. C. Sinclair, K. B. Mustapha, A. Acquaye, and D. Wang. "Are lead-free piezoelectric more environmentally friendly?" In: *MRS Communications* 7.1 (2017), pp. 1–7.
- [29] J. M. Crow. 2019. URL: <https://www.chemistryworld.com/features/perovskites-beyond-solar-cells/3010071.article>.

- [30] A. Extance. 2014. URL: <https://www.chemistryworld.com/7659.article>.
- [31] R. Resta. "Ab initio simulation of the properties of ferroelectric materials." In: *Modelling and Simulation in Materials Science and Engineering* 11.4 (2003), R69–R96.
- [32] P. M. Woodward. "Octahedral Tilting in Perovskites. I. Geometrical Considerations." In: *Acta Crystallographica Section B* 53.1 (1997), pp. 32–43.
- [33] C. J. Howard and H. T. Stokes. "Group-Theoretical Analysis of Octahedral Tilting in Perovskites." In: *Acta Crystallographica Section B* 54.6 (1998), pp. 782–789.
- [34] R. Beanland. "Structure of planar defects in tilted perovskites." In: *Acta Crystallographica Section A: Foundations of Crystallography* 67.3 (2011), pp. 191–199.
- [35] T. Ishihara. *Perovskite Oxide for Solid Oxide Fuel Cells*. Springer US, 2009.
- [36] P. M. Woodward. "Octahedral Tilting in Perovskites. II. Structure Stabilizing Forces." In: *Acta Crystallographica Section B* 53.1 (1997), pp. 44–66.
- [37] J. B. Goodenough and J.-S. Zhou. "Localized to Itinerant Electronic Transitions in Transition-Metal Oxides with the Perovskite Structure." In: *Chemistry of Materials* 10.10 (1998), 2980–2993.
- [38] G. King and P. M. Woodward. "Cation ordering in perovskites." In: *Journal of Materials Chemistry* 20.28 (2010), pp. 5785–5796.
- [39] S. Stølen, E. Bakken, and C. E. Mohn. "Oxygen-deficient perovskites: linking structure, energetics and ion transport." In: *Physical Chemistry Chemical Physics* 8.4 (2006), pp. 429–447.
- [40] C. J. Howard and H. T. Stokes. "Structures and phase transitions in perovskites – a group-theoretical approach." In: *Acta Crystallographica Section A: Foundations of Crystallography* 61.1 (2005), pp. 93–111.
- [41] H. T. Stokes, D. M. Hatch, and J. D. Wells. "Group-theoretical methods for obtaining distortions in crystals: Applications to vibrational modes and phase transitions." In: *Physical Review B* 43.13 (1991), pp. 11010–11018.
- [42] K. M. Rabe, C. H. Ahn, and J.-M. Triscone. *Physics of Ferroelectrics*. Springer, Berlin, Heidelberg, 2007.
- [43] V. M. Goldschmidt. "Die Gesetze der Krystallochemie." In: *Naturwissenschaften* 14.21 (1926), pp. 477–485.
- [44] M. Kunz and I. Brown. "Out-of-Center Distortions around Octahedrally Coordinated do Transition Metals." In: *Journal of Solid State Chemistry* 115.2 (1995), pp. 395–406.
- [45] URL: <http://www.me.utexas.edu/~benedekgroup/ToleranceFactorCalculator/#home> (visited on 04/16/2020).
- [46] D. Schütz, M. Deluca, W. Krauss, A. Feteira, T. Jackson, and K. Reichmann. "Lone-Pair-Induced Covalency as the Cause of Temperature- and Field-Induced Instabilities in Bismuth Sodium Titanate." In: *Advanced Functional Materials* 22.11 (2012), pp. 2285–2294.

- [47] A. M. Glazer. "The classification of tilted octahedra in perovskites." In: *Acta Crystallographica Section B: Structural Crystallography and Crystal Chemistry* 28.11 (1972), pp. 3384–3392.
- [48] A. M. Glazer. "Simple ways of determining perovskite structures." In: *Acta Crystallographica Section A* 31.6 (1975), pp. 756–762.
- [49] P. Ghosez *Lecture*. "Physics of Functional Oxides Theory and Modelling." Université de Liège Belgium. 2018.
- [50] G. Shirane, J. D. Axe, J. Harada, and J. P. Remeika. "Soft Ferroelectric Modes in Lead Titanate." In: *Physical Review B* 2.1 (1970), pp. 155–159.
- [51] J. Kreisel, P. Bouvier, B. Dkhil, P. A. Thomas, A. M. Glazer, T. R. Welberry, B. Chaabane, and M. Mezouar. "High-pressure x-ray scattering of oxides with a nanoscale local structure: Application to $\text{Na}_{1/2}\text{Bi}_{1/2}\text{TiO}_3$." In: *Physical Review B* 68.1 (2003).
- [52] R. A. Cowley, S. N. Gvasaliya, S. G. Lushnikov, B. Roessli, and G. M. Rotaru. "Relaxing with relaxors: a review of relaxor ferroelectrics." In: *Advances in Physics* 60.2 (2011), pp. 229–327.
- [53] L. E. Cross. "Relaxor ferroelectrics." In: *Ferroelectrics* 76.1 (1987), pp. 241–267.
- [54] C. W. Ahn et al. "A brief review on relaxor ferroelectrics and selected issues in lead-free relaxors." In: *Journal of the Korean Physical Society* 68.12 (2016), pp. 1481–1494.
- [55] A. Smolenskii, V. Isupov, A. Agranovskaya, and N. Krainik. "New Ferroelectrics of Complex Composition." In: *Soviet Physics, Solid State* 4 (1961), p. 2651.
- [56] K. Reichmann, A. Feteira, and M. Li. "Bismuth Sodium Titanate Based Materials for Piezoelectric Actuators." In: *Materials* 8.12 (2015), pp. 8467–8495.
- [57] G. O. Jones and P. A. Thomas. "Investigation of the structure and phase transitions in the novel A-site substituted distorted perovskite compound $\text{Na}_{0.5}\text{Bi}_{0.5}\text{TiO}_3$." In: *Acta Crystallographica Section B: Structural Science* 58.2 (2002), pp. 168–178.
- [58] G. Trolliard and V. Dorcet. "Reinvestigation of Phase Transitions in $\text{Na}_{0.5}\text{Bi}_{0.5}\text{TiO}_3$ by TEM. Part II: Second Order Orthorhombic to Tetragonal Phase Transition." In: *Chemistry of Materials* 20.15 (2008), pp. 5074–5082.
- [59] V. A. Shuvaeva, D. Zekria, A. M. Glazer, Q. Jiang, S. M. Weber, P. Bhattacharya, and P. A. Thomas. "Local structure of the lead-free relaxor ferroelectric $(\text{K}_x\text{Na}_{1-x})_{0.5}\text{Bi}_{0.5}\text{TiO}_3$." In: *Physical Review B* 71.17 (2005), p. 174114.
- [60] I. Levin and I. M. Reaney. "Nano- and Mesoscale Structure of $\text{Na}_{1/2}\text{Bi}_{1/2}\text{TiO}_3$: A TEM Perspective." In: *Advanced Functional Materials* 22.16 (2012), pp. 3445–3452.
- [61] J Kreisel, A. M. Glazer, G. Jones, P. A. Thomas, L. Abello, and G. Lucazeau. "An x-ray diffraction and Raman spectroscopy investigation of A-site substituted perovskite compounds: the $(\text{Na}_{1-x}\text{K}_x)_{0.5}\text{Bi}_{0.5}\text{TiO}_3$ ($0 \leq x \leq 1$) solid solution." In: *Journal of Physics: Condensed Matter* 12.14 (2000), pp. 3267–3280.

- [62] J Petzelt et al. "Infrared, Raman and high-frequency dielectric spectroscopy and the phase transitions in $\text{Na}_{1/2}\text{Bi}_{1/2}\text{TiO}_3$." In: *Journal of Physics: Condensed Matter* 16.15 (2004), pp. 2719–2731.
- [63] M. Gröting, S. Hayn, and K. Albe. "Chemical order and local structure of the lead-free relaxor ferroelectric $\text{Na}_{1/2}\text{Bi}_{1/2}\text{TiO}_3$." In: *Journal of Solid State Chemistry* 184.8 (2011), pp. 2041–2046.
- [64] K.-C. Meyer, L. Koch, and K. Albe. "Phase transformations in the relaxor $\text{Na}_{1/2}\text{Bi}_{1/2}\text{TiO}_3$ studied by means of density functional theory calculations." In: *Journal of the American Ceramic Society* 101.1 (2018), pp. 472–482.
- [65] V. Dorcet and G. Trolliard. "A transmission electron microscopy study of the A-site disordered perovskite $\text{Na}_{0.5}\text{Bi}_{0.5}\text{TiO}_3$." In: *Acta Materialia* 56.8 (2008), pp. 1753–1761.
- [66] R. Beanland and P. A. Thomas. "Imaging planar tetragonal sheets in rhombohedral $\text{Na}_{0.5}\text{Bi}_{0.5}\text{TiO}_3$ using transmission electron microscopy." In: *Scripta Materialia* 65.5 (2011), pp. 440–443.
- [67] E. Aksel, J. S. Forrester, H. M. Foronda, R. Dittmer, D. Damjanovic, and J. L. Jones. "Structure and properties of La-modified $\text{Na}_{0.5}\text{Bi}_{0.5}\text{TiO}_3$ at ambient and elevated temperatures." In: *Journal of Applied Physics* 112.5 (2012), p. 054111.
- [68] P. B. Groszewicz, M. Göting, H. Breitzke, W. Jo, K. Albe, G. Buntkowsky, and J. Rödel. "Reconciling Local Structure Disorder and the Relaxor State in $(\text{Bi}_{1/2}\text{Na}_{1/2})\text{TiO}_3$ - BaTiO_3 ." en. In: *Scientific Reports* 6.1 (2016), pp. 2045–2322.
- [69] E. Aksel, J. S. Forrester, J. L. Jones, P. A. Thomas, K. Page, and M. R. Suchomel. "Monoclinic crystal structure of polycrystalline $\text{Na}_{0.5}\text{Bi}_{0.5}\text{TiO}_3$." In: *Applied Physics Letters* 98.15 (2011), p. 152901.
- [70] S. Gorfman and P. A. Thomas. "Evidence for a non-rhombohedral average structure in the lead-free piezoelectric material $\text{Na}_{0.5}\text{Bi}_{0.5}\text{TiO}_3$." In: *Journal of Applied Crystallography* 43.6 (2010), pp. 1409–1414.
- [71] C. Ma, H. Guo, and X. Tan. "A New Phase Boundary in $(\text{Bi}_{1/2}\text{Na}_{1/2})\text{TiO}_3$ - BaTiO_3 Revealed via a Novel Method of Electron Diffraction Analysis." In: *Advanced Functional Materials* 23.42 (2013), pp. 5261–5266.
- [72] J. Pan, M. K. Niranjan, and U. V. Waghmare. "Aliovalent cation ordering, coexisting ferroelectric structures, and electric field induced phase transformation in lead-free ferroelectric $\text{Na}_{0.5}\text{Bi}_{0.5}\text{TiO}_3$." In: *Journal of Applied Physics* 119.12 (2016), p. 124102.
- [73] D. S. Keeble, E. R. Barney, D. A. Keen, M. G. Tucker, J. Kreisel, and P. A. Thomas. "Bifurcated Polarization Rotation in Bismuth-Based Piezoelectrics." In: *Advanced Functional Materials* 23.2 (2013), pp. 185–190.
- [74] B. N. Rao and R. Ranjan. "Electric-field-driven monoclinic-to-rhombohedral transformation in $\text{Na}_{1/2}\text{Bi}_{1/2}\text{TiO}_3$." In: *Physical Review B* 86.13 (2012), p. 134103.
- [75] B. N. Rao, A. N. Fitch, and R. Ranjan. "Ferroelectric-ferroelectric phase coexistence in $\text{Na}_{1/2}\text{Bi}_{1/2}\text{TiO}_3$." In: *Physical Review B* 87.6 (2013).

- [76] B. N. Rao, R. Datta, S. S. Chandrashekar, D. K. Mishra, V. Sathe, A. Senyshyn, and R. Ranjan. "Local structural disorder and its influence on the average global structure and polar properties in $\text{Na}_{0.5}\text{Bi}_{0.5}\text{TiO}_3$." In: *Physical Review B* 88.22 (2013).
- [77] R. Beanland and P. A. Thomas. "Symmetry and defects in rhombohedral single-crystalline $\text{Na}_{0.5}\text{Bi}_{0.5}\text{TiO}_3$." In: *Physical Review B* 89.17 (2014).
- [78] J. Carter, E. Aksel, T. Iamsasri, J. S. Forrester, J. Chen, and J. L. Jones. "Structure and ferroelectricity of nonstoichiometric $(\text{Na}_{0.5}\text{Bi}_{0.5})\text{TiO}_3$." In: *Applied Physics Letters* 104.11 (2014), p. 112904.
- [79] M. I. Aroyo, U. Müller, and H. Wondratschek. "Historical introduction." In: *International Tables for Crystallography Volume A1: Symmetry relations between space groups*. Ed. by H. Wondratschek and U. Müller. Dordrecht: Springer Netherlands, 2004, pp. 2–5.
- [80] M. K. Niranjan, T. Karthik, S. Asthana, J. Pan, and U. V. Waghmare. "Theoretical and experimental investigation of Raman modes, ferroelectric and dielectric properties of relaxor $\text{Na}_{0.5}\text{Bi}_{0.5}\text{TiO}_3$." In: *Journal of Applied Physics* 113.19 (2013), p. 194106.
- [81] R. Zuo, S. Su, Y. Wu, J. Fu, M. Wang, and L. Li. "Influence of A-site nonstoichiometry on sintering, microstructure and electrical properties of $(\text{Bi}_{0.5}\text{Na}_{0.5})\text{TiO}_3$ ceramics." In: *Materials Chemistry and Physics* 110.2 (2008), pp. 311–315.
- [82] J. M. Perez-Mato and M. I. Aroyo. *Tutorial on the application of the tools of the Bilbao Crystallographic Server in the study of group-subgroup phase transitions*. URL: http://www.cryst.ehu.es/html/cryst/tutorials/Tutorial_SPT_abr2010.pdf.
- [83] A. Devonshire. "XCVI. Theory of barium titanate." In: *The London, Edinburgh, and Dublin Philosophical Magazine and Journal of Science* 40.309 (1949), pp. 1040–1063.
- [84] A. Devonshire. "CIX. Theory of barium titanate—Part II." In: *The London, Edinburgh, and Dublin Philosophical Magazine and Journal of Science* 42.333 (1951), pp. 1065–1079.
- [85] A. Devonshire. "Theory of ferroelectrics." In: *Advances in Physics* 3.10 (1954), pp. 85–130.
- [86] L. Landau and E. Lifshitz. *Statistical Physics*. Bd. 5. Elsevier Science, 2013.
- [87] L. D. Landau. "On the theory of phase transitions." In: *Zhurnal Eksperimentalnoi i Teoreticheskoi Fiziki*. 7 (1937), pp. 19–32.
- [88] V. L. Ginzburg. "Phase transitions in ferroelectrics: some historical remarks." In: *Physics-Uspokhi* 44.10 (2001), pp. 1037–1043.
- [89] J. Varignon, M. Bibes, and A. Zunger. "Mott gapping in 3d ABO_3 perovskites without Mott-Hubbard interelectronic repulsion energy U ." In: *Physical Review B* 100.3 (2019), p. 035119.
- [90] P. Barone, K. Yamauchi, and S. Picozzi. "Jahn-Teller distortions as a novel source of multiferroicity." In: *Physical Review B* 92.1 (2015), p. 014116.

- [91] J. B. Goodenough and J.-S. Zhou. "Orbital ordering in orthorhombic perovskites." In: *Journal of Materials Chemistry* 17.23 (2007), pp. 2394–2405.
- [92] D. Amoroso, A. Cano, and P. Ghosez. "First-principles study of (Ba,Ca)TiO₃ and Ba(Ti,Zr)O₃ solid solutions." In: *Physical Review B* 97.17 (2018), p. 174108.
- [93] M. W. Lufaso and P. M. Woodward. "Prediction of the crystal structures of perovskites using the software program *SPuDS*." In: *Acta Crystallographica Section B* 57.6 (2001), pp. 725–738.
- [94] R. Wahl, D. Vogtenhuber, and G. Kresse. "SrTiO₃ and BaTiO₃ revisited using the projector augmented wave method: Performance of hybrid and semilocal functionals." In: *Physical Review B* 78.10 (2008).
- [95] J. Varignon and P. Ghosez. "Improper ferroelectricity and multiferroism in 2H-BaMnO₃." In: *Physical Review B* 87.14 (2013), p. 140403.
- [96] A. P. Levanyuk and D. G. Sannikov. "Improper ferroelectrics." In: *Soviet Physics Uspekhi* 17.2 (1974), pp. 199–214.
- [97] N. A. Benedek and C. J. Fennie. "Hybrid Improper Ferroelectricity: A Mechanism for Controllable Polarization-Magnetization Coupling." In: *Physical Review Letters* 106.10 (2011), p. 107204.
- [98] J. Holakovský. "A New Type of the Ferroelectric Phase Transition." In: *physica status solidi (b)* 56.2 (1973), pp. 615–619.
- [99] W. Cochran. "Crystal Stability and the Theory of Ferroelectricity." In: *Physical Review Letters* 3.9 (1959), pp. 412–414.
- [100] W. Cochran. "Crystal stability and the theory of ferroelectricity." In: *Advances in Physics* 9.36 (1960), pp. 387–423.
- [101] M. T. Dove. *Introduction to Lattice Dynamics*. Cambridge Topics in Mineral Physics and Chemistry. Cambridge University Press, 1993.
- [102] J. M. Perez-Mato, D. Orobengoa, and M. I. Aroyo. "Mode crystallography of distorted structures." In: *Acta Crystallographica Section A* 66.5 (2010), pp. 558–590.
- [103] U. Müller. "Remarks on Wyckoff positions." In: *International Tables for Crystallography Volume A1: Symmetry relations between space groups*. Ed. by H. Wondratschek and U. Müller. Dordrecht: Springer Netherlands, 2004, pp. 24–26.
- [104] C. Bradley and A. Cracknell. *The mathematical theory of symmetry in solids*. Clarendon Press, 1972.
- [105] M. T. Dove. "Theory of displacive phase transitions in minerals." In: *American Mineralogist* 82.3-4 (1997), pp. 213–244.
- [106] B. Xu, O. Hellman, and L. Bellaiche. "Order-disorder transition in the prototypical antiferroelectric PbZrO₃." In: *Physical Review B* 100.2 (2019), p. 020102.
- [107] R. E. Cohen. "Origin of ferroelectricity in perovskite oxides." In: *Nature* 358.6382 (1992), pp. 136–138.
- [108] M. E. Lines and A. M. Glass. *Principles and Applications of Ferroelectrics and Related Materials*. Oxford University Press, 1977.

- [109] P. Ghosez and J. Junquera. "First-Principles Modeling of Ferroelectric Oxide Nanostructures." In: *Handbook of Theoretical and Computational Nanotechnology*. Ed. by M. Rieth and W. Schommers. Vol. 9. American Scientific Publishers, 2006, pp. 623–728.
- [110] W. A. Harrison. *Electronic Structure and the Properties of Solids*. W. H. Freeman, San Fransisco, Eds., 1980.
- [111] W. Zhong, D. Vanderbilt, and K. M. Rabe. "First-principles theory of ferroelectric phase transitions for perovskites: The case of BaTiO₃." In: *Physical Review B* 52.9 (1995), pp. 6301–6312.
- [112] P. Giannozzi, S. de Gironcoli, P. Pavone, and S. Baroni. "Ab initio calculation of phonon dispersions in semiconductors." In: *Physical Review B* 43.9 (1991), pp. 7231–7242.
- [113] X. Gonze and C. Lee. "Dynamical matrices, Born effective charges, dielectric permittivity tensors, and interatomic force constants from density-functional perturbation theory." In: *Physical Review B* 55.16 (1997), pp. 10355–10368.
- [114] X. Wu, D. Vanderbilt, and D. R. Hamann. "Systematic treatment of displacements, strains, and electric fields in density-functional perturbation theory." In: *Physical Review B* 72.3 (2005), p. 035105.
- [115] X. Li, Q. Jing, Z. Xi, P. Liu, W. Long, and P. Fang. "Dielectric relaxation and electrical conduction in (Bi_xNa_{1-x})_{0.94}Ba_{0.06}TiO₃ ceramics." In: *Journal of the American Ceramic Society* 101.2 (2018), pp. 789–799.
- [116] L. Bellaiche. "Piezoelectricity of ferroelectric perovskites from first principles." In: *Current Opinion in Solid State and Materials Science* 6.1 (2002), pp. 19–25.
- [117] R. M. Martin. "Piezoelectricity." In: *Phys. Rev. B* 5 (4 1972), pp. 1607–1613.
- [118] D. R. Hamann, K. M. Rabe, and D. Vanderbilt. "Generalized-gradient-functional treatment of strain in density-functional perturbation theory." In: *Physical Review B* 72.3 (2005), p. 033102.
- [119] R. M. Martin. "Comment on "Piezoelectricity under Hydrostatic Pressure"." In: *Phys. Rev. B* 6 (12 1972), pp. 4874–4876.
- [120] R. E. Cohen and H. Krakauer. "Lattice dynamics and origin of ferroelectricity in BaTiO₃: Linearized-augmented-plane-wave total-energy calculations." In: *Physical Review B* 42.10 (1990), pp. 6416–6423.
- [121] P. Ghosez, J.-P. Michenaud, and X. Gonze. "Dynamical atomic charges: The case of ABO₃ compounds." In: *Physical Review B* 58.10 (1998), pp. 6224–6240.
- [122] W. Cochran. "Effective Ionic Charge in Crystals." In: *Nature* 191.4783 (1961), pp. 60–61.
- [123] R. S. Mulliken. "Electronic Structures of Molecules XI. Electroaffinity, Molecular Orbitals and Dipole Moments." In: *The Journal of Chemical Physics* 3.9 (1935), pp. 573–585.
- [124] R. S. Mulliken. "Criteria for the Construction of Good Self-Consistent-Field Molecular Orbital Wave Functions, and the Significance of LCAO-MO Population Analysis." In: *The Journal of Chemical Physics* 36.12 (1962), pp. 3428–3439.

- [125] R. F. W. Bader, T. T. Nguyen-Dang, and Y. Tal. "A topological theory of molecular structure." In: *Reports on Progress in Physics* 44.8 (1981), pp. 893–948.
- [126] P. Ghosez. "First-principles study of the dielectric and dynamical properties of barium titanate." PhD thesis. Belgium: Université Catholique de Louvain, 1997. URL: <http://hdl.handle.net/2268/31206>.
- [127] M. Born and M. Göppert-Mayer. "Dynamische Gittertheorie der Kristalle." In: *Aufbau Der Zusammenhängenden Materie*. Berlin, Heidelberg: Springer Berlin Heidelberg, 1933, pp. 623–794.
- [128] P. Ghosez, X. Gonze, and J.-P. Michenaud. "Lattice dynamics and ferroelectric instability of barium titanate." In: *Ferroelectrics* 194.1 (1997), pp. 39–54.
- [129] X. Gonze, J.-C. Charlier, D. C. Allan, and M. P. Teter. "Interatomic force constants from first principles: The case of α -quartz." In: *Physical Review B* 50.7 (1994), p. 4.
- [130] P. H. Ghosez, X. Gonze, and J. P. Michenaud. "Ab-initio phonon dispersion curves and interatomic force constants of barium titanate." In: *Ferroelectrics* 206.1 (1998), pp. 205–217.
- [131] P. Ghosez, E. Cockayne, U. V. Waghmare, and K. M. Rabe. "Lattice dynamics of BaTiO_3 , PbTiO_3 , and PbZrO_3 : A comparative first-principles study." In: *Physical Review B* 60.2 (1999), pp. 836–843.
- [132] S. Baroni, S. de Gironcoli, A. Dal Corso, and P. Giannozzi. "Phonons and related crystal properties from density-functional perturbation theory." In: *Reviews of Modern Physics* 73.2 (2001), pp. 515–562.
- [133] N. A. Hill. "Why Are There so Few Magnetic Ferroelectrics?" In: *The Journal of Physical Chemistry B* 104.29 (2000), pp. 6694–6709.
- [134] J. B. Goodenough. "Theory of the Role of Covalence in the Perovskite-Type Manganites $[\text{La}, \text{M}(\text{II})]\text{MnO}_3$." In: *Physical Review* 100.2 (1955), pp. 564–573.
- [135] A. Walsh and G. W. Watson. "The origin of the stereochemically active Pb(II) lone pair: DFT calculations on PbO and PbS." In: *Journal of Solid State Chemistry* 178.5 (2005), pp. 1422–1428.
- [136] A. Walsh, D. J. Payne, R. G. Egdell, and G. W. Watson. "Stereochemistry of post-transition metal oxides: revision of the classical lone pair model." In: *Chemical Society Reviews* 40.9 (2011), pp. 4455–4463.
- [137] L. E. Orgel. "769. The stereochemistry of B subgroup metals. Part II. The inert pair." In: *Journal of the Chemical Society*. 0 (1959), pp. 3815–3819.
- [138] I. B. Bersuker. "Pseudo-Jahn–Teller Effect—A Two-State Paradigm in Formation, Deformation, and Transformation of Molecular Systems and Solids." In: *Chemical Reviews* 113.3 (2013), 1351–1390.
- [139] J. A. Kilner and R. J. Brook. "A study of oxygen ion conductivity in doped non-stoichiometric oxides." In: *Solid State Ionics* 6.3 (1982), pp. 237–252.
- [140] M. Schie, R. Waser, and R. A. De Souza. "A Simulation Study of Oxygen-Vacancy Behavior in Strontium Titanate: Beyond Nearest-Neighbor Interactions." In: *The Journal of Physical Chemistry C* 118.28 (2014), pp. 15185–15192.

- [141] L. Li, M. Li, H. Zhang, I. M. Reaney, and D. C. Sinclair. "Controlling mixed conductivity in $\text{Na}_{1/2}\text{Bi}_{1/2}\text{TiO}_3$ using A-site non-stoichiometry and Nb-donor doping." In: *Journal of Materials Chemistry C* 4.24 (2016), pp. 5779–5786.
- [142] J. Maier. *Festkörper-Fehler und Funktion. Prinzipien der Physikalischen Festkörperchemie*. B. G. Teubner Stuttgart Leipzig, 2000.
- [143] R. A. De Souza. "Oxygen Diffusion in SrTiO_3 and Related Perovskite Oxides." In: *Advanced Functional Materials* 25.40 (2015), pp. 6326–6342.
- [144] W. Cai and W. D. Nix. *Imperfections in Crystalline Solids*. MRS-Cambridge Materials Fundamentals. Cambridge University Press, 2016.
- [145] J. B. Goodenough. "Oxide-Ion Electrolytes." In: *Annual Review of Materials Research* 33.1 (2003), pp. 91–128.
- [146] S. J. Skinner and J. A. Kilner. "Oxygen ion conductors." In: *Materials Today* 6.3 (2003), pp. 30–37.
- [147] P. Erhart and K. Albe. "Dopants and dopant–vacancy complexes in tetragonal lead titanate: A systematic first principles study." In: *Computational Materials Science* 103 (June 2015), pp. 224–230.
- [148] P. Erhart, R.-A. Eichel, P. Träskelin, and K. Albe. "Association of oxygen vacancies with impurity metal ions in lead titanate." In: *Physical Review B* 76.17 (2007).
- [149] A. Janotti, J. B. Varley, M. Choi, and C. G. Van de Walle. "Vacancies and small polarons in SrTiO_3 ." In: *Physical Review B* 90.8 (2014).
- [150] J. Maier. "Mass Transport in the Presence of Internal Defect Reactions—Concept of Conservative Ensembles: I, Chemical Diffusion in Pure Compounds." In: *Journal of the American Ceramic Society* 76.5 (1993), pp. 1212–1217.
- [151] J. Maier. "Mass Transport in the Presence of Internal Defect Reactions—Concept of Conservative Ensembles: III, Trapping Effect of Dopants on Chemical Diffusion." In: *Journal of the American Ceramic Society* 76.5 (1993), pp. 1223–1227.
- [152] J. A. Kilner and C. D. Waters. "The effects of dopant cation-oxygen vacancy complexes on the anion transport properties of non-stoichiometric fluoride oxides." In: *Solid State Ionics* 6.3 (1982), pp. 253–259.
- [153] F. Yang, H. Zhang, L. Li, I. M. Reaney, and D. C. Sinclair. "High Ionic Conductivity with Low Degradation in A-Site Strontium-Doped Nonstoichiometric Sodium Bismuth Titanate Perovskite." In: *Chemistry of Materials* 28.15 (2016), pp. 5269–5273.
- [154] H. Hayashi, H. Inaba, M. Matsuyama, N. Lan, M. Dokiya, and H. Tagawa. "Structural consideration on the ionic conductivity of perovskite-type oxides." In: *Solid State Ionics* 122.1 (1999), pp. 1–15.
- [155] R. L. Cook and A. F. Sammells. "On the systematic selection of perovskite solid electrolytes for intermediate temperature fuel cells." In: *Solid State Ionics* 45.3 (1991), pp. 311–321.
- [156] K.-C. Meyer and K. Albe. "Influence of phase transitions and defect associates on the oxygen migration in the ion conductor $\text{Na}_{1/2}\text{Bi}_{1/2}\text{TiO}_3$." In: *Journal of Materials Chemistry A* 5.9 (2017), pp. 4368–4375.

- [157] I.-T. Seo, S. Steiner, and T. Frömling. "The effect of A site non-stoichiometry on $0.94(\text{Na}_y\text{Bi}_x)\text{TiO}_3\text{-}0.06\text{BaTiO}_3$." In: *Journal of the European Ceramic Society* 37.4 (2017), pp. 1429–1436.
- [158] F. Yang, M. Li, L. Li, P. Wu, E. Pradal-Velázquez, and D. C. Sinclair. "Optimisation of oxide-ion conductivity in acceptor-doped $\text{Na}_{0.5}\text{Bi}_{0.5}\text{TiO}_3$ perovskite: approaching the limit?" In: *Journal of Materials Chemistry A* 5.41 (2017), pp. 21658–21662.
- [159] S. Steiner. "Defect Chemistry of Sodium Bismuth Titanate and its Solid Solutions." PhD thesis. Technische Universität Darmstadt, 2020. URL: <http://tuprints.ulb.tu-darmstadt.de/11552/>.
- [160] F. Yang, P. Wu, and D. C. Sinclair. "Enhanced bulk conductivity of A-site divalent acceptor-doped non-stoichiometric sodium bismuth titanate." In: *Solid State Ionics. Defect interactions and their influence on ionic and electronic transport* 299 (2017), pp. 38–45.
- [161] R. Bhattacharyya and S. Omar. "Electrical conductivity study of B-site Ga doped non-stoichiometric sodium bismuth titanate ceramics." In: *Journal of Alloys and Compounds* 746 (2018), pp. 54–61.
- [162] K. Carl and K. H. Hardtl. "Electrical after-effects in $\text{Pb}(\text{Ti}, \text{Zr})\text{O}_3$ ceramics." In: *Ferroelectrics* 17.1 (1977), pp. 473–486.
- [163] G. Arlt and U. Robels. "Aging and fatigue in bulk ferroelectric perovskite ceramics." In: *Integrated Ferroelectrics* 3.4 (1993), pp. 343–349.
- [164] L. Li, M. Li, I. M. Reaney, and D. C. Sinclair. "Mixed ionic–electronic conduction in $\text{K}_{1/2}\text{Bi}_{1/2}\text{TiO}_3$." In: *Journal of Materials Chemistry C* 5.25 (2017), pp. 6300–6310.
- [165] I. Levin, I. M. Reaney, E.-M. Anton, W. Jo, J. Rödel, J. Pokorny, L. A. Schmitt, H.-J. Kleebe, M. Hinterstein, and J. L. Jones. "Local structure, pseudosymmetry, and phase transitions in $\text{Na}_{1/2}\text{Bi}_{1/2}\text{TiO}_3\text{-K}_{1/2}\text{Bi}_{1/2}\text{TiO}_3$ ceramics." In: *Physical Review B* 87.2 (2013), p. 024113.
- [166] P. B. Groszewicz, L. Koch, S. Steiner, A. Ayrikyan, K. G. Webber, T. Frömling, K. Albe, and G. Buntkowsky. "The fate of aluminium in $(\text{Na},\text{Bi})\text{TiO}_3$ -based ionic conductors." In: *J. Mater. Chem. A* 8 (35 2020), pp. 18188–18197.
- [167] W. Peng, C. Mao, Z. Liu, X. Dong, F. Cao, and G. Wang. "Phase characteristics of $0.92\text{Bi}_{0.5}\text{Na}_{0.5}\text{TiO}_3\text{-}0.08\text{BiAlO}_3$ ceramics." In: *Applied Physics Letters* 106.9 (2015), p. 092903.
- [168] P. Fu, Z. Xu, R. Chu, X. Wu, W. Li, and X. Li. "Structure and electrical properties of $(1-x)(\text{Na}_{0.5}\text{Bi}_{0.5})_{0.94}\text{Ba}_{0.06}\text{TiO}_3\text{-}x\text{BiAlO}_3$ lead-free piezoelectric ceramics." In: *Materials & Design* 46 (2013), pp. 322–327.
- [169] H. Yu and Z.-G. Ye. "Dielectric, ferroelectric, and piezoelectric properties of the lead-free $(1-x)(\text{Na}_{0.5}\text{Bi}_{0.5})\text{TiO}_3\text{-}x\text{BiAlO}_3$ solid solution." In: *Applied Physics Letters* 93.11 (2008), p. 112902.
- [170] R.-A. Eichel. "Defect structure of oxide ferroelectrics—valence state, site of incorporation, mechanisms of charge compensation and internal bias fields." In: *Journal of Electroceramics* 19.1 (2007), pp. 11–23.

- [171] R.-A. Eichel. "Structural and dynamic properties of oxygen vacancies in perovskite oxides—analysis of defect chemistry by modern multi-frequency and pulsed EPR techniques." In: *Physical Chemistry Chemical Physics* 13.2 (2011), pp. 368–384.
- [172] H. Unoki and T. Sakudo. "Electron Spin Resonance of Fe^{3+} in SrTiO_3 with Special Reference to the 110°K Phase Transition." In: *Journal of the Physical Society of Japan* 23.3 (1967), pp. 546–552.
- [173] T. Sawai, Y. Yamaguchi, N. Kitamura, T. Date, S. Konishi, K. Taga, and K. Tanaka. "Pulse-based electron spin transient nutation measurement of BaTiO_3 fine particle: Identification of controversial signal around $g=2.00$." In: *Applied Physics Letters* 112.20 (2018), p. 202902.
- [174] D. J. A. Gainon. "Electron Paramagnetic Resonance of Fe^{3+} in the Strong Axial Field of PbTiO_3 Host." In: *Physical Review* 134.5A (1964), A1300–A1301.
- [175] H. Meštrić, R.-A. Eichel, K.-P. Dinse, A. Ozarowski, J. van Tol, and L. C. Brunel. "High-frequency electron paramagnetic resonance investigation of the Fe^{3+} impurity center in polycrystalline PbTiO_3 in its ferroelectric phase." In: *Journal of Applied Physics* 96.12 (2004), pp. 7440–7444.
- [176] H. Meštrić, R.-A. Eichel, T. Kloss, K.-P. Dinse, S. Laubach, S. Laubach, P. C. Schmidt, K. A. Schönau, M. Knapp, and H. Ehrenberg. "Iron-oxygen vacancy defect centers in PbTiO_3 : Newman superposition model analysis and density functional calculations." In: *Physical Review B* 71.13 (2005), p. 134109.
- [177] R. Eichel, H. Meštrić, K. Dinse, A. Ozarowski, J. Tol, L. Brunel, H. Kungl, and M. Hoffmann. "High-field/high-frequency EPR of paramagnetic functional centers in Cu^{2+} - and Fe^{3+} -modified polycrystalline $\text{Pb}[\text{Zr}_x\text{Ti}_{1-x}]\text{O}_3$ ferroelectrics." In: *Magnetic Resonance in Chemistry* 43.S1 (2005), S166–S173.
- [178] J. F. Stebbins. "Aluminum Substitution in Rutile Titanium Dioxide: New Constraints from High-Resolution ^{27}Al NMR." In: *Chemistry of Materials* 19.7 (2007), pp. 1862–1869.
- [179] A. Escudero, L. Delevoye, and F. Langenhorst. "Aluminum Incorporation in TiO_2 Rutile at High Pressure: An XRD and High-Resolution ^{27}Al NMR Study." In: *The Journal of Physical Chemistry C* 115.24 (2011), pp. 12196–12201.
- [180] J. Kim, A. J. Ilott, D. S. Middlemiss, N. A. Chernova, N. Pinney, D. Morgan, and C. P. Grey. " ^2H and ^{27}Al Solid-State NMR Study of the Local Environments in Al-Doped 2-Line Ferrihydrite, Goethite, and Lepidocrocite." In: *Chemistry of Materials* 27.11 (2015), pp. 3966–3978.
- [181] D. Rettenwander, J. Langer, W. Schmidt, C. Arrer, K. J. Harris, V. Terskikh, G. R. Goward, M. Wilkening, and G. Amthauer. "Site Occupation of Ga and Al in Stabilized Cubic $\text{Li}_{7-3(x+y)}\text{Ga}_x\text{Al}_y\text{La}_3\text{Zr}_2\text{O}_{12}$ Garnets As Deduced from ^{27}Al and ^{71}Ga MAS NMR at Ultrahigh Magnetic Fields." In: *Chemistry of Materials* 27.8 (2015), pp. 3135–3142.
- [182] E. Lippmaa, A. Samoson, and M. Magi. "High-resolution aluminum-27 NMR of aluminosilicates." In: *Journal of the American Chemical Society* 108.8 (1986), pp. 1730–1735.

- [183] P. Florian, E. Veron, T. F. G. Green, J. R. Yates, and D. Massiot. "Elucidation of the Al/Si Ordering in Gehlenite $\text{Ca}_2\text{Al}_2\text{SiO}_7$ by Combined ^{29}Si and ^{27}Al NMR Spectroscopy/Quantum Chemical Calculations." In: *Chemistry of Materials* 24.21 (2012), pp. 4068–4079.
- [184] B. Bouchevreau, C. Martineau, C. Mellot-Draznieks, A. Tuel, M. R. Suchomel, J. Tréboss, O. Lafon, J.-P. Amoureux, and F. Taulelle. "High-Resolution Structural Characterization of Two Layered Aluminophosphates by Synchrotron Powder Diffraction and NMR Crystallographies." In: *Chemistry of Materials* 25.11 (2013), pp. 2227–2242.
- [185] C. Cozzan, K. J. Griffith, G. Laurita, J. G. Hu, C. P. Grey, and R. Seshadri. "Structural Evolution and Atom Clustering in B-SiAlON: $\text{B-Si}_{6-z}\text{Al}_z\text{O}_z\text{N}_{8-z}$." In: *Inorganic Chemistry* 56.4 (2017), pp. 2153–2158.
- [186] S. M. Kim, W.-C. Liao, A. M. Kierzkowska, T. Margossian, D. Hosseini, S. Yoon, M. Broda, C. Copéret, and C. R. Müller. "In Situ XRD and Dynamic Nuclear Polarization Surface Enhanced NMR Spectroscopy Unravel the Deactivation Mechanism of CaO-Based, $\text{Ca}_3\text{Al}_2\text{O}_6$ -Stabilized CO_2 Sorbents." In: *Chemistry of Materials* 30.4 (2018), pp. 1344–1352.
- [187] J. Cui et al. "Aluminum Oxide Thin Films from Aqueous Solutions: Insights from Solid-State NMR and Dielectric Response." In: *Chemistry of Materials* 30.21 (2018), pp. 7456–7463.
- [188] H. J. Jakobsen, J. Skibsted, H. Bildsøe, and N. C. Nielsen. "Magic-angle spinning NMR spectra of satellite transitions for quadrupolar nuclei in solids." In: *Journal of Magnetic Resonance* 85 (1989), pp. 173–180.
- [189] M.-H. Lee, C.-F. Cheng, V. Heine, and J. Klinowski. "Distribution of tetrahedral and octahedral A1 sites in gamma alumina." In: *Chemical Physics Letters* 265.6 (1997), pp. 673–676.
- [190] B. Ollivier, R. Retoux, P. Lacorre, D. Massiot, and G. Férey. "Crystal structure of κ -alumina: an X-ray powder diffraction, TEM and NMR study." In: *Journal of Materials Chemistry* 7.6 (1997), pp. 1049–1056.
- [191] L. O'Dell, S. Savin, A. Chadwick, and M. Smith. "A ^{27}Al MAS NMR study of a sol-gel produced alumina: Identification of the NMR parameters of the θ - Al_2O_3 transition alumina phase." In: *Solid State Nuclear Magnetic Resonance* 31.4 (2007), pp. 169–173.
- [192] R. Dupree, M. H. Lewis, and M. E. Smith. "A high-resolution NMR study of the lanthanum-silicon-aluminum-oxygen-nitrogen system." In: *Journal of the American Chemical Society* 111.14 (1989), pp. 5125–5132.
- [193] D. Burum, R. Macfarlane, R. Shelby, and L. Mueller. "Temperature dependence of ^{27}Al NMR in YAlO_3 ." In: *Physics Letters A* 91.9 (1982), pp. 465–468.
- [194] J. F. Stebbins, S. Kroeker, and D. Andrault. "The mechanism of solution of aluminum oxide in MgSiO_3 perovskite." In: *Geophysical Research Letters* 28.4 (2001), pp. 615–618.
- [195] J. F. Stebbins, H. Kojitani, M. Akaogi, and A. Navrotsky. "Aluminum substitution in MgSiO_3 perovskite: Investigation of multiple mechanisms by ^{27}Al NMR." In: *American Mineralogist* 88.7 (2003), pp. 1161–1164.

- [196] J. F. Stebbins, L.-S. Du, K. Kelsey, H. Kojitani, M. Akaogi, and S. Ono. "Aluminum substitution in stishovite and MgSiO_3 perovskite: High-resolution ^{27}Al NMR." In: *American Mineralogist* 91.2-3 (2006), p. 337.
- [197] E. Lima, M.-E. Villafuerte-Castrejón, J. M. Saniger, A. Ibarra-Palos, J. E. Sánchez-Sánchez, and L. J. Álvarez. "Experimental XRD and NMR, and molecular dynamics study of Sr containing LaAlO_3 perovskite." In: *Solid State Ionics* 178.39 (2008), pp. 1944–1949.
- [198] D. Coster and J. J. Fripiat. "Memory effects in gel-solid transformations: coordinately unsaturated aluminum sites in nanosized aluminas." In: *Chemistry of Materials* 5.9 (1993), pp. 1204–1210.
- [199] C. A. Fyfe, J. L. Bretherton, and L. Y. Lam. "Solid-State NMR Detection, Characterization, and Quantification of the Multiple Aluminum Environments in US-Y Catalysts by ^{27}Al MAS and MQMAS Experiments at Very High Field." In: *Journal of the American Chemical Society* 123.22 (2001), pp. 5285–5291.
- [200] P. B. Groszewicz, H. Breitzke, R. Dittmer, E. Sapper, W. Jo, G. Buntkowsky, and J. Rödel. "Nanoscale phase quantification in lead-free $(\text{Bi}_{1/2}\text{Na}_{1/2})\text{TiO}_3$ - BaTiO_3 relaxor ferroelectrics by means of ^{23}Na NMR." In: *Physical Review B* 90.22 (2014), p. 220104.
- [201] P. B. Groszewicz, M. Gröting, H. Breitzke, W. Jo, K. Albe, G. Buntkowsky, and J. Rödel. "Reconciling Local Structure Disorder and the Relaxor State in $(\text{Bi}_{1/2}\text{Na}_{1/2})\text{TiO}_3$ - BaTiO_3 ." In: *Scientific Reports* 6 (2016), p. 31739.
- [202] J. Koruza, P. Groszewicz, H. Breitzke, G. Buntkowsky, T. Rojac, and B. Malič. "Grain-size-induced ferroelectricity in NaNbO_3 ." In: *Acta Materialia* 126 (2017), pp. 77–85.
- [203] S. E. Ashbrook, J. M. Griffin, and K. E. Johnston. "Recent Advances in Solid-State Nuclear Magnetic Resonance Spectroscopy." In: *Annual Review of Analytical Chemistry* 11.1 (2018), pp. 485–508.
- [204] M. Choi, K. Matsunaga, F. Oba, and I. Tanaka. " ^{27}Al NMR Chemical Shifts in Oxide Crystals: A First-Principles Study." In: *The Journal of Physical Chemistry C* 113.9 (2009), pp. 3869–3873.
- [205] E. Lam, A. Comas-Vives, and C. Copéret. "Role of Coordination Number, Geometry, and Local Disorder on ^{27}Al NMR Chemical Shifts and Quadrupolar Coupling Constants: Case Study with Aluminosilicates." In: *The Journal of Physical Chemistry C* 121.36 (2017), pp. 19946–19957.
- [206] J.-P. Amoureux and M. Pruski. "MQMAS Advances." In: *eMagRes*. American Cancer Society, 2007. URL: <https://onlinelibrary.wiley.com/doi/abs/10.1002/9780470034590.emrstm0319>.
- [207] E. Engel and R. M. Dreizler. *Density Functional Theory. An Advanced Course*. Springer, 2011.
- [208] W. Kohn and L. J. Sham. "Self-Consistent Equations Including Exchange and Correlation Effects." In: *Physical Review* 140.4A (1965), A1133–A1138.
- [209] G. Kresse and J. Furthmüller. "Efficient iterative schemes for *ab initio* total-energy calculations using a plane-wave basis set." In: *Physical Review B* 54.16 (1996), pp. 11169–11186.

- [210] G. Kresse and J. Furthmüller. "Efficiency of ab-initio total energy calculations for metals and semiconductors using a plane-wave basis set." In: *Computational Materials Science* 6.1 (1996), pp. 15–50.
- [211] J. P. Perdew, K. Burke, and M. Ernzerhof. "Generalized Gradient Approximation Made Simple." In: *Physical Review Letters* 77.18 (1996), pp. 3865–3868.
- [212] F.-K. Chiang, M.-W. Chu, F. C. Chou, H. T. Jeng, H. S. Sheu, F. R. Chen, and C. H. Chen. "Effect of Jahn-Teller distortion on magnetic ordering in Dy(Fe,Mn)O₃ perovskites." In: *Phys. Rev. B* 83 (24 2011), p. 245105.
- [213] S. P. Ong, L. Wang, B. Kang, and G. Ceder. "Li-Fe-P-O₂ Phase Diagram from First Principles Calculations." In: *Chemistry of Materials* 20.5 (2008), pp. 1798–1807.
- [214] A. Jain, G. Hautier, C. J. Moore, S. Ping Ong, C. C. Fischer, T. Mueller, K. A. Persson, and G. Ceder. "A high-throughput infrastructure for density functional theory calculations." In: *Computational Materials Science* 50.8 (2011), pp. 2295–2310.
- [215] B. F. Grosso and N. A. Spaldin. *Prediction of new low-energy phases of BiFeO₃ with large unit cell and complex tilts beyond Glazer notation*. 2021. arXiv: [2101.12114](https://arxiv.org/abs/2101.12114) [[cond-mat.mtrl-sci](https://arxiv.org/abs/2101.12114)].
- [216] S. L. Dudarev, G. A. Botton, S. Y. Savrasov, C. J. Humphreys, and A. P. Sutton. "Electron-energy-loss spectra and the structural stability of nickel oxide: An LSDA+U study." In: *Physical Review B* 57.3 (1998), pp. 1505–1509.
- [217] X. Gonze et al. "First-principles computation of material properties: the ABINIT software project." In: *Computational Materials Science* 25.3 (2002), pp. 478–492.
- [218] X. Gonze et al. "ABINIT: First-principles approach to material and nanosystem properties." In: *Computer Physics Communications* 180.12 (2009). 40 YEARS OF CPC: A celebratory issue focused on quality software for high performance, grid and novel computing architectures, pp. 2582–2615.
- [219] X. Gonze et al. "A brief introduction to the ABINIT software package." In: *Zeitschrift für Kristallographie - Crystalline Materials* 220 (2005), pp. 558–562.
- [220] X. Gonze et al. "The Abinit project: Impact, environment and recent developments." In: *Computer Physics Communications* 248 (2020), p. 107042.
- [221] M. van Setten, M. Giantomassi, E. Bousquet, M. Verstraete, D. Hamann, X. Gonze, and G.-M. Rignanese. "The PseudoDojo: Training and grading a 85 element optimized norm-conserving pseudopotential table." In: *Computer Physics Communications* 226 (2018), pp. 39–54.
- [222] M. I. Aroyo, A. Kirov, C. Capillas, J. M. Perez-Mato, and H. Wondratschek. "Bilbao Crystallographic Server. II. Representations of crystallographic point groups and space groups." In: *Acta Crystallographica Section A Foundations of Crystallography* 62.2 (2006), pp. 115–128.
- [223] M. Aroyo, J. Perez-Mato, C. Capillas, E. Kroumova, S. Ivantchev, A. K. Madariaga, and H. Wondratschek. "Bilbao Crystallographic Server: I. Databases and crystallographic computing programs." In: *Zeitschrift für Kristallographie - Crystalline Materials* 221.1 (2009), pp. 15–27.

- [224] M. I. Aroyo, J. Perez-Mato, D Orobengoa, E. Tasci, G. De la Flor Martin, and A Kirov. "Crystallography Online: Bilbao Crystallographic Server." In: *Bulgarian Chemical Communications* 43 (2011), pp. 183–197.
- [225] J. M. Perez-Mato, D. Orobengoa, and M. I. Aroyo. "Mode crystallography of distorted structures." In: *Acta Crystallographica Section A* 66.5 (2010), pp. 558–590.
- [226] D. Orobengoa, C. Capillas, M. I. Aroyo, and J. M. Perez-Mato. "AMPLIMODES: symmetry-mode analysis on the Bilbao Crystallographic Server." In: *Journal of Applied Crystallography* 42.5 (2009), pp. 820–833.
- [227] B. J. Campbell, H. T. Stokes, D. E. Tanner, and D. M. Hatch. "ISODISPLACE : a web-based tool for exploring structural distortions." In: *Journal of Applied Crystallography* 39.4 (2006), pp. 607–614.
- [228] H. T. Stokes, D. M. Hatch, and B. J. Campbell. *ISODISTORT, ISOTROPY Software Suite*. URL: iso.byu.edu.
- [229] H. T. Stokes and D. M. Hatch. "FINDSYM : program for identifying the space-group symmetry of a crystal." In: *Journal of Applied Crystallography* 38.1 (2005), pp. 237–238.
- [230] H. T. Stokes, D. M. Hatch, and B. J. Campbell. *FINDSYM, ISOTROPY Software Suite*. URL: iso.byu.edu.
- [231] H. T. Stokes, D. M. Hatch, and B. J. Campbell. *ISOTROPY Software Suite*. URL: iso.byu.edu.
- [232] *Vesta*. URL: <https://jp-minerals.org/vesta/en>.
- [233] K. Momma and F. Izumi. "VESTA: a three-dimensional visualization system for electronic and structural analysis." In: *Journal of Applied Crystallography* 41.3 (2008), pp. 653–658.
- [234] A. Stukowski. "Visualization and analysis of atomistic simulation data with OVITO—the Open Visualization Tool." In: *Modelling and Simulation in Materials Science and Engineering* 18.1 (2009), p. 015012.
- [235] S. P. Ong, W. D. Richards, A. Jain, G. Hautier, M. Kocher, S. Cholia, D. Gunter, V. L. Chevrier, K. A. Persson, and G. Ceder. "Python Materials Genomics (pymatgen): A robust, open-source python library for materials analysis." In: *Computational Materials Science* 68 (2013), pp. 314–319.
- [236] URL: <https://github.com/abinit/abipy> (visited on 02/25/2020).
- [237] L. J. Sham and M. Schlüter. "Density-Functional Theory of the Energy Gap." In: *Physical Review Letters* 51.20 (1983), pp. 1888–1891.
- [238] L. J. Sham and M. Schlüter. "Density-functional theory of the band gap." In: *Physical Review B* 32 (1985), pp. 3883–3889.
- [239] J. P. Perdew and M. Levy. "Physical Content of the Exact Kohn-Sham Orbital Energies: Band Gaps and Derivative Discontinuities." In: *Physical Review Letters* 51.20 (1983), pp. 1884–1887.
- [240] D. M. Ceperley and B. J. Alder. "Ground State of the Electron Gas by a Stochastic Method." In: *Physical Review Letters* 45.7 (1980), pp. 566–569.

- [241] S. Goedecker, M. Teter, and J. Hutter. "Separable dual-space Gaussian pseudopotentials." In: *Physical Review B* 54.3 (1996), pp. 1703–1710.
- [242] S. Lany and A. Zunger. "Assessment of correction methods for the band-gap problem and for finite-size effects in supercell defect calculations: Case studies for ZnO and GaAs." In: *Physical Review B* 78.23 (2008).
- [243] A. van de Walle and G. Ceder. "Correcting overbinding in local-density approximation calculations." In: *Physical Review B* 59.23 (1999), pp. 14992–15001.
- [244] C. Franchini, A. Sanna, M. Marsman, and G. Kresse. "Structural, vibrational, and quasiparticle properties of the Peierls semiconductor BaBiO₃ : A hybrid functional and self-consistent GW + vertex-corrections study." In: *Physical Review B* 81.8 (2010).
- [245] A. Khein, D. J. Singh, and C. J. Umrigar. "All-electron study of gradient corrections to the local-density functional in metallic systems." In: *Physical Review B* 51.7 (1995), pp. 4105–4109.
- [246] V. I. Anisimov, F. Aryasetiawan, and A. I. Lichtenstein. "First-principles calculations of the electronic structure and spectra of strongly correlated systems: the LDA + *U* method." In: *Journal of Physics: Condensed Matter* 9.4 (1997), pp. 767–808.
- [247] J. P. Perdew and A. Zunger. "Self-interaction correction to density-functional approximations for many-electron systems." In: *Physical Review B* 23.10 (1981), pp. 5048–5079.
- [248] A. J. Cohen, P. Mori-Sánchez, and W. Yang. "Challenges for Density Functional Theory." In: *Chemical Reviews* 112.1 (2012), pp. 289–320.
- [249] R. Gillen and J. Robertson. "A hybrid density functional view of native vacancies in gallium nitride." In: *Journal of Physics: Condensed Matter* 25.40 (2013), p. 405501.
- [250] M. Cococcioni and S. de Gironcoli. "Linear response approach to the calculation of the effective interaction parameters in the LDA + *U* method." In: *Physical Review B* 71.3 (2005).
- [251] F. Aryasetiawan, K. Karlsson, O. Jepsen, and U. Schönberger. "Calculations of Hubbard *U* from first-principles." In: *Physical Review B* 74.12 (2006).
- [252] A. Janotti, D. Segev, and C. G. Van de Walle. "Effects of cation d states on the structural and electronic properties of III-nitride and II-oxide wide-band-gap semiconductors." In: *Physical Review B* 74.4 (2006).
- [253] J. Hong, A. Stroppa, J. Íñiguez, S. Picozzi, and D. Vanderbilt. "Spin-phonon coupling effects in transition-metal perovskites: A DFT + *U* and hybrid-functional study." In: *Physical Review B* 85.5 (2012), p. 054417.
- [254] B. G. Janesko, T. M. Henderson, and G. E. Scuseria. "Screened hybrid density functionals for solid-state chemistry and physics." In: *Physical Chemistry Chemical Physics* 11.3 (2009), pp. 443–454.
- [255] J. Paier, M. Marsman, K. Hummer, G. Kresse, I. C. Gerber, and J. G. Ángyán. "Screened hybrid density functionals applied to solids." In: *The Journal of Chemical Physics* 124.15 (2006), p. 154709.

- [256] J. Heyd and G. E. Scuseria. "Efficient hybrid density functional calculations in solids: Assessment of the Heyd–Scuseria–Ernzerhof screened Coulomb hybrid functional." In: *The Journal of Chemical Physics* 121.3 (2004), pp. 1187–1192.
- [257] J. E. Moussa, P. A. Schultz, and J. R. Chelikowsky. "Analysis of the Heyd–Scuseria–Ernzerhof density functional parameter space." In: *The Journal of Chemical Physics* 136.20 (2012), p. 204117.
- [258] J. Heyd, G. E. Scuseria, and M. Ernzerhof. "Hybrid functionals based on a screened Coulomb potential." In: *The Journal of Chemical Physics* 118.18 (2003), pp. 8207–8215.
- [259] J. Heyd, G. E. Scuseria, and M. Ernzerhof. "Erratum: "Hybrid functionals based on a screened Coulomb potential"[J. Chem. Phys. 118, 8207 (2003)]." In: *The Journal of Chemical Physics* 124.21 (2006), p. 219906.
- [260] E. N. Brothers, A. F. Izmaylov, J. O. Normand, V. Barone, and G. E. Scuseria. "Accurate solid-state band gaps via screened hybrid electronic structure calculations." In: *The Journal of Chemical Physics* 129.1 (2008), p. 011102.
- [261] A. V. Krukau, O. A. Vydrov, A. F. Izmaylov, and G. E. Scuseria. "Influence of the exchange screening parameter on the performance of screened hybrid functionals." In: *The Journal of Chemical Physics* 125.22 (2006), p. 224106.
- [262] A. D. Becke. "Density-functional thermochemistry. III. The role of exact exchange." In: *The Journal of Chemical Physics* 98.7 (1993), pp. 5648–5652.
- [263] C. Lee, W. Yang, and R. G. Parr. "Development of the Colle-Salvetti correlation-energy formula into a functional of the electron density." In: *Physical Review B* 37.2 (1988), pp. 785–789.
- [264] C. Adamo and V. Barone. "Toward reliable density functional methods without adjustable parameters: The PBE0 model." In: *The Journal of Chemical Physics* 110.13 (1999), pp. 6158–6170.
- [265] C. Franchini. "Hybrid functionals applied to perovskites." In: *Journal of Physics: Condensed Matter* 26.25 (2014), p. 253202.
- [266] J. Paier, M. Marsman, and G. Kresse. "Dielectric properties and excitons for extended systems from hybrid functionals." In: *Physical Review B* 78.12 (2008).
- [267] H. Peng, D. O. Scanlon, V. Stevanovic, J. Vidal, G. W. Watson, and S. Lany. "Convergence of density and hybrid functional defect calculations for compound semiconductors." In: *Physical Review B* 88.11 (2013).
- [268] F. El-Mellouhi, E. N. Brothers, M. J. Lucero, and G. E. Scuseria. "Modeling of the cubic and antiferrodistortive phases of SrTiO₃ with screened hybrid density functional theory." In: *Physical Review B* 84.11 (2011).
- [269] L. Hedin. "New Method for Calculating the One-Particle Green's Function with Application to the Electron-Gas Problem." In: *Physical Review* 139.3A (1965), A796–A823.
- [270] F. Aryasetiawan and O. Gunnarsson. "The GW method." In: *Reports on Progress in Physics* 61.3 (1998), pp. 237–312.

- [271] P. Rinke, A. Janotti, M. Scheffler, and C. G. Van de Walle. "Defect Formation Energies without the Band-Gap Problem: Combining Density-Functional Theory and the $G W$ Approach for the Silicon Self-Interstitial." In: *Physical Review Letters* 102.2 (2009), p. 026402.
- [272] M. C. Payne, M. P. Teter, D. C. Allan, T. A. Arias, and J. D. Joannopoulos. "Iterative minimization techniques for *ab initio* total-energy calculations: molecular dynamics and conjugate gradients." In: *Reviews of Modern Physics* 64.4 (1992), pp. 1045–1097.
- [273] N. Ashcroft and N. Mermin. *Festkörperphysik*. Oldenbourg Wissenschaftsverlag GmbH, 2007.
- [274] M. Born and T. von Kármán. "On the distribution of natural vibrations of spot-lattices." In: *Physikalische Zeitschrift* 14 (1913), 65–71.
- [275] M. Born and T. von Kármán. "On fluctuations in spacial grids." In: *Physikalische Zeitschrift* 13 (1912), 297–309.
- [276] Dove, M.T. "Introduction to the theory of lattice dynamics." In: *Collection JDN* 12 (2011), pp. 123–159.
- [277] D. J. Chadi and M. L. Cohen. "Special Points in the Brillouin Zone." In: *Physical Review B* 8.12 (1973), pp. 5747–5753.
- [278] J. D. Joannopoulos and M. L. Cohen. "Electronic charge densities for ZnS in the wurtzite and zinblende structures." In: *Journal of Physics C: Solid State Physics* 6.9 (1973), pp. 1572–1585.
- [279] H. J. Monkhorst and J. D. Pack. "Special points for Brillouin-zone integrations." In: *Physical Review B* 13.12 (1976), pp. 5188–5192.
- [280] A. Baldereschi. "Mean-Value Point in the Brillouin Zone." In: *Physical Review B* 7.12 (1973), pp. 5212–5215.
- [281] V. Heine. "The Pseudopotential Concept." In: ed. by H. Ehrenreich, F. Seitz, and D. Turnbull. Vol. 24. *Solid State Physics*. Academic Press, 1970, pp. 1–36.
- [282] J. C. Phillips. "Energy-Band Interpolation Scheme Based on a Pseudopotential." In: *Physical Review* 112 (3 1958), pp. 685–695.
- [283] M. T. Yin and M. L. Cohen. "Theory of *ab initio* pseudopotential calculations." In: *Physical Review B* 25.12 (1982), pp. 7403–7412.
- [284] S. Baroni, P. Giannozzi, and A. Testa. "Green's-function approach to linear response in solids." In: *Physical Review Letters* 58.18 (1987), pp. 1861–1864.
- [285] X. Gonze. "First-principles responses of solids to atomic displacements and homogeneous electric fields: Implementation of a conjugate-gradient algorithm." In: *Physical Review B* 55.16 (1997), pp. 10337–10354.
- [286] X. Gonze and J.-P. Vigneron. "Density-functional approach to nonlinear-response coefficients of solids." In: *Physical Review B* 39.18 (1989), pp. 13120–13128.
- [287] S. Baroni, P. Giannozzi, and A. Testa. "Elastic Constants of Crystals from Linear-Response Theory." In: *Physical Review Letters* 59.23 (1987), pp. 2662–2665.

- [288] X. Gonze. "Perturbation expansion of variational principles at arbitrary order." In: *Physical Review A* 52.2 (1995), pp. 1086–1095.
- [289] S. de Gironcoli, S. Baroni, and R. Resta. "Piezoelectric properties of III-V semiconductors from first-principles linear-response theory." In: *Physical Review Letters* 62.24 (1989), pp. 2853–2856.
- [290] X. Gonze and J. P. Vigneron. "Erratum: Density-functional approach to nonlinear-response coefficients of solids." In: *Physical Review B* 44.7 (1991), pp. 3494–3494.
- [291] X. Gonze. "Adiabatic density-functional perturbation theory." In: *Physical Review A* 52.2 (1995), pp. 1096–1114.
- [292] R. P. Feynman. "Forces in Molecules." In: *Physical Review* 56.4 (1939), pp. 340–343.
- [293] H. Hellmann. "Einführung in die Quantenchemie." In: *Hans Hellmann: Einführung in die Quantenchemie: Mit biografischen Notizen von Hans Hellmann jr.* Ed. by D. Andrae. Berlin, Heidelberg: Springer Berlin Heidelberg, 2015, pp. 19–376.
- [294] R. Resta. "Theory of the electric polarization in crystals." In: *Ferroelectrics* 136.1 (1992), pp. 51–55.
- [295] N. A. Spaldin. "A beginner's guide to the modern theory of polarization." In: *Journal of Solid State Chemistry*. Polar Inorganic Materials: Design Strategies and Functional Properties 195 (2012), pp. 2–10.
- [296] R. M. Martin. "Comment on calculations of electric polarization in crystals." In: *Physical Review B* 9.4 (1974), pp. 1998–1999.
- [297] R. Resta. "Macroscopic polarization in crystalline dielectrics: the geometric phase approach." In: *Reviews of Modern Physics* 66.3 (1994), pp. 899–915.
- [298] R. D. King-Smith and D. Vanderbilt. "Theory of polarization of crystalline solids." In: *Physical Review B* 47.3 (1993), pp. 1651–1654.
- [299] J. Zak. "Berry's phase for energy bands in solids." In: *Physical Review Letters* 62.23 (1989), pp. 2747–2750.
- [300] F. Bruneval. *Electronic Structure of Point Defects in Semiconductors*. FRCEA-TH-5981. 2014. URL: http://inis.iaea.org/search/search.aspx?orig_q=RN:46012718.
- [301] C. W. M. Castleton and S. Mirbt. "Finite-size scaling as a cure for supercell approximation errors in calculations of neutral native defects in InP." In: *Physical Review B* 70.19 (2004).
- [302] F. Bruneval, J.-P. Crocombette, X. Gonze, B. Dorado, M. Torrent, and F. Jollet. "Consistent treatment of charged systems within periodic boundary conditions: The projector augmented-wave and pseudopotential methods revisited." In: *Physical Review B* 89.4 (2014).
- [303] R. M. Nieminen. "Issues in first-principles calculations for defects in semiconductors and oxides." In: *Modelling and Simulation in Materials Science and Engineering* 17.8 (2009), p. 084001.

- [304] C. Freysoldt, J. Neugebauer, and C. G.V. d. Walle. "Electrostatic interactions between charged defects in supercells." In: *physica status solidi (b)* 248.5 (2011), pp. 1067–1076.
- [305] S. B. Zhang and J. E. Northrup. "Chemical potential dependence of defect formation energies in GaAs: Application to Ga self-diffusion." In: *Physical Review Letters* 67.17 (1991), pp. 2339–2342.
- [306] C. Freysoldt, B. Grabowski, T. Hickel, J. Neugebauer, G. Kresse, A. Janotti, and C. G. Van de Walle. "First-principles calculations for point defects in solids." In: *Reviews of Modern Physics* 86.1 (2014), pp. 253–305.
- [307] B. Grabowski, T. Hickel, and J. Neugebauer. "Formation energies of point defects at finite temperatures." In: *physica status solidi (b)* 248.6 (2011), pp. 1295–1308.
- [308] J. Shim, E.-K. Lee, Y. J. Lee, and R. M. Nieminen. "Density-functional calculations of defect formation energies using supercell methods: Defects in diamond." In: *Physical Review B* 71.3 (2005).
- [309] C. Freysoldt, B. Lange, J. Neugebauer, Q. Yan, J. L. Lyons, A. Janotti, and C. G. Van de Walle. "Electron and chemical reservoir corrections for point-defect formation energies." In: *Physical Review B* 93.16 (2016), p. 165206.
- [310] J. Lento, J.-L. Mozos, and R. M. Nieminen. "Charged point defects in semiconductors and the supercell approximation." In: *Journal of Physics: Condensed Matter* 14.10 (2002), p. 2637.
- [311] F. Bruneval, C. Varvenne, J.-P. Crocombette, and E. Clouet. "Pressure, relaxation volume, and elastic interactions in charged simulation cells." In: *Physical Review B* 91.2 (2015).
- [312] M. Leslie and N. J. Gillan. "The energy and elastic dipole tensor of defects in ionic crystals calculated by the supercell method." In: *Journal of Physics C: Solid State Physics* 18.5 (1985), p. 973.
- [313] C. W. M. Castleton, A. Höglund, and S. Mirbt. "Managing the supercell approximation for charged defects in semiconductors: Finite-size scaling, charge correction factors, the band-gap problem, and the *ab initio* dielectric constant." In: *Physical Review B* 73.3 (2006).
- [314] S. E. Taylor and F. Bruneval. "Understanding and correcting the spurious interactions in charged supercells." In: *Physical Review B* 84.7 (2011).
- [315] G. Makov and M. C. Payne. "Periodic boundary conditions in *ab initio* calculations." In: *Physical Review B* 51.7 (1995), pp. 4014–4022.
- [316] Y. Kumagai and F. Oba. "Electrostatics-based finite-size corrections for first-principles point defect calculations." In: *Physical Review B* 89.19 (2014).
- [317] H.-P. Komsa, T. T. Rantala, and A. Pasquarello. "Finite-size supercell correction schemes for charged defect calculations." In: *Physical Review B* 86.4 (2012).
- [318] M. I. J. Probert and M. C. Payne. "Improving the convergence of defect calculations in supercells: An *ab initio* study of the neutral silicon vacancy." In: *Physical Review B* 67.7 (2003), p. 075204.

- [319] C. Varvenne and E. Clouet. "Elastic dipoles of point defects from atomistic simulations." In: *Physical Review B* 96.22 (2017).
- [320] C. Varvenne, F. Bruneval, M.-C. Marinica, and E. Clouet. "Point defect modeling in materials: Coupling ab-initio and elasticity approaches." In: *Physical Review B* 88.13 (2013).
- [321] E. Clouet, C. Varvenne, and T. Jourdan. "Elastic modeling of point-defects and their interaction." In: *Computational Materials Science* 147 (2018), pp. 49–63.
- [322] F. Bruneval and J.-P. Crocombette. "Ab initio formation volume of charged defects." In: *Physical Review B* 86.14 (2012).
- [323] A. Goyal, K. Mathew, R. G. Hennig, A. Chernatynskiy, C. R. Stank, S. T. Murphy, D. A. Andersson, S. R. Phillpot, and B. P. Uberuaga. "The conundrum of relaxation volumes in first-principles calculations of charge defects." In: *arXiv:1704.04044* (2017). arXiv: 1704.04044. URL: <http://arxiv.org/abs/1704.04044>.
- [324] F. Bruneval, M. Freyss, and J.-P. Crocombette. "Lattice constant in nonstoichiometric uranium dioxide from first principles." In: *Physical Review Materials* 2.2 (2018).
- [325] J. F. Janak. "Proof that $\partial E/\partial n_i = \epsilon$ in density-functional theory." In: *Physical Review B* 18.12 (1978), pp. 7165–7168.
- [326] C. G. Van de Walle. "Band lineups and deformation potentials in the model-solid theory." In: *Physical Review B* 39.3 (1989), pp. 1871–1883.
- [327] D. A. Freedman, D. Roundy, and T. A. Arias. "Elastic effects of vacancies in strontium titanate: Short- and long-range strain fields, elastic dipole tensors, and chemical strain." In: *Physical Review B* 80.6 (2009), p. 064108.
- [328] D. Bacon, D. Barnett, and R. Scattergood. "Anisotropic continuum theory of lattice defects." In: *Progress in Materials Science* 23 (1980), pp. 51–262.
- [329] D. M. Barnett. "The precise evaluation of derivatives of the anisotropic elastic Green's functions." In: *physica status solidi (b)* 49.2 (1972), pp. 741–748.
- [330] W. Cai, V. V. Bulatov, J. Chang, J. Li, and S. Yip. "Periodic image effects in dislocation modelling." In: *Philosophical Magazine* 83.5 (2003), pp. 539–567.
- [331] J. Bardeen and W. Shockley. "Deformation Potentials and Mobilities in Non-Polar Crystals." In: *Physical Review* 80.1 (1950), pp. 72–80.
- [332] Y.-H. Li, X. G. Gong, and S.-H. Wei. "Ab initio all-electron calculation of absolute volume deformation potentials of IV-IV, III-V, and II-VI semiconductors: The chemical trends." In: *Phys. Rev. B* 73 (24 2006), p. 245206.
- [333] C. G. Van de Walle. "Theoretical study of band offsets at semiconductor interfaces." In: *Physical Review B* 35.15 (1987), p. 12.
- [334] R. Resta, L. Colombo, and S. Baroni. "Absolute deformation potentials in semiconductors." In: *Physical Review B* 41.17 (1990), pp. 12358–12361.
- [335] C. G. Van de Walle and R. M. Martin. "'Absolute' deformation potentials: Formulation and ab initio calculations for semiconductors." In: *Phys. Rev. Lett.* 62 (17 1989), pp. 2028–2031.

- [336] A. Franceschetti, S.-H. Wei, and A. Zunger. "Absolute deformation potentials of Al, Si, and NaCl." In: *Physical Review B* 50.24 (1994), pp. 17797–17801.
- [337] A. Baldereschi, S. Baroni, and R. Resta. "Band Offsets in Lattice-Matched Heterojunctions: A Model and First-Principles Calculations for GaAs/AlAs." In: *Physical Review Letters* 61.6 (1988), pp. 734–737.
- [338] D. D. Nolte, W. Walukiewicz, and E. E. Haller. "Deep-level defects in silicon and the band-edge hydrostatic deformation potentials." In: *Physical Review B* 36.17 (1987), pp. 9392–9394.
- [339] Y.-H. Li, X. G. Gong, and S.-H. Wei. "Ab-initio calculation of hydrostatic absolute deformation potential of semiconductors." In: *Applied Physics Letters* 88.4 (2006), p. 042104.
- [340] Y.-H. Li, X. G. Gong, and S.-H. Wei. "Ab-initio all-electron calculation of absolute volume deformation potentials of IV-IV, III-V, and II-VI semiconductors: The chemical trends." In: *Physical Review B* 73.24 (24 2006), p. 245206.
- [341] G. Henkelman, B. P. Uberuaga, and H. Jónsson. "A climbing image nudged elastic band method for finding saddle points and minimum energy paths." In: *The Journal of Chemical Physics* 113.22 (2000), pp. 9901–9904.
- [342] G. Henkelman and H. Jónsson. "Improved tangent estimate in the nudged elastic band method for finding minimum energy paths and saddle points." In: *The Journal of Chemical Physics* 113.22 (2000), pp. 9978–9985.
- [343] D. Sheppard, P. Xiao, W. Chemelewski, D. D. Johnson, and G. Henkelman. "A generalized solid-state nudged elastic band method." In: *The Journal of Chemical Physics* 136.7 (2012), p. 074103.
- [344] S. E. Ashbrook and D. McKay. "Combining solid-state NMR spectroscopy with first-principles calculations – a guide to NMR crystallography." In: *Chemical Communications* 52.45 (2016), pp. 7186–7204.
- [345] C. J. Pickard and F. Mauri. "Calculations of Magnetic Resonance Parameters in Solids and Liquids Using Periodic Boundary Conditions." In: *Calculation of NMR and EPR Parameters*. John Wiley & Sons, Ltd, 2004. Chap. 16, pp. 265–277.
- [346] C. J. Pickard and F. Mauri. "All-electron magnetic response with pseudopotentials: NMR chemical shifts." In: *Physical Review B* 63.24 (2001), p. 245101.
- [347] J. R. Yates, C. J. Pickard, and F. Mauri. "Calculation of NMR chemical shifts for extended systems using ultrasoft pseudopotentials." In: *Physical Review B* 76.2 (2007).
- [348] C. Bonhomme et al. "First-Principles Calculation of NMR Parameters Using the Gauge Including Projector Augmented Wave Method: A Chemist's Point of View." In: *Chemical Reviews* 112.11 (2012), pp. 5733–5779.
- [349] S. J. Clark, M. D. Segall, C. J. Pickard, P. J. Hasnip, M. I. J. Probert, K. Refson, and M. C. Payne. "First principles methods using CASTEP." In: *Zeitschrift für Kristallographie – Crystalline Materials* 220 (2005), p. 567.
- [350] P. Giannozzi et al. "QUANTUM ESPRESSO: a modular and open-source software project for quantum simulations of materials." In: *Journal of Physics: Condensed Matter* 21.39 (2009), p. 395502.

- [351] G. A. de Wijs, R. Laskowski, P. Blaha, R. W. A. Havenith, G. Kresse, and M. Marsman. "NMR shieldings from density functional perturbation theory: GI-PAW versus all-electron calculations." In: *The Journal of Chemical Physics* 146.6 (2017), p. 064115.
- [352] C. G. Van de Walle and P. E. Blöchl. "First-principles calculations of hyperfine parameters." In: *Physical Review B* 47.8 (1993), pp. 4244–4255.
- [353] J. Mason. "Conventions for the reporting of nuclear magnetic shielding (or shift) tensors suggested by participants in the NATO ARW on NMR shielding constants at the University of Maryland, College Park, July 1992." In: *Solid State Nuclear Magnetic Resonance* 2.5 (1993), pp. 285–288.
- [354] R. Dronskowski and P. E. Blöchl. "Crystal orbital Hamilton populations (COHP): energy-resolved visualization of chemical bonding in solids based on density-functional calculations." In: *The Journal of Physical Chemistry* 97.33 (1993), pp. 8617–8624.
- [355] V. L. Deringer, A. L. Tchougréeff, and R. Dronskowski. "Crystal Orbital Hamilton Population (COHP) Analysis As Projected from Plane-Wave Basis Sets." In: *The Journal of Physical Chemistry* 115.21 (2011), pp. 5461–5466.
- [356] R. S. Mulliken. "Electronic Population Analysis on LCAO–MO Molecular Wave Functions. I." In: *The Journal of Chemical Physics* 23.10 (1955), pp. 1833–1840.
- [357] S. Maintz, V. L. Deringer, A. L. Tchougréeff, and R. Dronskowski. "LOBSTER: A tool to extract chemical bonding from plane-wave based DFT." In: *Journal of Computational Chemistry* 37.11 (2016), pp. 1030–1035.
- [358] R. Nelson, C. Ertural, J. George, V. L. Deringer, G. Hautier, and R. Dronskowski. "LOBSTER: Local orbital projections, atomic charges, and chemical-bonding analysis from projector-augmented-wave-based density-functional theory." In: *Journal of Computational Chemistry* 41.21 (2020), pp. 1931–1940.
- [359] S. Maintz, V. L. Deringer, A. L. Tchougréeff, and R. Dronskowski. "Analytic projection from plane-wave and PAW wavefunctions and application to chemical-bonding analysis in solids." In: *Journal of Computational Chemistry* 34.29 (2013), pp. 2557–2567.
- [360] S. Steinberg and R. Dronskowski. "The Crystal Orbital Hamilton Population (COHP) Method as a Tool to Visualize and Analyze Chemical Bonding in Intermetallic Compounds." In: *Crystals* 8.5 (2018).
- [361] P. E. Blöchl, O. Jepsen, and O. K. Andersen. "Improved tetrahedron method for Brillouin-zone integrations." In: *Physical Review B* 49.23 (1994), pp. 16223–16233.
- [362] V. L. Deringer, W. Zhang, M. Lumeij, S. Maintz, M. Wuttig, R. Mazzarello, and R. Dronskowski. "Bonding Nature of Local Structural Motifs in Amorphous GeTe." In: *Angewandte Chemie International Edition* 53.40 (2014), pp. 10817–10820.
- [363] L. Koch, S. Steiner, K.-C. Meyer, I.-T. Seo, K. Albe, and T. Frömling. "Ionic conductivity of acceptor doped sodium bismuth titanate: influence of dopants, phase transitions and defect associates." In: *Journal of Materials Chemistry C* 5.35 (2017), pp. 8958–8965.

- [364] G. Kresse and D. Joubert. "From ultrasoft pseudopotentials to the projector augmented-wave method." In: *Physical Review B* 59.3 (1999), pp. 1758–1775.
- [365] P. E. Blöchl. "Projector augmented-wave method." In: *Physical Review B* 50.24 (1994), pp. 17953–17979.
- [366] R. Merkle and J. Maier. "Defect association in acceptor-doped SrTiO₃: case study for Fe'_{Ti}V_Ö and Mn''_{Ti}V_Ö." In: *Physical Chemistry Chemical Physics* 5.11 (2003), pp. 2297–2303.
- [367] G. E. Murch. "The Nernst-Einstein equation in high-defect-content solids." In: *Philosophical Magazine A* 45.4 (1982), pp. 685–692.
- [368] K. A. Lurie and A. V. Cherkaev. "Exact estimates of the conductivity of a binary mixture of isotropic materials." In: *Proceedings of the Royal Society of Edinburgh Section A: Mathematics* 104.1-2 (1986), pp. 21–38.
- [369] Y. Grabovsky. "The G-closure of two well-ordered, anisotropic conductors." In: *Proceedings of the Royal Society of Edinburgh: Section A Mathematics* 123.3 (1993), 423–432.
- [370] G. Allaire. *Introduction to homogenization theory*. 2010. URL: <http://www.cmap.polytechnique.fr/~allaire/homog/lect1.pdf>.
- [371] M. Wang and N. Pan. "Predictions of effective physical properties of complex multiphase materials." In: *Materials Science and Engineering: R: Reports* 63.1 (2008), pp. 1–30.
- [372] K.-C. Meyer, M. Gröting, and K. Albe. "Octahedral tilt transitions in the relaxor ferroelectric Na_{1/2}Bi_{1/2}TiO₃." In: *Journal of Solid State Chemistry* 227 (2015), pp. 117–122.
- [373] N. Hainovsky and J. Maier. "Simple phenomenological approach to premelting and sublattice melting in Frenkel disordered ionic crystals." In: *Physical Review B* 51.22 (1995), pp. 15789–15797.
- [374] J. Suchanicz. "Elastic constants of Na_{0.5}Bi_{0.5}TiO₃ single crystal." In: *Journal of Materials Science* 37.3 (2002), pp. 489–491.
- [375] R. Bujakiewicz-Korońska and Y. Natanzon. "Determination of elastic constants of Na_{0.5}Bi_{0.5}TiO₃ from ab initio calculations." In: *Phase Transitions* 81.11-12 (2008), pp. 1117–1124.
- [376] W. Setyawan and S. Curtarolo. "High-throughput electronic band structure calculations: Challenges and tools." In: *Computational Materials Science* 49.2 (2010), pp. 299–312.
- [377] N. Vonrüti and U. Aschauer. "Band-gap engineering in AB(O_xS_{1-x})₃ perovskite oxysulfides: a route to strongly polar materials for photocatalytic water splitting." In: *Journal of Materials Chemistry A* 7.26 (2019), pp. 15741–15748.
- [378] N. Vonrüti and U. Aschauer. "Epitaxial strain dependence of band gaps in perovskite oxynitrides compared to perovskite oxides." In: *Physical Review Materials* 2.10 (2018), p. 105401.
- [379] A. V. Ushakov, S. V. Streltsov, and D. I. Khomskii. "Crystal field splitting in correlated systems with negative charge-transfer gap." In: *Journal of Physics: Condensed Matter* 23.44 (2011), p. 445601.

- [380] J. B. Goodenough. "Perspective on Engineering Transition-Metal Oxides." In: *Chemistry of Materials* 26.1 (2014), pp. 820–829.
- [381] P. S. Halasyamani. "Asymmetric Cation Coordination in Oxide Materials: Influence of Lone-Pair Cations on the Intra-octahedral Distortion in d⁰ Transition Metals." In: *Chemistry of Materials* 16 (2004), pp. 3586–3592.
- [382] J. A. Dawson, H. Chen, and I. Tanaka. "Crystal structure, defect chemistry and oxygen ion transport of the ferroelectric perovskite, Na_{0.5}Bi_{0.5}TiO₃: insights from first-principles calculations." In: *Journal of Materials Chemistry A* 3.32 (2015), pp. 16574–16582.
- [383] J. R. Kim et al. "Stabilizing hidden room-temperature ferroelectricity via a metastable atomic distortion pattern." In: *Nature Communications* 11 (2020), p. 4944.
- [384] R. M. Pick, M. H. Cohen, and R. M. Martin. "Microscopic Theory of Force Constants in the Adiabatic Approximation." In: *Physical Review B* 1.2 (1970), pp. 910–920.
- [385] P. Ghosez, X. Gonze, and J.-P. Michenaud. "Role of the coulomb interaction on the ferroelectric instability of barium titanate." In: *Ferroelectrics* 186.1 (1996), pp. 73–76.
- [386] X. He and K.-J. Jin. "Persistence of polar distortion with electron doping in lone-pair driven ferroelectrics." In: *Physical Review B* 94.22 (2016), p. 224107.
- [387] R. A. Evarestov, S. Piskunov, E. A. Kotomin, and G. Borstel. "Single impurities in insulators: Ab initio study of Fe-doped SrTiO₃." In: *Physical Review B* 67.6 (2003), p. 064101.
- [388] I. Levin, F. Yang, R. Maier, W. J. Laws, D. S. Keeble, G. Cibin, and D. C. Sinclair. "Displacive Order–Disorder Behavior and Intrinsic Clustering of Lattice Distortions in Bi-Substituted NaNbO₃." In: *Advanced Functional Materials* 30.30 (2020), p. 2001840.
- [389] M. Choi, F. Oba, Y. Kumagai, and I. Tanaka. "Anti-ferrodistortive-Like Oxygen-Octahedron Rotation Induced by the Oxygen Vacancy in Cubic SrTiO₃." In: *Advanced Materials* 25.1 (2013), pp. 86–90.
- [390] C. Lasota, C.-Z. Wang, R. Yu, and H. Krakauer. "Ab initio linear response study of SrTiO₃." In: *Ferroelectrics* 194.1 (1997), pp. 109–118.
- [391] X. Ren. "Large electric-field-induced strain in ferroelectric crystals by point-defect-mediated reversible domain switching." In: *Nature Materials* 3 (2004), pp. 91–94.
- [392] X. Ren and K. Otsuka. "Universal Symmetry Property of Point Defects in Crystals." In: *Phys. Rev. Lett.* 85 (5 2000), pp. 1016–1019.
- [393] W. Dong et al. "Collective nonlinear electric polarization via defect-driven local symmetry breaking." In: *Mater. Horiz.* 6 (8 2019), pp. 1717–1725.
- [394] S. Liu and R. E. Cohen. "Multiscale simulations of defect dipole-enhanced electromechanical coupling at dilute defect concentrations." In: *Applied Physics Letters* 111.8 (2017), p. 082903.

- [395] H. Zhang, A. H. H. Ramadan, and R. A. D. Souza. "Atomistic simulations of ion migration in sodium bismuth titanate (NBT) materials: towards superior oxide-ion conductors." In: *Journal of Materials Chemistry A* 6.19 (2018), pp. 9116–9123.
- [396] K. Okhotnikov, T. Charpentier, and S. Cadars. "Supercell program: a combinatorial structure-generation approach for the local-level modeling of atomic substitutions and partial occupancies in crystals." In: *Journal of Cheminformatics* 8 (2016), p. 17.
- [397] R. D. Shannon. "Revised effective ionic radii and systematic studies of interatomic distances in halides and chalcogenides." In: *Acta Crystallographica Section A* 32.5 (1976), pp. 751–767.
- [398] F. Yang, J. S. Dean, Q. Hu, P. Wu, E. Pradal-Velázquez, L. Li, and D. C. Sinclair. "From insulator to oxide-ion conductor by a synergistic effect from defect chemistry and microstructure: acceptor-doped Bi-excess sodium bismuth titanate $\text{Na}_{0.5}\text{Bi}_{0.51}\text{TiO}_{3.015}$." In: *J. Mater. Chem. A* 8 (47 2020), pp. 25120–25130.
- [399] T. Frömling *oral communication*. "Conductivity and defect chemistry in sodium bismuth titanate." en. oral communication. 2019.
- [400] C. W. M. Castleton, J. Kullgren, and K. Hermansson. "Tuning LDA+U for electron localization and structure at oxygen vacancies in ceria." In: *The Journal of Chemical Physics* 127.24 (2007), p. 244704.
- [401] X. He and Y. Mo. "Accelerated materials design of $\text{Na}_{0.5}\text{Bi}_{0.5}\text{TiO}_3$ oxygen ionic conductors based on first principles calculations." In: *Physical Chemistry Chemical Physics* 17.27 (2015), pp. 18035–18044.
- [402] L. Zhang, B. Liu, H. Zhuang, P. R. C. Kent, V. R. Cooper, P. Ganesh, and H. Xu. "Oxygen vacancy diffusion in bulk SrTiO_3 from density functional theory calculations." In: *Computational Materials Science* 118 (June 2016), pp. 309–315.
- [403] G. Kresse and J. Hafner. "Ab initio molecular-dynamics simulation of the liquid-metal-amorphous-semiconductor transition in germanium." In: *Physical Review B* 49.20 (1994), pp. 14251–14269.
- [404] G. Kresse. "Ab initio molecular dynamics for liquid metals." In: *Journal of Non-Crystalline Solids. Structure of Non-Crystalline Materials* 6 192-193 (1995), pp. 222–229.
- [405] I. Abrahams, A. Bush, G. Hawkes, and T. Nunes. "Structure and Oxide Ion Conductivity Mechanism in $\text{Bi}_2\text{Al}_4\text{O}_9$ by Combined X-Ray and High-Resolution Neutron Powder Diffraction and ^{27}Al Solid State NMR." In: *Journal of Solid State Chemistry* 147.2 (1999), pp. 631–636.
- [406] F. Oudich, N. David, S. Mathieu, and M. Vilasi. "Phase equilibria investigations and thermodynamic modeling of the system $\text{Bi}_2\text{O}_3\text{--Al}_2\text{O}_3$." In: *Journal of Nuclear Materials* 457 (2015), pp. 72–79.
- [407] D Massiot, C Bessada, J. Coutures, and F Taulelle. "A quantitative study of ^{27}Al MAS NMR in crystalline YAG." In: *Journal of Magnetic Resonance* (1969) 90.2 (1990), pp. 231–242.

- [408] P. B. Groszewicz, H. Breitzke, W. Jo, J. Rödel, and G. Buntkowsky. "Local structure of the B-site in BNT-xBT investigated by $^{47,49}\text{Ti}$ NMR: Effect of barium content." In: *Journal of Applied Physics* 121.11 (2017), p. 114104.
- [409] Y. Watanabe, Y. Hiruma, H. Nagata, and T. Takenaka. "Fabrication and Electrical Properties of $(\text{Bi}_{1/2}\text{Na}_{1/2})\text{TiO}_3\text{-BiAlO}_3$ Ferroelectric Ceramics." In: *Electroceramics in Japan XI*. Vol. 388. Key Engineering Materials. Trans Tech Publications, 2009, pp. 229–232.
- [410] J. Koettgen, S. Grieshammer, P. Hein, B. O. H. Grope, M. Nakayama, and M. Martin. "Understanding the ionic conductivity maximum in doped ceria: trapping and blocking." In: *Physical Chemistry Chemical Physics* 20.21 (2018), pp. 14291–14321.
- [411] Y. S. Sung, J. M. Kim, J. H. Cho, T. K. Song, M. H. Kim, H. H. Chong, T. G. Park, D. Do, and S. S. Kim. "Effects of Na-nonstoichiometry in $(\text{Bi}_{0.5}\text{Na}_{0.5+x})\text{TiO}_3$ ceramics." In: *Applied Physics Letters* 96.2 (2010), p. 022901.
- [412] Y. S. Sung, J. M. Kim, J. H. Cho, T. K. Song, M. H. Kim, and T. G. Park. "Effects of Bi nonstoichiometry in $(\text{Bi}_{0.5+x}\text{Na})\text{TiO}_3$ ceramics." In: *Applied Physics Letters* 98.1 (2011), p. 012902.
- [413] C. Lin, C. Mitra, and A. A. Demkov. "Orbital ordering under reduced symmetry in transition metal perovskites: Oxygen vacancy in SrTiO_3 ." In: *Physical Review B* 86.16 (2012), p. 161102.
- [414] J. Maier. "Mass Transport in the Presence of Internal Defect Reactions—Concept of Conservative Ensembles: II, Evaluation of Electrochemical Transport Measurements." In: *Journal of the American Ceramic Society* 76.5 (1993), pp. 1218–1222.
- [415] K.-C. Meyer. "Phase Transformation Kinetics and Oxygen Transport in the Relaxor Ferroelectric $\text{Na}_{1/2}\text{Bi}_{1/2}\text{TiO}_3$ studied by First-Principles Calculations." PhD thesis. Technische Universität, 2017. URL: <http://tuprints.ulb.tu-darmstadt.de/6517/>.
- [416] G. Trimarchi, Z. Wang, and A. Zunger. "Polymorphous band structure model of gapping in the antiferromagnetic and paramagnetic phases of the Mott insulators MnO, FeO, CoO, and NiO." In: *Physical Review B* 97.3 (2018), p. 035107.
- [417] P. Erhart and K. Albe. "Thermodynamics of mono- and di-vacancies in barium titanate." In: *Journal of Applied Physics* 102.8 (2007), p. 084111.
- [418] J. P. Allen and G. W. Watson. "Occupation matrix control of d- and f-electron localisations using DFT + U." In: *Physical Chemistry Chemical Physics* 16.39 (2014), pp. 21016–21031.
- [419] T. Zacherle, A. Schriever, R. A. De Souza, and M. Martin. "Ab initio analysis of the defect structure of ceria." In: *Physical Review B* 87.13 (2013), p. 134104.
- [420] M. Swift, A. Janotti, and C. G. Van de Walle. "Small polarons and point defects in barium cerate." In: *Physical Review B* 92.21 (2015).
- [421] P. Erhart, A. Klein, D. Åberg, and B. Sadigh. "Efficacy of the DFT + U formalism for modeling hole polarons in perovskite oxides." In: *Physical Review B* 90.3 (July 2014). (Visited on 06/28/2018).

- [422] H. Raebiger, S. Lany, and A. Zunger. "Charge self-regulation upon changing the oxidation state of transition metals in insulators." In: *Nature* 453.7196 (2008), pp. 763–766.
- [423] H. Katayama-Yoshida and A. Zunger. "Exchange-Correlation-Induced Negative Effective U." In: *Physical Review Letters* 55.15 (1985), pp. 1618–1621.
- [424] G. M. Dalpian, Q. Liu, C. C. Stoumpos, A. P. Douvalis, M. Balasubramanian, M. G. Kanatzidis, and A. Zunger. "Changes in charge density vs changes in formal oxidation states: The case of Sn halide perovskites and their ordered vacancy analogues." In: *Physical Review Materials* 1.2 (2017), p. 025401.
- [425] G. M. Dalpian, Q. Liu, J. Varignon, M. Bibes, and A. Zunger. "Bond disproportionation, charge self-regulation, and ligand holes in s – p and in d-electron ABX₃ perovskites by density functional theory." In: *Physical Review B* 98.7 (2018), p. 075135.
- [426] M. Vračar, A. Kuzmin, R. Merkle, J. Purans, E. A. Kotomin, J. Maier, and O. Mathon. "Jahn-Teller distortion around Fe⁴⁺ in Sr(Fe_xTi_{1-x})O_{3-δ} from x-ray absorption spectroscopy, x-ray diffraction, and vibrational spectroscopy." In: *Physical Review B* 76.17 (2007), p. 174107.
- [427] Q. Liu, G. M. Dalpian, and A. Zunger. "Antidoping in Insulators and Semiconductors Having Intermediate Bands with Trapped Carriers." In: *Physical Review Letters* 122.10 (2019), p. 106403.
- [428] M. J. Gillan. "The elastic dipole tensor for point defects in ionic crystals." In: *Journal of Physics C: Solid State Physics* 17.9 (1984), pp. 1473–1488.
- [429] M. J. Aziz. "Thermodynamics of diffusion under pressure and stress: Relation to point defect mechanisms." In: *Applied Physics Letters* 70.21 (1997), pp. 2810–2812.
- [430] J. S. Wróbel, M. R. Zemła, D. Nguyen-Manh, P. Olsson, L. Messina, C. Domain, T. Wejrzanowski, and S. L. Dudarev. *Elastic dipole tensors and relaxation volumes of point defects in concentrated random magnetic Fe-Cr alloys*. 2020. arXiv: [2007.15424](https://arxiv.org/abs/2007.15424) [[cond-mat.mtrl-sci](https://arxiv.org/abs/2007.15424)].
- [431] E. Finazzi, C. Di Valentin, G. Pacchioni, and A. Selloni. "Excess electron states in reduced bulk anatase TiO₂: Comparison of standard GGA, GGA+U, and hybrid DFT calculations." In: *The Journal of Chemical Physics* 129.15 (2008), p. 154113.
- [432] U. Aschauer and N. A. Spaldin. "Interplay between strain, defect charge state, and functionality in complex oxides." In: *Applied Physics Letters* 109.3 (2016), p. 031901.
- [433] Y. Qiao, W. Li, Y. Zhao, Y. Zhang, W. Cao, and W. Fei. "Local Order and Oxygen Ion Conduction Induced High-Temperature Colossal Permittivity in Lead-Free Bi_{0.5}Na_{0.5}TiO₃-Based Systems." In: *ACS Applied Energy Materials* 1.3 (2018), pp. 956–962.
- [434] M. Moreau, S. M. Selbach, and T. Tybell. "Octahedral coupling in (111)- and (001)-oriented La_{2/3}Sr_{1/3}MnO₃/SrTiO₃ heterostructures." In: *Journal of Applied Physics* 124.18 (2018), p. 185301.

- [435] J. C. Wojdeł, P. Hermet, M. P. Ljungberg, P. Ghosez, and J. Íñiguez. “First-principles model potentials for lattice-dynamical studies: general methodology and example of application to ferroic perovskite oxides.” In: *Journal of Physics: Condensed Matter* 25.30 (2013), p. 305401.
- [436] C. Escorihuela-Sayalero, J. C. Wojdeł, and J. Íñiguez. “Efficient systematic scheme to construct second-principles lattice dynamical models.” In: *Physical Review B* 95.9 (2017).
- [437] *Multibinit*. URL: <https://docs.abinit.org/guide/multibinit/>.
- [438] C. Varvenne, O. Mackain, L. Proville, and E. Clouet. “Hydrogen and vacancy clustering in zirconium.” In: *Acta Materialia* 102 (2016), pp. 56–69.
- [439] C. Varvenne, O. Mackain, and E. Clouet. “Vacancy clustering in zirconium: An atomic-scale study.” In: *Acta Materialia* 78 (2014), pp. 65–77.
- [440] J. M. Polfus, B. Yildiz, and H. L. Tuller. “Origin of fast oxide ion diffusion along grain boundaries in Sr-doped LaMnO₃.” In: *Physical Chemistry Chemical Physics* 20.28 (2018), pp. 19142–19150.
- [441] T. Albright, J. Burdett, and M. Whangbo. *Orbital Interactions in Chemistry*. Wiley, 2013.
- [442] M. Dresselhaus, G. Dresselhaus, and A. Jorio. *Group Theory: Application to the Physics of Condensed Matter*. Springer Berlin Heidelberg, 2007.
- [443] I. I. Mazin and V. I. Anisimov. “Insulating gap in FeO: Correlations and covalency.” In: *Physical Review B* 55.19 (1997), pp. 12822–12825.
- [444] B. R. McGarvey and J. Telser. “Simple Ligand-Field Theory of d₄ and d₆ Transition Metal Complexes with a C₃ Symmetry Axis.” In: *Inorganic Chemistry* 51.11 (2012), pp. 6000–6010.
- [445] P. V. C. Medeiros, S. Stafström, and J. Björk. “Effects of extrinsic and intrinsic perturbations on the electronic structure of graphene: Retaining an effective primitive cell band structure by band unfolding.” In: *Physical Review B* 89.4 (2014), p. 041407.
- [446] P. V. C. Medeiros, S. S. Tsirkin, S. Stafström, and J. Björk. “Unfolding spinor wave functions and expectation values of general operators: Introducing the unfolding-density operator.” In: *Physical Review B* 91.4 (2015), p. 041116.